



Optical and magnetic control of exciton valley pseudospin in layered two-dimensional semiconductors

Thomas Patrick Lyons

Department of Physics and Astronomy
The University of Sheffield

This thesis is submitted for the degree of
Doctor of Philosophy

December 2019

Abstract

The experiments detailed in this thesis bring together two well established fields within solid state physics, namely the optical properties of Coulomb-bound complexes known as excitons, and the application of novel quantum degrees of freedom towards information processing, storage and communication. The material basis for these investigations are the monolayer transition metal dichalcogenides (TMDs), atomically thin direct band gap semiconductors which exhibit exceptional coupling to light, via tightly bound exciton states which are stable beyond room temperature. These materials may be easily thinned down to single atomic monolayers, in which a unique regime of broken crystal inversion symmetry, time reversal symmetry, and strong spin-orbit coupling together give rise to a valley pseudospin, which acts as a spin-1/2 degree of freedom for charge carriers and excitons alike. Robust optical selection rules allow selective addressability of the exciton valley pseudospin via circularly polarised light, paving the way towards all-optical valley computation or memory.

Here, various ways in which the exciton valley pseudospin may be enhanced or controlled are explored. In Chapter 4, the interaction between negatively charged exciton valley pseudospin and strong magnetic fields is discussed, where lifting of degeneracy of opposite valley states is demonstrated, leading to new understanding of the valley magnetism. In Chapter 5, monolayer TMDs are embedded in energy-tunable zero dimensional optical microcavities, in which the TMD excitons strongly couple to the confined photonic modes, forming composite quasiparticles known as exciton-polaritons. By control of the optical density of states via tuning of cavity length, the signatures of exciton valley pseudospin in emission may be enhanced by several times relative to the uncoupled monolayer. Finally, in Chapter 6, a monolayer TMD is placed in direct proximity to a ferromagnetic van der Waals layered material, realising an exciton valley pseudospin switch controllable via milliTesla range magnetic fields.

List of Publications

Journal Publications

S. Dufferwiel, **T. P. Lyons**, D. D. Solnyshkov, A. A. P. Trichet, F. Withers, S. Schwarz, G. Malpuech, J. M. Smith, K. S. Novoselov, M. S. Skolnick, D. N. Krizhanovskii, A. I. Tartakovskii, “*Valley addressable polaritons in atomically thin semiconductors*”, Nature Photonics **11**, 497-501 (2017)

S. Dufferwiel, **T. P. Lyons**, D. D. Solnyshkov, A. A. P. Trichet, A. Catanzaro, F. Withers, G. Malpuech, J. M. Smith, K. S. Novoselov, M. S. Skolnick, D. N. Krizhanovskii, A. I. Tartakovskii, “*Valley coherent exciton-polaritons in a monolayer semiconductor*”, Nature Communications **9**, 4797 (2018)

T. P. Lyons, S. Dufferwiel, M. Brooks, F. Withers, T. Taniguchi, K. Watanabe, K. S. Novoselov, G. Burkard, A. I. Tartakovskii “*The valley Zeeman effect in inter- and intra-valley triions in monolayer WSe₂*”, Nature Communications **10**, 2330 (2019)

D. Polak, R. Jayaprakash, **T. P. Lyons**, A. Leventis, K. J. Fallon, H. Coulthard, D. G. Bossanyi, K. Georgiou, A. J. Petty II, J. Anthony, H. Bronstein, A. I. Tartakovskii, D. G. Lidzey, J. Clark, A. Musser, “*Manipulating matter with strong coupling: harvesting triplet excitons in organic exciton microcavities*”, submitted (2019)

T. P. Lyons, D. Gillard, A. Molina-Sánchez, A. Misra, F. Withers, A. Kozikov, T. Taniguchi, K. Watanabe, K. S. Novoselov, J Fernández-Rossier, A. I. Tartakovskii, “*Valley polarisation by spin-selective band hybridisation in MoSe₂ / CrBr₃ van der Waals heterostructures*”, in preparation (2019)

T. P. Lyons, J. Puebla, D. Gillard, P. Muduli, C. Louca, Y. Otani, A. I. Tartakovskii, “*Magnetic proximity effects on exciton-polaron valley dynamics*”, in preparation (2019)

A. Genco, D. Gillard, **T. P. Lyons**, S. Ahn, H. S. Shin, A. I. Tartakovskii, “*Observation of strong exciton-photon coupling in CVD-grown MoSe₂ / WSe₂ heterostructures*”, in preparation (2019)

Conference Contributions

"Suppression of inter-valley relaxation in monolayer WSe₂ with small magnetic fields" **Poster presentation**, Graphene Week, Warsaw, June 2016

"Suppression of inter-valley relaxation in monolayer WSe₂ with small magnetic fields" **Oral presentation**, UK Semiconductors, Sheffield, July 2016

"Van der Waals heterostructures in photonics and polaritonics" **Oral presentation**, The 12th International Symposium on Photonic and Electromagnetic Crystal Structures (PECS-XII), York, July 2016

"Exciton-polaritons in van der Waals heterostructures embedded in tunable microcavities" **Oral presentation**, Workshop on 2-D layered materials: synthesis, properties and applications, Zermatt, August 2016

"Suppression of inter-valley relaxation in monolayer WSe₂ with small magnetic fields" **Oral presentation**, TMD-UK, Bath, September 2016

"Valley addressable exciton-polaritons in MoSe₂" **Poster presentation**, Graphene Flagship EU-US workshop on 2D materials, heterostructures and devices, Manchester, October 2016

"Valley addressable exciton-polaritons in MoSe₂" **Oral presentation**, Graphene Flagship Work Package 1: Fundamental Science International Workshop, Villard de Lans, January 2017

"Magneto-spectroscopy and valley polaritonics with monolayer TMDs" **Oral presentation**, ATOM-OPTO Kick-Off International Workshop, Warsaw, May 2017

"Valley coherent exciton-polaritons in atomically thin semiconductors" **Oral presentation**, TMD-UK, Sheffield, July 2017

"Valley addressable exciton-polaritons in atomically thin semiconductors" **Oral presentation**, 18th International Conference on Modulated Semiconductor Structures (MSS-18), Penn State University, August 2017

"Exciton-polariton valley dynamics in atomically thin semiconductors" **Invited oral presentation**, International Conference on Optics of Excitons in Confined Systems (OECS), Bath, September 2017

“Valley polarization enhancement and switching in monolayer semiconductor-ferromagnet van der Waals heterostructures” **Oral presentation**, TMD-UK, Sheffield, July 2018

“Valley polarization enhancement and switching in monolayer semiconductor-ferromagnet van der Waals heterostructures” **Oral presentation**, Flatlands Beyond Graphene, Leipzig, September 2018

“Valley physics in ferromagnet-semiconductor van der Waals heterostructures” **Oral presentation**, Rank Prize Funds Symposium on Optoelectronics of 2-Dimensional Materials, Grasmere, April 2019

“Valley polarisation by spin-selective band hybridisation in $\text{MoSe}_2 / \text{CrBr}_3$ van der Waals heterostructures” **Poster presentation**, Spin Transport and Dynamics in new Geometries, Materials and Nanostructures - Gordon Research Conference, Les Diablerets, July 2019

Acknowledgements

Firstly, I would like to thank all members of the LDS group in Sheffield, past and present, who have contributed to the success of this thesis and made my time here all the more enjoyable. Particular thanks are due to my colleagues in the 2D materials sub-group, Armando, Luca, Panaiot, Dan, Charalambos, Robbie and Oleksandr, with whom I have shared many discussions and hours in the lab. I am grateful to Andrew Foster for going the extra mile in supervising my Masters project, and Stefan Schwarz for introducing me to the field of 2D materials during my undergraduate years, ultimately motivating me to take on the project which has since proven very fruitful and resulted in this thesis. I thank Evgeny Alexeev and Tillmann Godde for their respective training in sample fabrication and optical spectroscopy during the first months of my PhD, and Phil Taylor and Chris Vickers for their professionalism in keeping my cryostat supplied with helium year round, along with teaching me a lot of technical skills. I am indebted to all the excellent researchers with whom I have had the privilege to collaborate, in particular Freddie in Manchester/Exeter for his fabrication expertise, Matt in Konstanz for his crucial brainpower, and Jorge in Tokyo for hosting me at RIKEN. Without these collaborations, the results presented here would not have been possible. Special thanks go to Qingqing, Joe, and Alessandro for their friendship over the last years. Joe in particular is a good friend who has been with me since week one of the undergraduate physics course, right through to completion of the PhD. Together we have weathered everything the University of Sheffield has thrown at us for eight years and come out (mostly) alive!

Most prominently, the level of knowledge and skills I have developed directly from the training provided to me by Scott Dufferwiel is truly beyond measure - without his excellent guidance, my transition from student to researcher would certainly have been thrown into doubt. Huge thanks are also due to my supervisor Sasha, who has been the driving force behind all of the results I have achieved, and has been especially instrumental in my professional development, giving me great advice and the opportunity to travel the world presenting at conferences and visiting our collaborators.

Lastly, special thanks go to Jaz and my parents for their support and encouragement over the years.

Contents

List of figures	xv
1 Introduction	1
1.1 Background: 2-dimensional materials	1
1.2 Motivation: all-optical valleytronics for information processing	2
1.3 Scope of thesis	3
2 Optical properties of monolayer transition metal dichalcogenides	5
2.1 Molybdenum and tungsten disulphides and diselenides	5
2.1.1 Crystal structure	5
2.1.2 Electronic band structure	7
2.1.3 Spin and the valley pseudospin	8
2.1.4 Symmetry considerations: valley magnetism and Berry phase	10
2.1.5 Optical selection rules	13
2.2 Excitons	17
2.2.1 Quasi-hydrogenic binding energy	17
2.2.2 Optical signatures of excitons	20
2.3 Exciton valley pseudospin	22
2.3.1 Valley-orbit coupling	22
2.3.2 Exciton valley polarisation and coherence	24
2.3.3 The valley Zeeman effect	26
3 Experimental methods	29
3.1 Techniques of 2-D material sample fabrication	29
3.1.1 Exfoliation of monolayer films	29
3.1.2 Chemical vapour deposition	31
3.1.3 Flake transfer via viscoelastic stamping	33
3.1.4 Fabrication of van der Waals heterostructures	35

3.2	Micro-photoluminescence spectroscopy	38
3.2.1	Magneto-optical measurements	41
3.3	Optical microcavities	43
3.3.1	Distributed Bragg reflectors	43
3.3.2	Zero dimensional discrete photonic modes	45
3.3.3	Low temperature tunable open-access microcavity system	50
3.3.4	Open cavity data fitting procedure	52
4	The trion valley Zeeman effect in monolayer WSe₂	57
4.1	Background - intervalley and intravalley trions	58
4.2	hBN encapsulated monolayer WSe ₂	61
4.3	Optically probing the trion fine structure	62
4.3.1	Temperature dependent trion photoluminescence	64
4.3.2	Multiple peak fitting	65
4.4	Magneto-optical response of singlet and triplet trions	66
4.4.1	Trion peak substructure evolution under a magnetic field	66
4.4.2	Magnetic moment contributions to the observed line shifts	70
4.5	Full picture of the trion valley Zeeman effect in monolayer WSe ₂	73
4.5.1	Extraction of contributory g-factors	73
4.5.2	Landau level contribution	75
4.5.3	Significance of results	77
4.6	Summary	78
5	Exciton valley dynamics in the strong light-matter coupling regime	81
5.1	Background - exciton-polaritons in 2D materials	82
5.2	Monolayer films of MoSe ₂ and WSe ₂ on distributed Bragg reflectors	85
5.2.1	Anomalous valley polarisation of monolayer MoSe ₂	86
5.2.2	Control of exciton valley coherence in monolayer WSe ₂	87
5.3	Strong exciton-photon coupling in TMD monolayers	91
5.3.1	Exciton-polaritons in WSe ₂	91
5.3.2	Exciton-trion-polaritons in MoSe ₂	92
5.4	Valley addressable exciton-polaritons	95
5.4.1	Valley polarised polaritons in MoSe ₂ and WSe ₂	95
5.4.2	Valley coherent polaritons in WSe ₂	98
5.4.3	Coherent manipulation of polariton valley pseudospin	101
5.5	Cavity modified pseudospin relaxation dynamics	103
5.5.1	Valley depolarisation in a three level strongly coupled system	104

5.5.2	Pseudospin decoherence processes	108
5.6	Summary	110
6	Exciton valley physics in semiconductor-ferromagnet heterostructures	113
6.1	Background - ferromagnetism in 2D materials	114
6.2	MoSe ₂ / CrBr ₃ van der Waals heterostructures	116
6.2.1	Hole doping in optically pumped MoSe ₂ / CrBr ₃ interfaces	118
6.3	Polarisation resolved magneto-photoluminescence	122
6.4	Valley dependent proximity effects	124
6.4.1	Valley polarisation switching	124
6.4.2	Extraction of the effective Curie temperature	126
6.4.3	Lifting of valley degeneracy	127
6.4.4	High magnetic field regime	128
6.5	Spin dependent interlayer scattering	130
6.5.1	Heterobilayer electronic band structure	130
6.5.2	Valley selective non-radiative decay channel	131
6.6	Insight into ferromagnetic domain dynamics in CrBr ₃	134
6.6.1	Perpendicular magnetocrystalline anisotropy	135
6.6.2	Spontaneous magnetic nucleation	135
6.7	Summary	137
7	Conclusion	139
7.1	Summary of findings	139
7.2	Outlook	141
7.2.1	Optical routing of exciton-polariton valley pseudospin	141
7.2.2	Ferromagnetic proximity coupling to TMD exciton-polaritons	142
7.2.3	Enhanced valley splitting in MoSe ₂ on EuS substrates via interfacial magnetic exchange field	143
	References	145

List of figures

2.1	Crystal structure of monolayer group VI TMDs	6
2.2	Layer dependence of group VI TMD band structure	7
2.3	Valley pseudospin and spin-orbit splitting in momentum space	9
2.4	Berry curvature and the valley Hall effect	11
2.5	Chiral optical selection rules	15
2.6	Circular polarisation of MoS ₂ luminescence	17
2.7	Excitons in monolayer TMDs	19
2.8	Optical signatures of excitons	21
2.9	Valley-orbit coupling in the exciton dispersion	24
2.10	Valley polarisation and coherence	25
2.11	The valley Zeeman effect in monolayer WSe ₂	27
3.1	Exfoliation of monolayer films	30
3.2	Chemical vapour deposition growth of TMDs	32
3.3	Viscoelastic flake transfer	34
3.4	Fabrication of van der Waals heterostructures	36
3.5	Diagram of photoluminescence setup	39
3.6	Photograph of vector magnet system	42
3.7	Transfer matrix simulation of open cavity	45
3.8	Focused ion-beam milled concave structures	46
3.9	Cylindrical Laguerre-Gaussian and Ince-Gaussian mode profiles	48
3.10	Measurement of cavity Q-factor	49
3.11	Open tunable cavity system	51
3.12	Example of open cavity raw data	52
3.13	Fitting polariton spectra to coupled oscillator model	54
4.1	Gapped Dirac cones of trion dispersion in monolayer WSe ₂	59
4.2	Trion valley splitting in literature	60

List of figures

4.3	Microscope images of hBN encapsulated WSe ₂	61
4.4	Narrow trion photoluminescence in encapsulated WSe ₂	62
4.5	Scheme of singlet and triplet trions in WSe ₂	63
4.6	Zero field temperature dependence of WSe ₂ PL	64
4.7	Thermal population of triplet trion state	65
4.8	Multiple peak fitting to trion fine structure	66
4.9	Temperature dependent trion photoluminescence at non-zero B-fields	67
4.10	Trion photoluminescence magneto-optical response	68
4.11	Extracting peak shifts vs magnetic field	69
4.12	Extracted valley Zeeman peak shifts of trion fine structure	69
4.13	Energy level diagram for trion fine structure	72
4.14	Extracted energy separations between trion fine structure	74
4.15	Landau level effects in WSe ₂	76
4.16	Comparison of g-factors extracted by various methods	77
5.1	Illustration of coupled oscillator model and light-matter coupling	82
5.2	Exciton-polaritons in van der Waals heterostructures	84
5.3	Comparison of MoSe ₂ and WSe ₂ polarisation resolved photoluminescence	87
5.4	Valley coherence in monolayer WSe ₂	88
5.5	Control of exciton valley pseudospin in WSe ₂	89
5.6	Strong light-matter coupling in WSe ₂	91
5.7	Strongly coupled three level system in MoSe ₂	93
5.8	Anticrossing between MoSe ₂ trion and cavity mode	94
5.9	Extracted Hopfield coefficients for MoSe ₂ polariton states	95
5.10	Circular polarisation resolved spectra from MoSe ₂ at various detunings	96
5.11	Circular polarisation degree of MoSe ₂ vs detuning	97
5.12	Circular polarisation degree of WSe ₂ vs detuning	98
5.13	Linear polarisation resolved WSe ₂ polariton spectra at various detunings	99
5.14	Linear polarisation degree of WSe ₂ vs detuning	100
5.15	Orientation of polariton linearly polarised emission	100
5.16	Coherent manipulation of polariton valley pseudospin vector	101
5.17	Linear polarisation degree of LPB	102
5.18	Cavity modified exciton relaxation	104
5.19	Decay of valley coherence during exciton relaxation	109
6.1	Layer dependent ferromagnetism in CrI ₃	114
6.2	CrI ₃ / WSe ₂ van der Waals heterostructures	115

6.3	hBN / CrBr ₃ / MoSe ₂ / hBN van der Waals heterostructure	117
6.4	DFT calculated band structure of CrBr ₃ / MoSe ₂ heterobilayer	119
6.5	Type-II band alignment over CrBr ₃ / MoSe ₂ interface	121
6.6	Magneto-photoluminescence from CrBr ₃ / MoSe ₂ heterostructures	122
6.7	Polarisation resolved PL during B-field sweeps	123
6.8	Polarisation degree colourmaps in both sweep directions	125
6.9	Polarisation degree from integrated intensities both sweep directions	125
6.10	Comparison of trion polarisation degree under σ^+ and σ^- laser helicity	126
6.11	Temperature dependence of trion polarisation degree	127
6.12	Valley splitting extracted by Gaussian peak fitting	127
6.13	Valley polarisation and Zeeman splitting up to B = 8 T	129
6.14	DFT calculated band structure of CrBr ₃ / MoSe ₂ heterobilayer	130
6.15	Photoluminescence linewidths of exciton and trion	133
6.16	Spontaneous magnetic nucleation of CrBr ₃ domains	136
6.17	Magnetic ordering and anisotropy of CrI ₃ , CrBr ₃ , and CrCl ₃	137
7.1	Polariton waveguides and valley routers	141
7.2	Enhanced valley polarisation and Zeeman effect in MoSe ₂ on EuS	143

Chapter 1

Introduction

1.1 Background: 2-dimensional materials

Two dimensional materials are flat atomically thin crystals characterised by strong intralayer bonds and relatively weak interlayer van der Waals attraction. As such, they are intrinsically stable in the form of single atomically thin flakes, known as monolayers. Since the first discovery of the hexagonal 2D carbon lattice called graphene, a vast research field within condensed matter physics has risen to global prominence. Since then, the family of 2D materials has grown dramatically, now encompassing excellent electrical conductors, insulators, indirect and direct gap semiconductors, topological insulators, superconductors, and most recently ferromagnets and antiferromagnets. The ubiquity of 2D material research around the world has been accelerated by the ease of access to the materials, which are quite cheap, and the fact that samples can be made by just about anybody, with only a piece of sticky tape, using the exfoliation method originally demonstrated for graphene. This considerably lowers the funding bar for entry into the field, as expensive epitaxial deposition and lithography technology are not required to produce research-quality samples. Indeed, some of the most remarkable and ground breaking scientific discoveries surrounding 2D materials have been made with samples cobbled together on dusty office desks, a far cry from the world of highly controlled cleanroom nanofabrication.

The inherent geometry of 2D materials is responsible for much of their scientific interest; they represent a material platform to study solid state physics and quantum phenomena at the ultimate 2-dimensional limit, in the extreme of surface to volume ratio. The reduced dimensionality and associated quantum confinement lead to a variety of intriguing effects, as will be discussed in Chapter 2. The van der Waals attraction of monolayers to adjacent surfaces opens many prospects for incorporation of active monolayers onto any conceivable substrate, not even limited to being flat, with monolayers variously suspended over holes,

draped over micropillars or nanobeams, incorporated into photonic crystals, dispersed in inks for printing, and even implanted into living tissue for biosensing. However, a notable advantage of the van der Waals attraction is the ability to stack different 2D monolayers on top of one another, to form so-called *van der Waals heterostructures*, which may be designed arbitrarily to perform any desired device capability, from light emitting diodes to transistors or photodetectors, all on the nanometre scale.

Overall, 2D materials represent a very versatile and cheap material platform to develop future technology. Recent gains in the quality of large area grown monolayers and heterostructures are opening new routes towards scalability and mass production. Furthermore, the inherently atomic thicknesses of 2D materials make them eminently suitable for the miniaturisation of technology, combined with their mechanical flexibility and semi-transparent characteristics, meaning they may easily be incorporated into ergonomic devices of the future.

1.2 Motivation: all-optical valleytronics for information processing

As will be discussed throughout this thesis, certain 2D materials possess an unusual property whereby their electronic band structure features multiple degenerate energy extrema at different points within the Brillouin zone. Owing to the generally parabolic shape of these band minima and maxima, they are termed valleys, and can effectively localise free electrons or holes in their local potential in momentum space. This gives rise to a new degree of freedom for unbound charge carriers, known as a valley degree of freedom. In analogy to electronic spin, which has been proposed as an information carrier in a field of research called spintronics, the valley degree of freedom has been proposed as a spin-1/2 system in which information may theoretically be encoded, manipulated or stored. This has given rise to a field of research generally termed *valleytronics*, which explores methods of control of the valley degree of freedom in these materials for the aim of applications in information technology. As will be introduced in Chapter 2, excitons are quasiparticles found in semiconducting 2D materials which can also experience a valley degree of freedom. Excitons are also highly amenable to optical interfacing, as they can be created and annihilated with absorption or emission of a photon. As such, excitons offer a bridge to realise all-optical valley information processing, which would take advantage of the high speed of optical communications, avoid the heating inherent to electrical charge currents, and may even offer a route to valley-based quantum computing.

1.3 Scope of thesis

This thesis opens with a review of relevant literature, starting with the crystal structure of monolayer transition metal dichalcogenides, encompassing the electronic band structure and valley pseudospin, Coulomb bound states known as excitons, and ending on the concept of exciton valley pseudospin. Then follows a methods chapter, covering sample fabrication, details of the equipment used to obtain the experimental results presented here, and some discussion of the more complex aspects of data analysis which have been required. Chapters 4, 5, and 6 each then present a self contained experimental project, all sharing the common theme of gaining control of the excitonic valley degree of freedom. “Control” in this context means either inducing a desired energy shift or lifting of degeneracy between given excitonic valley states, or inducing a population imbalance of occupation of opposite valley states, i.e. creating a static valley pseudospin polarisation. All of the experimental results presented in this thesis are acquired by optical investigations; electrical control of exciton valley pseudospin is not considered. Various experimental tools are applied to gain control of the valley pseudospin, such as strong or weak external magnetic fields (Chapters 4, 5, 6), or optical microcavities (Chapter 5), or ferromagnetic proximity effects (Chapter 6).

In each of Chapters 4, 5 and 6, the presentation of optical experimental data is followed by supporting theoretical calculations, developed by collaborators. In Chapter 4, a theoretical framework is constructed to quantitatively describe the observed behaviour. The derived equations are then applied to the data to extract valley Zeeman g-factors of each of the four fine structure components of the negatively charged trion in monolayer WSe₂. In Chapter 5, a rate equation model is devised to describe the transfer of excitons between opposite valley states, and between reservoir and polariton states. By feeding parameters from literature into the model, the observed experimental data can be reproduced. In Chapter 6, the theoretical contribution is purely in the calculation of the electronic band structure of the semiconductor-ferromagnet heterostructure, which allows the optical data to be interpreted.

All of the results presented in this thesis may be considered as fundamental science; any references to technological applications are purely for motivation and context. The demonstration of all-optical valleytronic exciton-based prototype devices which may be implemented for information processing or data memory are beyond the scope of this thesis. As the entire family of 2D materials, and especially the monolayer transition metal dichalcogenides, are a relatively recent discovery in the monolayer form, their innate properties must first be understood before applications may be developed. This thesis contributes to the physical understanding of this new class of semiconductors.

Chapter 2

Optical properties of monolayer transition metal dichalcogenides

This chapter presents a broad overview of the properties of semiconducting 2D materials, most prominently the transition metal dichalcogenides (TMDs) molybdenum disulphide (MoS_2), molybdenum diselenide (MoSe_2), tungsten disulphide (WS_2), and tungsten diselenide (WSe_2). These materials are direct band gap semiconductor analogues of graphene, and as such offer a range of excellent properties complementary to those of the first known 2D carbon material. In particular, the optical properties of these 2D films are highly promising for the development of optoelectronic devices on the nanoscale.

2.1 Molybdenum and tungsten disulphides and diselenides

2.1.1 Crystal structure

Group VI TMDs of the form MX_2 where M is a transition metal such as Mo or W, and X is a chalcogen such as S or Se, are layered materials similar to graphite or mica, characterised by covalent intralayer bonds and relatively weak electrostatic dipolar van der Waals attraction between adjacent layers. In the macroscopic, multilayered form, they are termed as *bulk crystals*, while each single covalently bonded sheet is known as a *monolayer* (Fig. 2.1).

Monolayer TMDs are most thermodynamically stable in the $2H$ (trigonal prismatic) crystal phase, although a metastable $1T$ (octahedral) phase also exists. In both cases, the monolayer consists of three atomic planes in the order $X - M - X$. In the $2H$ phase, the top and bottom chalcogen atoms are vertically aligned, giving an overall atomic stacking order of $A - B - A$. In the $1T$ phase, the chalcogen atoms are not vertically overlapping, and so the stacking is $A - B - C$ (Fig. 2.1). For the entirety of this work, only the most stable $2H$ phase

Optical properties of monolayer transition metal dichalcogenides

will be discussed, associated with highly symmetry dependent semiconductor properties as detailed in this chapter.

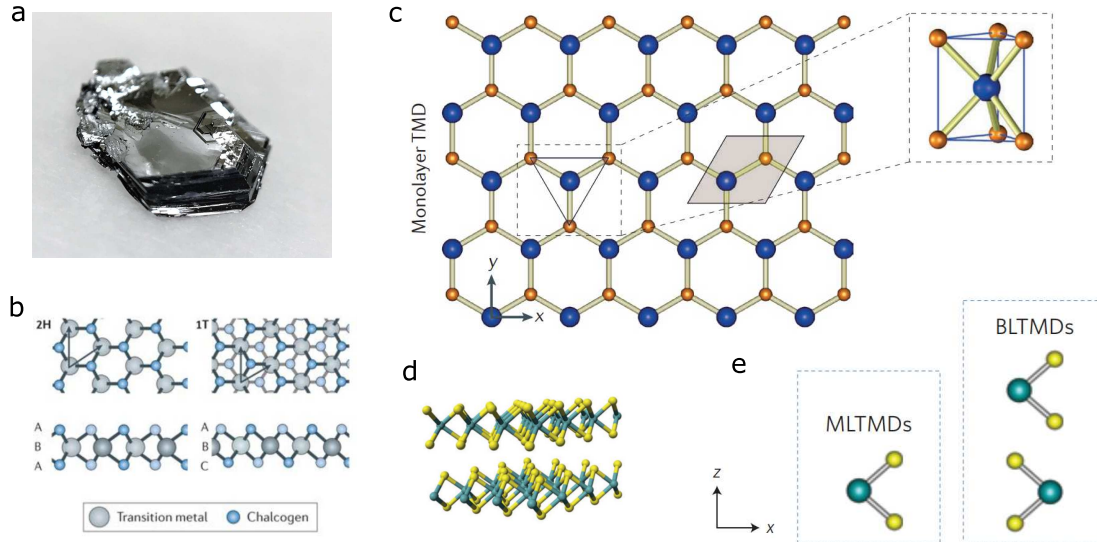


Fig. 2.1 (a) Photograph of a MoS₂ bulk crystal. *Image credit: 2D Semiconductors.* (b) Comparison of 2H and 1T monolayer crystalline phases. *Image from Ref [1].* (c) Top view of a monolayer 2H-TMD. The primitive cell, shaded in grey, contains either a single metal atom or two chalcogen atoms on each sublattice site. The side view, shown on the right, reveals the trigonal prismatic structure, lacking an inversion centre. *Image from Ref [2].* (d) Illustration of a bilayer 2H-TMD. Intralayer bonds are covalent, while interlayer bonds are van der Waals dipole type. *Image from Ref [3].* (e) Side views of the primitive cells of monolayer (ML) and bilayer (BL) 2H-TMDs. Inversion symmetry is broken in the monolayer, and restored in the bilayer. *Image from Ref [4].*

Multilayer stacking in the 2H phase has an $A - B - A - B \dots$ order, with a unit cell comprised of two monolayer unit cells, as shown in Fig. 2.1e. The bulk unit cell is inversion symmetric, being of the D_{6h}^4 point group, whereby the two monolayer unit cells are 180° in-plane rotations of one another, so the metal atoms of one monolayer are vertically aligned with the chalcogen atoms of the other monolayer, and vice versa. This creates an inversion axis about which symmetry is maintained. In a monolayer, however, the honeycomb lattice is comprised of two sublattices, with each sublattice site occupied by either a single metal atom or two chalcogen atoms (Fig. 2.1e). Therefore, in TMD monolayers, which are described by the D_{3h}^1 point group, inversion symmetry is explicitly broken. This can be seen from the trigonal prismatic cell in Fig. 2.1c: if the metal atom is taken as an inversion centre, and the six chalcogen atoms at position vectors \mathbf{r}_i are transformed to positions $-\mathbf{r}_i$, then each atom is mapped onto a vacant site [5, 3].

2.1.2 Electronic band structure

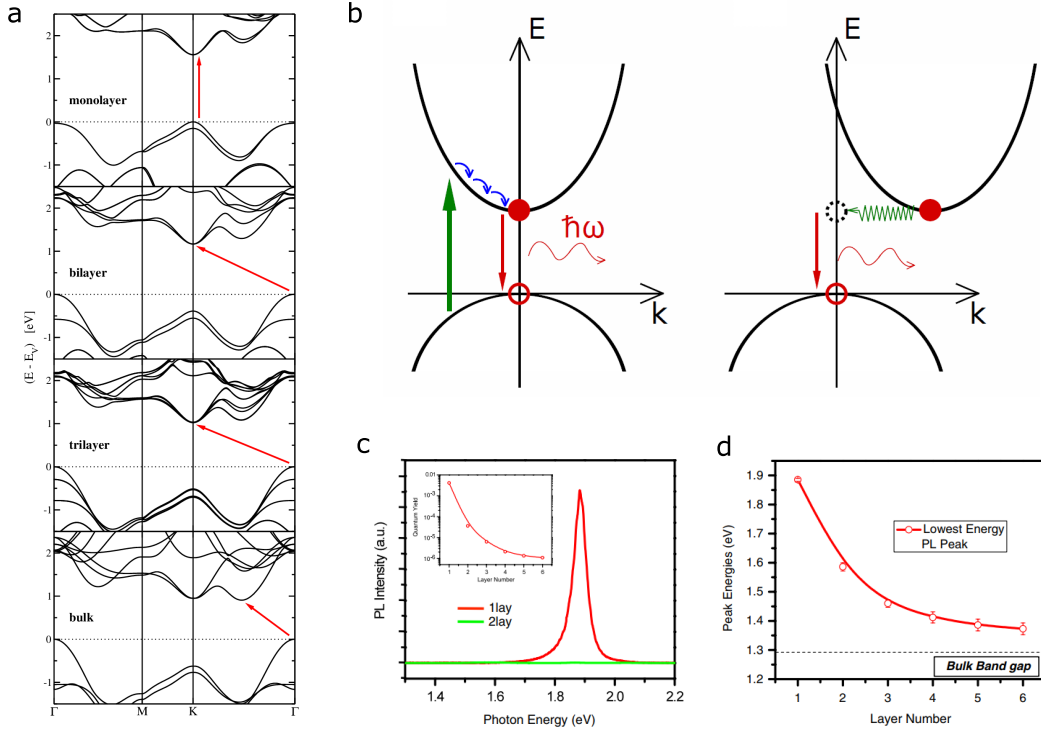


Fig. 2.2 (a) Band structure of mono-, bi-, tri-layer and bulk MoS₂ calculated by density functional theory (DFT). The lowest energy interband transition is marked by the arrow. *Image from Ref [6]*. (b) Comparison of interband radiative recombination in direct gap (left) and indirect gap (right) semiconductors. Radiative recombination must involve no change of momentum, and is therefore significantly less efficient in indirect gap materials, where a momentum transfer (for instance via a phonon) is necessary. (c) Comparison of luminescence intensity between bilayer and monolayer MoS₂. The indirect to direct band gap transition results in much higher quantum yield (inset figure). *Image from Ref [7]*. (d) Layer number dependence of the peak luminescence energy, reflecting the changing band structure. *Image from Ref [7]*.

In the bulk form, 2H-TMDs are indirect band gap semiconductors. They have a valence band (VB) maximum at the Γ point in the centre of the Brillouin zone, and a conduction band (CB) minimum half way between the Γ and K points, as shown in Fig. 2.2a. While the Γ point of the VB is comprised of a combination of anti-bonding p_z orbitals from the chalcogen atoms and d_{z^2} orbitals from the transition metal atoms, the $\pm K$ points are comprised predominantly of transition metal d -orbitals. This localises the electronic states at the $\pm K$ points within the transition metal atom plane, shielding them from any spatial overlap of orbitals from adjacent monolayers. Consequently, the Γ point is far more sensitive to decreasing layer number than

the $\pm K$ points, causing the indirect transition to become larger than the direct $\pm K$ energy gap (which remains largely unaffected) when going from the bilayer to the monolayer case. This indirect to direct band gap transition results in monolayer TMDs having a much stronger light-matter interaction than their multilayered counterparts, as no momentum transfer is required for the absorption or emission of photons (Fig. 2.2c). Once promoted into the CB, leaving behind a *hole* of effective charge +1 in the VB, an electron rapidly relaxes to the local band minimum. In direct gap semiconductors, the electron can easily recombine with the hole thanks to the equal wavevector between band extrema, emitting a photon of the band gap energy. If the band gap is indirect, the inequivalent carrier momenta must be compensated by interaction with a phonon, decreasing the recombination efficiency. The increased quantum yield of monolayer TMDs makes them particularly promising for optoelectronic applications on the extreme nanoscale. Along with a huge increase in emission intensity when crossing over from two layers to one, there is an accompanying energy shift of the luminescence, reflecting the changing band structure (Fig. 2.2d).

2.1.3 Spin and the valley pseudospin

In reciprocal space, the Brillouin zone of monolayer TMDs is hexagonal, with the CB and VB extrema located at the $+K$ and $-K$ points at the edges, as shown in Fig. 2.3. Although there are nominally six K-points in the Brillouin zone, three-fold rotation symmetry of the TMD monolayer lattice leads to reduction of the band structure to two inequivalent K symmetry points, often termed K and K'. At these points, the energy bands are quasi-parabolic, leading to their being termed *valleys*. The CB is an upright parabola while the VB is an upturned parabola, with the respective band extrema centred on the $\pm K$ points. Strong Zeeman-like spin-orbit coupling associated with the heavy transition metal *d*-orbitals, under the effect of strong quantum confinement in the single layer, lifts the degeneracy between spin states at these band extrema, with the spin splitting being of opposite sign in opposite valleys as a consequence of time reversal symmetry, $E_{\uparrow}(+K) = E_{\downarrow}(-K)$ (Fig. 2.3) [9, 11]. The spin projection on the *c*-axis perpendicular to the monolayer is well defined due to quantum confinement [11]. Fig. 2.3 shows DFT calculated energy bands at the $-K$ point of Mo and W based monolayers. In the VB, comprised of transition metal $d_{x^2-y^2}$ and d_{xy} orbitals hybridised as $d_{x^2-y^2} \pm id_{xy}$ in the $\pm K$ valleys, the spin splitting is typically hundreds of meV, while in the CB, comprised of d_{z^2} orbitals, the splitting is only up to tens of meV [3, 12]. Furthermore, the CB spin sub-bands are reversed between Mo and W based TMDs, which has significant consequences for optical properties of these materials, as detailed in Section 2.1.5. The energy bands at the $+K$ point will be time reversal partners of those plotted here.

2.1 Molybdenum and tungsten disulphides and diselenides

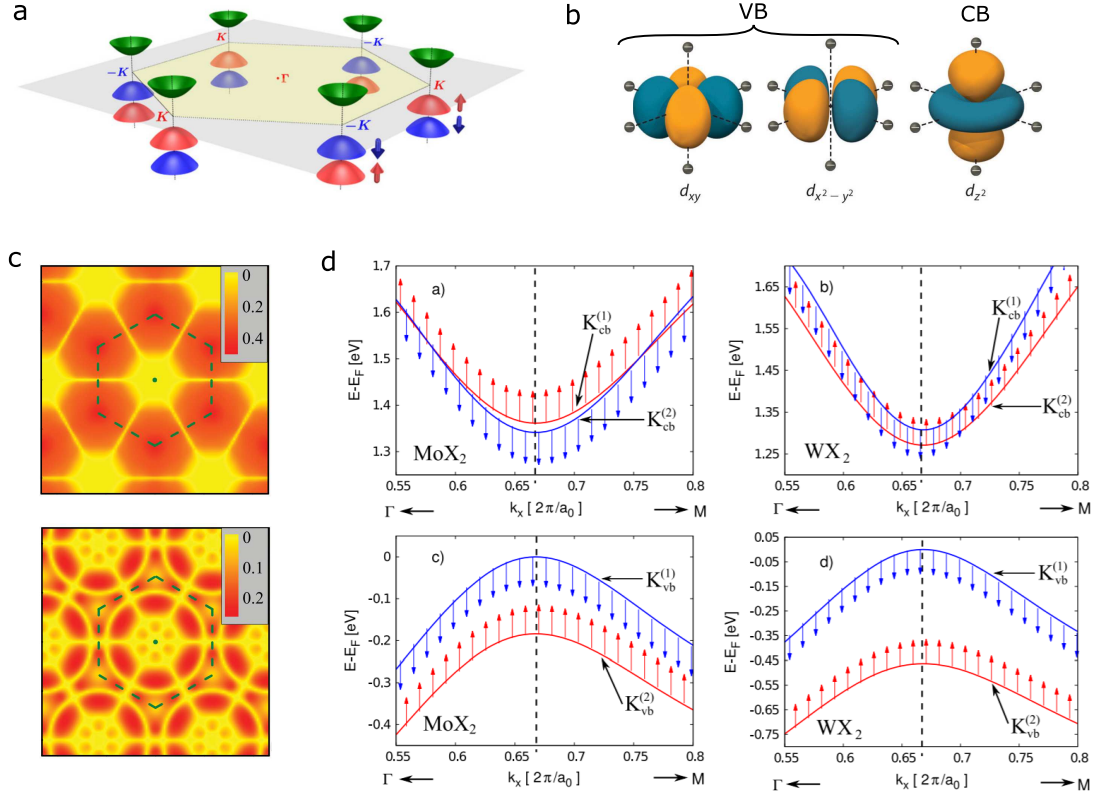


Fig. 2.3 (a) The hexagonal Brillouin zone of a monolayer TMD. The direct band gap is located at the $+K$ and $-K$ points at the corners. Strong spin-orbit coupling splits the valence band (VB) spin states into quasi-parabolic sub-bands, with the spin splitting related by time reversal symmetry between the $+K$ and $-K$ points. There is also spin splitting of the conduction band (CB), but this is much smaller than in the VB, and has opposite sign between Mo and W based TMDs. *Image from Ref [5]*. (b) Illustration of the different transition metal d -orbitals which constitute the VB and CB extrema at the $\pm K$ points. The x and y axes lie in the monolayer plane, and z is along the monolayer normal. *Image from Ref [8]*. (c) Calculated spin-orbit splitting in WSe_2 for the (top) VB and (bottom) CB. Scale bar units are eV. Dashed lines indicate the Brillouin zone. *Image from Ref [9]*. (d) Density functional theory (DFT) calculated energy bands at the $-K$ point of monolayer TMDs. Spin-orbit coupling polarises the spin states creating two spin sub-bands at the CB and VB edges. The spin splitting is of opposite sign in the conduction band of Mo based TMDs compared to W based materials. For each subfigure, the $+K$ energy bands are identical but with opposite spin states due to time reversal symmetry. The quasi-parabolic form of the bands gives rise to the term *valleys*. *Image from Ref [10]*.

An electron or hole can occupy a spin state in either the $+K$ or $-K$ valleys, and as such inherits a *valley degree of freedom*, termed a *valley pseudospin*, in that it acts much like a spin- $\frac{1}{2}$ system. A particle in the $+K$ valley can be termed valley pseudospin up, and in the $-K$ valley pseudospin down. In combination with the spin-orbit coupling and time reversal symmetry, the spin and valley pseudospin are considered *locked* together, as an electron of a fixed energy must occupy either the $+K$ or $-K$ valley depending on its spin. Single particle valley pseudospin is expected to be very robust, as a momentum transfer of the order of the inverse lattice constant would be required, along with an energetically unfavourable spin flip, for a carrier to scatter between valleys. A reversal of orbital angular momentum would also be required, as detailed in the next section [13]. As the spin-orbit splitting of the VB is much stronger than the CB, holes are expected to have particularly long valley lifetimes, experimentally measured to be ~ 1 ns at cryogenic temperatures [14]. Such robust valley lifetimes have led to proposals to utilise the valley pseudospin as an information carrier in much the same way as conventional spin, opening up the field of valleytronics, a cousin of spintronics.

2.1.4 Symmetry considerations: valley magnetism and Berry phase

The breaking of inversion symmetry in monolayer crystals has profound consequences for their electronic and optical properties. Two key physical quantities describing electrons of wavevector \mathbf{k} in reciprocal space are the Berry curvature $\mathbf{\Omega}(\mathbf{k})$, a pseudovector which modifies the equations of motion of Bloch electrons when perturbed by electric fields, and the magnetic moment $\mathbf{m}(\mathbf{k})$, which relates the orbital motion of electron wavepackets in momentum space to energy changes arising under an external magnetic field. In inversion symmetric structures, such as graphene or bilayer TMDs, then $\mathbf{\Omega}(\mathbf{k}) = \mathbf{\Omega}(-\mathbf{k})$ and $\mathbf{m}(\mathbf{k}) = \mathbf{m}(-\mathbf{k})$. In monolayer TMDs, however, the lack of an inversion centre allows the Berry curvature and magnetic moment to take inequivalent values at opposite wavevector \mathbf{k} .

Although spatial inversion symmetry is broken in monolayer TMDs, time reversal symmetry is upheld. Therefore, $\mathbf{\Omega}(\mathbf{k}) = -\mathbf{\Omega}(-\mathbf{k})$ and $\mathbf{m}(\mathbf{k}) = -\mathbf{m}(-\mathbf{k})$. The striking conclusion of broken inversion symmetry in the presence of time reversal symmetry is that these physical parameters take exactly opposite values at opposite points in momentum space. As such, the magnetic moments at the $\pm K$ points have the same magnitude but opposite sign. In this way, the valley pseudospin is associated with a unique magnetic moment in much the same way as conventional electron spin is associated with the Bohr magneton. Under an applied external magnetic field, the degeneracy between valley states is lifted in a process known as the *valley Zeeman effect*, in close analogy to the conventional spin Zeeman effect.

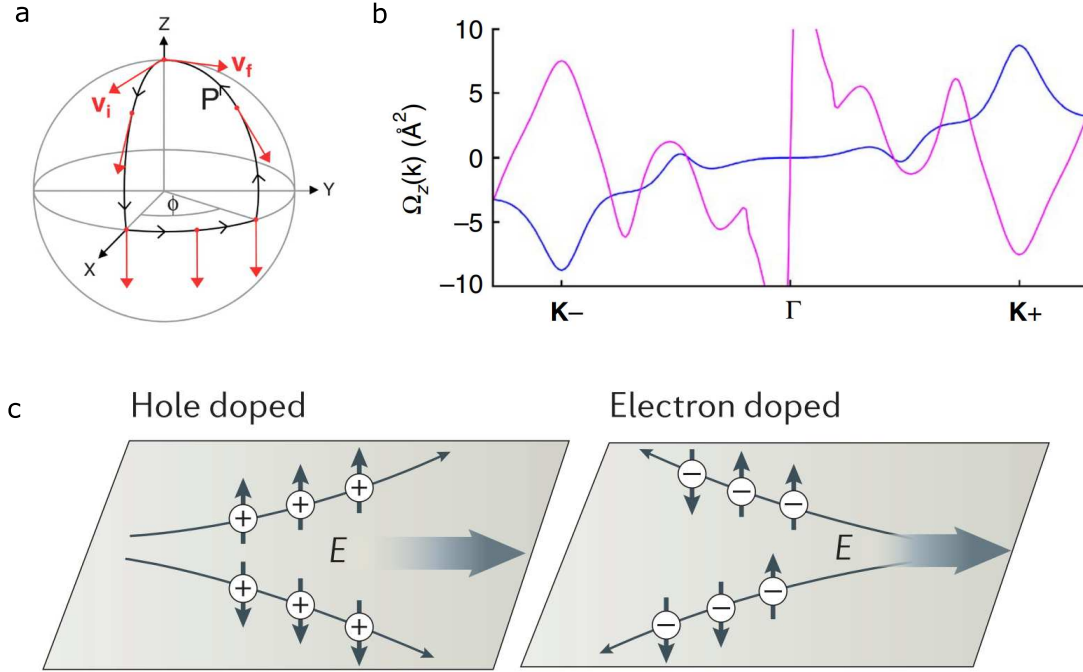


Fig. 2.4 (a) The parallel transport of a vector along a loop on a sphere is a classical analogue of the Berry phase. From the initial position at the north pole, with the vector pointing in the x direction, the vector moves along the surface of the sphere, along the path P . The direction of the vector relative to the surface does not change, it always remains tangential. After completing the loop, the vector returns to its original position, but it has now rotated by an angle ϕ , which is the Berry phase. The integral of the curvature of the surface bounded by the loop is the Berry curvature. If the surface was flat, with no curvature, then no phase change would occur after the loop. This analogue demonstrates the purely geometric origin of the Berry phase. *Image from Ref. [15]*. (b) Calculated Berry curvature in the out of plane direction, where $\mathbf{\Omega}_n(\mathbf{k}) = \mathbf{\Omega}_{n,z}(\mathbf{k})\hat{z}$, along the $-K \rightarrow \Gamma \rightarrow +K$ path of the MoS_2 Brillouin zone. The blue curve is the top of the VB, while the pink curve is the bottom of the CB. $\mathbf{\Omega}_z(\mathbf{k})$ has opposite sign between bands at the $\pm K$ points, and it is strong in the CB zone centre due to degeneracy of bands. *Image from Ref. [16]*. (c) Illustration of the valley Hall effect for holes and electrons. The transverse velocity is opposite in the CB and VB within the same valley, with opposite valleys related by time reversal symmetry. Particularly strong spin-orbit coupling in the VB leads to resultant transverse spin separation, which is weaker for electrons. *Image from Ref. [2]*.

To understand the Berry curvature, it is necessary to define the Berry phase. When the external parameters influencing a quantum state undergo a slow, adiabatic evolution and eventually return to their original values, thereby completing a loop in parameter space, the state will similarly return to its original value, although it will have acquired a phase difference, known as the Berry phase [17]. In the case of crystalline solids, the Bloch functions describing the potential landscape experienced by electrons in momentum space are periodic, and are therefore associated with a Berry phase, if allowed by crystal symmetries. Mathematically, the Berry phase may be expressed as an integral of a field known as the Berry curvature [2]. Fig. 2.4a demonstrates the purely geometric origin of the Berry phase and its relation to the geometric curvature. Very similar concepts exist beyond solid state physics, such as the phase associated with a charged particle in a loop enclosing a magnetic field, in this case known as the Aharonov-Bohm phase [17]. The Berry curvature is often considered as an effective magnetic field, although it acts in momentum space rather than real space. It can be shown that the velocity \mathbf{v}_n of a Bloch electron of wavevector \mathbf{k} in band n depends upon:

$$\mathbf{v}_n(\mathbf{k}) = \frac{\delta \varepsilon_n(\mathbf{k})}{\hbar \delta(\mathbf{k})} - \frac{e}{\hbar} \mathbf{E} \times \mathbf{\Omega}_n(\mathbf{k}) \quad (2.1)$$

where $\varepsilon_n(\mathbf{k})$ is the energy dispersion and $\mathbf{\Omega}_n(\mathbf{k})$ the Berry curvature of band n , and \mathbf{E} the electric field. For a derivation of Eq. 2.1 see Ref. [17]. The first term on the right hand side is the conventional group velocity of an electron in a solid, and the second term describes the anomalous velocity arising from the Berry curvature. In crystals simultaneously subject to both time reversal and inversion symmetries, such as graphene, the only permissible value of $\mathbf{\Omega}_n(\mathbf{k})$ is zero throughout the Brillouin zone. Therefore, Eq. 2.1 reduces to the simple gradient of the band dispersion. However, in monolayer TMDs, the valley-contrasting non-zero Berry curvature induces an anomalous velocity which is always transverse to the electric field. Fig. 2.4b shows the calculated z -component of Berry curvature of the CB and VB on the $-K \rightarrow \Gamma \rightarrow +K$ path of the MoS₂ Brillouin zone. As can be seen, $\mathbf{\Omega}_{n,z}(\mathbf{k})\hat{z}$ takes opposite signs in each band within the same valley. Electrons and holes of matching valley pseudospin therefore acquire transverse velocity in opposite directions when an electric field is applied in a TMD monolayer plane. Overall, the presence of non-zero Berry phase in monolayer TMDs indicates an underlying nontrivial topology of the band structure, where the modification to the electron Lorentz force is the origin of the *valley Hall effect*, in analogy to the spin Hall effect, although no magnetic field is required [18]. In a simple monolayer TMD with an in-plane electric field applied, time reversal symmetry dictates that $+K$ valley electrons will move to the same edge of the monolayer as $-K$ valley holes, therefore, no net transverse bias is generated. In order to utilise the valley Hall effect to generate Hall charge

currents, it is necessary to artificially break time reversal symmetry, and create a carrier population imbalance between the valleys [2]. As described in the next section, this can be achieved via the valley dependent optical selection rules.

2.1.5 Optical selection rules

To begin, we define the *circular dichroism*, η , as a function of \mathbf{k} :

$$\eta(\mathbf{k}) = \frac{|\mathcal{P}_+^{cv}(\mathbf{k})|^2 - |\mathcal{P}_-^{cv}(\mathbf{k})|^2}{|\mathcal{P}_+^{cv}(\mathbf{k})|^2 + |\mathcal{P}_-^{cv}(\mathbf{k})|^2} \quad (2.2)$$

which is the normalised difference between absorption strengths of σ^+ and σ^- polarised light in an interband transition, from the VB to the CB, at a given point in \mathbf{k} -space. $\mathcal{P}_\pm^{cv}(\mathbf{k})$ are the coupling strengths of interband transitions to σ^\pm optical fields, given by the interband matrix element of the canonical momentum operator [5, 19, 16].

Considering that monolayer TMDs have effectively two inequivalent sets of band extrema separated by the lowest band gap energy E_g , we introduce the index $\tau_K = \pm 1$ to denote an interband transition at the $\pm K$ point of the Brillouin zone. It can be shown (see Ref. [19]) that the valley dependent interband matrix elements may then be expressed as:

$$|\mathcal{P}_\pm^{cv}(\mathbf{k})|^2 = m_e^2 v_0^2 (1 \pm \tau_K \cos \theta)^2 \quad (2.3)$$

where m_e is the electron mass and v_0 the Fermi velocity (velocity associated with an electron moving with kinetic energy equal to the Fermi energy in the system), and $\cos \theta = E_g / [\varepsilon_c(\mathbf{k}) - \varepsilon_v(\mathbf{k})]$ [19]. Here, $\varepsilon_c(\mathbf{k})$ and $\varepsilon_v(\mathbf{k})$ are the CB and VB dispersion relations, respectively. Therefore, exactly at the K-points, $\cos \theta = 1$, and the matrix elements reduce to:

$$\begin{aligned} |\mathcal{P}_+^{cv}(+K)|^2 &= 4m_e^2 v_0^2 \\ |\mathcal{P}_-^{cv}(+K)|^2 &= 0 \\ |\mathcal{P}_+^{cv}(-K)|^2 &= 0 \\ |\mathcal{P}_-^{cv}(-K)|^2 &= 4m_e^2 v_0^2 \end{aligned} \quad (2.4)$$

which substitutes into Eq. 2.2 to give:

$$\eta(\pm K) = \pm 1 \quad (2.5)$$

corresponding to 100% coupling of interband transitions at the $\pm K$ points to σ^\pm helicities of light [19, 16]. Here lies justification for the immense scientific interest surrounding monolayer

Optical properties of monolayer transition metal dichalcogenides

TMDs, as they offer a direct and easy way to optically access the valley pseudospin, via these chiral optical selection rules, bringing opto-valleytronics into the realms of possibility.

Elsewhere in the Brillouin zone, away from the K-points, $\cos \theta$ is no longer equal to 1, and as such η diminishes. However, the reduction of η is relatively insensitive to \mathbf{k} close to the K-points, and η only rapidly changes sign at the midpoint between the K-points in the Brillouin zone, as shown in Fig. 2.5a [16]. This ensures the optical selection rules are robust even when addressing wavevectors slightly removed from the K-points, for instance when pumping the monolayer with light of energy $> E_g$.

The fundamental origin of the chiral optical selection rules in monolayer TMDs lies with intercellular phase winding of Bloch electrons in \mathbf{k} -space, described by periodic terms in the corresponding Bloch functions [20, 5, 16, 21, 22]. This form of orbital angular momentum is quantified by the valley contrasting magnetic moment introduced in the previous section, $\mathbf{m}(\mathbf{k})$. Considering that any orbital motion must occur in the monolayer plane, the angular momentum is always perpendicular to the plane, so can be expressed as $\mathbf{m}(\mathbf{k}) \cdot \hat{\mathbf{z}}$. The relation between interband matrix elements of circularly polarised optical fields, $\mathcal{P}_{\pm}^{cv}(\mathbf{k})$, incident along the z -axis, and the magnetic moment $\mathbf{m}(\mathbf{k}) \cdot \hat{\mathbf{z}}$, may be expressed as:

$$\mathbf{m}(\mathbf{k}) \cdot \hat{\mathbf{z}} = -\frac{\mu_B}{2} \left(\frac{|\mathcal{P}_{+}^{cv}(\mathbf{k})|^2 - |\mathcal{P}_{-}^{cv}(\mathbf{k})|^2}{m_e[\epsilon_c(\mathbf{k}) - \epsilon_v(\mathbf{k})]} \right) \quad (2.6)$$

where μ_B is the Bohr magneton [5, 19, 16]. The bracketed expression on the right hand side of Eq. 2.6 is simply the difference between oscillator strengths of σ^+ and σ^- polarised light as a function of wavevector, where the *oscillator strength* describes the probability of absorption or emission of a photon in a transition between VB \leftrightarrow CB. As such, it can be directly linked to the definition of circular dichroism, η , found in Eq. 2.2, and solved to find:

$$\eta(\mathbf{k}) = \frac{\mathbf{m}(\mathbf{k}) \cdot \hat{\mathbf{z}}}{\mu_B^*(\mathbf{k})} \quad (2.7)$$

where $\mu_B^*(\mathbf{k})$ is the *effective* Bohr magneton, which depends on the electron effective mass as $e\hbar/2m^*$. For a full derivation see Ref. [19]. As discussed in the previous section, inversion symmetry breaking and time reversal symmetry act on the magnetic moment to ensure that $\mathbf{m}(\mathbf{k}) = -\mathbf{m}(-\mathbf{k})$, i.e. the magnetic moment takes opposite values at opposite wavevectors. From Eq. 2.7, it becomes clear that $\eta(\mathbf{k})$ therefore must also take exactly opposite values at opposite \mathbf{k} . This reveals that the contrasting circular dichroism in the Brillouin zone of monolayer TMDs is a direct consequence of symmetry considerations. In essence, the circular dichroism appears because it is not prohibited by inversion symmetry, and it takes an extreme form at the high symmetry K-points, leading to the nominal 100% degree of circular polarisation in the region around the lowest energy band gap.

2.1 Molybdenum and tungsten disulphides and diselenides

Going further, we combine Eq. 2.5 with Eq. 2.7 to find that:

$$\mathbf{m}(\pm\mathbf{K}) \cdot \hat{\mathbf{z}} = \pm\mu_B^*(\pm\mathbf{K}) \quad (2.8)$$

indicating that μ_B^* quantifies the valley pseudospin magnetic moment much as μ_B quantifies the conventional spin magnetic moment. Nominally, $\mathbf{m}(\pm\mathbf{K})$ is equal between CB and VB, however, in reality the breakdown of electron-hole symmetry leads to some inequivalence between bands arising from carrier effective mass discrepancies [21]. Furthermore, μ_B^* is not a fundamental constant as the effective masses also differ between TMDs with different chemical composition [20].

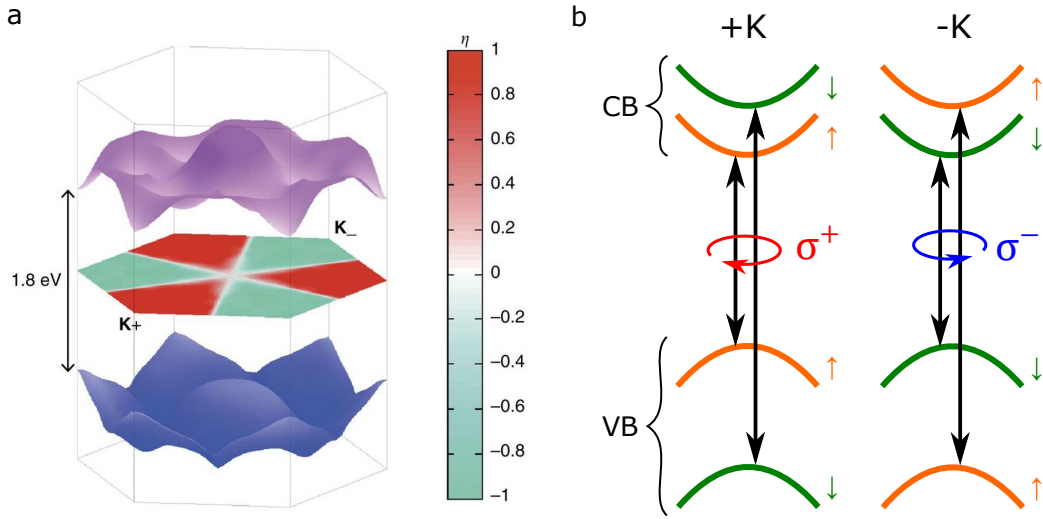


Fig. 2.5 (a) Modelled lowest conduction band (purple) and highest valence band (blue) over the Brillouin zone of monolayer MoS₂. The direct band gap is at the K-points with $E_g = 1.8$ eV. The hexagon is a colourmap of circular dichroism η (defined in Eq. 2.2) showing 100% chiral selectivity of optical transitions at the K-points. *Image from Ref. [16].* (b) Schematic of the band structure, incorporating spin-orbit coupling, of a Mo-based TMD monolayer around the K-points, showing the chiral optical selection rules. Interband optical transitions conserve spin and momentum, and have opposite circular polarization in opposite valleys. The arrows represent the electron spin in the given subband, related by time reversal symmetry between valleys. For W-based TMDs, the spin-orbit coupling in the conduction band has opposite sign. By choice of photon energy and helicity, both spin and valley pseudospin can be selectively optically addressed.

To complete the picture of the optical selection rules in monolayer TMDs, we must also consider the strong spin orbit coupling (discussed in Section 2.1.3) which splits the CB and VB edges into spin polarised subbands related by time reversal symmetry. As the chiral optical selection rules introduced here couple only to the orbital part of the electronic wavefunctions, spin is conserved in interband transitions [20, 5]. As such, the valley optical

Optical properties of monolayer transition metal dichalcogenides

selection rules also become spin optical selection rules, as light of appropriate energy and helicity can be used to create a spin polarisation in either valley. For example, pumping with σ^+ polarised light resonant with the band gap energy will populate photocarriers only into the lower spin subband of the +K valley. Likewise, measuring polarisation resolved emission provides information about the relative valley populations of free carriers. We can now schematically draw the valleys around the K-points along with the corresponding optical selection rules, as shown in Fig. 2.5b.

In emission, rather than absorption, the circular dichroism picture is slightly more complicated. This is because there is a characteristic timescale involved with radiative recombination of electron hole pairs, and this time window could allow some intervalley scattering of carriers, which would reduce the circular polarization in luminescence, defined similarly to η , as:

$$\rho = \frac{I_{co} - I_{cross}}{I_{co} + I_{cross}} \quad (2.9)$$

where ρ is the degree of circular polarisation, I_{co} (I_{cross}) is the intensity of photoluminescence co(cross)-circularly polarized to a pump laser. Indeed, early photoluminescence measurements on monolayer MoS₂ revealed circular polarization degrees lower than 1; ranging from ~ 0.3 to ~ 0.9 , as shown in Fig. 2.6 [16, 13, 11, 23].

A simple rate equation mode can be built to describe the polarisation degree in luminescence:

$$\frac{\rho}{\eta} = \frac{(1 - \delta)^2}{1 + \tau/\tau_v} \quad (2.10)$$

where $\eta \sim 1$ is the theoretical polarisation degree from the selection rules [16]. $(1 - \delta)^2$ is the valley selectivity of excitation, τ is the recombination time, and τ_v is the valley lifetime. Intervalley excitation may be allowed by scattering with impurities or phonons, and so $\delta = \delta_{imp} + \delta_{ph}$. The recombination time $\tau^{-1} = \tau_r^{-1} + \tau_{nr}^{-1}$ is the sum of radiative and non-radiative recombination timescales. Non-radiative decay may arise for instance due to carriers being trapped by defects or lost into the substrate. In a very clean sample, without crystal defects, and at low temperature to suppress phonons, δ should be small, and so Eq. 2.10 implies that $\rho < 1$ must arise from a short valley lifetime relative to the recombination time.

However, in monolayer TMDs, the valley lifetime is expected to be very robust, as a carrier scattering between valley states must undergo a transfer of momentum of the order of the inverse lattice constant, flip its spin, and reverse its orbital angular momentum described by $\mathbf{m}(\mathbf{k})$. Therefore, there must be another mechanism allowing relatively efficient intervalley relaxation. The explanation arises when considering that the optical response of monolayer

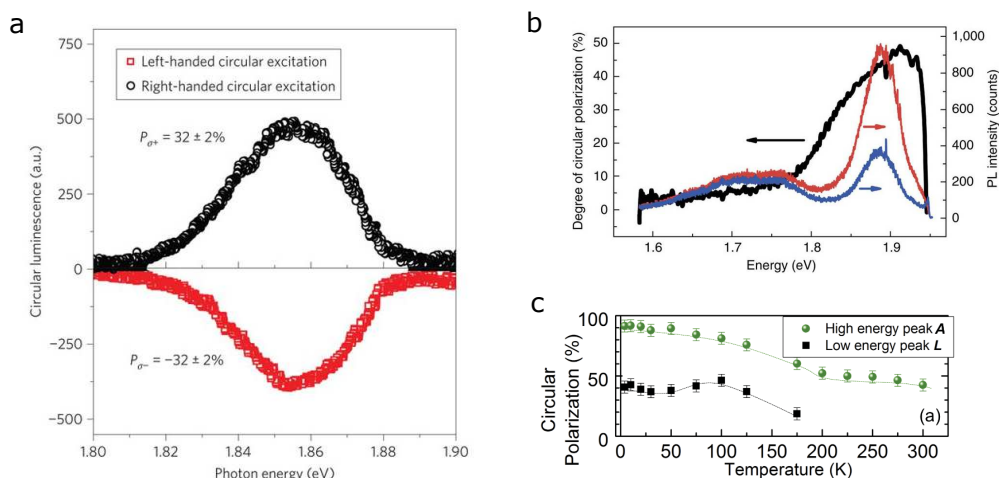


Fig. 2.6 Examples of early experimental reports of circular dichroism in photoluminescence in monolayer MoS₂. (a) Comparison of opposite polarisation degrees when exciting with σ^+ or σ^- polarised light, at cryogenic temperature, indicating selective population of time reversal symmetric valleys. *Image from Ref. [23]*. (b) Polarisation resolved photoluminescence spectra and corresponding polarisation degree from monolayer MoS₂ at cryogenic temperature. *Image from Ref. [16]*. (c) Degree of circular polarisation of photoluminescence as a function of temperature, demonstrating robustness of valley selectivity. In this study, the authors identified two peaks in their spectrum, some early evidence of excitonic effects in monolayer TMDs. *Image from Ref. [13]*.

TMDs is not governed by simple single particle interband transitions, but is instead strongly subject to electron-hole Coulomb interactions which modify both the optical properties and valley pseudospin dynamics considerably [11, 20, 24, 4]. These electronic excitations in crystalline solids are common in nanostructures with reduced dimensionality, and are known as *excitons*.

2.2 Excitons

2.2.1 Quasi-hydrogenic binding energy

The conduction band of semiconductor materials, including monolayer TMDs, is characterised by many empty states which may be populated by electrons, for instance by the absorption of photons of appropriate energy. Each promoted electron leaves behind a hole, or electron vacancy, in the valence band, which takes an effective charge of +1. The electron, with charge -1, is therefore attracted to the hole via electrostatic Coulomb forces [24]. In much the same way as a Hydrogen atom, the electron and hole bind together to form a two-body quasiparticle known as an exciton. In inorganic crystalline semiconductors, excitons

Optical properties of monolayer transition metal dichalcogenides

are typically of the *Wannier-Mott* type, with approximate size larger than the crystal unit cell, and consequently are not fixed to a specific atomic site [25]. In monolayer TMDs, the exciton Bohr radius is very small, so they are therefore at the lower limit of Wannier-Mott classification, verging towards the localised Frenkel type excitons common in organic molecules. However, they are still free to move through the crystal and so the Wannier-Mott picture is a suitable description for TMD excitons.

To be stable against dissociation by collisions with thermally activated phonons, the exciton binding energy E_B must exceed the thermal energy $k_B T$ where k_B is the Boltzmann constant and T is temperature:

$$E_B > k_B T \quad (2.11)$$

Following the Bohr model, the series of exciton states with principal quantum number n have binding energies from the Coulomb interaction:

$$E_B = \frac{\mu}{m_0} \frac{1}{\epsilon_r^2} \frac{R_H}{n^2} = \frac{R_X}{n^2} \quad (2.12)$$

where m_0 is the electron rest mass, ϵ_r the dielectric constant of the medium, and R_H the hydrogen Rydberg constant (13.6 eV) [25]. Considering that an exciton is distinct from a hydrogen atom, the effective mass approximation must be used:

$$\frac{1}{\mu} = \frac{1}{m_e^*} + \frac{1}{m_h^*} \quad (2.13)$$

where m_e^* and m_h^* are the effective electron and hole masses, taking account of conduction and valence band curvature. The corresponding Bohr radii are given

$$r_n = \frac{m_0}{\mu} \epsilon_r n^2 a_H = n^2 a_X \quad (2.14)$$

where a_H is the hydrogen Bohr radius. From Eqs. 2.12 and 2.14 it is clear that excited states of excitons have increasingly small binding energies and large radii [25]. To create an exciton optically, the photon energy must equal the free particle band gap of the material less the exciton binding energy:

$$E_n = E_g - \frac{R_X}{n^2} \quad (2.15)$$

Here, it is important to note that the free particle band gap E_g is renormalised from the absolute band gap by the so-called self energy term, which is typically very similar to the exciton binding energy but with opposite sign. Therefore, to create an exciton, the photon

must have sufficient energy to create a free electron-hole pair, less the exciton binding energy. The two energies almost cancel each other out, such that the exciton absorption is usually quite close to the absolute band gap energy measured between conduction and valence bands [24].

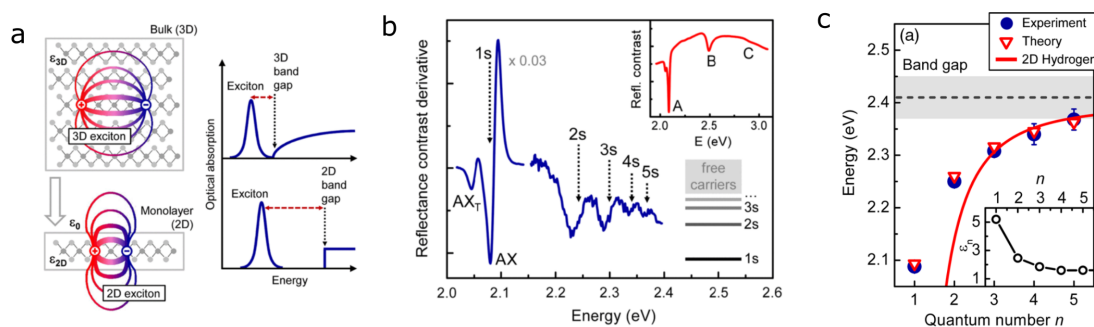


Fig. 2.7 (a) Comparison of exciton binding energy and Bohr radius in 3D and 2D systems. In a bulk semiconductor, there is significant screening from the surrounding material with dielectric constant ϵ_{3D} . In a monolayer, there is no surrounding material, so the dielectric constant $\epsilon_0 < \epsilon_{3D}$, and the 2D exciton is correspondingly more strongly bound, with a smaller Bohr radius. The optical absorption of the exciton is the free particle band gap less the binding energy. (b) Rydberg series of ground and excited exciton states in monolayer MoS₂, measured by reflectivity, showing increasing principle quantum number n . (c) Fitting of the data to the Hydrogenic Bohr model reveals discrepancy for the 1s and 2s excitons, which may be compensated by considering a changing effective dielectric constant as a function of n , shown in the inset. *All images from Ref. [26].*

Due to strong confinement and the reduced dimensionality of atomically thin TMD monolayers, along with large effective masses at the K point band edges, excitons have very small Bohr radii (~ 1 nm) and large binding energies (~ 0.5 eV), as shown schematically in Fig. 2.7a [27–30]. Indeed, absorption measurements of single monolayers have revealed signatures of the excitonic Rydberg series up to $n = 5$, as shown in Fig. 2.7b [26]. Strikingly, the data does not fit well with the hydrogenic Rydberg series, with a deviation observed in the $n = 1$ and $n = 2$ exciton states (Fig. 2.7c). However, this discrepancy could be compensated by introducing a dependence of dielectric constant on principle quantum number, as $\epsilon_r(n)$. With variable dielectric constant, as shown in the inset of Fig. 2.7c, the experimental data could be well described by this modified quasi-hydrogenic model [26]. The origin of this discrepancy lies in the unique geometry of monolayer TMDs, whereby the dielectric constant becomes highly anisotropic owing to the substrate and environment below and above the monolayer, which provides reduced screening of the electric field between the carriers, subsequently modifying the binding energy. This effect highlights the sensitivity of 2D

materials to their immediate environment, which is to blame for many properties of 2D materials, such as the exciton photoluminescence energy varying quite strongly between different samples of the same material.

2.2.2 Optical signatures of excitons

As introduced in Section 2.1.3, the strong spin-orbit coupling in monolayer TMDs splits the valence band by several hundreds of meV, and the optical selection rules conserve spin (see Fig. 2.5b). As such, the optical transitions in monolayer TMDs may be classed as A and B, with A indicating transitions involving the topmost valence subband and B involving the lower valence subband, as shown in Fig. 2.8a. The large spin splitting is therefore evident in optical absorption, where distinct absorption resonances are visible corresponding to neutral exciton absorption from the A or B transitions, as shown in the upper panel of Fig. 2.8b for the case of MoSe₂ [31]. The photoluminescence from monolayer TMDs looks markedly different from the absorption, as can be seen in the lower panel of Fig. 2.8b. While there is strong emission from the A exciton, there is no emission from the B exciton (despite optical excitation above the B exciton energy), and furthermore, a secondary peak appears at lower energy than the A exciton [31].

To understand the photoluminescence, it is instructive to consider that excitons are not restricted to simple electron-hole pairs, and more elaborate species can and do form in monolayer TMDs. A bound state of two electrons and one hole forms a negatively charged *trion*, with overall charge -1 , whereas two holes and one electron form a positively charged trion [31, 32]. Furthermore, two electrons and two holes may bind to form a *biexciton* [33, 34] (Fig. 2.8d), and there are also experimental signatures of five body excitonic complexes known as *quintons* [35, 36]. Owing to the additional binding energy required for a neutral exciton to capture an extra carrier, these excitonic states emit at energies several tens of meV below the exciton luminescence. For instance, the trion (X^-) binding energy is ~ 30 meV relative to the neutral exciton (X^0) [32, 31]. Upon heating MoSe₂ from 15 K to room temperature, as shown in Fig. 2.8c, the trion emission drops to zero around $T > 100$ K owing to the additional electron escaping the bound state and leaving behind a neutral exciton, which remains stable beyond room temperature, albeit with thermal line broadening [31].

The population densities of the different exciton species depends on the excess charge doping in the monolayer and the pumping power. In samples with very low doping, neutral excitons are dominant, and so luminescence from the sample will display a prominent X^0 peak [31, 37]. As excess positive or negative charge carriers are added to the system, creating an n-type or p-type doping level, the corresponding negative or positive trion state will become dominant and the neutral exciton will diminish. At very high pumping powers,

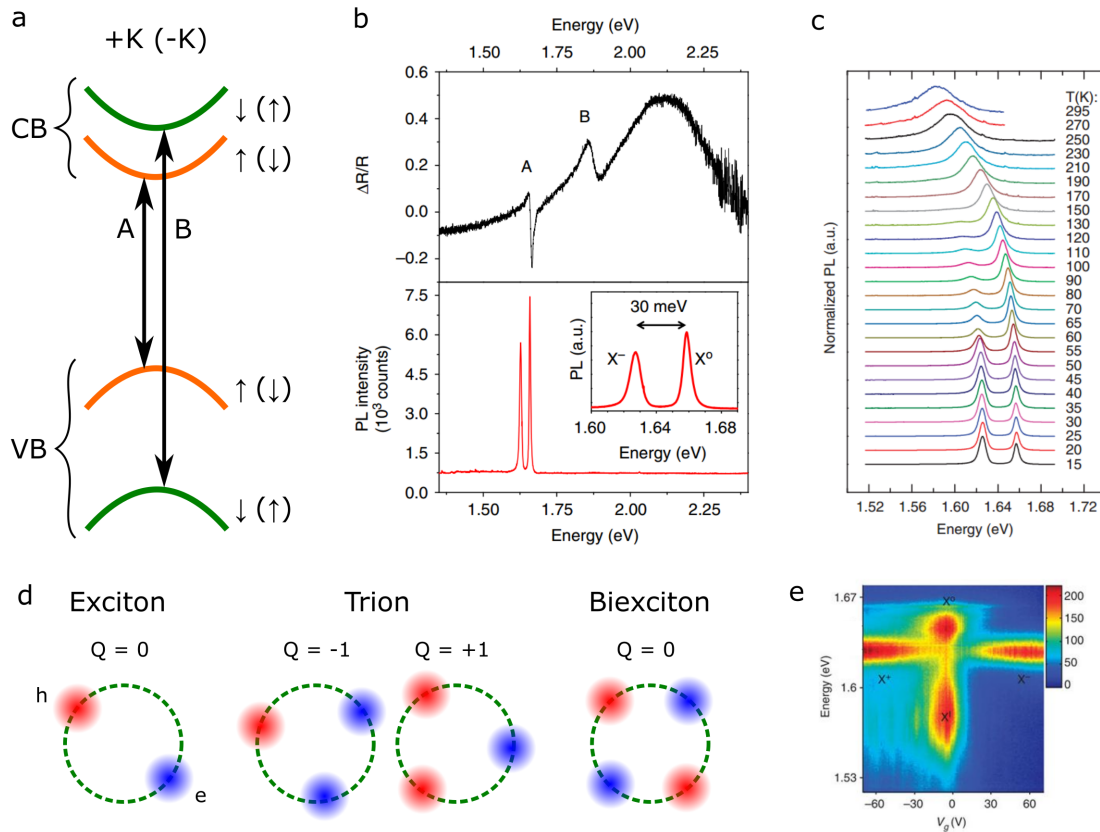


Fig. 2.8 (a) Schematic of the conduction and valence bands at the K (-K) point of the Brillouin zone in monolayer MoSe₂. The lowest energy optical transition corresponds to the A exciton, and the higher energy transition between the other spin subbands corresponds to the B exciton. (b) Comparison of reflectivity (top panel) and photoluminescence (bottom panel) from monolayer MoSe₂. In absorption, the A and B excitons are visible, while in photoluminescence, the A-exciton and A-trion are visible. *Image from Ref. [31]*. (c) Temperature dependence of MoSe₂ photoluminescence, showing thermalisation of the trion and broadening of the neutral exciton up to room temperature. *Image from Ref. [31]*. (d) Illustration of Coulomb-bound excitonic complexes, where red and blue circles denote the hole and electron, respectively, and Q is the total charge. (e) MoSe₂ photoluminescence as a function of back-gate voltage. As more electrons (holes) are accumulated in the monolayer, the neutral exciton emission gives way to negative (positive) trion emission. Low energy band at 0 V corresponds to localised neutral excitons. *Image from Ref. [31]*.

but near zero doping, the neutral exciton density is very high, and biexcitons will begin to form [33–36]. Fig. 2.8e shows the photoluminescence from monolayer MoSe₂ under positive or negative applied back-gate voltages, thereby creating excess electron or hole populations, respectively. The neutral exciton emission at 0 V can be seen to evolve into either positive or negative trion emission depending on the applied voltage [31]. The lower energy emission at 0 V is attributed to localised states, which feature to varying degrees in photoluminescence spectra from the four main TMD materials. The exact origin of these states remains somewhat ambiguous, with phonon replicas, lattice defects or strain induced exciton trapping all variously proposed; notably resulting in observation of single photon emission from highly confined low energy excitons [38–41]. However, in this thesis, focus is maintained on neutral exciton and trion spectroscopy only.

2.3 Exciton valley pseudospin

Given that the chiral optical selection rules in monolayer TMDs are valley dependent, it follows that optically generated excitons may too be associated with a valley index, inherited from their constituent electron and hole. As such, excitons possess a valley pseudospin, so long as they are *optically bright*, that is, they may radiatively recombine without any spin flip or momentum changes. The implication of this is that excitons behave as charge-neutral composite bosons with a unique pseudospin degree of freedom, which may be optically addressed with ease via the selection rules. This opens the possibility of all-optical valley based information processing or communication at the atomic limit.

2.3.1 Valley-orbit coupling

The electron-hole Coulomb interactions which influence excitons can be separated into *direct* and *exchange* contributions. The direct Coulomb interaction describes the attraction between positive and negative charge distributions of the electron and hole, and is therefore largely responsible for the exciton binding energy [24]. It is also sensitive to the dielectric environment, leading to exciton energy variation when monolayer TMDs are placed on substrates of differing dielectric constant [42].

The Coulomb exchange interaction, on the other hand, may be further separated into short range and long range types. The short range interaction arises from wavefunction overlap between the constituent electron and hole, and is highly sensitive to their relative spin and valley indices owing to the Pauli exclusion principle [24]. As such, the short range exchange interaction gives rise to energy splitting between singlet and triplet excitons, and contributes

to energy differences between optically bright and dark excitons [24, 43], and has particular significance for the results presented in Chapter 4 regarding the WSe₂ trion fine structure.

The long range electron-hole exchange interaction, while a much weaker effect than the direct component, plays a very prominent role in the optical response of excitons in monolayer TMDs. It is responsible for coupling between exciton states of opposite valley index, and allows efficient inter-valley scattering of excitons without the need of momentum transfer or a spin flip [2, 4, 20, 24, 43]. Here, the long range Coulomb exchange interaction creates an energy splitting between excitons with their microscopic dipole moment parallel or perpendicular (*longitudinal* or *transverse*) to the in-plane wavevector, $\mathbf{k} = (k_x, k_y)$, termed the LT-splitting [43, 20, 44–46]. The coupling between K and K' valley excitons is represented by the following Hamiltonian:

$$H(\mathbf{k}) = \frac{\hbar}{2}(\boldsymbol{\Omega}_{\mathbf{k}} \cdot \boldsymbol{\sigma}) \quad (2.16)$$

where $\boldsymbol{\Omega}_{\mathbf{k}} = (\Omega_x, \Omega_y)$ is an effective precession frequency for the valley pseudospin, represented by a vector of Pauli matrices, $\boldsymbol{\sigma} = (\sigma_x, \sigma_y)$. The precession components are $\hbar\Omega_x = 2\alpha k^2 \cos 2\theta$ and $\hbar\Omega_y = 2\alpha k^2 \sin 2\theta$, where θ is the angle between \mathbf{k} and the k_x axis, and α is the valley coupling parameter arising from the long-range electron-hole exchange interaction [43, 20]. The eigenmode splitting is therefore given by $\hbar\Omega_k = 2\alpha k^2$, however, the coupling term becomes weaker at larger wavevectors, resulting in $\hbar\Omega_k \propto k$. The nominally parabolic exciton dispersion consequently acquires an energy splitting, increasing at larger wavevectors, between the longitudinal and transverse components, which each couple to orthogonally linearly polarised light [44].

$\boldsymbol{\Omega}_{\mathbf{k}}$ therefore behaves as an effective magnetic field acting on the valley pseudospin, causing precession, with strength proportional to k and a double winding in-plane orientation about $k = 0$, as shown in Fig. 2.9a. The interaction which gives rise to this effective magnetic field is therefore responsible for a coupling of K and K' exciton valley pseudospin, which in real terms allows valley pseudospin flips of optically bright excitons, and explains the lower than unity circular polarisation degrees observed in exciton photoluminescence, despite the robust optical selection rules [43, 20, 44, 45].

In TMDs, the giant exciton binding energies and small Bohr radii contribute to a very strong LT-splitting, predicted to be ~ 2 orders of magnitude larger than in GaAs quantum wells [44]. As such, the splitting is prominent even at very low wavevectors, when $\boldsymbol{\Omega}_{\mathbf{k}}$ is at its weakest. At the extreme lower limit, that is, close to $k = 0$ within the light cone, corresponding to overall wavevector equal to $\pm K$, the exciton dispersion takes a conical linear dispersion in the form of a Dirac cone, as shown in Fig. 2.9b. The striking consequence of this is that bright excitons localised at the K-points are essentially massless quasiparticles

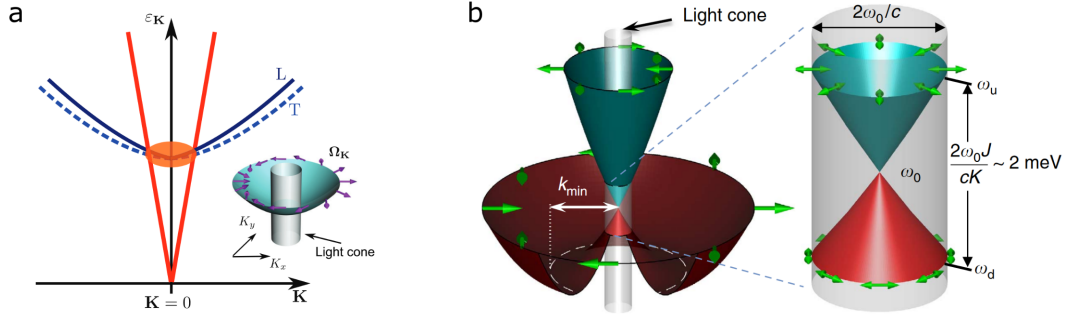


Fig. 2.9 (a) Illustration of the neutral exciton dispersion with a longitudinal-transfer (LT) splitting, which is proportional to wavevector \mathbf{K} . The orange lines indicate the light cone, in which an exciton may recombine with the emission of a photon. Inset: top view of the dispersion showing the orientation of the effective magnetic field $\Omega_{\mathbf{K}}$ arising from LT-splitting, about which the pseudospin precesses. *Image from Ref. [20]*. (b) Closer view of the exciton dispersion at low wavevectors, where the strength of the valley-orbit coupling realises a massless Dirac cone in the exciton dispersion in the light cone, as shown in the inset. Single headed green arrows denote the valley pseudospin at various wavevector, double headed arrows indicate the orientation of linear polarisation of photons. *Image from Ref. [44]*. The overall effect of this valley-orbit coupling is to allow depolarisation of the exciton valley pseudospin, with a stronger effect at larger wavevectors.

associated with robust valley pseudospin, which theoretically offers many intriguing avenues of research, but in reality is somewhat limited by the extremely rapid exciton radiative decay within the light cone [44, 47].

2.3.2 Exciton valley polarisation and coherence

It is instructive to consider the exciton valley pseudospin in the Bloch sphere formalism, in which the pseudospin is represented as a vector pointing from the origin of the Bloch sphere onto the surface. The pseudospin vector pointing to the north pole of the sphere corresponds to the exciton state $|K\rangle$, while the south pole corresponds to $| -K\rangle$. Similarly, the vector pointing anywhere on the equator denotes a coherent superposition of the two [48, 4]. The chiral optical selection rules of monolayer TMDs therefore allow preparation of an exciton state with the pseudospin vector pointing to any arbitrary position on the surface of the sphere, via the polarisation state of the photon [49, 48]. σ^+ or σ^- polarised light will address the north and south poles, while linearly polarised light, which is a superposition of σ^+ and σ^- , will initialise the vector to the equator. In principle, elliptical polarisation would allow arbitrary initialisation of the vector to anywhere between the poles, corresponding to an arbitrarily mixed valley state [49].

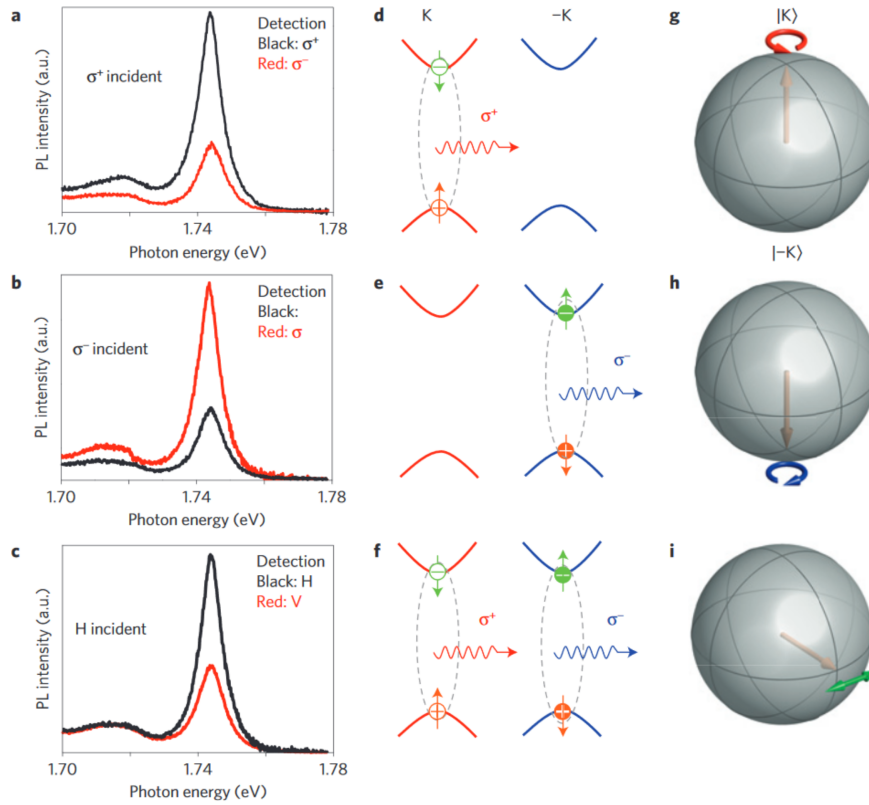


Fig. 2.10 (a-c) Polarisation resolved photoluminescence from the neutral exciton in monolayer WSe₂, under different excitation and detection polarisations. In each case, the injected polarisation is retained in the emission, indicating optical generation of valley polarisation and coherence. (d-f) Simplified band diagrams for the σ^+ , σ^- and linearly polarised exciton states contributing to emission in (a-c), with electron and hole spin indicated. (g-i) Pseudospin vector orientation on the Bloch sphere corresponding to K, K', or superposition states. *Image from Ref. [4].*

Optical properties of monolayer transition metal dichalcogenides

The optical addressability of excitons in monolayer TMDs can be studied in a straightforward manner by performing polarisation resolved optical spectroscopy. For instance, pumping a monolayer with a σ^+ circularly polarised laser creates only $|K\rangle$ valley excitons, creating a valley polarisation of the exciton population [11, 50–52]. By time reversal symmetry, the same applies for σ^- polarisation. Similarly, pumping with a linearly polarised laser generates excitons in a coherent linear superposition of valley states, a phenomenon known as *valley coherence* [48, 49, 53, 54].

In order for the valley pseudospin to be of any potential use for the goal of information processing, it must be long lived. In particular, the optically initialised valley state must remain well defined until the exciton radiatively recombines. Therefore, to measure the *degree of valley polarisation*, a simple method is to excite a sample with circularly polarised light, and measure the photoluminescence in a co-polarised and cross-polarised basis. Any intensity difference between the two indicates some retention of valley polarisation over the radiative lifetime [4, 48, 11]. As introduced in the previous section, the long range electron-hole exchange interaction efficiently couples $|K\rangle$ and $|-K\rangle$ exciton pseudospin states, offering a route for depolarisation, which typically results in valley polarisation degrees in photoluminescence far from unity [43, 20, 44, 45].

Fig. 2.10 shows a series of polarisation resolved photoluminescence measurements of the neutral exciton emission in monolayer WSe₂. Clear intensity differences are observed between co-polarised and cross-polarised emission, both for circularly polarised and linearly polarised light [48, 4]. These measurements indicate that WSe₂ is able to maintain an arbitrary pseudospin state to a significant degree over the time between photogeneration and recombination of the exciton, pointing to either a relatively long valley lifetime, or relatively short radiative lifetime. It is important to note that the degrees of valley polarisation vary strongly between the various TMDs, for instance, MoSe₂ tends to only retain a negligible valley polarisation in the exciton photoluminescence [55]. Fundamentally, the amount of valley polarisation (or coherence) remaining in the emission signal depends on the ratio of valley lifetime to radiative lifetime, as will be explored in detail in Chapter 5.

2.3.3 The valley Zeeman effect

The valley magnetic moment $\mathbf{m}(\mathbf{k})$ introduced in Section 2.1.4 is associated with the valley pseudospin in analogy to the Bohr magneton being associated with the conventional electron spin [4]. Bloch states at the conduction and valence band extrema in opposite valleys are Kramers doublets, related by time reversal symmetry, and so the magnetic moment takes the same magnitude with opposite sign [51]. This provides a means to gain control of the valley pseudospin by the application of an external magnetic field, which lifts the

degeneracy between opposite valley states, in a process known as the *valley Zeeman effect* [56, 21, 51, 57, 58, 50].

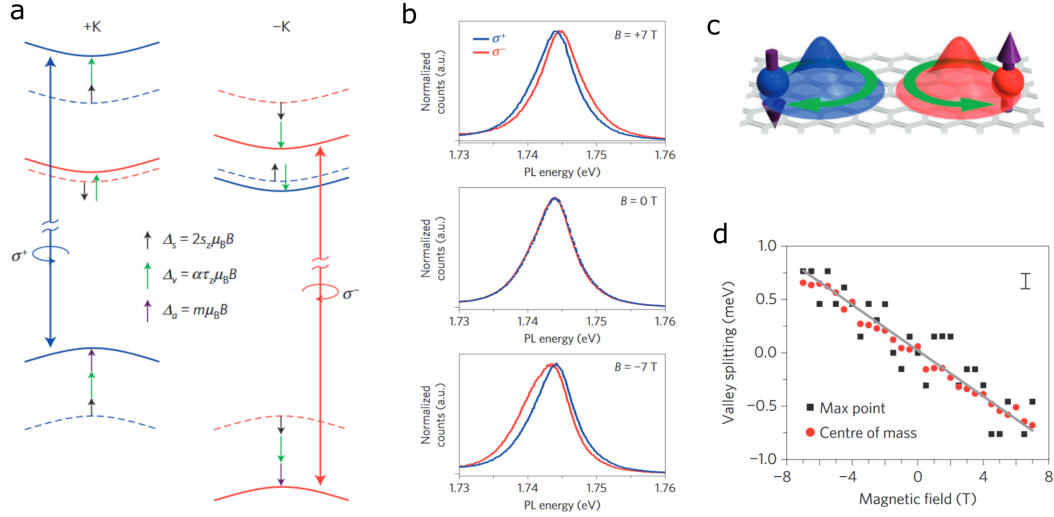


Fig. 2.11 (a) Scheme of magnetic moments which cause each spin subband in each valley to shift in energy in response to an external magnetic field B . Terms are defined in the text. The measured valley Zeeman splitting is the difference in shifts of the spin-parallel subbands within each valley. (b) Measured valley Zeeman splitting of the neutral exciton in WSe_2 , symmetric about the field orientation. (c) Illustration of the valley contrasting magnetic moments. Blue and red are spin up and down, respectively. The green arrow represents opposite self-rotation of the Bloch wavepacket giving rise to the valley magnetic moment. The purple arrows indicate the atomic orbital magnetic moment which shifts the valence band states. *Images from Ref. [56].*

However, the valley magnetic moment is not alone, but rather accompanied by magnetic moments arising from conventional electron spin, and the magnetic moments of the transition metal d -orbitals which constitute the conduction and valence band edges (Fig. 2.3b). As such, each conduction and valence spin subband will shift in energy by a total amount representing the sum of these three moments [56, 21, 57]. The resulting change in photon emission energy from neutral exciton recombination reflects the difference in shifts between the spin-parallel conduction and valence bands, involved in the optical recombination.

Following the notation used in Ref. [56] and shown in Fig. 2.11a, the spin magnetic moment leads to a shift of each spin subband by $\Delta_s = 2s_z\mu_B B$ where s_z is the electron spin $\pm 1/2$. This, however, has no effect on the PL emission from a sample as optically bright transitions must conserve spin, so the initial and final states are shifted by the same amount. Next, the valley magnetic moment introduced above will induce a shift of each subband $\Delta_v = \alpha_{c,v}\tau_z\mu_B B$ where $\alpha_{c,v}$ is the valley g -factor for the conduction and valence

Optical properties of monolayer transition metal dichalcogenides

bands, respectively, and τ_z is the valley index $\pm K$, giving the sign of the shift (as α is always positive) [56]. The valley magnetic moment therefore shifts all subbands in the K valley to higher energy, and all subbands in the K' valley to lower energy. While the valley g-factor is expected to be equal for the conduction and valence bands, the difference $\Delta\alpha = \alpha_c - \alpha_v$ has recently been reported as having a finite value in some samples, due to the inequivalent effective masses of the conduction and valence bands [56]. Finally, there is a shift arising from the atomic orbitals which constitute the band edge states in the two valleys, which are mainly tungsten d -orbitals with $m = 0$ in the conduction band and $m = \pm 2$ in the $+K$ and $-K$ valence bands, respectively [56, 21]. As such the atomic orbital angular momentum associated shift of conduction band states is zero, while the valence band states shift by $\Delta_a = 2\tau\mu_B B$.

The cumulative effect of the valley and orbital magnetic moments, Δ_v and Δ_a , therefore leads to an effective Zeeman splitting of the exciton emission energy by $\Delta(B) = 2(2 - \Delta\alpha)\mu_B B$ between optical resonances in opposite valleys, which is linear in B [56]. Indeed this is observed, as shown in Fig. 2.11b, where the σ^+ and σ^- circularly polarised exciton emission splits under a magnetic field applied out of the monolayer plane, with the splitting reversed depending on the sign of the field. In this case, the splitting was measured to be $E(\sigma^+) - E(\sigma^-) \approx -1.8\mu_B B$, where -1.8 is here termed the *valley Zeeman g-factor* [56]. The fact that this is smaller than -4 , as predicted from the orbital magnetic moment of the valence band, suggests $\Delta\alpha$ is non-zero, perhaps pointing to inequivalent effective electron and hole masses. However, in repeated experiments on different samples, a g-factor of -4 is most commonly measured, consistent with the expectation [21, 57, 51, 50, 58].

While the valley Zeeman splitting of the neutral exciton in all four of the main TMDs is now fairly well understood, there remains some ambiguity surrounding the trion valley Zeeman effect in tungsten based TMD monolayers, with valley splittings ranging between $-4\mu_B B$ to $-13\mu_B B$ reported [57, 21, 58, 59]. This mystery will be the focus of investigation in Chapter 4.

Chapter 3

Experimental methods

In Chapter 2 the significance of the monolayer form of TMDs such as MoSe₂ and WSe₂ was discussed, associated with a direct band gap, strong excitonic effects, and a regime of coupled spin and valley physics. As such, a controllable and reproducible method for fabrication of monolayer TMDs is crucial to enable new research. Furthermore, the ability to selectively incorporate monolayer TMDs into a variety of sample architectures opens a multitude of new research avenues focused on the interactions of these materials with their environment. In this chapter, such fabrication methods are discussed, followed by a description of various experimental techniques which may be employed to reveal new insights into these novel materials.

3.1 Techniques of 2-D material sample fabrication

3.1.1 Exfoliation of monolayer films

The Nobel prize winning work which involved the isolation of stable monolayers of graphene used a technique known as *micromechanical exfoliation*, whereby single layers of graphene were pulled away from bulk graphite using adhesive tape [61, 62]. This is achieved by peeling the surface of the bulk crystal with tape of strong enough adhesion to overcome the van der Waals attractive forces holding adjacent monolayers together. After peeling away from a bulk crystal, the tape will be covered with thin flakes which previously constituted the surface layers of the bulk crystal (Fig. 3.1a). There will be a thickness distribution of these flakes, ranging down to individual monolayers. The tape is then pressed onto a desired surface and peeled off again, transferring both monolayer flakes and thicker material onto the new substrate (Fig. 3.1b). Methodically searching such a substrate by eye under a microscope allows identification of monolayers suitable for further study (Fig. 3.1c).

Experimental methods

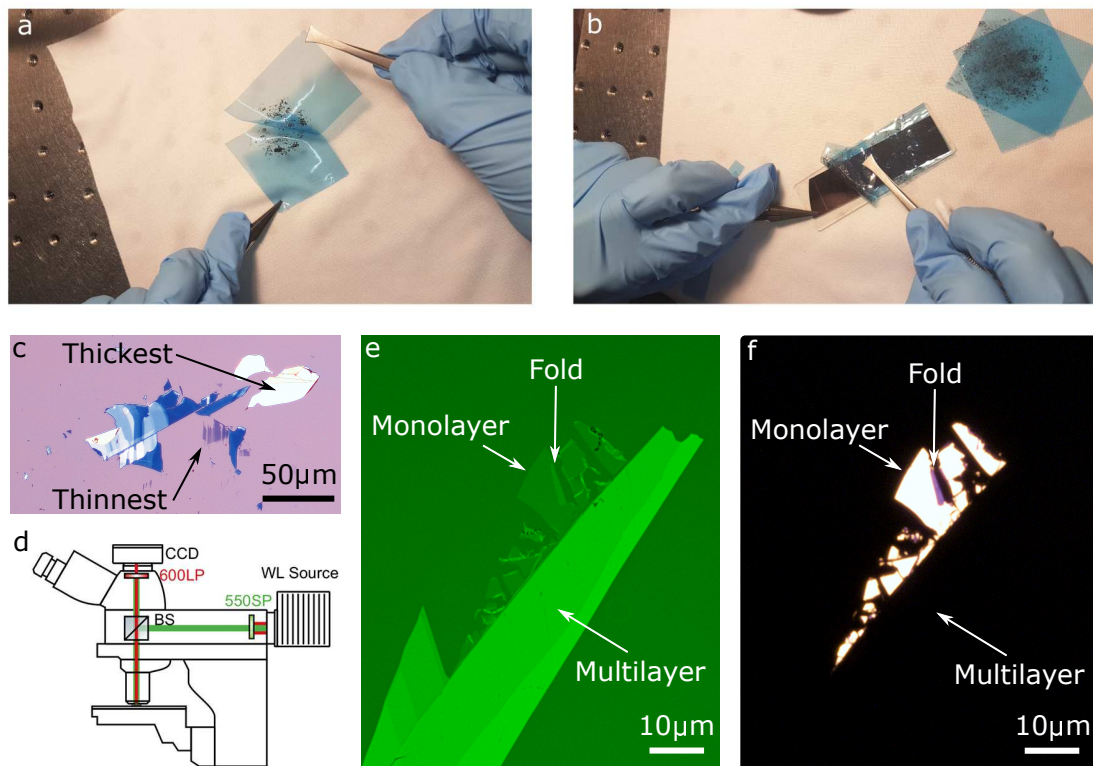


Fig. 3.1 (a) Photograph of tape exfoliation of MoSe₂. Repeated peeling between two pieces of tape thins down a bulk crystal to a wide distribution of thicknesses. (b) The tape is then pressed onto a substrate, in this case Si / SiO₂, warmed on a hotplate for a few minutes to promote adhesion, then the tape is peeled off, leaving exfoliated material on the surface. (c) Bright field microscope image of some exfoliated material on Si /SiO₂. Individual monolayers can be identified by eye under the microscope by their appearance, with colours and transparency both indicative of thickness. (d) Diagram of a bright field optical microscope modified to perform photoluminescence imaging using a white light excitation source. A combination of short-pass and long-pass edge filters and a beamsplitter allow a CCD to image the photoluminescence from exfoliated material, by acquiring with several seconds exposure time to gather the low levels of luminescence. *Image from Ref. [60]*. (e,f) Comparison between a green-filtered bright field image and a photoluminescence image of the same MoSe₂ exfoliated flake. Only the monolayer region emits brightly, owing to the direct band gap. A fold in the monolayer shows dim luminescence associated with the bilayer band structure.

3.1 Techniques of 2-D material sample fabrication

In the years since, despite some refinements, this method remains the best way to obtain high quality monolayers for experiment [63]. Problems still remain with this method, most prominently the low yield of sample fabrication. This is largely due to the low probability of isolation of monolayers as opposed to few-layer material during exfoliation [62]. This inefficiency is compounded by the difficulty in distinguishing and identifying monolayers on a substrate after exfoliation. Only certain substrates allow monolayers to be seen through bright field optical microscopy, many others, such as glass or metal, leave monolayers as almost entirely transparent [62]. To combat this problem, 2-D materials may be exfoliated onto a thin (~ 100 nm) layer of dielectric or polymer on top of an opaque base substrate such as silicon. The optical interference effects of this thin film typically provide much greater contrast between a monolayer and the underlying substrate, allowing higher visibility.

A highly reliable method to identify the layer number of a flake is atomic force microscopy (AFM), but the cumbersome nature of AFM is a limiting factor; it is not feasible to scan entire substrates searching for monolayers using AFM [62]. A common alternative method of identifying a monolayer is by exposing it to a light source and observing photoluminescence (PL), as a monolayer will typically be tens or hundreds of times brighter in emission than a bilayer owing to the indirect-to-direct band gap transition in the single layer [64]. It is possible to modify a standard bright field optical microscope to detect emission from monolayers simply by using a short-pass filter in front of the white light bulb, allowing only higher energy light through, and a long-pass filter in front of the CMOS camera, to allow only low energy emission to be detected (Fig. 3.1d) [60]. PL imaging reveals a wealth of detail about the monolayers, as the intensity of luminescence can indicate degradation, and the high resolution of the microscope allows sub-micron structure to be studied, revealing cracks or other damage, alongside providing a clear distinction between mono- and bi-layer material (Fig. 3.1e,f). Imaging PL in this way offers a much quicker and easier way to characterize flakes than mounting them in a PL spectroscopy setup and exciting them with a laser.

Overall, exfoliation and PL imaging allow individual monolayers to be relatively rapidly identified from large areas of exfoliated waste material, but the process still requires methodical searching by eye. This bottleneck in fabrication is the key limiting factor to the scalability of 2-D material based devices. Micromechanical exfoliation alone is unlikely to be viable as a method of mass production of future optoelectronics incorporating TMDs, due to the lack of control of monolayer size and position, along with the low yield [65].

3.1.2 Chemical vapour deposition

An alternative to micromechanical exfoliation, which is a “top-down” method, is to synthesise monolayer films directly onto a substrate of choice, in a bottom-up manner. This can be

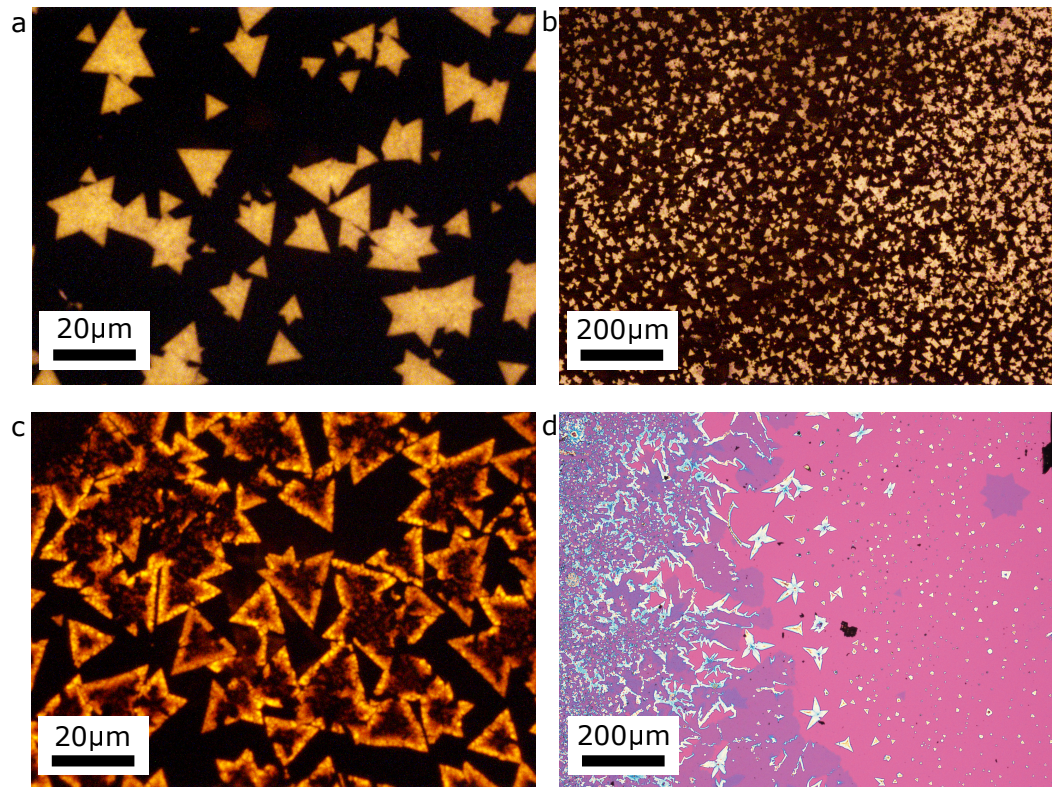


Fig. 3.2 (a) Photoluminescence microscopy image of CVD-grown MoSe₂, showing the characteristic triangular monolayers which are a hallmark of the hexagonal crystal structure. *Sample grown by collaborators at UNIST, Korea.* (b) Lower magnification photoluminescence image of the sample from (a), showing uniform coverage of monolayers over large substrates, unachievable with standard exfoliation techniques. *Sample grown by collaborators at UNIST, Korea.* (c) Photoluminescence image of CVD-grown WSe₂, showing poor growth quality, as indicated by the lack of emission from the central regions of each monolayer. *Sample grown by collaborators at UNIST, Korea.* (d) Bright field microscopy image of CVD-grown MoS₂ doped with cobalt atoms during the growth process, in an attempt to induce ferromagnetism in the TMD. CVD offers unique fabrication possibilities such as this. *Sample grown by collaborators at NTU, Singapore.*

3.1 Techniques of 2-D material sample fabrication

achieved by a process known as *chemical vapour deposition* (CVD), whereby precursor materials are sublimed into a gas which flows over a cooled substrate [66–68]. A chemical reaction occurs on the substrate leading to growth of crystalline material. Once started, the growth extends laterally following the crystal axes of the material being grown. TMDs therefore tend to form equilateral triangle shaped monolayers, as can be seen in Fig. 3.2a. CVD can cover entire large substrates with ensembles of monolayers, as shown in Fig. 3.2b, constituting a huge advantage of yield over the exfoliation method. However, very often poor growth quality is observed (Fig. 3.2c) and it can be difficult to optimize growth parameters reproducibly. However, after significant improvements in the techniques of CVD, growers now have generally good control over the sizes of the monolayers, and are currently developing methods to control the alignment of crystal axes and avoid bilayer formation, which will ultimately lead to reproducible wafer-scale growth of single monolayers, an ideal building block for mass production of 2D material devices [69].

An advantage of CVD grown flakes is that molecules other than the necessary precursors may be introduced to the chamber, to dope and modify the physical properties of the grown material. For example, cobalt, nickel, or iron may be added, producing TMD monolayers with ferromagnetic islands (Fig. 3.2d), leading to unusual and unexplored properties.

Despite the progress made in CVD fabrication methods, the optical quality of the grown monolayers remains overall quite low [70]. Luminescence from excitons is generally of much broader linewidth and lower intensity than exfoliated flakes of the same materials. However, improvements are being made, and possibly CVD methods will provide the combination of high quality and scalability necessary for implementation of monolayer TMDs into future technology. It should be noted that other methods of monolayer growth exist, such as molecular beam epitaxy [71] and metal-organic vapour phase epitaxy [72], however, CVD remains the most popular method owing to relative simplicity and cheapness of implementation [66–68].

3.1.3 Flake transfer via viscoelastic stamping

Micromechanical exfoliation produces high optical quality monolayer TMDs, but offers little to no control over various important considerations for sample design, such as size, shape, position, and orientation of the monolayer. After exfoliation, monolayers are often adjoined to much thicker material, i.e. they are not isolated laterally, posing problems for certain types of research. While it is possible to transfer a monolayer onto a desired substrate simply by pressing the post-exfoliation tape onto the surface and peeling off, this provides no control down to the level of individual monolayer placement. In order to produce a sample ready for

Experimental methods

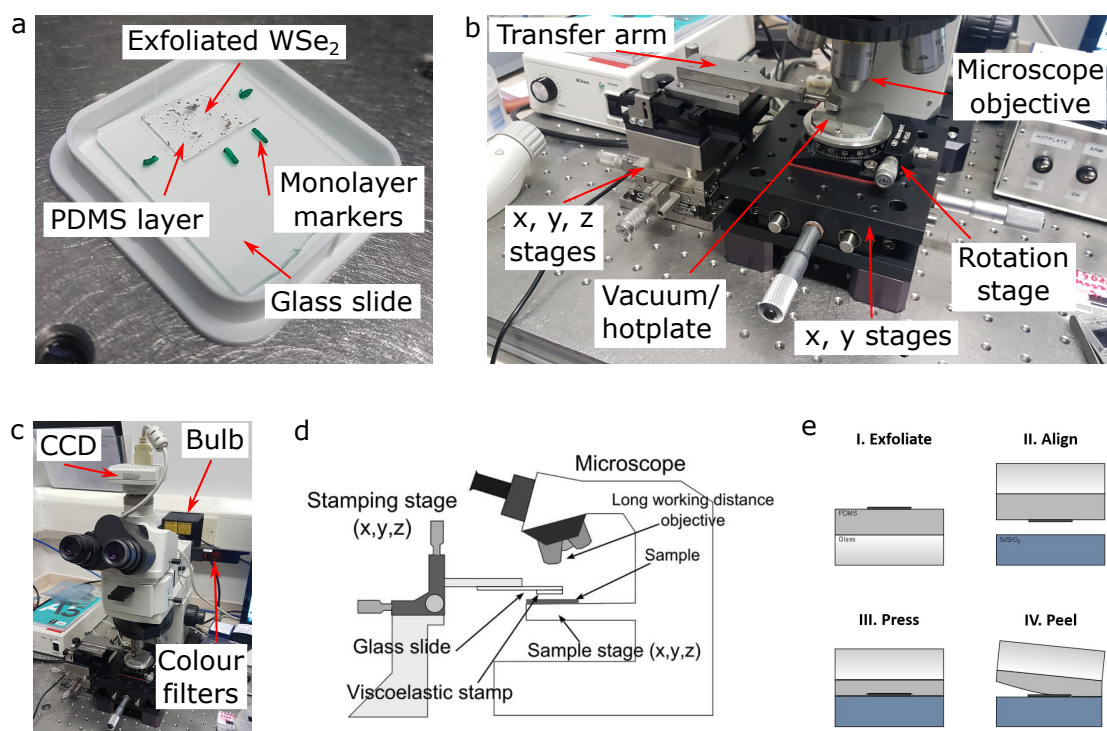


Fig. 3.3 (a) Photograph of a typical PDMS film on a glass slide, with exfoliated TMD material on top. The pen marks are used to indicate the approximate coordinates of any monolayers identified after exfoliation. (b) Photograph of the flake transfer setup under the microscope. The arm, on which the glass slide is mounted upside down via vacuum, is positioned above a hotplate for the target substrate. x , y , z micrometer stages allow precise positioning of the transferred flake. All is contained beneath a long working distance microscope. (c) Photograph of the transfer microscope, showing the selection of colour filters in front of the light source. Colour filters can improve monolayer contrast which helps monitor the transfer. (d) Diagram of a flake transfer microscope system. *Image from Ref. [70]*. (e) PDMS stamping process. After exfoliation onto the PDMS and identification of a suitable monolayer, the stamp is aligned and lowered onto the target substrate using a microscope as in (d). The viscoelastic properties of PDMS ensure low adhesion to the monolayer when being peeled off very slowly, ensuring a high chance of successful transfer.

3.1 Techniques of 2-D material sample fabrication

experiment, a monolayer of the correct size and shape must be identified, then transferred onto the requisite substrate in the chosen location.

This may be achieved by exfoliating the material onto a viscoelastic polymer film, such as polydimethylsiloxane (PDMS), which is itself on a hard transparent substrate such as a glass slide (Fig. 3.3a). After exfoliation, microscopy may be used to locate a monolayer suitable for transfer. Once located, the glass slide is turned upside down and mounted on an arm under a microscope, as shown in Fig. 3.3 [70]. The microscope is equipped with both a camera and eyepieces, along with various colour filters to improve the visibility of monolayers. There is a choice of long working distance objective lenses, ranging from 5x magnification to 50x. The monolayer, now facing down, may be viewed through the transparent glass and PDMS layers. A substrate suitable for the planned experiment is then placed underneath the monolayer, on a hotplate which has a small hole in the middle from which a vacuum may be applied to fix the substrate in place. The hotplate is mounted on x and y translation stages and a rotation stage, allowing precision tuning of the relative angle between the flake and substrate, which may be of interest in certain van der Waals heterostructures [73]. The arm is carefully lowered down until the PDMS makes contact with the substrate. During the lowering, the lateral position of the monolayer over the substrate may be controlled to micrometer precision, allowing precise positioning relative to substrate features or other previously transferred flakes. Due to the viscoelastic properties of the PDMS, it displays reduced adhesion when lifted away from the substrate very slowly [70]. This, along with the option to heat the target substrate, ensures a high probability of successful transfer of the monolayer (Fig. 3.3).

3.1.4 Fabrication of van der Waals heterostructures

While viscoelastic stamping methods allow accurate placement of single monolayers onto substrates of choice, alternative transfer techniques allow stacking of a variety of 2D materials on top of one another, forming *van der Waals heterostructures* [76, 74] (Fig. 3.4a). By stacking a predetermined sequence of 2D conductors (graphene), insulators (such as hexagonal boron nitride, hBN), TMDs, and other 2D materials with complementary properties, van der Waals heterostructure analogues of existing multilayered semiconductor technology can be created [74]. These structures can be electrically connected to external circuits by conventional lithography and metallisation techniques [77], or by using graphene flakes as low resistance electrodes [78]. Such prototype electrically contacted devices include field effect transistors [79], photodetectors [80], and electroluminescent devices based on multiple quantum wells [81].

The standard method for fabricating van der Waals heterostructures is outlined in Fig. 3.4b. Firstly, material is exfoliated onto a polymer bilayer which lies on top of a silicon wafer.

Experimental methods

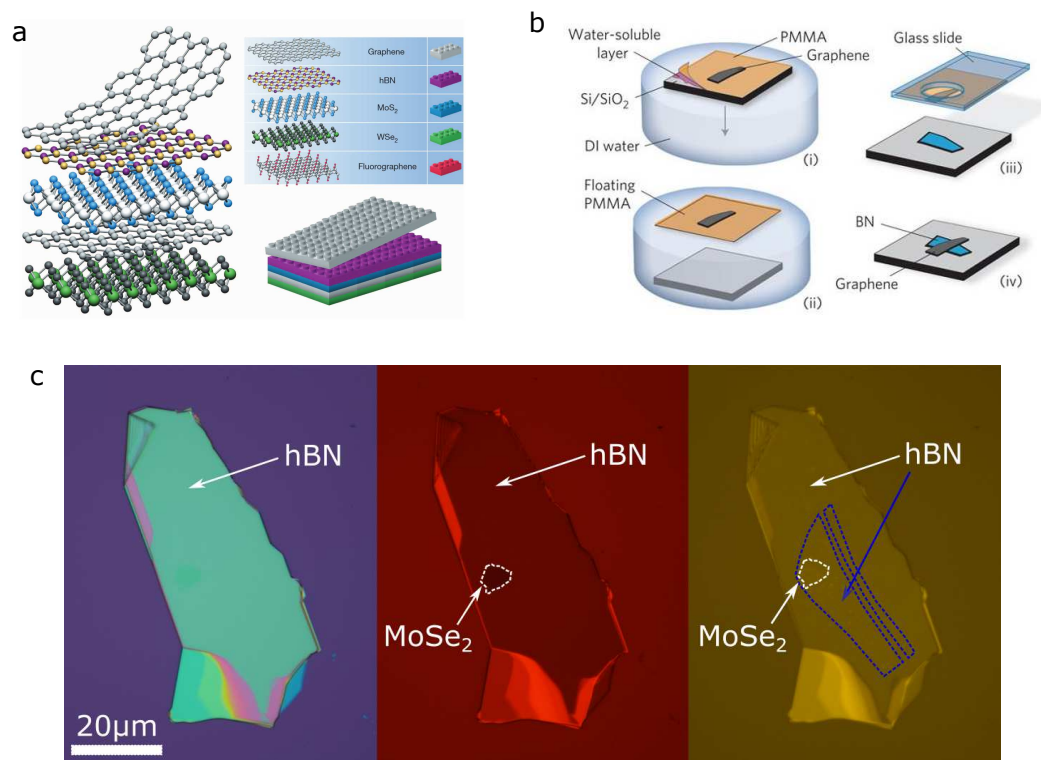


Fig. 3.4 (a) Illustration of a van der Waals heterostructure consisting of random 2D materials stacked up together. The freedom to stack arbitrary layers on top of one another is analogous to stacking LEGO bricks, in contrast to conventional epitaxy methods for bulk semiconductors, where lattice matching and dangling bonds pose limitations. *Image from Ref. [74]*. (b) Schematic of PMMA assisted bottom-up heterostructure fabrication. A water soluble polymer layer allows a hydrophobic PMMA membrane with exfoliated monolayer to be isolated from a Si substrate. The membrane can then be stamped and peeled off a target flake or substrate to build a heterostructure, as described in the text. *Image from Ref. [75]*. (c) Example of a hBN / MoSe₂ / hBN heterostructure fabricated by the author with the method described in (b). A MoSe₂ monolayer is transferred from a PMMA membrane onto a thick hBN flake exfoliated onto a Si / SiO₂ substrate. Then an encapsulating few-layer hBN flake is transferred on top of the MoSe₂ by repeating the same method.

3.1 Techniques of 2-D material sample fabrication

The lower polymer layer is water soluble, typically polymethylglutarimide (PMGI), with a hydrophobic layer on top, such as poly(methyl methacrylate) (PMMA) [75, 82]. Once a suitable monolayer is identified by microscopy, the whole structure is placed into a beaker of de-ionized water, which dissolves the PMGI layer, causing the Si to sink. This leaves the PMMA membrane, complete with monolayer, floating on the surface of the water. The membrane is fished out of the beaker by a glass or metal slide with a hole in the middle, which is upturned and mounted in the transfer microscope (see Fig. 3.3a). The hole causes the membrane to stretch taut while it dries, making the transfer easier. The monolayer is then laterally aligned above a target flake or unfinished heterostructure on the target substrate, and lowered down into contact. The target substrate is then heated to $\sim 60^\circ$ to promote adhesion, while the membrane is lifted away, leaving the monolayer transferred on top of the target monolayer or heterostructure [75, 82]. An example of a hBN / MoSe₂ / hBN heterostructure fabricated by the author is shown in Fig. 3.4c.

There are other advantages of stacking 2D materials beyond allowing complex device design. hBN provides an atomically flat surface, much smoother than typical dielectric or metallic surfaces, owing to its layered structure, and so is ideal for acting as a substrate beneath an active monolayer for experiments [75]. This has the added benefit of isolating the TMD from potential adverse effects of the underlying substrate, such as trapped charges in SiO₂ [75]. Going further, a TMD monolayer may be encapsulated by hBN layers both beneath and above it, providing excellent protection against adverse environmental effects which would otherwise lead to degradation of the monolayer and associated loss of luminescence intensity and line broadening [42].

A significant problem with existing sample fabrication methods is contamination of the monolayers. This has been observed with transmission electron microscopy as the presence of hydrocarbons and other chemical adsorbates on the surface of the monolayer [76, 83]. Such contamination, while potentially problematic for single monolayers, is mitigated somewhat in van der Waals heterostructures because the contaminants are pushed together into isolated bubbles between the layers [76]. As such, fabrication of high quality monolayer samples is achievable by incorporating them into heterostructures, where the interfaces between adjacent layers are atomically clean [81].

As an alternative to building a heterostructure bottom-up with repeated PMMA transfers, the entire heterostructure can be assembled top-down by picking up lower layers with the planned final top layer, then transferring the whole completed sample onto the final target substrate [77, 82]. In this case, for example, a thin hBN flake on a polymer membrane can be lowered into contact with a TMD monolayer which has been exfoliated onto a hard inert surface such as glass. By carefully raising the polymer membrane, it is possible to pick

Experimental methods

the TMD monolayer up from the substrate, purely by van der Waals attraction to the hBN. This TMD / hBN stack may then be transferred on top of another hBN flake elsewhere, leaving a fully encapsulated TMD monolayer which has never been in contact with potential contaminants such as PMMA; only glass and hBN. Additional layers can be added arbitrarily by picking them up successively before the final transfer, which typically involves removing the polymer membrane from the heterostructure on the target substrate by washing with a solvent [77, 82]. This method generally provides the very cleanest and highest quality samples, and is used to fabricate the samples measured in Chapters 4 and 6.

3.2 Micro-photoluminescence spectroscopy

The principles of photoluminescence with respect to monolayer TMDs have been described in Chapter 2, and here the implementation of micro-photoluminescence spectroscopy in the laboratory is discussed. In order to measure the luminescence from a sample, a series of optical components must firstly be used to guide an excitation light source onto the sample. The resulting emission is collected, dispersed by a diffraction grating in a spectrometer, and a narrow range of emission of desired energy is focused onto a high resolution charge-coupled device (CCD), where data indicating photoluminescence intensity as a function of wavelength may be recorded digitally. A schematic of the optical apparatus used in this work is shown in Fig. 3.5.

The excitation source used in this work is a continuous wave diode laser operating with a wavelength of 637nm (1.946 eV). This laser energy is significantly higher than the absorption edge of excitonic resonances in MoSe₂ and WSe₂, and is therefore sufficient to generate electron-hole pairs in these materials. After passing through a variable neutral density filter to control the transmitted power, the laser beam is focused into a single mode optical fiber. This strongly attenuates all modes except the fiber mode, and therefore transforms the distorted spot from the laser into a symmetric spot with a Gaussian intensity profile, ideal for being focused down to a highly concentrated spot on the sample. The fiber terminates on an optics board where the output beam is collimated by an aspheric lens into free space. On the optics board, the beam is reflected by two adjustable mirrors, which allow full alignment of the beam to ensure that it enters the objective lens centrally and with perpendicular incidence. The beam is then linearly polarized by a Glan-Thompson prism (LP in Fig. 3.5), followed by a half-wave plate ($\lambda/2$), which allows the the plane of the linear polarization to be rotated relative to the sample. Next, the laser enters a cube beamsplitter which splits the beam into reflected and transmitted components of equal power. The reflected beam is directed into the cryostat to the sample, while the transmitted beam is used to measure the laser power. In this

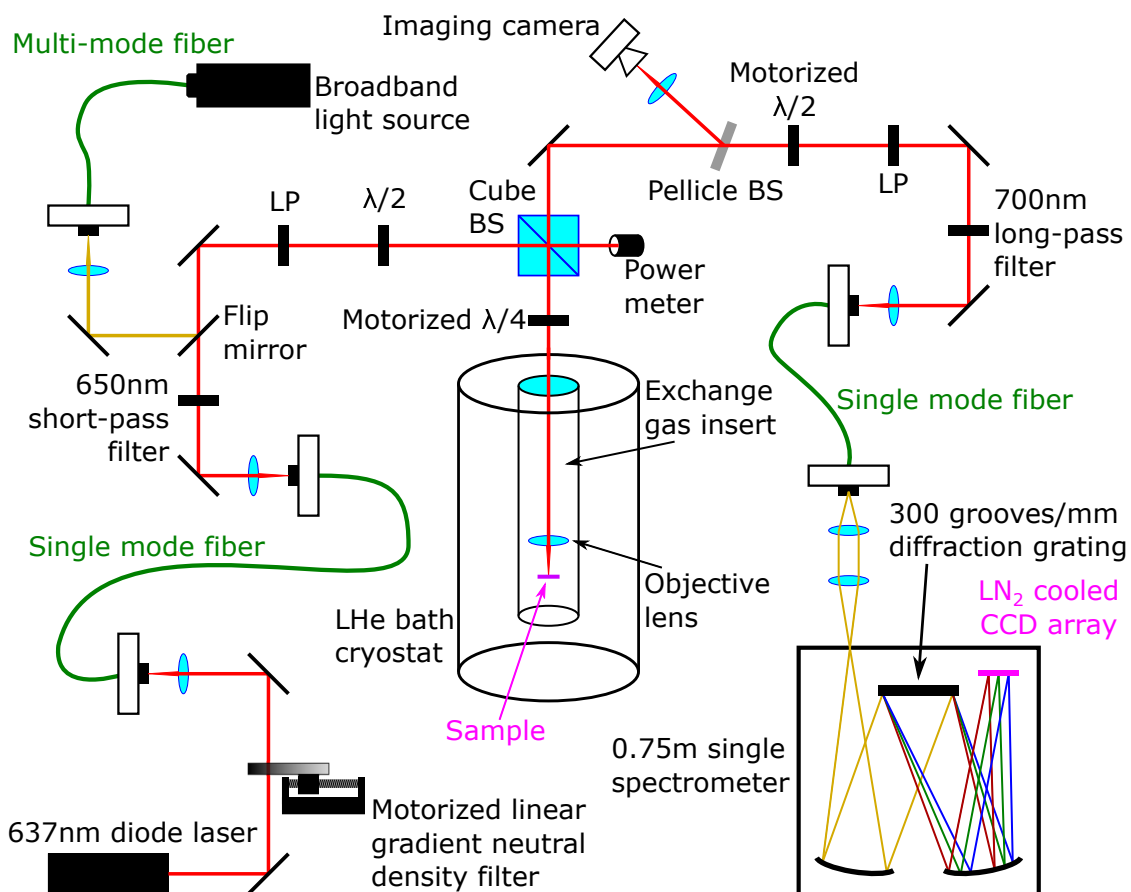


Fig. 3.5 Diagram of photoluminescence setup used throughout the projects included in this thesis. It can perform fully automated polarization resolved optical spectroscopy, with automatically stabilized laser power and high long-term stability owing to the sample being mounted in a helium bath cryostat. Spectra are acquired with a low noise high sensitivity nitrogen cooled charge-coupled device, with pixel size $20\ \mu\text{m}$ in an array 1340×400 pixels. A 300 grooves/mm diffraction grating is used, which provides $\sim 0.9\ \text{nm/pixel}$ spectral resolution. LP is a linear polariser, BS a beamsplitter, $\lambda/2$ a half-wave plate and $\lambda/4$ a quarter-wave plate.

Experimental methods

system, the power meter is connected via computer to the variable neutral density filter next to the laser, to ensure highly stable laser power is always directed to the sample. Influences such as temperature and humidity can cause a drift in power over time, particularly arising from movement in the fiber, so this power stabilization technique is vital when running several hour long automated measurements. Between the beamsplitter and cryostat there is a quarter-wave plate ($\lambda/4$) which converts the laser from linear polarization to σ^\pm circular polarization, when the optic axis is set to $\pm 45^\circ$ from the linear polarization plane. This wave plate is mounted in a motorised rotation stage, allowing automated switching between both left and right handed circularly polarised laser excitation, necessary to selectively initialise valley populations in TMD monolayers. Furthermore, by setting the $\lambda/4$ optic axis parallel to the laser linear polarization, it will be transmitted without modification, allowing coherent pumping of both valley states in the TMD. The objective lens is an achromatic doublet, 5 mm in diameter with a focal length of 7.5 mm. As such, the numerical aperture is 0.3, corresponding to a nominal diffraction limit of 1.0 μm at the laser wavelength of 637 nm. However, the laser spot size afforded by this objective lens in the system, measured as the full width at half maximum of the focused laser spot, has diameter 2.4 μm , larger than the diffraction limit owing to cumulative influences from the other optics in the system as a whole.

Circularly polarised emission from the sample is collimated by the objective lens and passes backwards through the quarter-wave plate again, becoming linearly polarised. The $\lambda/4$ will simultaneously convert left and right handed circularly polarised luminescence into two orthogonally linearly polarised components, which are partially transmitted back through the beamsplitter. Then follows an analyser half-wave plate followed by a linear polariser, which in combination allow selective transmission of one or the other orthogonally polarised components. This can be controlled by rotating the $\lambda/2$ between parallel and 45° from the linear polariser axis, which in this setup is automated and motorised. As such, σ^+ or σ^- circularly polarised photoluminescence from the sample can be selectively detected, allowing insight into opposite exciton valley states via the optical selection rules. The transmitted emission is then focused into another single mode fiber, which has the effect of spatially filtering the detection spot to closely match the laser excitation spot, maximising the detection of photoluminescence and minimising background light, thereby improving the signal-to-noise ratio. This filtering also improves the spatial resolution of the setup, crucial in order to avoid measuring the average luminescence properties of a large sample area. The collection fiber output is collimated and then re-focused onto a spectrometer slit of width 100 μm . Inside the spectrometer, monochromatic images of the slit are focused onto the CCD pixel array as a linear function of wavelength by a series of two concave mirrors and

3.2 Micro-photoluminescence spectroscopy

a diffraction grating. The CCD used in this work is cooled to -120°C to minimise dark current, and has a pixel size of $20\ \mu\text{m}$ in a 1340×400 array. The diffraction grating used most commonly in this work has 300 grooves/mm, and overall a spectrum of wavelength range $\sim 120\ \text{nm}$ may be recorded from each CCD exposure, with resolution $\sim 0.09\ \text{nm}$ / pixel. During a CCD exposure, counts from columns of pixels are binned vertically, to improve signal-to-noise ratio in the final spectrum. Background counts are removed during post-processing of data by subtracting a reference spectrum acquired by moving the laser spot off the sample onto adjacent substrate.

In order to ensure that only emission from the sample is detected by the CCD, a combination of optical filters are added into the setup. A 650 nm short-pass filter is added into the excitation beam path before the sample, to block any higher order laser modes or luminescence generated within the fiber. Then, a 700 nm long-pass filter is added into the detection path after the sample, to attenuate the main laser mode and any other background light of under 700 nm wavelength. The 50 nm overlap between these two filters ensures that any light around the filter cut-on and cut-off wavelengths is also blocked.

Finally, a combination of white light source and small camera are added to the setup, to allow real-time imaging of the sample, so the exact position of the laser spot on the sample can be seen. The sample is mounted on piezo nanopositioners allowing precision lateral and vertical adjustment, which can be monitored by the camera. This allows fine control of sample position and enables the laser to be focused down to a $2.4\ \mu\text{m}$ diameter spot. The white light source is coupled to multi-mode fiber with a wide $400\ \mu\text{m}$ core, bringing as much light as possible into the cryostat. The light is introduced by raising a mirror on a flip mount or hinge, which blocks the laser and feeds the white light beam into the optical path. A pellicle beamsplitter reflects $\sim 8\%$ of the light coming from the sample towards a small colour camera, allowing live imaging of the sample illuminated by white light. Alternatively, the laser spot can be imaged, vital when focusing the beam or adjusting the alignment.

3.2.1 Magneto-optical measurements

A powerful technique for probing the physical processes at work in TMD monolayers is by carrying out micro-photoluminescence spectroscopy while applying a magnetic field (B-field) over the monolayer, with direction either perpendicular or parallel to the monolayer plane. This is achieved with a pair of superconducting coils mounted around the sample space inside the helium bath cryostat. Field strengths up to 9T out-of-plane (known as the *Faraday geometry*) and 4.5T in-plane (the *Voigt geometry*) are possible.

For the magneto-photoluminescence measurements presented in Chapter 4, automated scans (written in National Instruments LabView software) ramp the current in the Faraday

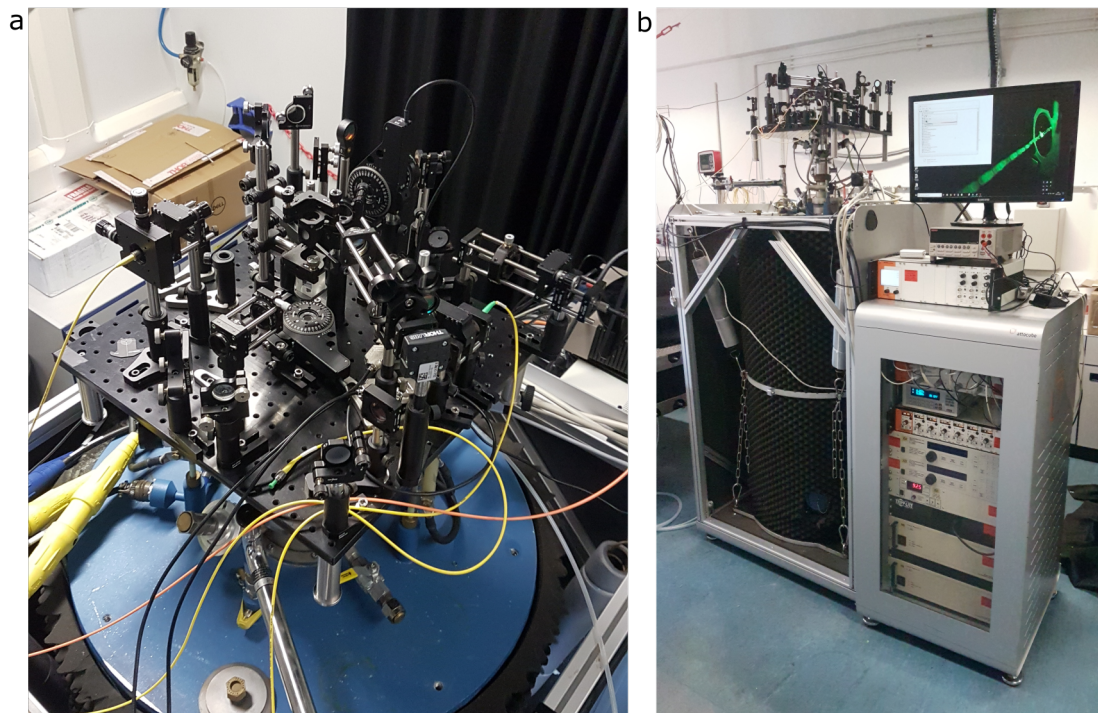


Fig. 3.6 (a) Photograph of optics board on top of helium bath cryostat. These optics correspond to the schematic in Fig. 3.5. Optical fibers connect the board to the laser, spectrometer, and white light source which are all on an adjacent optical table. (b) Photograph of the helium bath cryostat, containing a 2-axis 9 T / 4.5 T vector magnet system, with the optics board from (a) on top. The trolley next the the cryostat contains all control elements, for the magnets, piezo nanospositioners to move the sample, monitor liquid helium level, monitor the temperature and apply heat to the sample.

coil to a value calibrated to provide the desired field strength over the sample, in the magnet bore. This will be one increment of a desired step size; a typical example being a step size of 200mT for a total scan range from $B = -8$ T to $B = +8$ T. Once at the target field, polarisation resolved PL spectra are acquired by automated rotation of $\lambda/4$ and $\lambda/2$ waveplates on the optics board, alternating with automated exposures of the CCD, typically for up to 10 s per exposure.

For the results presented in Chapter 6, in which ferromagnetic hysteresis is measured, automation scripts were written which sweep the magnetic field over a loop from a minimum to maximum value, and back again. At each field increment of the sweep (typically 2 mT in the case of scans running between $B = \pm 200$ mT), a spectrum is acquired, with the waveplates only being rotated after each loop is complete. Therefore, two full loops consisting of two forwards and two reverse sweeps each are performed, to record PL spectra first in σ^+ and then σ^- polarisation.

In the case of Chapter 5, where microcavity spectroscopy is performed at various fixed magnetic field strengths, the magnet may be ramped to a desired current, and then set into *persistent mode* whereby a superconducting element effectively short circuits the coil, creating an infinite current loop with no resistance. The current does not decay in such a situation, and so a stable fixed magnetic field is generated during the several hours typically required to run automated microcavity spectroscopy measurements.

3.3 Optical microcavities

3.3.1 Distributed Bragg reflectors

An optical microcavity can be formed by confining light between two mirrors over a length scale of the order of the wavelength, creating standing waves inside the structure. In this thesis cavities were formed between two facing distributed Bragg reflectors (DBRs), which are layered structures consisting of alternating pairs of high and low refractive index (n_H , n_L respectively) dielectrics. At the interface between each alternating layer, the reflectivity is given by

$$r = \frac{n_L - n_H}{n_L + n_H} \quad (3.1)$$

In order to maximise the reflectivity of the DBR for a desired wavelength λ , the thicknesses of the layers are chosen such that the reflections from each interface interfere constructively over the periodic structure, creating a photonic band gap which prevents transmission

Experimental methods

of waves, and leading to near 100% reflection. This condition is satisfied when the phase shift of each reflection $\Delta\phi_r = \pi$. The phase shift depends upon:

$$\Delta\phi_r = \frac{4\pi}{\lambda}d_{L,H}n_{L,H} \quad (3.2)$$

and so the required thickness of each layer is given by $d_{L,H} = \lambda/4n_{L,H}$. Increasing repetitions N of high and low index pairs increases the overall reflectivity, which is given by

$$R = \left(\frac{1 - \frac{n_1}{n_2} \left(\frac{n_L}{n_H} \right)^{2N}}{1 + \frac{n_1}{n_2} \left(\frac{n_L}{n_H} \right)^{2N}} \right)^2 \quad (3.3)$$

where n_1 and n_2 are the refractive indices of the regions on either side of the DBR. Typically, this is vacuum on one side, within the cavity, and silica on the other (the substrate used for DBR growth) which gives $n_1 = 1$ and $n_2 = 1.5$. The refractive index contrast $\Delta n = n_H - n_L$ determines the spectral width Δ_{sb} of the photonic band gap, known as the *stopband*, over which the reflectivity is highest:

$$\Delta_{sb} = \frac{2\lambda\Delta n}{\pi n_{eff}} \quad (3.4)$$

where λ is the design wavelength of the DBR, which occurs in the centre of the stopband, and $n_{eff} = 2\left(\frac{1}{n_L} + \frac{1}{n_H}\right)^{-1}$ is the effective refractive index of the whole DBR structure.

Therefore, in planning microcavity experiments, DBRs are designed by choosing two suitable materials and an appropriate number of pairs per mirror in order to give the desired microcavity. Typically, SiO_2 is used as a low index dielectric, at $n_L \sim 1.4$, and Nb_2O_5 or Ta_2O_5 are used as high index, with $n_H \sim 2.5$ and 2.3 respectively. The design wavelength is usually chosen to be the neutral exciton resonance of the particular TMD planned for investigation (for instance, 750 nm in MoSe_2). The number of pairs are chosen to give a slightly lower reflectivity of one DBR compared to the other, such that the majority of photoluminescence will escape through one side of the cavity, which is the side facing the objective lens. Fig. 3.7 shows a simulation of the electric field profile within an optical microcavity formed by two DBRs of alternating SiO_2 and Nb_2O_5 layers, with a design wavelength of 750 nm. This simulation was performed using a transfer matrix open source software package called CAMFR, developed by researchers at the University of Ghent, Belgium. A simulation such as this is performed to test possible DBR designs suitable for a planned experiment, and then an order can be placed with an external supplier to deposit the DBR layers by ion-beam sputtering.

In Fig. 3.7, it can be seen that one DBR terminates with a high index layer, while the other terminates with a low index layer, facing into the cavity space. The termination layer

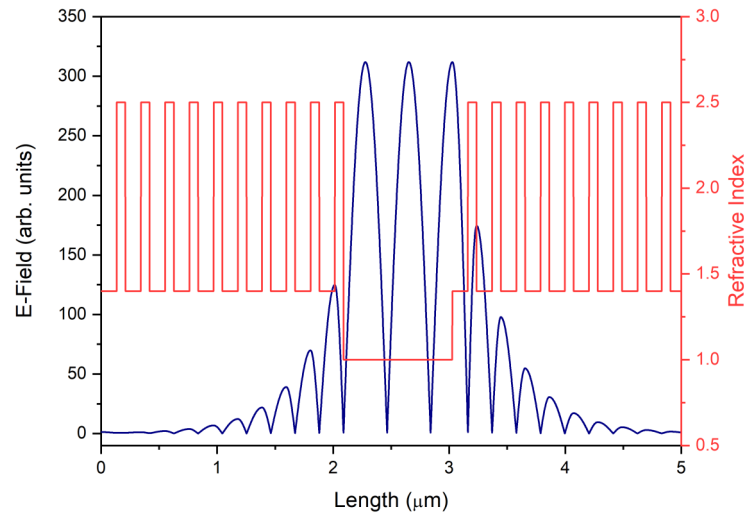


Fig. 3.7 Transfer matrix simulation of the electric field magnitude within the microcavity, confined between two DBRs of alternating high and low refractive index. The right hand DBR represents the bottom planar mirror, which terminates in a low index material (SiO_2) such that a monolayer TMD placed on the surface of the DBR lies at one of the E-field maxima, increasing the light matter coupling strength. As the mirror separation changes, the wavelength of the cavity mode changes accordingly.

refractive index determines the strength of the local E-field, as can be seen in the figure, the E-field has a node at the high index terminating DBR and an antinode at the low index terminating DBR. In this way, a TMD monolayer placed on the surface of the low index terminating DBR will be positioned at the maximum E-field strength, and so the light-matter interaction will be maximised.

3.3.2 Zero dimensional discrete photonic modes

While the simulation in Fig. 3.7 concerns a microcavity formed by two planar DBRs, in reality the microcavities used in this thesis are zero-dimensional, in that they confine the E-field in all three dimensions. This allows much smaller mode volumes to be realised, further enhancing the light-matter coupling and offering other advantages as will be explored in Chapter 5. To realise a zero-dimensional microcavity experimentally, a hemispherical geometry is adopted, by using a planar DBR in conjunction with a concave DBR.

The concave DBRs are made by depositing the dielectric layers onto a substrate with arrays of concave features on them, which are created by focused ion beam (FIB) milling using gallium ions to bombard the thick SiO_2 substrate and remove material. The arrays of

Experimental methods

concave features are milled into a *plinth* structure, which is a raised plateau rising $\sim 100 \mu\text{m}$ above the surrounding substrate. This geometry allows the concave mirrors be brought into direct contact with an adjacent planar DBR to form the cavity. Figs. 3.8a and b show two plinth designs, one circular and one square, before and after DBR layer deposition, respectively. Figs. 3.8c-e show profilometry data of concave features after FIB milling, indicating excellent uniformity and sub-nm surface roughness, which all contribute to a high cavity quality factor.

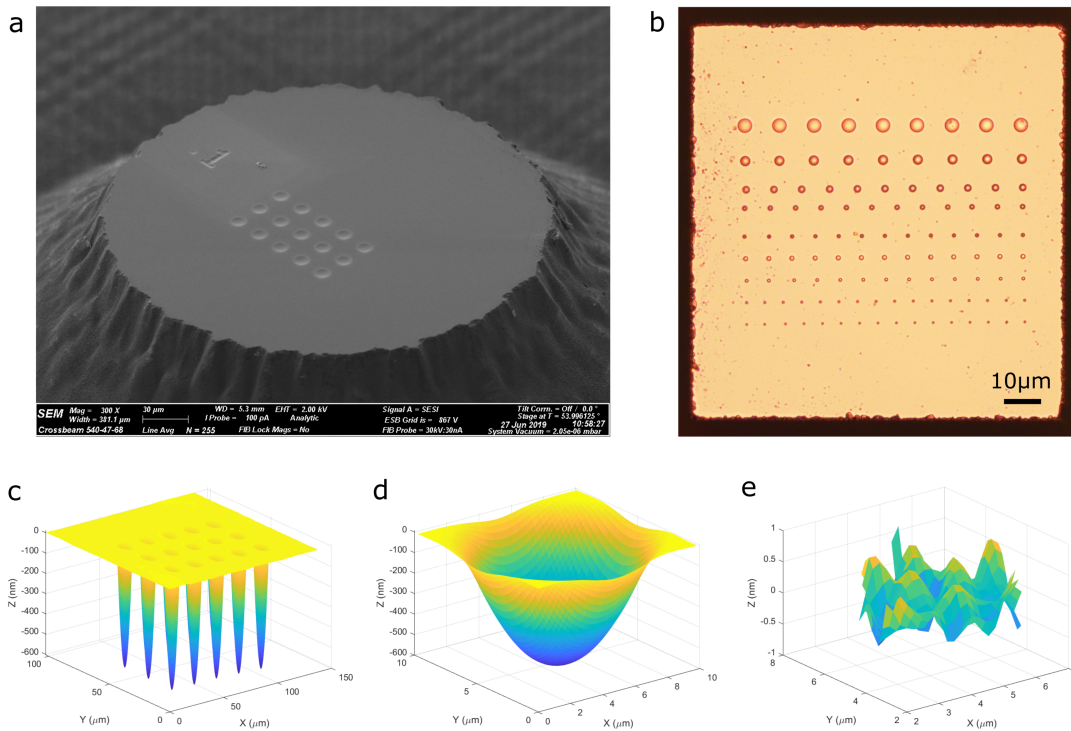


Fig. 3.8 (a) Scanning electron microscope image of a circular plinth design, with an array of identical concave features, of radius of curvature $\sim 20 \mu\text{m}$. Image taken directly after FIB milling of SiO_2 . *Image credit: Oxford HighQ.* (b) Microscope image of an array of concave features on a square plinth, after DBR layers have been deposited on top. This design incorporates concave features of varying radius of curvature, with the largest ones $\sim 20 \mu\text{m}$. *Fabrication performed by collaborators in the University of Oxford, UK.* (c) Profilometry data for the array of features shown in (a), showing almost identical shape and uniform depth. *Image credit: Oxford HighQ.* (d) Profile of a single concave feature from the plinth in (a). *Image credit: Oxford HighQ.* (e) Residual after polynomial fitting of the profile in (d), indicating sub-nm surface roughness and high uniformity, achievable by focused ion-beam milling. *Image credit: Oxford HighQ.*

A hemispherical optical microcavity modifies the photonic density of states supported inside the cavity by introducing confinement to a freely propagating Gaussian beam. As

such, the modified electric field profile becomes describable by a series of discrete Gaussian longitudinal modes, each associated with a series of higher order transverse modes. The longitudinal modes satisfy a round trip phase $\phi(k, L_{opt})$ within the cavity equal to an integer multiple of 2π :

$$\phi(k, L_{opt}) = 2kL_{opt} + \phi_{DBR}(k) = 2a\pi \quad (3.5)$$

where k is the wavenumber, L_{opt} the optical cavity length, a an integer, and ϕ_{DBR} the sum of reflection phases of the two mirrors (a structural constant for a given microcavity). The general description for the eigenfrequencies of the confined E-field within a zero-dimensional resonator formed by a planar mirror and a concave mirror with radius of curvature RoC is given by

$$\nu_{qmn} = \frac{c}{2n_{cav}L_{opt}} \left[q + \frac{(m+n+1)}{\pi} \cos^{-1} \left(1 - \frac{L_{cav}}{RoC} \right) \right] \quad (3.6)$$

where q is the longitudinal and m, n the associated transverse Gaussian mode indices, and n_{cav} is the refractive index inside the cavity (in an open tunable cavity $n = 1$). The distinction between the optical cavity length L_{opt} and the mirror separation length L_{cav} arises because the cavity modes penetrate into the DBRs before being fully reflected, and so L_{opt} is the sum of L_{cav} and the sub-micron penetration depths of each mirror. The eigenfrequencies depend on the RoC owing to the boundary condition that the phase front of the confined beam at each mirror surface must match the radius of curvature of the respective mirror. However, given that the planar mirror has infinite radius of curvature, the eigenfrequencies depend only the RoC of the concave mirror.

The cavity modes are supported as long as the *stability condition* is met, that $L_{cav} < RoC$, in which case the Gaussian modes converge to focus as a minimum beam waist on the planar mirror surface. In the system used in this work, a $20 \mu\text{m}$ RoC mirror is always used, giving a beam waist on the planar mirror $\sim 1 \mu\text{m}$ diameter, smaller than the laser spot diameter achievable using the objective lens in the cryostat, which is $\sim 2.4 \mu\text{m}$. The shortest attainable cavity length in the system is around $2.5 \mu\text{m}$, calculated by measuring the frequency $\Delta\nu$ between two adjacent longitudinal modes ($\Delta q = 1$ and $m = n = 0$) and rearranging Eq. 3.6 as:

$$L_{opt} = \frac{c}{2n_{cav}\Delta\nu} \quad (3.7)$$

The hemispherical cavity nominally has perfect cylindrical symmetry, and so the allowed discrete photonic states correspond to Laguerre-Gaussian mode profiles. These are solutions of the paraxial Helmholtz equation using a cylindrical coordinate basis, and the result is a

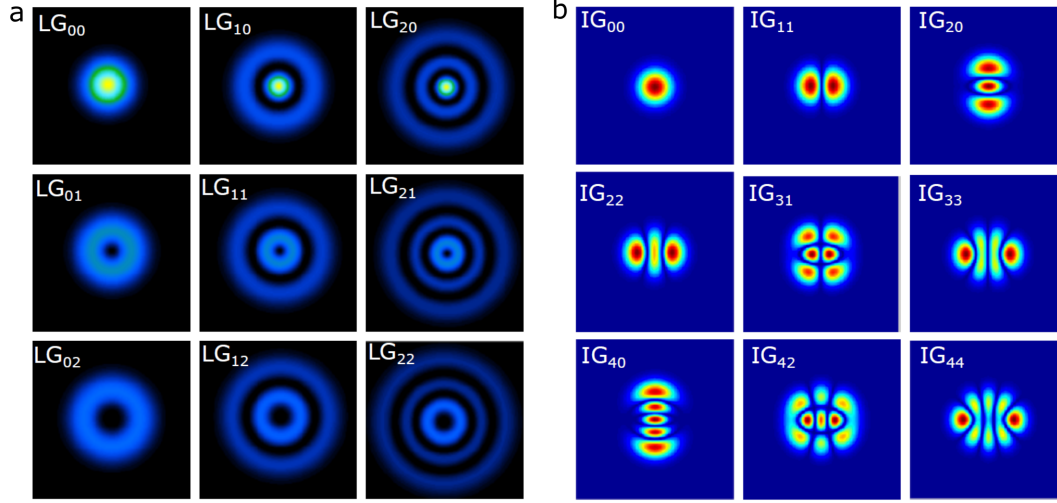


Fig. 3.9 (a) First nine Laguerre-Gaussian cylindrical mode profiles LG_{lp} . (b) Examples of Ince-Gaussian beam profiles, more likely to be observed in the cavity owing to very slight ellipticity in the concave top DBR. All modes above the ground state 00 mode are neglected in experiments in this thesis. In Ref. [84] a series of LG modes are imaged in an identical system to the one used in this thesis, showing that such cylindrical modes are certainly achievable.

series of E-field amplitude profiles describing the transverse electromagnetic (TEM) modes of a Gaussian beam propagating along the z axis with the origin at the centre of the beam waist (i.e. from the planar mirror surface towards the concave mirror). The spatial E-field distribution of the TEM modes may be expressed as (see Ref. [85] for a derivation):

$$E_{lp}(r, \theta, z) = E_0 \frac{\omega_0}{\omega(z)} \left(\frac{r\sqrt{2}}{\omega(z)} \right)^l L_p^l \left(\frac{2r^2}{\omega(z)^2} \right) \exp(-il\theta) \times \exp\left(\frac{-r^2}{\omega(z)^2}\right) \exp\left(\frac{-ikr^2}{2R(z)}\right) \exp\left(i(2p+l+1)\tan^{-1}\left(\frac{z}{z_R}\right)\right) \quad (3.8)$$

where l and p are the azimuthal and radial mode indices, respectively, E_0 is the E-field amplitude at the origin, ω_0 is the radius of the beam waist, L_p^l are generalised Laguerre polynomials, k is the wavenumber, $R(z)$ is the radius of curvature of the beam wavefront at position z , $z_R = \pi\omega_0^2/\lambda$ is the Rayleigh length, and $\omega(z)$ is the radius of the beam at position z where the E-field amplitude drops to $1/e$ of the value at $r = 0$, expressed as

$$\omega(z) = \omega_0 \sqrt{1 + \left(\frac{z}{z_R}\right)^2} \quad (3.9)$$

In reality, however, the cavity is unlikely to be sufficiently symmetrical to support Laguerre-Gaussian mode profiles, and instead the elliptical coordinate solutions to the wave equation are observed, corresponding to Ince-Gaussian modes. Fig. 3.9 shows a comparison of the LG_{lp} and IG_{mp} E-field profiles. Here, it can be seen that although the higher order transverse modes differ significantly, the ground state TEM_{00} modes are essentially identical. Considering that all the experiments in this thesis use only the ground state mode, the exact form of the higher order modes is not a concern for the experimental results.

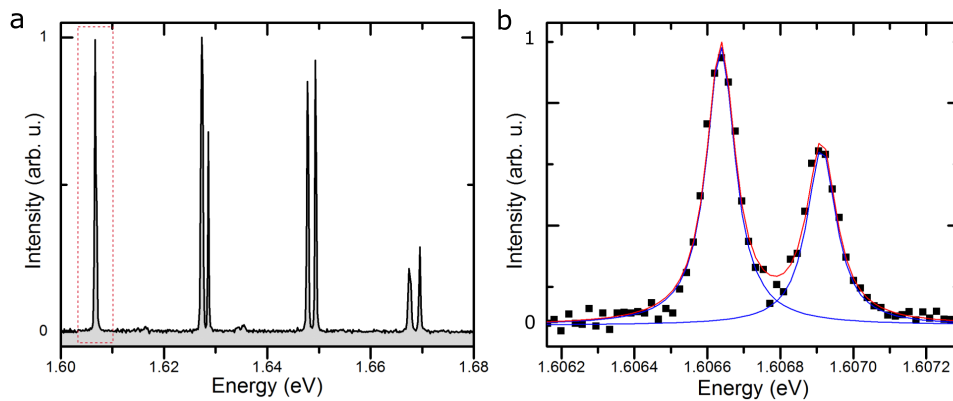


Fig. 3.10 (a) Photoluminescence spectrum of hemispherical cavity modes, showing the LG_{00} mode at lowest energy (highlighted), and associated higher order transverse modes. (b) A high spectral resolution measurement of the LG_{00} mode, revealing the TE-TM splitting, in this case equal to $270 \mu\text{eV}$. The mode linewidths are $\sim 100 \mu\text{eV}$, indicating a cavity Q-factor $\sim 16\,000$.

Fig. 3.10a shows a photoluminescence spectrum taken from the hemispherical cavity used in this thesis. The LG_{00} longitudinal ground state mode can be seen at the lowest energy, with the transverse modes incrementally appearing at higher energy. The origin of the splitting in the higher order modes is asymmetry in the cavity causing a splitting between nominally degenerate modes. Fig. 3.10b shows the LG_{00} mode when measuring with a much higher spectral resolution (by changing to a diffraction grating with more grooves/mm). Here, a splitting is visible, which corresponds to transverse-electric transverse-magnetic (TE-TM) splitting, arising due to birefringence in the cavity DBRs [84]. This may be considered as photonic spin-orbit coupling, as it relates the polarisation of the electric and magnetic fields to the propagation direction, which is of particular relevance to the results presented in Chapter 5.

3.3.3 Low temperature tunable open-access microcavity system

The hemispherical cavity is realised in the laboratory by mounting both DBRs inside the 2-inch bore insert of the helium bath cryostat shown in Fig. 3.6. The DBRs are mounted independently, each on their own stack of piezo nanopositioners, which allow complete movement of each mirror relative to the other. The cavity is arranged such that the planar DBR is situated on the larger bottom stack of nanopositioners, while the top DBR with the plinth and concave features is mounted upside down above it. The x , y , z nanopositioner stack for the top DBR is offset within the insert bore such that an objective lens in a long thin tube can be mounted along the central axis of the bore, which corresponds to the optical path. The top DBR itself is attached to an arm which protrudes out from the stack of nanopositioners, such that the laser can be focused down onto the back of the top DBR substrate to pump the cavity, and PL can be collected from the cavity (the concave top DBR is designed with fewer dielectric layers to ensure the majority of signal escapes the cavity in to the detection side). As such, the top DBR can be completely moved sideways out of the optical path, allowing direct optical spectroscopy of the monolayer / heterostructure to be performed. The objective used in this thesis is a 5 mm diameter achromatic doublet, which is designed to give a good compromise of diffraction limited performance between the laser and PL wavelengths, at 637 nm and 700 - 800 nm, respectively. The focal length is 7.5 mm and the numerical aperture is ~ 0.5 . Fig. 3.11 shows a schematic of the open cavity compared to a photo of the real system. For experiments, the insert is pumped to high vacuum, then small amount of helium exchange gas is vented into the insert to keep the sample cold, as the piezo stages are not an efficient thermal bridge.

The bottom planar DBR, on which there will be the sample (single monolayer or heterostructure) is mounted on 5 piezo nanopositioners which give x , y , z movement and θ , ϕ tilt control. The tilt control is necessary in order to bring the two DBRs to be parallel, to allow the shortest possible cavity length to be achieved. Any angle between the DBRs leads to the mirrors touching each other far from the concave feature, which limits the mirror separation at the location of the cavity itself. The angle between the DBRs may be minimised by viewing the cavity with a broadband light source and observing the etalon-like interference fringes which form with periodicity reflecting the steepness of angle between mirrors. By changing the θ and ϕ stages, the period of the interference fringes can be visibly increased until no more bands can be observed, at which point the mirrors are very close to being parallel.

Once the DBRs are parallel, the laser is focused and aligned onto the back of one of the concave features on the plinth structure, and the detection path is aligned onto the same spot, by feeding a laser backwards through the optical components above the cryostat.

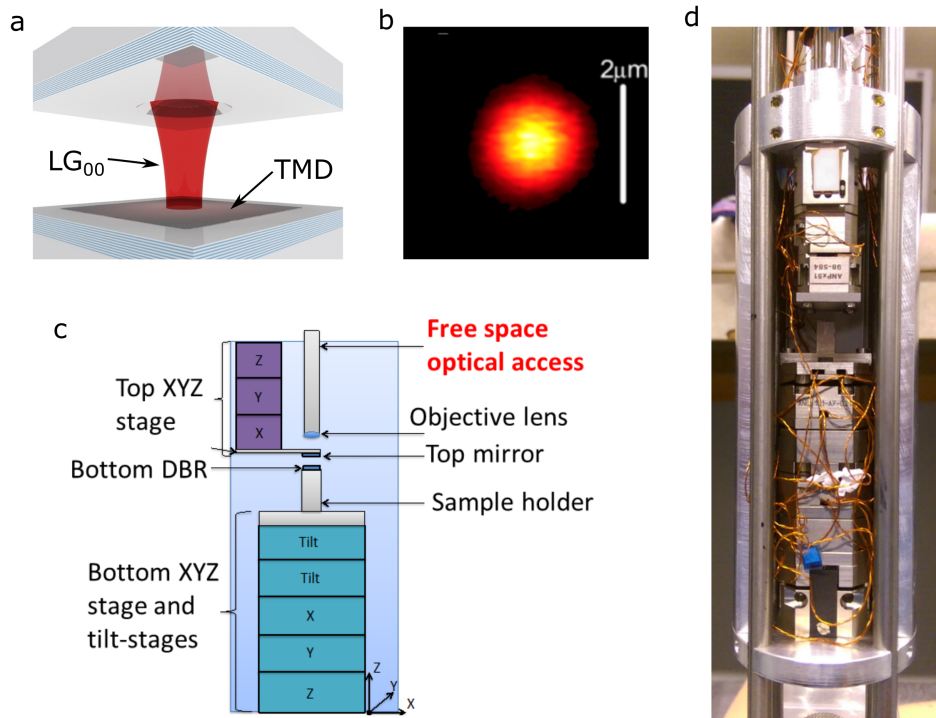


Fig. 3.11 (a) Illustration of the microcavity itself, with a concave top DBR and planar bottom DBR with transferred TMD monolayer. The LG_{00} mode is pictured. (b) Real space image of the LG_{00} mode in an identical system to the one used in this thesis, taken from Ref. [84]. The beam waist is $\sim 1 \mu\text{m}$. (c) Schematic of the tunable open cavity DBRs mounted independently on piezo nanopositioners, allowing full control of each mirror, and cavity length tunability. (d) Photo of the open cavity system used in this thesis. The five bottom piezo stages can be seen, along with three top piezo stages offset towards the camera. The objective lens lies behind the top three stages. The structure is housed in an aluminium cylinder to provide stability, and the whole assembly lies at the bottom of a $\sim 2 \text{ m}$ long bath cryostat insert which contains a small volume of helium exchange gas to maintain a low sample temperature. The open cavity assembly pictured sits inside the bore of a superconducting magnet coil. Free space optical access is afforded from above by a window in the top of the long insert vacuum housing, giving a direct path between the objective lens and the optics pictured in Fig. 3.6.

Experimental methods

Then, microcavity experiments may be performed by laterally moving the monolayer / heterostructure region of the bottom planar DBR directly underneath the concave top DBR, and then bringing the bottom DBR up to meet the top DBR, until they touch. Touching the mirrors is an efficient way to increase the cavity Q-factor by bringing the mirror vibrations into phase. Once in this state, the cavity length may be decreased a very small amount by applying a DC voltage to the bottom z nanopositioner, squeezing the mirrors together slightly. This reduction in cavity length increases the energy of the supported cavity modes, allowing the LG_{00} mode to be swept through resonance with the excitonic absorption in the sample, which is the fundamental procedure of all the cavity experiments covered in this thesis.

3.3.4 Open cavity data fitting procedure

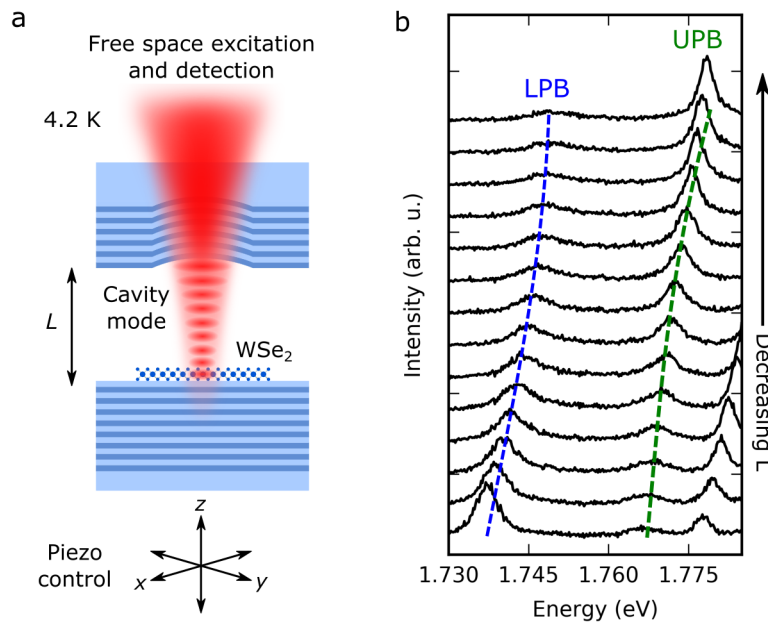


Fig. 3.12 (a) Schematic of a typical cavity experiment. Photoluminescence is measured while the cavity length is decreases incrementally by applying a DC voltage to the bottom planar DBR z -axis piezo nanopositioner. (b) Example of polariton photoluminescence spectra while decreasing cavity length. Polariton spectra are characterised by two emission peaks, the lower and upper polariton branches (LPB, UPB). These shift their energy as a function of applied piezo voltage.

The definition of the strong light-matter coupling regime and associated Rabi splitting will be introduced fully in Chapter 5, which presents all results relating to microcavities in this thesis. As detailed in the previous section, a microcavity may be formed by moving a

concave DBR into the optical path above a monolayer on the planar DBR substrate, and bringing the two mirrors to a separation shorter than the radius of curvature of the concave feature. Upon pumping the monolayer with off-stopband laser light, it will emit into the cavity modes and form exciton-polaritons, which characteristically split the LG₀₀ cavity mode into two non-degenerate eigenstates (termed polariton branches), each a mixture of excitonic and photonic character (see Chapter 5). The microcavity geometry used in this work allows tuning of the LG₀₀ mode energy by changing the cavity length, by applying a DC voltage to a piezo nanopositioner (Fig. 3.12a). A typical experiment therefore involves incrementally applying increasing DC voltage while taking photoluminescence spectra corresponding to polariton emission. Fig. 3.12b shows a series of spectra, taken for increasing voltage, showing the energy evolution of two peaks corresponding to lower and upper polariton branches (LPB and UPB), highlighted by the dashed lines.

A crucial part of the analysis of microcavity polariton spectra is measurement of the Rabi splitting $\hbar\Omega_R$, which is the smallest energy difference between the two modes (see Chapter 5). Therefore, from cavity spectra such as those in Fig. 3.12b, it is necessary to fit the lower and upper polariton PL peaks to Lorentzian functions and extract the peak energies as a function of piezo voltage. Each scan of the cavity length therefore gives two datasets, $E_L(V)$ and $E_U(V)$. These two arrays are then fitted to the eigenstates of the exciton-photon coupling Hamiltonian, which is given by the matrix:

$$\begin{pmatrix} E_x & g_{xp} \\ g_{xp} & E_p(V) \end{pmatrix}$$

where E_x is the uncoupled exciton energy, in this case constant, and $g_{xp} = \frac{\hbar\Omega_R}{2}$ is the exciton-photon coupling term, corresponding to half of the Rabi splitting. The uncoupled cavity photon energy $E_p(V)$ may not respond linearly with applied voltage, and so is described by the equation $E_p(V) = y_0 + aV + bV^2$ where y_0 , a and b depend on the piezo response and particular experimental conditions.

The eigenstates of the Hamiltonian are the lower and upper polariton dispersions $E_L(V)$ and $E_U(V)$, while the corresponding eigenvectors give the excitonic/photonic compositions of each eigenstate. These are the *Hopfield coefficients*, functions of voltage which describe the transition from photon-like to exciton-like for the LPB, and vice versa for the UPB, as the cavity mode is tuned through resonance with the exciton. The Hamiltonian may be diagonalised using the *Hopfield transformations*

$$\begin{aligned} L_V &= \kappa_x^L X_V + \kappa_p^L P_V \\ U_V &= -\kappa_p^U X_V + \kappa_x^U P_V \end{aligned} \quad (3.10)$$

Experimental methods

where L_V and U_V are the annihilation operators for the new lower and upper polariton eigenstates, and X_V and P_V are the annihilation operators for excitons and cavity photons, respectively. $\kappa_{x,p}^{(i)}$ are the Hopfield coefficients for the polariton branch $i = L, U$, where $(\kappa_x^{(i)})^2$ and $(\kappa_p^{(i)})^2$ give the exciton and photon fraction of each branch, respectively. As such, $(\kappa_x^{(i)})^2 + (\kappa_p^{(i)})^2 = 1$, and are defined as

$$\begin{aligned} (\kappa_x^L)^2 &= (\kappa_p^U)^2 = \frac{1}{2} \left(1 + \frac{\Delta_{xp}(V)}{\sqrt{\Delta_{xp}(V)^2 + 4g_{xp}^2}} \right) \\ (\kappa_p^L)^2 &= (\kappa_x^U)^2 = \frac{1}{2} \left(1 - \frac{\Delta_{xp}(V)}{\sqrt{\Delta_{xp}(V)^2 + 4g_{xp}^2}} \right) \end{aligned} \quad (3.11)$$

where $\Delta_{xp}(V) = E_p(V) - E_x$ is the *detuning*. From Eqs. 3.10 and 3.11 the Hamiltonian may be diagonalised to give the polariton dispersions

$$E_{U,L}(V) = \frac{1}{2} \left[E_x + E_p(V) \pm \sqrt{\Delta_{xp}(V)^2 + 4g_{xp}^2} \right] \quad (3.12)$$

from which it is clear that in the resonance condition, when $E_p(V) = E_x$, the eigenenergies become $E_U = E_x + g_{xp}$ and $E_L = E_x - g_{xp}$, i.e. the polariton modes are separated by the Rabi splitting. This coincides with $(\kappa_x^L)^2 = (\kappa_p^L)^2 = (\kappa_x^U)^2 = (\kappa_p^U)^2 = 0.5$, indicating that at resonance, exciton-polaritons are exactly half-light-half-matter quasiparticles.

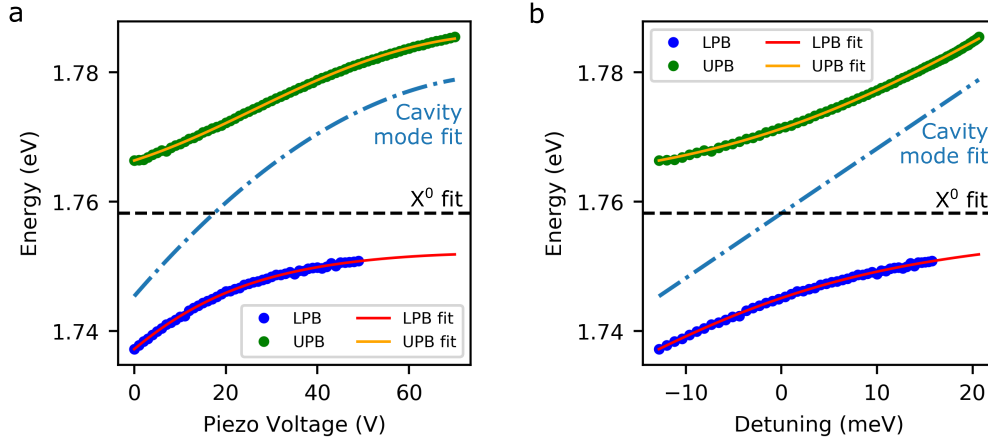


Fig. 3.13 (a) Example of the peak energies of the LPB and UPB (extracted by Lorentzian peak fitting to each spectrum) as a function of piezo voltage fitted to Eq. 3.12. (b) The same fitted data with the piezo voltage scale converted to a detuning scale, $E(\text{cavity}) - E(\text{exciton})$, ensuring the cavity mode is linear and any nonlinear response of cavity length to applied voltage is compensated.

The datasets $E_L(V)$ and $E_U(V)$ from a cavity scan are then fitted to Eq. 3.12 using a least squares method, where $E_x, E_p(V) = y_0 + aV + bV^2$, and g_{xp} are all fitting parameters. This is how the Rabi splitting is measured for a given sample. Often, cavity scans are performed with the two mirrors touching one another in order to keep their vibrations in phase and therefore increase cavity stability. However, touching the mirrors while increasing the DC voltage can lead to the cavity mode energy increasing less and less with each additional applied volt, as the mirrors resist being squeezed closer together. This can cause the cavity spectra $E_{L,U}(V)$ to appear distorted, as shown in Fig. 3.13a. It is therefore beneficial to convert the piezo voltage scale to a detuning scale, using the fitting outputs E_x and $E_p(V)$, for which the cavity mode energy $E_p(\Delta_{xp}(V))$ is always linear. A comparison of raw data, $E_{L,U}(V)$, fitted to Eq. 3.12, and the same data converted to a detuning scale are shown in Fig 3.13b.

The above analysis is carried out to process the data from each sweep of the cavity length, in order to extract all results as functions of detuning, which is a universal scale, unlike the piezo voltage, which is arbitrary. Data presented in Chapter 5 which depends on the detuning is therefore the result of processing with the above method.

Chapter 4

The trion valley Zeeman effect in monolayer WSe₂

In Chapter 2 the electron hole complexes known as excitons and trions were introduced, followed by a description of the valley Zeeman effect observed in neutral exciton luminescence. In this chapter, the valley Zeeman effect is extended to consider negatively charged trions, complexes of two electrons and one hole, in monolayer tungsten diselenide. These trions inherit several properties arising from their three-body nature which are absent in neutral excitons, most notably a charge of -1 , a larger effective mass, and a much smaller binding energy (the energy required to ionise the trion and leave an exciton and a single electron in the conduction band) [32]. While the valley Zeeman splitting of neutral excitons in WSe₂ is fairly consistently reported to be $E(\sigma^+) - E(\sigma^-) \approx -4\mu_B B$ [56, 21, 57], where μ_B is the Bohr magneton (see Chapter 2), values reported in literature for the negatively charged trion vary from $-4\mu_B B$ to $-13\mu_B B$ [21, 57–59], and are the subject of some speculation and ambiguity as to the cause of the reported variation. Typically, trion emission dominates the photoluminescence spectra from monolayer WSe₂, thanks to intrinsic electron doping inherent to exfoliated flakes. As such, a full understanding of the magneto-optics of trions in WSe₂ is crucial to clarify major ambiguities in the valley magnetism.

The results presented in this chapter are already published as below:

T. P. Lyons, S. Dufferwiel, M. Brooks, F. Withers, T. Taniguchi, K. Watanabe, K. S. Novoselov, G. Burkard, A. I. Tartakovskii, “*The valley Zeeman effect in inter- and intra-valley trions in monolayer WSe₂*”, Nature Communications **10**, 2330 (2019)

4.1 Background - intervalley and intravalley trions

As mentioned in Section 2.2.2, a trion consists of a neutral exciton bound to an additional carrier. The charge of this carrier determines the charge of the trion, either negative in the case of an electron or positive for a hole [46]. In exfoliated monolayer TMDs, however, an overall n-type doping is typically observed, ascribed to the presence of dopants or substrate interactions [32, 79]. Consequently, negatively charged trions are preferentially formed, by photogenerated neutral excitons binding to an excess electron in the conduction band [32, 86].

In monolayer WSe₂, optical selection rules dictate that negative trions must have an electron with the same valley index as the hole, and opposite spin, in order to allow radiative recombination (i.e. spin and momentum are conserved). As such, an electron must always occupy the upper spin state of the conduction band, allowing the excess electron to occupy the lower energy conduction spin subband, in either valley. This gives a total of four different ground state bright A-trion configurations, which are illustrated in Fig. 4.1. Two of these trion configurations are intravalley, with all three carriers in the same valley, and the other two are intervalley, with the excess electron in the opposite valley to the e-h pair which may recombine with the emission of a photon [56, 87]. For the two trions with excess electron in the +K (-K) valley, the trion centre of mass wavevector is $\mathbf{q}_{X^-} = \mathbf{K} + \mathbf{k}$ ($\mathbf{q}_{X^-} = -\mathbf{K} + \mathbf{k}$), where $\pm\mathbf{K}$ is the vector from the Γ -point to the $\pm\mathbf{K}$ -point (therefore $K = \frac{4\pi}{3a}$ where a is the lattice constant), and $\mathbf{k} = (k \cos \theta, k \sin \theta)$ is the trion wavevector taking the $\pm\mathbf{K}$ -points as the origin [44]. As such, the energy extrema of the trion dispersions are located at $q_{X^-}/K = \pm 1$, on the K-points, as shown in Fig. 4.1.

The binding to an extra electron has the effect of opening a gap at the Dirac point of the neutral exciton dispersion (shown in Fig. 2.9b), giving the trion a gapped Dirac cone associated with a large effective mass [44]. The large mass at the gapped Dirac points is linked to a strong Berry curvature, which takes opposite values in the upper and lower branches of the gapped dispersion, in much the same way as single electrons occupying Bloch bands at the K-points are associated with a Berry curvature, giving rise to their valley Hall effect, as discussed in Chapter 2. In this way, both electrons and trions in monolayer TMDs may be considered as massive Dirac fermions, in contrast to neutral excitons which are massless within the light cone [44, 4]. Indeed, there is no light cone as such in the trion dispersion, as the excess electron can nominally compensate any momentum transfer associated with radiative recombination at non-zero wavevectors. In reality, however, the likelihood of trion emission (known as trion *brightness*, plotted in Fig. 4.1) decays exponentially with increasing wavevector from $\pm\mathbf{K}$, as $\sim \exp\left(\frac{-k^2}{(0.01K)^2}\right)$ [44]. This restricts trion emission to the K-points, where the Berry curvature is strongest, and takes opposite sign in opposite valleys by time

4.1 Background - intervalley and intravalley trions

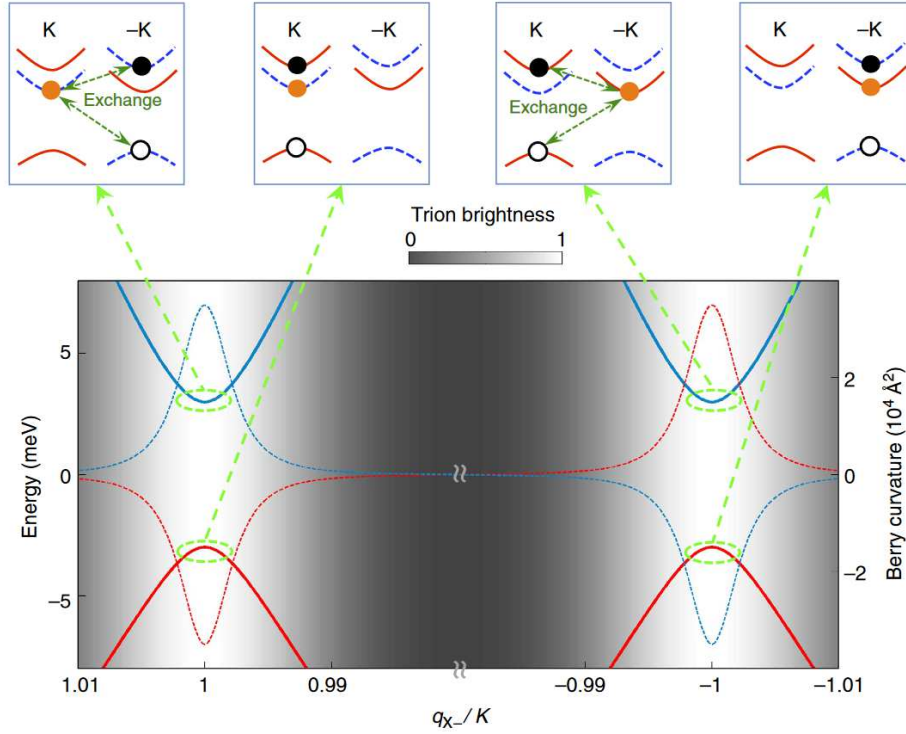


Fig. 4.1 Top: four ground state trion carrier valley configurations in monolayer WSe_2 , where hollow circles are holes, solid black (orange) circles are recombining (excess) electrons. Intervalley trion configurations have an additional exchange interaction between the electron-hole pair and excess electron, which opens a gap at the Dirac point of the trion dispersion, as shown in the lower panel, where a few-meV gap is seen between inter- and intra-valley trion states. The x -axis q_{x-}/K is defined in the text. Owing to the large effective mass at the K -points, the trion is associated with strong Berry curvature with sign depending on the valley index of the recombining electron-hole pair. This is further associated with chiral optical selection rules, giving circularly polarised emission from the dispersion branch extrema. The black-white colour scale of the plot represents trion brightness, which decreases exponentially with wavevector away from the K -points. *Image from Ref. [44].*

The trion valley Zeeman effect in monolayer WSe₂

reversal symmetry, as shown in Fig. 4.1. The Berry curvature at the K-points is also linked to the chiral optical selection rules in TMDs, leading to opposite circular polarisation of trion emission from upper and lower gapped dispersion branches, despite nominally having the same centre of mass wavevector [44].

The opening of the gap at the Dirac point of the trion dispersion is a consequence of intervalley Coulomb exchange between an electron-hole pair in one valley and an excess electron in the opposite valley. As such, the gap is opened by raising the energy of the intervalley trion states above the intravalley trion states, by an amount corresponding to the exchange interaction, expected to be a few meV [44]. In luminescence, this energy gap gives rise to trion fine structure, which has been observed experimentally in WS₂ and WSe₂ [88–91, 87]. The fine structure splitting is typically reported to be ~ 6 meV, which is often far less than the trion photoluminescence linewidth in the majority of samples. As such, it is only possible to observe trion fine structure experimentally in exceptionally high quality samples with linewidths of the order of the exchange splitting.

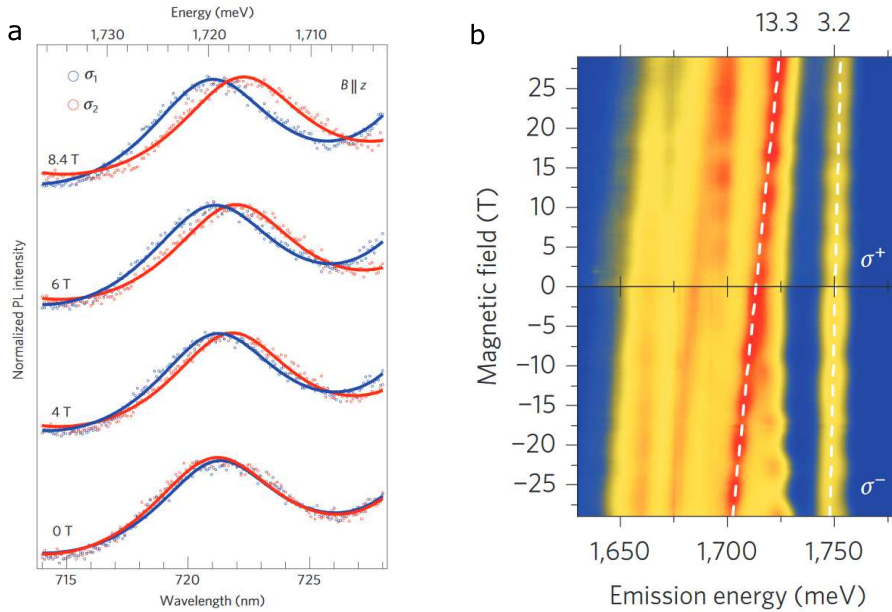


Fig. 4.2 (a,b) Examples of trion valley Zeeman splitting $E(\sigma^+) - E(\sigma^-) = g\mu_B B$ reported in literature. The measured g-factors are (a) -6.3 and (b) -13.3, a factor of 2 apart, despite both samples being the same material. *Images from Refs. [21, 59] respectively.*

Owing to this limitation, magneto-optical studies of the valley Zeeman effect in monolayer WSe₂ typically consider the trion emission as a single photoluminescence peak, and any measurement of the valley Zeeman splitting $E(\sigma^+) - E(\sigma^-)$ is taken from the polarisation resolved single peak energies. There have been various reports of the trion valley Zeeman splitting, with effective g-factors ranging between $-4\mu_B B$ to $-13\mu_B B$ [57, 21, 58, 59], two

examples of which are shown in Fig. 4.2. It is highly likely that the complex nature of the gapped trion dispersion and associated fine structure may be responsible, considering that the fine structure splitting and valley Zeeman splitting are both of the order of a few meV. In this chapter, the trion valley Zeeman effect is measured, with particular consideration for the independent behaviour of all fine structure complexes, enabled by very high sample quality.

4.2 hBN encapsulated monolayer WSe₂

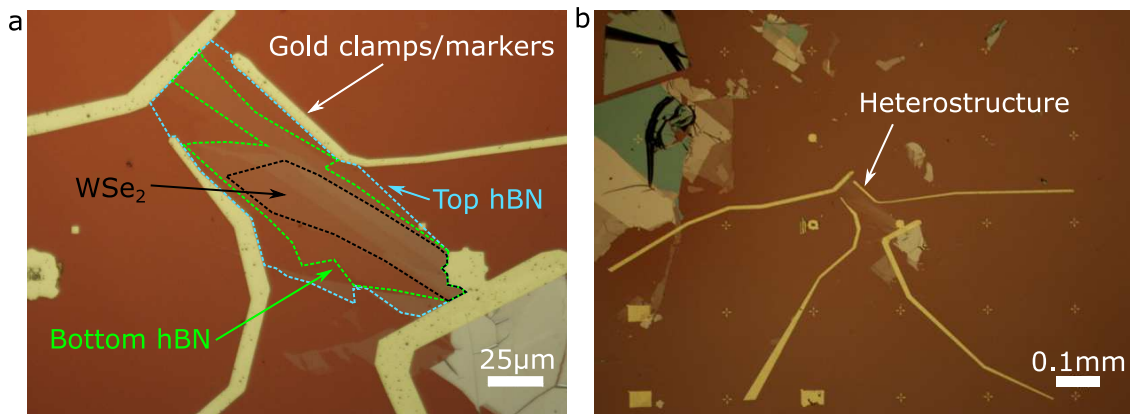


Fig. 4.3 (a) Microscope image of an hBN encapsulated WSe₂ monolayer. Evaporated gold clamps serve to fix the sample in place during fabrication and help identify the location of the heterostructure on the substrate. (b) Sample image at lower magnification.

The sample used in this investigation consists of a monolayer of mechanically exfoliated WSe₂, encapsulated on both sides by few-layer hexagonal boron nitride (hBN) [92]. In particular, the hBN used in this sample has been synthesised under highly controlled conditions by collaborators at NIMS, Japan, and is known to effectively suppress inhomogeneous broadening of excitonic luminescence in monolayer TMDs, owing to atomically clean and flat interfaces and exceptional purity [42, 92]. Along with protecting the WSe₂ layer from contaminants from above, the hBN also isolates the WSe₂ from the SiO₂ substrate below, which may otherwise introduce adverse effects ultimately leading to spectral line broadening [93, 42].

This sample, fabricated by collaborators at the University of Manchester, has been made using a so-called “pick-up” method which introduces the least possible contamination to the WSe₂ monolayer, as detailed in Section 3.1.4. The sample is shown in Fig. 4.3, where evaporated gold clamps can also be seen, employed to affix the heterostructure down to the substrate to prevent it washing away when solvents are used to remove the polymer transfer membrane.

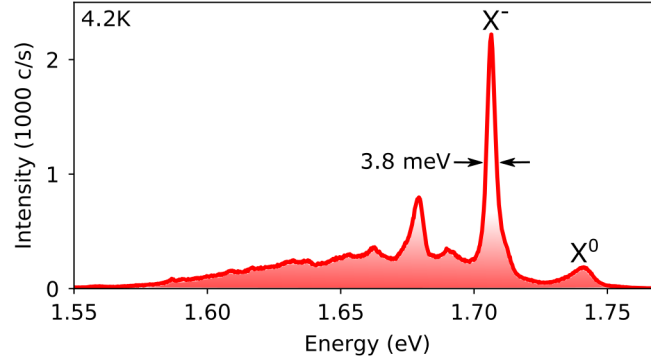


Fig. 4.4 Photoluminescence (PL) spectrum from the sample under non-resonant laser excitation at 4.2 K. Peaks attributed to the neutral A-exciton (X^0) and trion (X^-) can be seen. The trion linewidth is exceptionally narrow, at 3.8 meV, owing to complete encapsulation in high purity hBN.

A PL spectrum from the sample at 4.2 K, excited by continuous wave laser light at 1.946 eV, can be seen in Fig. 4.4. Peaks corresponding to the neutral A exciton (X^0) and negatively charged trion (X^-) are visible, typical of WSe₂ [48], although the trion here displays an exceptionally narrow linewidth of 3.8 meV, significantly narrower than the typical 10 - 20 meV values for bare WSe₂ [48] and approaching the intrinsic homogeneous linewidth [94]. Consequently, this sample is well suited for a study of the fine structure magneto-optical response.

4.3 Optically probing the trion fine structure

It is convenient to define the four trion ground state carrier configurations introduced in Section 4.1 as spin *singlet* or *triplet* trions, where the cumulative spin of the electron pair is equal to 0 or 1, respectively. These are shown in Fig. 4.5, along with their exchange-split dispersions (shown over a much larger wavevector range than in Fig. 4.1, which shows the gapped Dirac cone at the K-points) and carrier configurations in the conduction and valence spin-subbands, labelled for reference as v1, c1, c2. Overall, the four ground state trion configurations can be defined as:

Singlet s^+ with σ^+ optical helicity and excess electron spin down

Singlet s^- with σ^- optical helicity and excess electron spin up

Triplet t^+ with σ^+ optical helicity and excess electron spin up

Triplet t^- with σ^- optical helicity and excess electron spin down

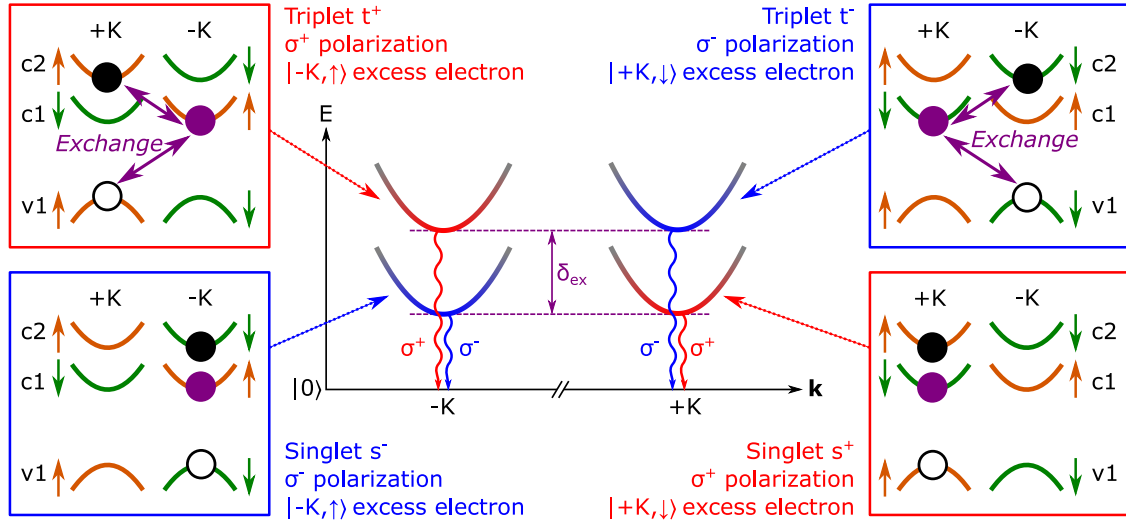


Fig. 4.5 Generalised trion dispersion relations $E(\mathbf{k})$, where \mathbf{k} is the centre of mass wavevector, of the four optically bright ground state negative trions in monolayer WSe_2 . Side panels illustrate the spin-valley configurations of the constituent carriers of each trion variety. $v1$ is the topmost spin-subband within the valence band, while $c1$ ($c2$) is the lower (upper) energy spin-orbit split conduction band. Based on optical selection rules, the black electron (black filled circle) and hole (black empty circle) are the recombining pair, while the purple electron (purple filled circle) is excess and occupies band $c1$. Orange (green) conduction and valence band states are spin up (down). Red (blue) colours denote σ^+ (σ^-) helicity of the bright transition. The trion states are labelled X^Y where $X = s, t$ for singlet or triplet, $Y = +, -$ for σ^+ or σ^- emission helicity. Purple arrows indicate the intervalley Coulomb exchange interaction arising from parallel electron spin, present only in triplet trions, which raises the energy of the triplets by an amount δ_{ex} above the singlets. This energy gap gives rise to the trion fine structure in emission.

4.3.1 Temperature dependent trion photoluminescence

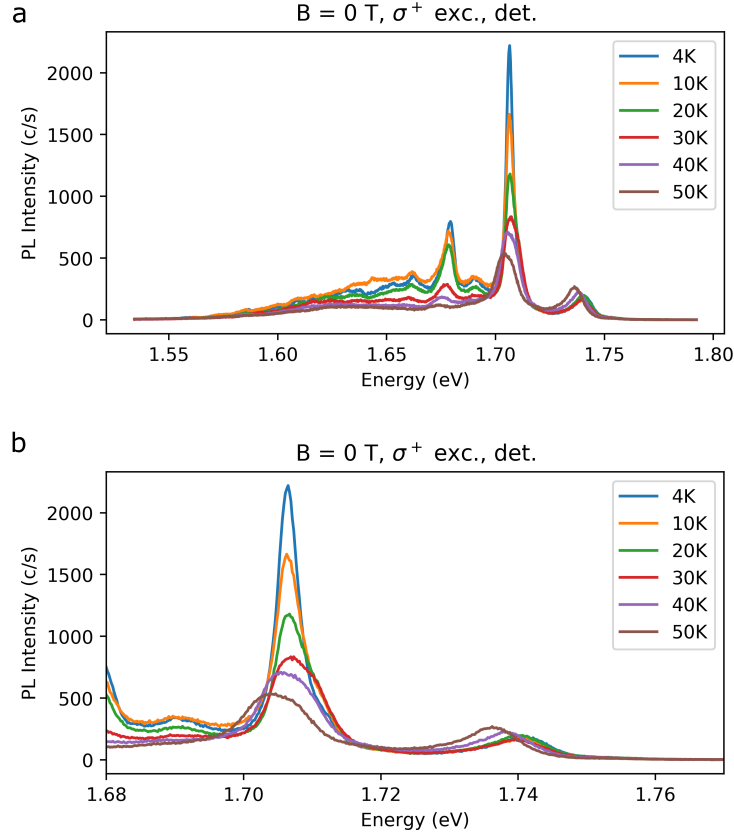


Fig. 4.6 (a,b) Temperature dependence of photoluminescence from the sample, over (a) the whole spectral range and (b) the exciton and trion region, with σ^+ excitation and detection, and no external magnetic field. Spectra for σ^- excitation and detection look effectively identical owing to time reversal symmetry of exciton and trion states.

Given that the reported trion fine structure splitting is ~ 6 meV, it should be clearly visible in the PL spectrum from the sample in Fig. 4.4, in which the trion linewidth is 3.8 meV. However, it is absent, although there appears to be a small shoulder on the high energy side of the trion peak. To investigate further, the sample was heated up from the base temperature of 4.2 K up to 50 K, with resulting spectra shown in Fig. 4.6. Here, the main trion peak can be seen to get dimmer with increasing temperature, while the high energy shoulder gets brighter up to 30 K, then gets dimmer again as it becomes indistinguishable from the broadened trion feature.

Upon plotting the trion PL feature vs temperature, with normalised intensity, it becomes clear that the high energy shoulder grows relative to the main peak, as shown in Fig. 4.7a. Such intensity renormalisation is attributed to thermal population of the higher energy triplet

4.3 Optically probing the trion fine structure

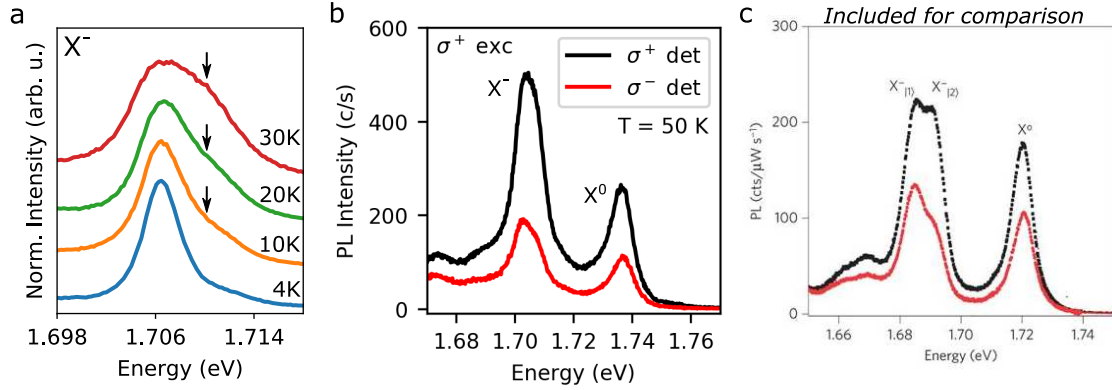


Fig. 4.7 (a) Temperature dependence of the trion photoluminescence from 4.2 K to 30 K. Increasing thermal population of the higher energy triplet states can be inferred from the increasing spectral weight of the high energy shoulder of the trion peak, indicated by the black arrows. (b) PL spectra from the sample at 50 K co- and cross- circularly polarised to the σ^+ polarised excitation laser. There is a very close similarity to the spectra in (c), taken from the earliest reports of trion fine structure in WSe_2 [91].

states. This is consistent with the Boltzmann distribution, whereby increasing temperature leads to increasing probability of occupancy the triplet states, p_i , relative to the singlet, p_s , as $p_t/p_s = \exp\left(\frac{-\Delta E}{k_B T}\right)$ [95]. At 30 K, the triplet luminescence is of comparable intensity to the singlet, although the fine structure is not spectrally resolvable owing to line broadening associated with the elevated temperature. To confirm the attribution of the high energy shoulder to the triplet trion states, polarisation resolved PL spectra at raised temperature may be compared with literature (from Ref. [91]), as shown in Fig. 4.7b,c, where a very close similarity is observed. The discrepancy in absolute emission energy between the two samples is attributed to a modified dielectric environment influencing the exciton binding energy, owing to different hBN used in each sample [96].

4.3.2 Multiple peak fitting

Fig. 4.8 shows the region of interest of the PL spectrum at 30 K, fitted to five Lorentzian peaks, each corresponding to a different emissive state. 30 K is an ideal temperature to use as it populates the triplet state sufficiently for peak fitting, but avoids the overall line broadening and dimming observed at 40 K and 50 K in Fig. 4.6, thereby allowing the greatest insight into the magneto-optical response of the fine structure. The trion feature fits accurately to a doublet peak structure, indicating the presence of non-degenerate singlet and triplet trion emission. The singlet is 33 meV below X^0 , and the triplet is 29 meV below, meaning the exchange splitting $\delta_{\text{ex}} = 4$ meV. This value is smaller than previously reported values ≈ 6

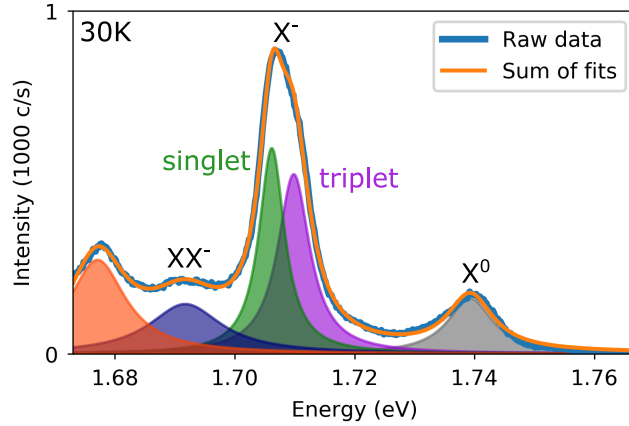


Fig. 4.8 Photoluminescence spectrum from the sample at 30 K, fitted to 5 lorentzian peaks corresponding to various optically active states. The trion peak fits well to 2 peaks corresponding to the fine structure components, separated by ~ 4 meV. The navy blue peak may be the recently reported negatively charged biexciton, XX^- , ~ 50 meV below X^0 .

meV [91], with the difference likely due to influences of the dielectric environment on the relative singlet and triplet binding energies in our fully encapsulated sample [97, 98]. The fourth peak is 48 meV below X^0 , very close to the reported binding energy of the negatively charged biexciton [33–36].

4.4 Magneto-optical response of singlet and triplet trions

4.4.1 Trion peak substructure evolution under a magnetic field

Fig. 4.9 shows polarisation resolved PL spectra from the sample as a function of temperature, with an external magnetic field $B = \pm 8$ T applied out of the sample plane. The high energy shoulder seen in Fig. 4.6, attributed to triplet trion emission, can now be seen to appear or disappear at opposite B-field or polarisation, and the entire lineshape of the trion feature has a strong dependence on magnetic field, most notably at raised temperatures. These spectra appear to indicate that substructure of the trion PL feature is shifting with the B-field in non-uniform ways, leading to changing asymmetry in the trion line.

To elucidate this response, spectra at 30 K in both polarisations at positive and negative fields are shown in Fig. 4.10. Initially at zero external B-field, an asymmetric trion feature composed of an unresolved lower energy singlet peak and higher energy triplet peak is observed, as shown in the 0 T traces of Fig. 4.10. As depicted in Fig. 4.5, emission from t^+ (s^+) and t^- (s^-) is at the same energy in the absence of an external B-field, and there is a

4.4 Magneto-optical response of singlet and triplet trions

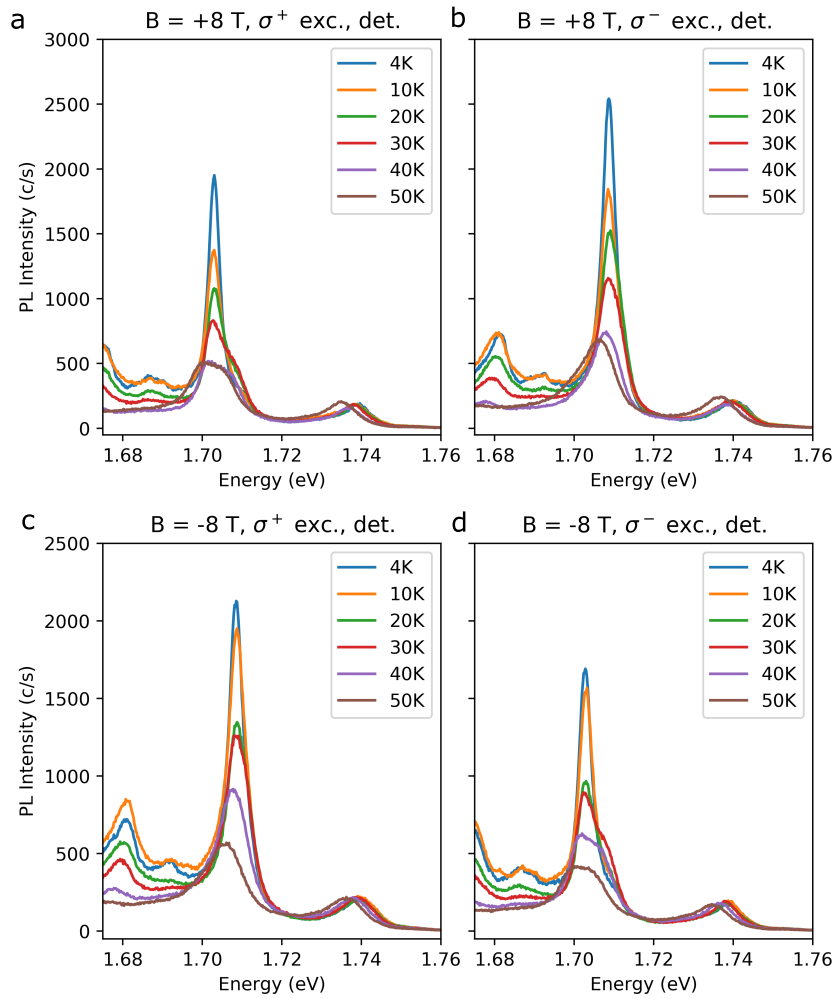


Fig. 4.9 (a,b,c,d) Temperature dependence of photoluminescence in both σ^+ and σ^- polarisations, and at $B = \pm 8 \text{ T}$ applied perpendicular to the sample. The high energy shoulder, attributed to unresolved triplet trions, appears to respond to the field in a different manner than the main trion peak, indicating inequivalent response of trion fine structure to the external B-field.

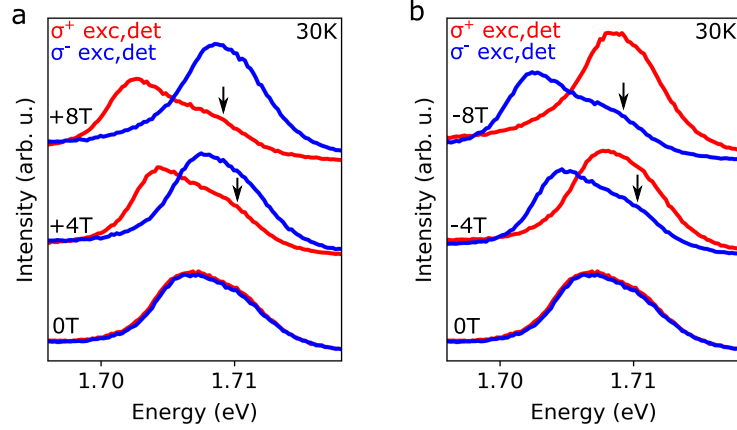


Fig. 4.10 (a,b) Polarisation resolved trion PL spectra (a) at positive B-fields and (b) negative B-fields, all at a sample temperature of 30 K. The spectra indicate inequivalent valley Zeeman g-factors of the unresolved trion fine structure. Black arrows indicate the shoulder, attributed to the triplet trions, which becomes more prominent in σ^+ (σ^-) polarisation at negative (positive) B-fields.

few meV energy gap δ_{ex} between the triplet emission and singlet emission, arising from the intervalley exchange coupling.

Upon applying an external B-field perpendicular to the sample, up to $B = \pm 8$ T, the σ^+ and σ^- components of the emission shift spectrally away from one another, with σ^- emission shifting to higher energy when $B > 0$, consistent with the valley Zeeman effect. However, as is clear from the ± 4 T and ± 8 T traces of Fig. 4.10, there is an accompanying lineshape evolution of the trion feature with external field. It appears that when shifting to lower energy, the singlet and triplet increase their energy separation, as evidenced by the prominent shoulder appearing in the σ^+ (σ^-) emission at $B > 0$ ($B < 0$), highlighted by black arrows. Conversely, when shifting to higher energy, the singlet and triplet peaks appear to reduce their energy separation, resulting in the overall brighter and narrower emission profile seen in the σ^- (σ^+) emission at $B > 0$ ($B < 0$).

By applying the same fitting procedure as used in Fig. 4.8 for zero-field PL, the photon energies of the four different trion states, i.e. s^+ , s^- , t^+ , t^- , may be extracted as a function of external magnetic field at 30 K. An example of the fitted fine structure is shown in Fig. 4.11a, at $B = 4$ T, where it is clear that four distinct peaks exist in total, corresponding to the four ground state trion varieties. Each of these fitted Lorentzian peaks is distinct from the other three by either photon energy, helicity, or both. As such, it is possible to isolate and trace the energy shift of each trion state independently over the external B-field range, as shown for s^+ and t^+ overlaid on the raw σ^+ spectra in Fig. 4.11b.

4.4 Magneto-optical response of singlet and triplet trions

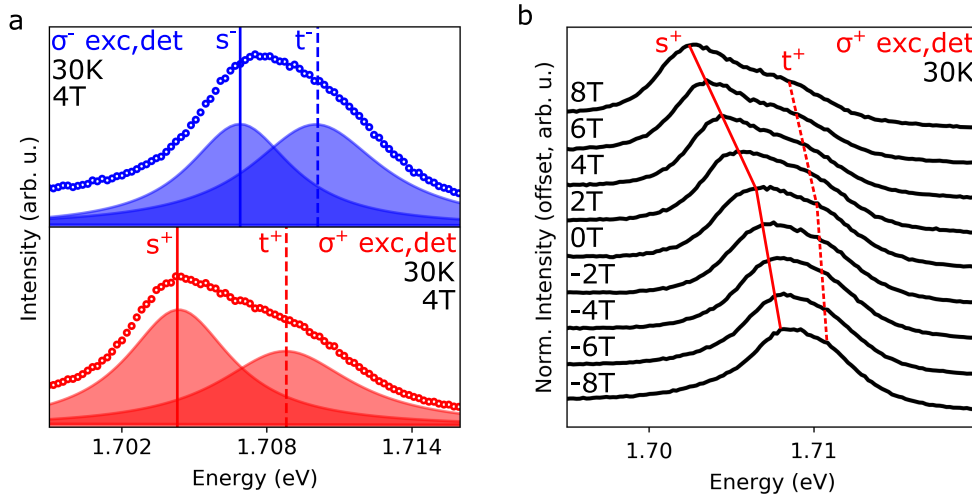


Fig. 4.11 (a) The trion fine structure may be fitted to two Lorentzian peaks in each photon helicity, showing all four trion configurations at $B = 4$ T. Open circles are the CCD data. (b) B-field dependent trion PL in σ^+ polarisation. Solid and dashed red lines trace the approximate peak energies of the fitted Lorentzian functions for s^+ and t^+ , respectively, shown in (a) for $B = 4$ T.

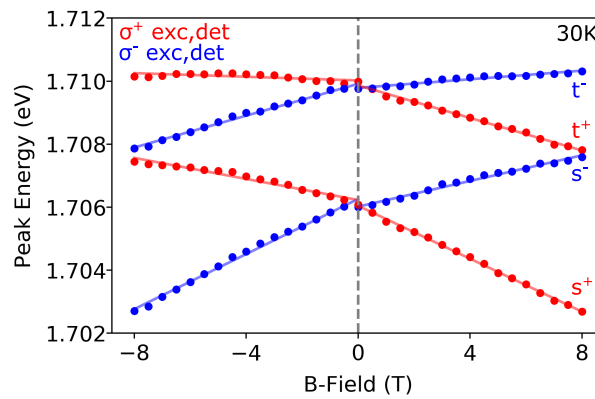


Fig. 4.12 Fitted peak energies of the fine structure components as a function of external B-field. Solid lines are linear fits to the data for either positive or negative field ranges. The rates of shift are inequivalent for each trion state between positive and negative B-fields.

Fig. 4.12 plots the fitted peak energies of all four trion varieties over the entire B-field range, from which two key observations can be made. Firstly, there is a much larger apparent valley splitting between singlet trions than between triplet trions, consistent with what may be inferred from the raw spectra in Fig. 4.10. Secondly, there is a small redshift affecting all four trion states which appears to depend only on the magnitude of the B-field, and is independent of sign. As such, when $B > 0$, the σ^- trions appear to have lower rates of shift than their σ^+ counterparts, in other words, $t^- (s^-)$ is less sensitive to the external field than $t^+ (s^+)$. Conversely, when $B < 0$, $t^+ (s^+)$ is less sensitive than $t^- (s^-)$, resulting in a striking change of gradient as each trion state crosses $B = 0$ T in Fig. 4.12.

4.4.2 Magnetic moment contributions to the observed line shifts

The change in emitted photon energy $\Delta E_{h\nu}$ from trion radiative recombination under an external magnetic field may be broadly expressed as:

$$\Delta E_{h\nu} = \Delta E_Z - \Delta E_R \quad (4.1)$$

where ΔE_Z is the neutral exciton-like valley Zeeman shift in the initial state trion, and ΔE_R describes all changes in photon energy arising from the recoil of the excess electron, essentially the change in final state after recombination. Eq. 4.1 neglects a quadratic diamagnetic shift of the trion lines, expected to become significant only at stronger field strengths of tens of Tesla [99].

Firstly, ΔE_Z is considered. The factors influencing ΔE_Z are the same as those which give rise to the valley Zeeman splitting of a neutral exciton, which is to be expected, considering that Eq. 4.1 reduces simply to $\Delta E_{h\nu} = \Delta E_Z$ if there is no excess electron and the final state is simply a lone photon. The trion initial state consists of either a singlet, or a triplet at a raised energy δ_{ex} . Each of these trion complexes are subject to energy shifts arising from the atomic orbital and Berry curvature associated magnetic moments inherent to monolayer WSe₂, which apply also to the neutral exciton, as discussed in detail in Section 2.3.3 [56, 21, 57, 44]. The atomic orbitals constituting the valence band edge (band v1 in Fig. 4.5) have a magnetic moment of magnitude $2\mu_B$, which leads to an expected valley splitting of magnitude $4\mu_B B$ [56, 21]. In the same manner as the neutral exciton valley Zeeman effect, we can express the photon energy change arising from the B-field dependence of the initial state trion as

$$\Delta E_Z = \frac{1}{2} \tau_z g_z \mu_B B \quad (4.2)$$

where $\tau_z = \pm 1$ for σ^\pm emission helicity, and g_z describes the cumulative effect of atomic orbital and Berry curvature magnetic moments.

4.4 Magneto-optical response of singlet and triplet trions

From the initial state t^- or s^+ (t^+ or s^-), the final state after trion recombination will be a photon and a single electron in the conduction band state $|+K, \downarrow\rangle$ ($|-K, \uparrow\rangle$). In each of these two final states, the electron experiences magnetic moments due to both the spin and valley pseudospin, which counteract one another in the case of band c1 in WSe₂ (see Fig. 2.11) [56]. The cumulative spin-valley electron g-factor g_e in band c1 therefore depends on the difference between these two opposing magnetic moments. The energy shift ΔE_e of an electron in band c1 may be expressed as

$$\Delta E_e = \frac{1}{2} \tau_e g_e \mu_B B \quad (4.3)$$

where $\tau_e = \pm 1$ for the electron in the $\pm K$ valley, as a consequence of time reversal symmetry. Upon radiative recombination of the spin/momentum allowed electron-hole pair of a trion, the excess electron must occupy a free conduction band state, and so ΔE_e modifies the emitted photon energy. The electron recoil effect described by g_e is trion-specific, and is responsible for the larger singlet-singlet splitting in Fig. 4.12 than triplet-triplet splitting.

In addition to the spin and valley energy shifts, both the initial state (a trion) and final state (photon plus electron) of trion emission are subject to Landau level (LL) effects, both being (quasi)particles of charge $= -1$. The associated cyclotron frequencies will be $\omega_{X^-} = e|B|/m_{X^-}$ in the case of the trion, and $\omega_e = e|B|/m_e$ for the electron, where e is the electron charge and m_{X^-} (m_e) are the trion (electron) effective masses. The frequency ω_{X^-} will be smaller than ω_e owing to the much larger trion effective mass. Consequently, when a trion radiatively recombines, the additional energy of the electron LL relative to the trion LL is deducted from the photon energy. This leads to a LL-associated global redshift ΔE_l of trion PL with increasing B-field magnitude, insensitive to spin or valley, which may be quantified by an effective g-factor g_l as

$$\Delta E_l = \hbar \omega_e (n_e + 1) - \hbar \omega_{X^-} (n_{X^-} + 1) = g_l \mu_B |B| \quad (4.4)$$

where n_e and n_{X^-} are the LL index of the electron and trion, respectively. In Fig. 4.12, g_l gives rise to the inequivalent rates of shift of each trion state between positive and negative B-field.

Considering that ΔE_e and ΔE_l may both be considered as arising from the action of the excess electron, absent for the neutral exciton, then the change in photon energy arising from recoil effects may be defined as $\Delta E_R = \Delta E_e + \Delta E_l$. This, in combination with Eqns. 4.1 and 4.2, allows the total energy shift of each trion state PL line to be expressed as a function of change in B-field ΔB as

$$\begin{aligned}
 \Delta E_{hv}(s^+) &= \frac{1}{2}(g_z - g_e)\mu_B\Delta B - g_l\mu_B|\Delta B| \\
 \Delta E_{hv}(s^-) &= \frac{1}{2}(-g_z + g_e)\mu_B\Delta B - g_l\mu_B|\Delta B| \\
 \Delta E_{hv}(t^+) &= \frac{1}{2}(g_z + g_e)\mu_B\Delta B - g_l\mu_B|\Delta B| \\
 \Delta E_{hv}(t^-) &= \frac{1}{2}(-g_z - g_e)\mu_B\Delta B - g_l\mu_B|\Delta B|
 \end{aligned} \tag{4.6}$$

4.5 Full picture of the trion valley Zeeman effect in monolayer WSe₂

4.5.1 Extraction of contributory g-factors

In order to extract the g-factors in Eq. 4.5 from the magneto-PL measurements, the photon energy separations between trions of opposite PL polarisation are calculated, in the convention $E(\sigma^+) - E(\sigma^-)$, as plotted in Fig. 4.14a. Remarkably, despite the complexities of three distinct g-factors acting on four distinct trion states, the inherent symmetries in the system cause the energy splittings to become quite simplistic. Table 4.1 lists the measured gradients of each line in Fig. 4.14a, and the corresponding description calculated from Eq. 4.5. The associated energy separations when $B > 0$ are shown schematically in Fig. 4.14b. Table 4.1 reveals that $g_z = -7.9 \pm 0.1$, corresponding to an energy splitting of $\approx -7.9\mu_B B$. This is approximately double the value expected from purely atomic orbital contributions in the valence band ($-4\mu_B B$), implying a large Berry curvature associated magnetic moment of all trion states before recombination, present in the initial state but absent in the final state, considering that g_z is a linear sum of atomic orbital and Berry curvature contributions [21, 90, 44]. The opening of the energy gap δ_{ex} between oppositely circularly polarised dispersion minima (Fig. 4.1), absent for neutral excitons, transforms the trion into a massive Dirac particle, associated with a large Berry curvature $\Omega(\mathbf{k})$, as discussed in Section 4.1 [44, 4]. The additional orbital magnetic moment $\mu_\Omega(\mathbf{k})$ of the trion associated with the exchange-induced Berry curvature may be expressed as

$$\mu_\Omega(\pm K) = \frac{e}{2\hbar}\delta_{ex}\Omega(\pm K) \tag{4.7}$$

from Ref. [21], which may further be expressed as an effective g-factor,

$$g_\Omega = \frac{m_e}{2\hbar^2}\delta_{ex}\Omega(\pm K) \tag{4.8}$$

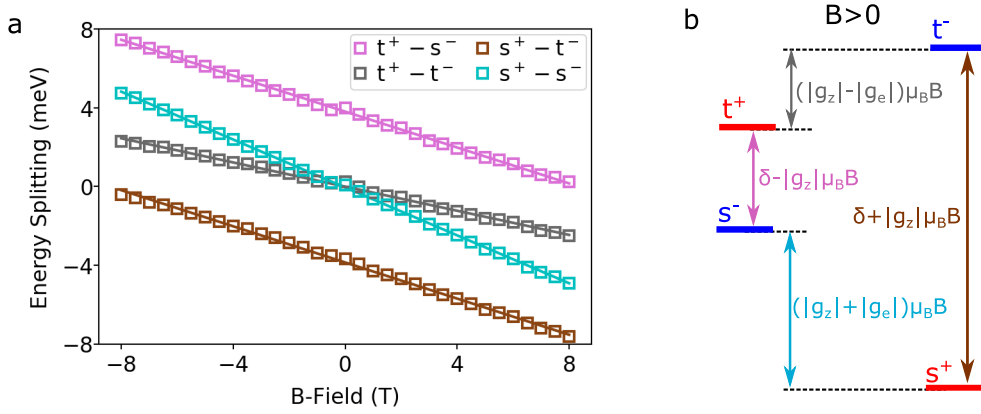


Fig. 4.14 (a) Photon energy separation as a function of external B-field between oppositely circularly polarised trion configurations, calculated from $E(\sigma^+) - E(\sigma^-)$ in photoluminescence. Open squares are data points, while solid lines are linear fits used to extract gradients. (b) Schematic of the energy separations between photon energies from each trion state when $B > 0$, calculated from Eq. 4.5. Solid red or blue lines specifically indicate photon energy in PL, rather than trion energy, with the colour representing the photon polarisation. The colour of text and arrows corresponds with the data in (a).

Energy Separation	Measured Gradient	Corresponds to:
$E(s^+) - E(t^-)$	$(-7.9 \pm 0.1)\mu_B$	$g_z\mu_B$
$E(t^+) - E(s^-)$	$(-7.9 \pm 0.1)\mu_B$	$g_z\mu_B$
$E(t^+) - E(t^-)$	$(-5.3 \pm 0.1)\mu_B$	$(g_z + g_e)\mu_B$
$E(s^+) - E(s^-)$	$(-10.5 \pm 0.1)\mu_B$	$(g_z - g_e)\mu_B$

Table 4.1 List of measured gradients extracted from data shown in Fig. 4.14a, and their representations in terms of g_z and g_e from Eq. 4.5, illustrated in Fig. 4.14b. The data suggest $g_z = -7.9 \pm 0.1$ and $g_e = 2.6 \pm 0.1$.

g-factor	Extracted value	Physical origin
g_z	-7.9 ± 0.1	Trion valley Zeeman splitting
g_e	2.6 ± 0.1	Band c1 spin-valley splitting
g_l	1.9 ± 0.1	Trion \rightarrow electron LL energy

Table 4.2 Summary of extracted g-factors in this study, corresponding to Eq. 4.5.

4.5 Full picture of the trion valley Zeeman effect in monolayer WSe₂

The data suggest that g_Ω amounts to ~ 4 , as $|g_z| \approx 8$ and the atomic orbital contribution ~ 4 . Additionally, the measured exchange splitting in this sample is $\delta_{ex} \sim 4$ meV, and so Eq. 4.8 yields a value of $\Omega(\pm K) \sim 1.5 \times 10^4 \text{ \AA}^2$. This is in excellent agreement with the predicted value when modelling the trion as a massive Dirac fermion, as plotted in Fig. 4.1 (the slightly larger Berry curvature in Fig. 4.1 reflects the larger value of $\delta_{ex} = 6$ meV taken in those calculations) [44].

From Table 4.1 we also extract g_e by inserting $g_z = -7.9 \pm 0.1$ into $(g_z \pm g_e)\mu_B$. The result is a valley splitting of band c1 of $E_{|+K,\downarrow} - E_{|-K,\uparrow} = g_e\mu_B B = (2.6 \pm 0.1)\mu_B B$, corresponding to a single electron magnetic moment of $\pm(1.3 \pm 0.1)\mu_B$ in the $\pm K$ valley of band c1. This is in good agreement with the predicted c1 magnetic moment in a single particle picture, which is $\sim 1.5\mu_B$ [100]. This value is the sum of spin and valley magnetic moments, where the latter is a type of orbital magnetic moment arising from cyclic motion of electron Bloch states in momentum space, with opposite rotation between valleys, as introduced in Chapter 2 [101].

Inserting $g_z = -7.9 \pm 0.1$ and $g_e = 2.6 \pm 0.1$ into Eq. 4.5 allows extraction of g_l by taking the gradients of the linear fits in Fig. 4.12. Calculating g_l from each of the eight gradients (positive and negative B-field ranges for each of the four trion states) yields a mean $g_l = 1.9 \pm 0.1$. Table 4.2 lists the three g-factors in Eq. 4.5 extracted in this study.

4.5.2 Landau level contribution

Next, g_l is considered, which describes the asymmetry between rates of shift of the same trion state at positive and negative B-fields. Landau level spectroscopy performed on monolayer WSe₂ has revealed that many-body interactions are quite weak in the band c1, ensuring that a single particle picture remains valid to describe the dynamics of the excess electron upon recoil [100]. Taking a theoretically predicted electron effective mass in the WSe₂ band c1 of $0.29m_e$ [10] gives a cyclotron energy of $\sim 6.9\mu_B B$, larger than the measured c1 valley splitting of $\sim 2.6\mu_B B$. As such, the conduction band LL quantisation will have the form shown in Fig. 4.15a.

Below, two regimes are proposed whereby g_l takes either the same value regardless of excess electron valley index, or inequivalent values, depending on the Fermi level of the sample. These are illustrated in Fig. 4.15b. The larger cyclotron energy than valley splitting in the band c1 leads to a staggered energy ladder of successive LLs when $B > 0$ [100, 102]. In the scenario A, the next available empty states which the excess electron can occupy upon trion recombination are the $n = 2$ LLs in both valleys. Therefore, g_l should be equal regardless of excess electron valley index. However, in the scenario B, the $n = 2$ LL is completely filled in the $-K$ valley, but empty in $+K$. As such, the excess electron must

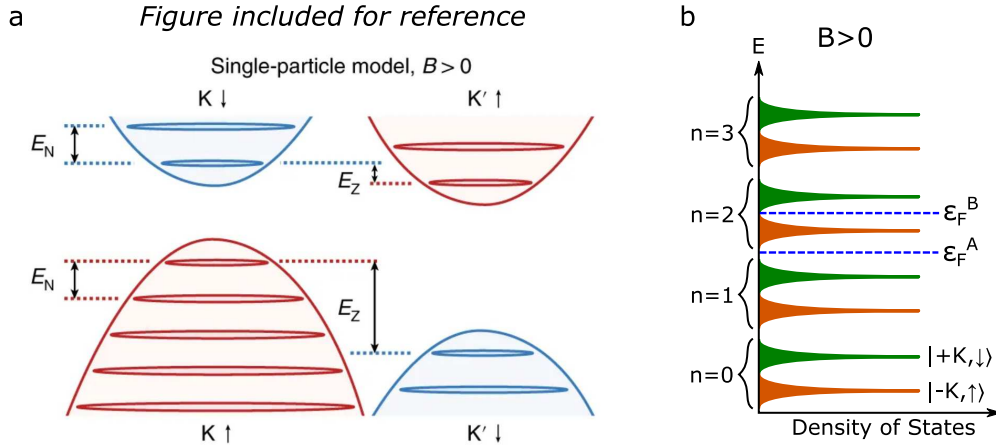


Fig. 4.15 (a) Under a magnetic field, the conduction and valence band dispersions begin to quantise into discrete Landau levels. In a single particle picture, valid in the conduction band of WSe₂ [100], the cyclotron energy between adjacent LLs is greater than the Zeeman splitting. The valence band is not relevant for discussion of the excess electron involved in trion recombination. *Image from Ref. [100]*. (b) Illustration of spin-valley polarised Landau levels in the band c1 when $B > 0$. The density of states is quantised into LLs separated by the cyclotron energy due to the B-field. These LLs then split into pairs due to the magnetic moment of the band c1. ϵ_F^A and ϵ_F^B indicate the Fermi level in two different scenarios A and B described in the text.

occupy a LL of different n in opposite valleys. This would induce an additional PL redshift, amounting to $\hbar\omega_e$, from trion states with the excess electron in the $-K$ valley. This picture is simplistic and neglects Landau level broadening [103, 104], or the kinetic energy involved in trion recombination, which are all likely to depend on temperature [105]. However, it demonstrates how g_l can take inequivalent values for different trion states, depending on the arbitrary Fermi level in a given sample, offering another contribution to the wide ranging trion valley splittings reported in literature. While in this work the observed global redshift is attributed to Landau level effects in the initial and final states of trion recombination, it is important to note that there may be an increase in trion binding energy with increasing magnetic field strength, which would also contribute a slight redshift to the observed PL emission with increasing $|B|$ [106]. Both of these processes may contribute to the measured redshift component here quantified with g_l . To fully separate these possible contributions to g_l , experiments with electron density controlled samples in high magnetic fields are required, to enter the regime of low LL filling factor, and significant binding energy modification.

4.5 Full picture of the trion valley Zeeman effect in monolayer WSe₂

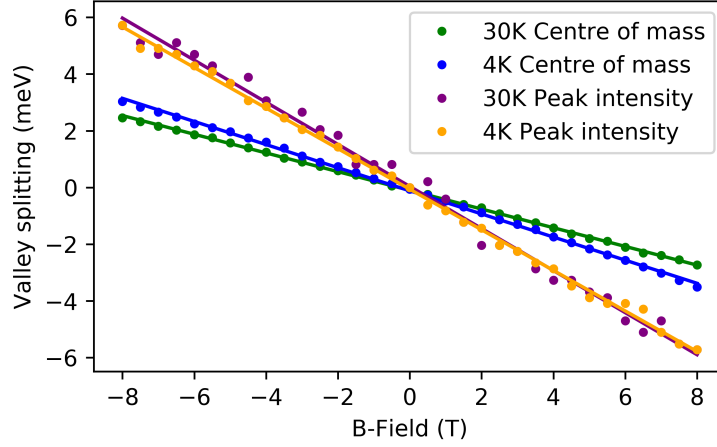


Fig. 4.16 Comparison of trion PL valley splitting $E(\sigma^+) - E(\sigma^-)$ measured by two different methods, both without taking the trion fine structure into account, as described in the text.

4.5.3 Significance of results

This investigation reveals that any measurement of the trion valley splitting when treating it as a single resonance (without fine structure) risks a high degree of inaccuracy, as the measured value will depend on the relative contributions of the four fine structure components, each of which have different rates of shift, as shown in Fig. 4.12, alongside variable relative PL intensities, as shown in Figs. 4.6 - 4.9. It cannot be excluded that the varying contributions to the overall trion PL from the four underlying states may have influenced the measured g-factors in an uncontrolled manner in existing published reports. To compound the problem, typical exfoliated WSe₂ monolayers exhibit trion linewidths much broader than the few meV exchange energy separation, making it impossible to isolate the fine structure components in all but the highest quality samples.

Temperature	Peak analysis method	Measured overall g-factor
4 K	Peak intensity	-12.8 ± 0.2
30 K	Peak intensity	-12.4 ± 0.1
4 K	Centre of mass	-7.04 ± 0.04
30 K	Centre of mass	-5.69 ± 0.02

Table 4.3 Summary of extracted trion PL g-factors ($E(\sigma^+) - E(\sigma^-) = g\mu_B B$) when the trion fine structure is not taken into account, corresponding to the data shown in Fig. 4.16.

To demonstrate how neglecting the fine structure can lead to extraction of erroneous g-factors, the valley splitting of the total trion emission (the spectral feature comprising unresolved singlet and triplet PL) is measured at 4 K and 30 K, by two methods commonly

used to extract a valley splitting [56]. The *centre of mass* method is calculated as $(\sum(E \times I)_n)/(\sum I_n)$, where E and I are the energy and intensity of the n th CCD pixel, whereas the *peak intensity* is the energy corresponding to the pixel with the most counts per second. The results are shown in Fig. 4.16 and Table. 4.3, and reveal two key conclusions. Firstly, the centre of mass and peak intensity do not agree with each other at either temperature. This strongly indicates the presence of peak substructure which is not negligible. Secondly, none of these g-factors correspond to the values accurately extracted using multiple peak fitting, listed in Table 4.1. This comparison demonstrates that when the trion fine structure is neglected, the uncontrolled influences on the overall PL line shifts can lead to extraction of valley Zeeman splittings ranging from $\sim -5\mu_B B$ to $\sim -13\mu_B B$, all from the same sample, and corresponding quite closely to the range of trion g-factors already reported in literature [21, 57–59]. Therefore, only by simultaneous consideration of both singlet and triplet trions is it possible to extract the strength of the valley splitting of the initial states, g_z .

4.6 Summary

This study uncovers the complexities of the trion valley Zeeman effect in monolayer WSe₂, demonstrating that the trion energy splitting in PL does not reflect the underlying valley Zeeman splitting of the initial state. Instead, the process of trion radiative recombination itself modifies the emitted photon energy, via electron recoil to valley polarised conduction band states, having the effect of enhancing the singlet-singlet splitting, and diminishing the triplet-triplet splitting. On top of this asymmetry, the action of a third process is observed, also associated with the electron recoil, attributed to Landau level quantization of both initial and final states. Furthermore, the relative PL intensity of singlet and triplet trions is found to strongly depend on temperature, such that heating a WSe₂ monolayer from 4 K to 30 K thermally populates the triplet states, allowing simultaneous measurement of the magneto-optical response of the trion fine structure components.

Each of the four trion fine structure valley configurations are seen to display inequivalent rates of field-dependent spectral shift, which is incompatible with the valley Zeeman framework reported for neutral excitons. A true valley Zeeman splitting of $(-7.9 \pm 0.1)\mu_B B$ is extracted for all trion states, which may be measured only by consideration of both singlet and triplet trions. The deviation of this value from the known atomic orbital contribution of $\sim -4\mu_B B$ is attributed to a strong Berry curvature associated magnetic moment unique to WSe₂ trions. However, this true trion valley Zeeman splitting is observed to be masked by energetic recoil processes of the additional electron, which modify the measured trion energy

shifts in low temperature magneto-PL studies and are likely to depend heavily on external factors such as doping level, which vary from sample to sample.

The results presented here gain critical insight into the magneto-photoluminescence of trion fine structure in monolayer WSe₂, information which will be crucial in future research involving the spin and valley dynamics of monolayer TMDs and their applications in valleytronics.

Chapter 5

Exciton valley dynamics in the strong light-matter coupling regime

The valley Zeeman effect discussed for neutral excitons in Chapter 2 and for trions in Chapter 4 offers a good degree of control over the excitonic valley states in monolayer TMDs. However, for any appreciable changes in optical transition energy of these states, or any appreciable suppression of inter-valley pseudospin relaxation processes, large external magnetic fields are required. This is highly impractical for the application of 2-D materials for information processing, as strong magnetic fields require large amounts of power, space, equipment, and typically are restricted to cryogenic temperatures. In this chapter, an alternative method of control of the exciton valley pseudospin is presented, based around the use of photonic structures. Specifically, by incorporating monolayer TMDs inside optical microcavities, the light-matter interaction may be enhanced to such a degree as to enter the strong coupling regime, associated with the formation of exciton-polaritons. As is shown in this chapter, the properties of exciton-polaritons hosted by monolayer TMDs are highly amenable to external control via modification of the photonic structure itself.

The results presented in this chapter are already published as below:

S. Dufferwiel, **T. P. Lyons**, D. D. Solnyshkov, A. A. P. Trichet, F. Withers, S. Schwarz, G. Malpuech, J. M. Smith, K. S. Novoselov, M. S. Skolnick, D. N. Krizhanovskii, A. I. Tartakovskii, “Valley addressable polaritons in atomically thin semiconductors”, *Nature Photonics* **11**, 497-501 (2017)

S. Dufferwiel, **T. P. Lyons**, D. D. Solnyshkov, A. A. P. Trichet, A. Catanzaro, F. Withers, G. Malpuech, J. M. Smith, K. S. Novoselov, M. S. Skolnick, D. N. Krizhanovskii, A. I. Tartakovskii, “Valley coherent exciton-polaritons in a monolayer semiconductor”, *Nature Communications* **9**, 4797 (2018)

5.1 Background - exciton-polaritons in 2D materials

As discussed in Chapter 2, excitons in monolayer TMDs are characterised by very large binding energies (hundreds of meV), arising from the reduced dimensionality of the lattice, which provides a highly anisotropic dielectric environment and associated weak screening of the electron-hole Coulomb interaction [26, 30, 29]. They also have a very short radiative recombination time, associated with a high oscillator strength, giving rise to strong absorption of light at the exciton resonance energy, between 10-20% for a single monolayer, and around 2 orders of magnitude stronger than for single particle interband transitions [7, 52, 30].

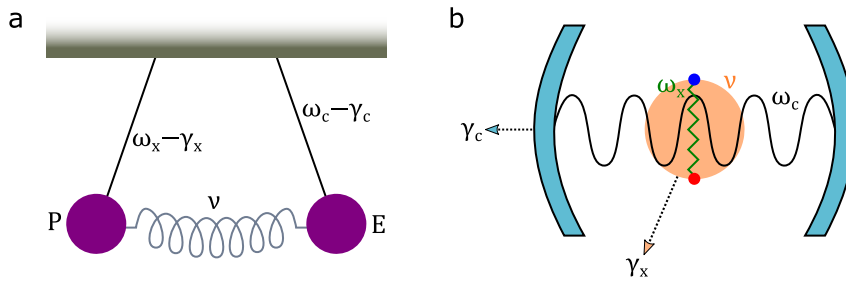


Fig. 5.1 (a) Illustration of coupled oscillators with exciton and cavity frequencies ω_x and ω_c , damping γ_x and γ_c , and coupling term v . The exciton is represented by dielectric polarisation \mathbf{P} in the monolayer, while the cavity is represented by the E-field \mathbf{E} . (b) Schematic of a microcavity with an exciton and cavity photon coupled by v . Here, γ_x represents non-radiative decay of the exciton, and γ_c represents tunnelling of the photon through one of the cavity mirrors.

The strong oscillator strength of monolayer TMDs becomes highly advantageous when they are embedded inside an optical microcavity with the aim of enhancing the light-matter interaction. In a cavity of sufficiently high quality factor, which confines photons around the TMD exciton absorption resonance, a cyclical transfer of energy can occur between the exciton and cavity mode, corresponding to repeated absorption and re-emission of a cavity photon by the exciton. This recurrent light-matter interaction is well described by a classical coupled oscillator model (Fig. 5.1a) where the electric field of the cavity mode, \mathbf{E} , and the dielectric polarisation, \mathbf{P} , of the TMD monolayer represent the two oscillators, of uncoupled frequencies ω_c and ω_x , respectively, with a coupling term v between them. The system may be represented by the two effective equations of motion

$$\begin{aligned} i \frac{d\mathbf{E}}{dt} &= (\omega_c - i\gamma_c)\mathbf{E} + v\mathbf{P} \\ i \frac{d\mathbf{P}}{dt} &= (\omega_x - i\gamma_x)\mathbf{P} + v\mathbf{E} \end{aligned} \quad (5.1)$$

5.1 Background - exciton-polaritons in 2D materials

where γ_x and γ_c are the damping terms of the oscillators, corresponding in real terms to the linewidths of the exciton absorption and cavity mode, respectively [30]. This can be understood as the exciton experiencing radiative damping as energy is lost to a photon. Fig. 5.1b shows how the model applies to a real microcavity, in which v is the light-matter coupling strength, γ_c the photon losses through the mirrors (caused by non-unity reflectivity), and γ_x is non-radiative decay of the exciton state, for example via scattering to a dark state. Describing the polarisation and E-field as harmonic oscillators, i.e. $\mathbf{P}, \mathbf{E} \propto e^{-i\omega t}$, and solving Eqs. 5.1 gives the quadratic equation

$$(\omega - \omega_x + i\gamma_x)(\omega - \omega_c + i\gamma_c) = v^2 \quad (5.2)$$

the two roots of which are the eigenfrequencies ω_{\pm} of the coupled oscillator system [30]. The core definition of the strong light-matter coupling regime occurs at the resonance condition $\omega_c = \omega_x \equiv \omega_0$, in which case the eigenfrequencies are

$$\omega_{\pm} = \omega_0 - i\frac{\gamma_x + \gamma_c}{2} \pm \frac{\sqrt{4v^2 - (\gamma_x - \gamma_c)^2}}{2} \quad (5.3)$$

from which it is clear that the final term becomes imaginary if $2v < |\gamma_x - \gamma_c|$, in which case the oscillators are said to be weakly coupled, and their respective frequencies meet at ω_0 . However, if $2v > |\gamma_x - \gamma_c|$, the oscillators enter the *strong coupling regime*, whereby the last term is real, and modifies the energy spectrum of the system by opening a gap between the two eigenfrequencies ω_{\pm} [30, 107]. This creates a characteristic *anticrossing* allowing definition of higher and lower energy eigenmodes called *upper* and *lower polariton branches*, which are a signature of strong coupling and denote exciton-polariton formation, rather than simply Purcell enhancement of an exciton state. The energy separation at exciton-cavity resonance is given by the *Rabi splitting* $\hbar\Omega_R = \sqrt{4v^2 - (\gamma_x - \gamma_c)^2}$ (here Ω_R is the Rabi frequency), which may be measured experimentally to determine the coupling strength of a given system. In reality, the polariton branch linewidths may be comparable to the Rabi splitting, and so they may be spectrally unresolved, making it difficult to determine if the system is in the strong or weak coupling regimes.

The coupling term v depends on the physical characteristics of the microcavity (such as quality factor and mode volume) and on the exciton oscillator strength, related to the radiative decay rate. The losses depend on disorder and phonon interactions in the monolayer, which leads to scattering of excitons and non-radiative decay, while the photonic damping depends on the reflectivity of the cavity mirrors and stability of the system [30].

Strong coupling between TMD excitons and microcavity modes has successfully been realised over recent years in a variety of materials and cavity geometries [108–110, 37], but of

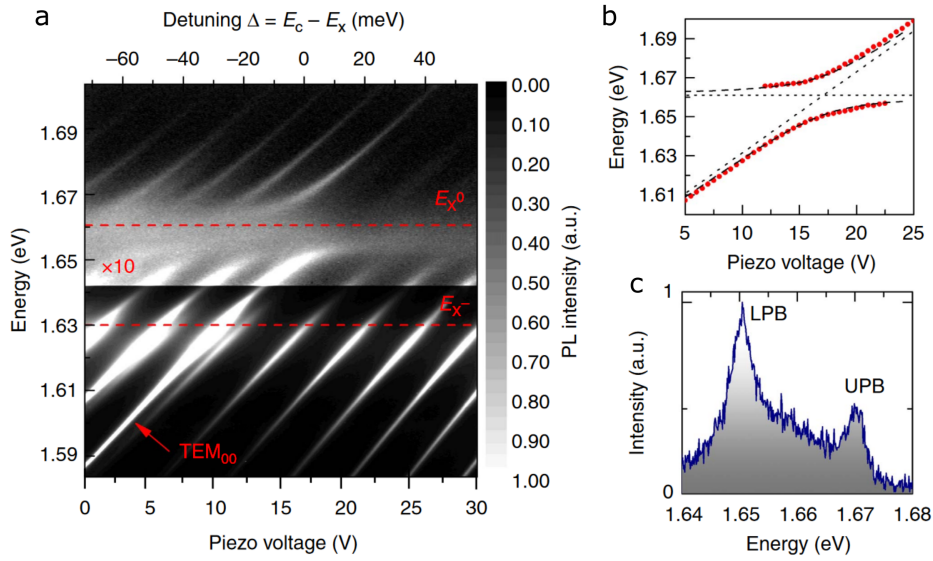


Fig. 5.2 (a) Unambiguous early demonstration in photoluminescence of strong light-matter coupling in monolayer MoSe₂ embedded in a tunable zero dimensional microcavity. Increasing piezo voltage corresponds to reduction of cavity length. This tunes the cavity mode through resonance with the neutral exciton X⁰, where a clear anticrossing is visible, indicating strong coupling. The brightening of the mode when in resonance with the trion X⁻ corresponds to weak coupling and associated Purcell enhancement. (b) Fit of the polariton mode spectral peak positions to a coupled oscillator model, from which the Rabi splitting 20 meV is extracted. (c) PL spectrum of the polariton states at exciton-photon resonance. The linewidths are much smaller than the Rabi splitting, making the polariton formation unambiguous. *All subfigures from Ref. [107].*

5.2 Monolayer films of MoSe₂ and WSe₂ on distributed Bragg reflectors

particular note is the demonstration of polariton formation in zero dimensional hemispherical microcavities of the type introduced in Section 3.3 [107]. In this work, a monolayer of MoSe₂ encapsulated in hBN was embedded inside a microcavity of high reflectivity paired dielectric distributed Bragg reflectors (DBRs), one of which is hemispherical, leading to confinement of the photonic mode in all directions. The tunable cavity length allowed control of the 0D cavity mode energy, which was passed through resonance with the exciton transition in MoSe₂. At resonance, a clear anticrossing was observed between the exciton and cavity mode, defining upper and lower polariton branches unambiguously, and confirming the strong-light matter coupling regime [107]. The Rabi splitting was measured to be ~ 20 meV, much larger than the polariton linewidths of a few meV, and also much larger than typical Rabi splitting displayed by exciton-polaritons in III-V semiconductor quantum well microcavities of $\sim 3 - 4$ meV, reflecting the giant discrepancy in oscillator strength [111].

The study of TMD excitons in the strong light-matter coupling regime represents the combination of two rich fields of research. In polariton systems in other materials, such as III-V semiconductor quantum wells, a wealth of nonlinear effects have been observed, such as Bose-Einstein condensation [112], superfluidity [113], soliton propagation [114], and novel topological phases [115]. There are many advantages inherent to monolayer TMDs for the study of polaritons, notably the large binding energy allowing room temperature strong coupling, the relative ease of electrical injection, opening the possibility of electrically pumped polariton lasers, and the ability for spatial propagation of polaritons, either for non-trivial topological diffusion patterns or towards polaritonic circuit elements. In particular, polariton systems are highly promising in the study of novel spin textures, for instance with demonstrations of controllable ferromagnetic type spin interactions between adjacent spatially localised polariton condensates [116]. However, in line with the topic of this thesis, it is the exciton valley pseudospin, unique to TMDs, which will be this chapter's focus of investigation in the strong light-matter coupling regime.

5.2 Monolayer films of MoSe₂ and WSe₂ on distributed Bragg reflectors

To study TMDs in the strong light-matter coupling regime, they must be incorporated into optical microcavities. The results presented in this chapter are from one sample consisting of monolayer MoSe₂ on thin (3-4 nm) hBN on a DBR, and from another consisting of a single WSe₂ monolayer viscoelastically stamped onto a DBR, without hBN. The use of hBN has advantages for exciton linewidth and reduced sample disorder, nominally leading to

larger Rabi splitting, but unavoidably comes with the disadvantage of shifting the active layer slightly away from the antinode of the electric field, located on the surface of the planar DBR, which reduces the Rabi splitting. A description of the DBR substrates, the microcavities, and the sample fabrication techniques used in the experiments in this chapter can be found in Chapter 3 - methods.

A striking consequence of the coupled spin and valley regime described in detail in Chapter 2 is the optical selection rules which apply to interband transitions in the K and K' valleys, where the direct band gap is found. Here, light of σ^+ or σ^- helicity is tied to transitions in the K and K' valleys, respectively. As such, it becomes possible to optically initialise the excitonic population in one valley or the other simply by optically pumping a sample with a given circular polarisation. Likewise, it is possible to measure the imbalance between valley exciton populations by collecting light of σ^+ and σ^- polarisation, and comparing their intensities [19]. A crucial equation, introduced as Eq. 2.9, is the *polarisation degree*, $\rho = (I_{\text{co}} - I_{\text{cross}})/(I_{\text{co}} + I_{\text{cross}})$ where I_{co} (I_{cross}) is the intensity of emission of light co-polarised (cross-polarised) to the excitation beam. This applies to either circularly or linearly polarised light, whereby it serves as a measure of retention of valley polarisation or coherence, respectively. For the most part, this chapter explores how the polarisation degree of excitonic states in monolayer TMDs may be modified or otherwise controlled when the excitons strongly couple to photonic modes in a microcavity.

Therefore, before incorporating MoSe₂ and WSe₂ monolayers into microcavities, they are characterised using polarisation resolved photoluminescence (PL), to give insight into their exciton valley dynamics, and to consequently enable direct comparison to the cavity-modified valley dynamics in the polariton states. Spectroscopy of the bare flakes, which rest on planar DBR substrates, is enabled by moving the top hemispherical mirror out of the optical path inside the cryostat using piezo nanopositioners, allowing direct optical access to the monolayers.

5.2.1 Anomalous valley polarisation of monolayer MoSe₂

While it is inefficient for a single charge carrier to scatter between valleys, due to the large valley contrasting spin splitting and overall momentum difference involved, the measured polarisation degree of TMD monolayers under non-resonant circularly polarised optical excitation is not unity [13, 11, 117–119]. This is because the optical properties of TMD monolayers are dominated by excitons, rather than individual carriers. Excitons, unlike lone carriers, may effectively flip their valley pseudospin via the long range electron-hole exchange interaction, aided by the presence of disorder potentials over the monolayer crystal, as discussed in Chapter 2 [120, 43, 121, 44]. While this does act as a limiting factor, polarisation

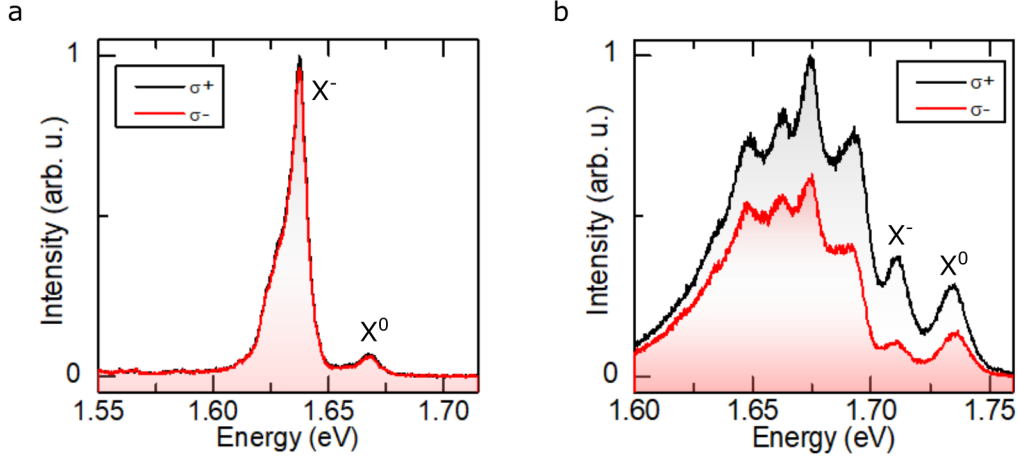


Fig. 5.3 Circular polarisation resolved PL spectra from monolayer (a) MoSe₂ and (b) WSe₂, under σ^+ polarised non-resonant continuous wave laser excitation. Neutral (X^0) and negatively charged (X^-) excitonic species are labelled. While WSe₂ displays strong valley polarisation $\sim 50\%$, MoSe₂ does not.

resolved PL studies of MoS₂, WS₂, and WSe₂ nevertheless report high polarisation degrees, of up to 90%, 40%, and 60%, respectively [13, 122, 118, 48, 123, 124, 11, 117]. MoSe₂, however, does not follow the pattern of these other TMDs, with polarisation degrees of $< 5\%$ typically reported [125, 57, 50, 55]. Fig. 5.3 shows circular polarisation resolved photoluminescence spectra from monolayer MoSe₂ and WSe₂ under continuous wave σ^+ polarised laser excitation at 1.946 eV and 4.2 K. While in WSe₂ there is a large intensity difference between co-polarised and cross-polarised emission, in MoSe₂ the emission from opposite valleys is almost of equal intensity. It is not possible to identify the cause of the anomalously low polarisation degree of MoSe₂ from these steady state PL measurements alone. It may be related to inefficiencies in the optical valley initialisation, or it may arise from extremely rapid valley depolarisation. Whatever the origin, this poor retention of valley polarisation remains a vital barrier to the exploitation of MoSe₂ in future information processing valleytronic applications.

5.2.2 Control of exciton valley coherence in monolayer WSe₂

Although monolayer WSe₂ can display degrees of circular polarisation up to several tens of percent in the excitonic photoluminescence [124, 57, 56], it has also been reported to display a non-zero linear polarisation degree in the neutral exciton emission. In this case, optical pumping with a linearly polarised laser leads to linearly polarised emission, with polarisation axis parallel to the laser polarisation plane (Fig. 5.4a). This is indicative of

Exciton valley dynamics in the strong light-matter coupling regime

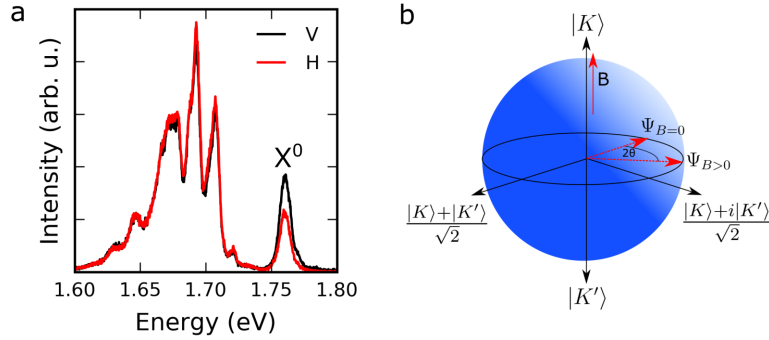


Fig. 5.4 (a) Linear polarisation resolved PL from a WSe₂ monolayer, under linearly polarised laser excitation in the vertical ("V") plane. The neutral exciton peak preferentially emits in vertical over horizontal ("H") polarisation, indicating retention of injected valley coherence. (b) Bloch sphere representation of the valley pseudospin vector. Valley polarised states ($|K\rangle$ and $|K'\rangle$) lie on the poles of the sphere while valley coherence is represented by a Bloch vector lying on the equator. The application of a perpendicular magnetic field leads to precession of the pseudospin vector around the equator due to the valley Zeeman effect, rotating through an angle 2θ .

an optically induced effect, rather than the linearly polarised emission arising from some crystalline anisotropy. No retention of linear polarisation is observed in MoSe₂, as may be expected considering the lack of valley polarisation.

In a Bloch sphere representation of the exciton valley pseudospin, as shown in Fig. 5.4b, the Bloch vector pointing to the north pole corresponds to the K valley state, while pointing to the south pole corresponds to the K' valley state, and pointing to a position on the equator denotes a coherent superposition state between both valleys. As such, pumping a monolayer with linearly polarised light, which is a linear combination of σ^+ and σ^- polarisations, prepares excitons in a coherent linear superposition of K and K' valley states as $|X\rangle = \frac{1}{\sqrt{2}}(|K\rangle + |K'\rangle)$ [118, 49, 48, 126, 53, 54, 127]. However, the lifetime of such exciton valley coherence has been estimated to be a few hundred femtoseconds, limiting the degree to which the valley pseudospin may be coherently controlled [49, 53, 54, 127]. A short lifetime is consistent with the reports of valley coherence only manifesting in the neutral exciton PL, as it is likely to be the only emitting state in WSe₂ with a short enough radiative lifetime to retain any of the injected coherence in the emission.

The linear polarisation degree of the exciton peak in Fig. 5.4a is 23%. In the spectra, vertically linearly polarised (V) emission corresponds to coherent emission from the exciton population, while horizontally linearly polarised (H) emission is in reality unpolarised incoherent background emission, which may only be measured in the H-basis to filter out the V-component. This is distinct from the case of valley polarisation, where opposite

5.2 Monolayer films of MoSe₂ and WSe₂ on distributed Bragg reflectors

circular polarisations correspond to well defined pseudospin vectors pointing to the poles, and the circular polarisation degree gives a measure of intervalley relaxation. Here, the linear polarisation degree given by V and H intensities under V illumination indicates the degree of valley coherence remaining upon radiative recombination, relative to incoherent exciton emission with no defined Bloch vector [53].

Much as with valley depolarisation, valley decoherence arises from the long range electron-hole Coulomb interaction, aided by momentum scattering on disorder, which randomises the pseudospin vector orientation within the exciton population such that the overall coherence is lost, as discussed in Chapter 2 [128, 45, 44, 121]. While in principle electrons and holes are free of this particular dephasing process, and may hold longer valley coherence times, they suffer from a lack of optical control, along with a tendency to efficiently form excitons and trions, which inevitably leads back to the fast dephasing problem [129, 130].

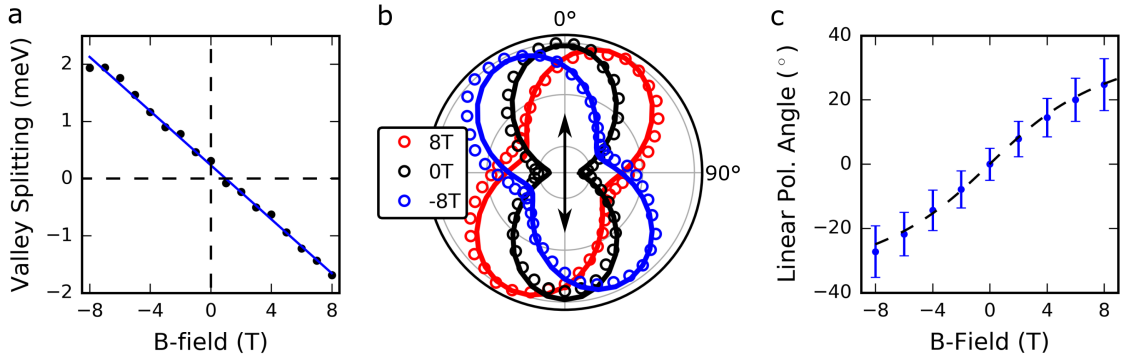


Fig. 5.5 (a) Valley Zeeman splitting of the neutral exciton in monolayer WSe₂. The extracted g -factor is -4.1 . (b) Intensity of neutral exciton emission as a function of linear polarisation detection angle. The black arrow indicates laser polarisation at 0° (termed "vertical"). Applying a magnetic field rotates the polarisation of emission. The fit corresponds to Eq. 5.7. (c) Extracted rotation angle of emission as a function of B-field strength. Errorbars arise from error in fitting polar data in (b) at each value of B-field. The fit corresponds to Eq. 5.5.

As discussed in Section 2.3.3 and Chapter 4, the application of a magnetic field B perpendicular to a monolayer TMD lifts the degeneracy between exciton valley states via the valley Zeeman effect, where the energy splitting is given by the excitonic Larmor frequency Ω_B as $\hbar\Omega_B = g\mu_B B$, where g is the g -factor and μ_B the Bohr magneton [21, 56]. Fig. 5.5a shows the valley Zeeman splitting of the exciton in WSe₂. The measured g -factor is -4.1 , in excellent agreement with the expected value [56, 21, 57].

Introducing an energy separation between the valley states on the poles of the pseudospin Bloch sphere causes a precession of the pseudospin vector around the equator, constituting a

Exciton valley dynamics in the strong light-matter coupling regime

change in relative phase between the superposition of $|K\rangle$ and $|K'\rangle$ (Fig. 5.4b) [49, 54]. The time evolution of the superposition is given by

$$|X\rangle = \frac{1}{\sqrt{2}}(|K\rangle e^{-i\Omega_B t/2} + |K'\rangle e^{i\Omega_B t/2}) \quad (5.4)$$

which leads to rotation of the vector around the equator by an angle

$$2\theta = \arctan(\Omega_B T_2^*) \quad (5.5)$$

where the characteristic time T_2^* is defined as

$$1/T_2^* = 1/T_1 + 1/T_2 \quad (5.6)$$

where T_1 is the state lifetime, quantifying population decay, and T_2 is the valley coherence time [49, 54].

In real terms, precession of the pseudospin vector around the equator by an angle 2θ leads to a rotation of the plane of linearly polarised photoluminescence by an angle θ from the laser [49]. Therefore, the final state of the pseudospin vector after manipulation by a magnetic field can be read-out optically, by measuring the angle between the laser and PL linear polarisation axes [49, 54]. The linear polarisation axis of the PL is measured by acquiring spectra as a function of rotation angle ϕ of a half-waveplate placed in front of a linear polariser. $\phi = 0^\circ$ corresponds to vertical-polarisation, matching the laser. As such, when $B=0$, the maximum intensity of the exciton PL is detected at $\phi = 0^\circ$. Any field induced rotation leads to a maximum intensity when $2\phi = \theta$. This is shown in Fig. 5.5b, where a clear rotation of the linearly polarised neutral exciton PL can be seen when fields of $B = \pm 8$ T are applied. The polarisation rotation angle θ may be extracted by fitting the polar intensity data to

$$r(\phi) = A_0 + A_1 \cos(2\phi - \theta) \quad (5.7)$$

allowing θ to be plotted against B , as shown in Fig. 5.5c. This data is fitted to Eq. 5.5 to extract $T_2^* = (0.52 \pm 0.05)$ ps. Given the exciton lifetime is expected to be a few ps in WSe₂ [131, 47], this suggests a sub-ps valley coherence time, in agreement with previous reports [53, 49, 54]. In one instance the exciton lifetime has been measured as 1.8 ps, which suggests a coherence time of ~ 0.7 ps for this sample.

5.3 Strong exciton-photon coupling in TMD monolayers

5.3.1 Exciton-polaritons in WSe₂

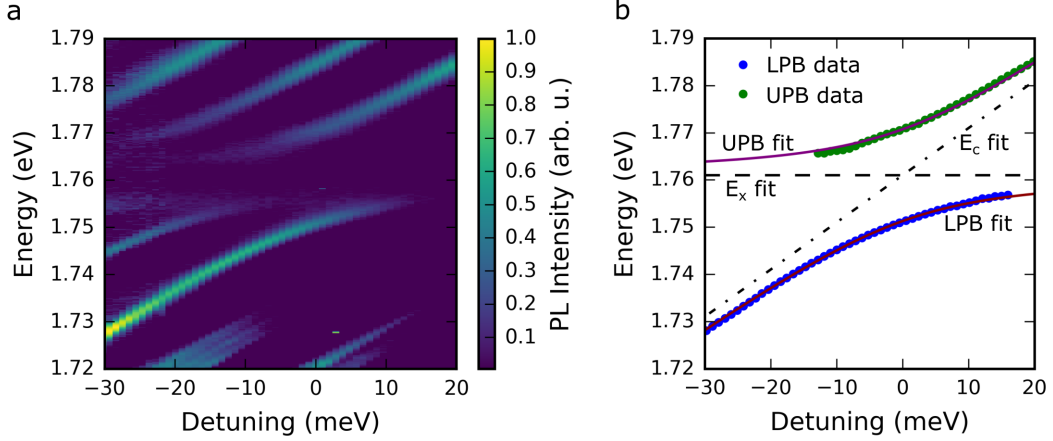


Fig. 5.6 (a) Colourmap of cavity photoluminescence spectra as a function of detuning $\Delta = E_c - E_x$. A clear anticrossing can be seen in the ground state LG₀₀ cavity mode. Higher order modes also couple to the exciton, but these are neglected in the results. (b) Peak energies extracted from the data shown in (a) fitted to the eigenstates of the 2-level exciton-photon coupling Hamiltonian, plotted as a function of detuning, revealing a Rabi splitting of (19.5 ± 0.1) meV.

By introducing a concave top DBR into the optical path above the WSe₂ monolayer on a planar DBR, and bringing the DBR separation to ~ 2.5 μm , the exciton state in the monolayer is observed to strongly couple to the confined photonic field within the newly formed microcavity. Full details of the hemispherical microcavity geometry and laboratory implementation are given in Section 3.3. By decreasing the cavity length, the energy of the zero-dimensional ground state Laguerre-Gaussian LG₀₀ mode may be tuned through resonance with the neutral exciton, allowing observation of splitting of the mode into two eigenstates known as lower and upper polariton branches (LPB, UPB). Fig. 5.6a shows a photoluminescence colourmap of the cavity spectra as a function of detuning $\Delta = E_p - E_x$, where E_p and E_x are the uncoupled photon and exciton energies, respectively. See Section 3.3.4 for a description of fitting cavity data to a detuning scale. Moving from left to right corresponds to decreasing cavity length, and increasing mode energy. A clear anticrossing is visible, defined by a splitting of the LG₀₀ mode as it passes through resonance with the neutral exciton energy. Fig. 5.6b shows the peak energies of the lower and upper polariton branches fitted to the eigenstates of the exciton-photon coupling Hamiltonian:

$$\begin{pmatrix} E_x & g_{xp} \\ g_{xp} & E_p(V) \end{pmatrix}$$

where E_p is a function of piezo voltage (i.e. cavity length), and g_{xp} is the exciton photon coupling strength, equal to half the Rabi splitting, $g_{xp} = \hbar\Omega_R/2$. By fitting the spectral polariton branches to the eigenstates of this Hamiltonian, as described in detail in Section 3.3.4, the Rabi splitting may be extracted, and in this sample it is $\hbar\Omega_R = (19.5 \pm 0.1)$ meV, significantly larger than the polariton branch linewidths, and therefore unambiguous evidence of exciton-polariton formation with monolayer WSe₂.

5.3.2 Exciton-trion-polaritons in MoSe₂

The same experiment described above for WSe₂ is next repeated with MoSe₂, by creating a zero-dimensional microcavity around the monolayer and measuring the upper and lower polariton dispersions by decreasing the cavity length. The resulting photoluminescence colourmap is shown in Fig. 5.7a. As with WSe₂, a very clear anticrossing is visible as the LG₀₀ mode tunes through resonance with the neutral exciton absorption at 1.667 eV, indicating exciton-polariton formation.

However, the situation differs from WSe₂ in that the lower branch is observed to interact with the trion state in MoSe₂, ~ 30 meV below the neutral exciton. Upon closer inspection of the trion-cavity resonance region, the mode can be seen to contain two polariton branches separated by a small anticrossing. Fig. 5.7b shows multiple peak fitting of the mode as it passes through trion-cavity resonance, indicating the presence of two polariton eigenstates, defined as the lower and middle polariton branches (LPB, MPB), indicating that the MoSe₂ exciton and trion form a strongly coupled three level system with the cavity mode.

Consequently, the two level coupled oscillator model is no longer applicable to the case of MoSe₂, and the exciton-photon coupling Hamiltonian presented above is modified to incorporate an additional strongly coupled trion state:

$$\begin{pmatrix} E_x & 0 & g_{xp} \\ 0 & E_t & g_{tp} \\ g_{xp} & g_{tp} & E_p(V) \end{pmatrix}$$

where the uncoupled exciton and trion energies E_x and E_t are constant, and the uncoupled photon energy remains a function of cavity length, as previously. The additional term g_{tp} describes the trion-photon coupling strength. In this case, the Hamiltonian has three eigenvalues corresponding to the dispersions of L,M,UPB, with the three corresponding

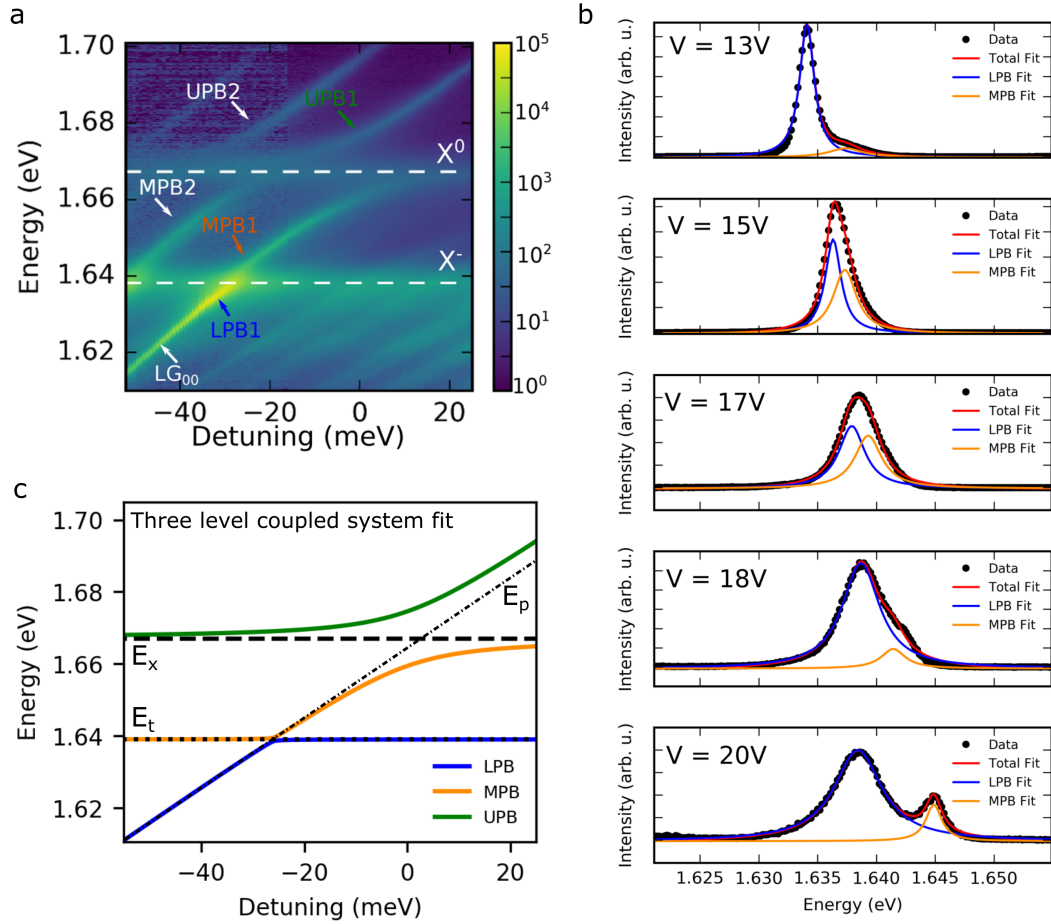


Fig. 5.7 (a) Colourmap of cavity photoluminescence spectra plotted against detuning. The ground state cavity mode (LG_{00}) first couples to the trion then the exciton. The much larger Rabi splitting at the exciton resonance reflects the larger oscillator strength than the trion. (b) Series of spectra when tuning through resonance with the trion, fitting the emission two two polariton branches at each stage. (c) Peak energies from (a) and (b) fitted to eigenstates of a three level strongly coupled Hamiltonian, defining the lower, middle and upper polariton branches. The exciton and trion Rabi splittings are (15.2 ± 0.1) meV (1.3 ± 0.1) meV respectively.

Exciton valley dynamics in the strong light-matter coupling regime

eigenvectors giving the Hopfield coefficients (exciton, trion, photon fractions) of each branch. Fig. 5.7c shows the polariton dispersions described by the 3x3 matrix above after fitting to the cavity data shown in Fig. 5.7a. From this fitting, the exciton-photon coupling strength is $2g_{xp} = (15.2 \pm 0.1)$ meV and the trion-photon coupling strength is $2g_{tp} = (1.3 \pm 0.1)$ meV.

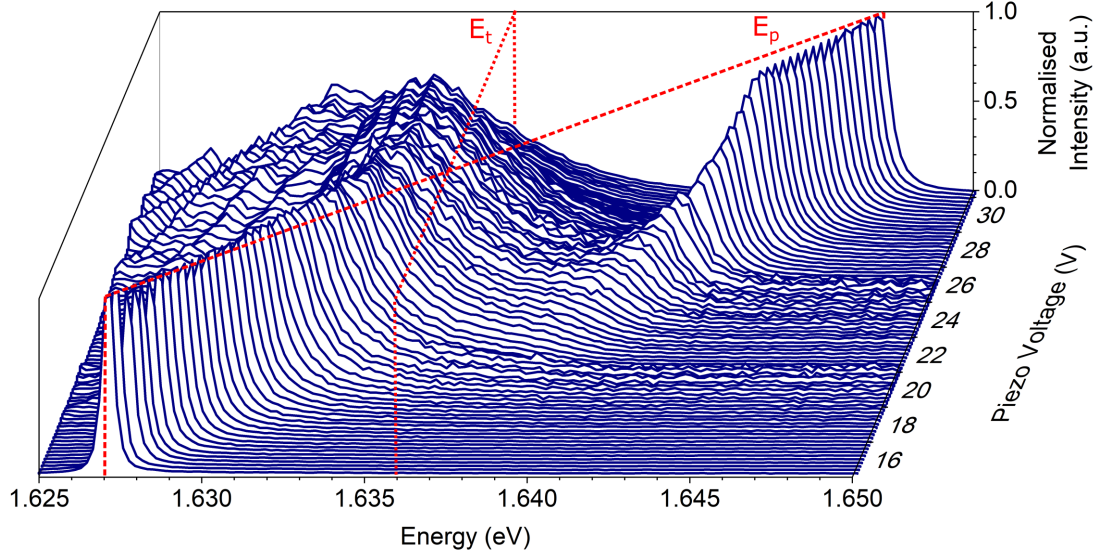


Fig. 5.8 Waterfall plot of cavity spectra as the LG_{00} mode is tuned through resonance with the trion state in monolayer MoSe_2 . The red lines indicate uncoupled trion and cavity energies. A clear mode splitting is seen corresponding to trion-polariton formation. The Rabi splitting is 5 meV. *Note: this data is from an additional sample.*

Although the trion-photon coupling strength is relatively low in this sample, repeat measurements on an additional sample reveal a far clearer trion-cavity anticrossing, as shown in Fig. 5.8. In this additional sample, the trion-photon coupling strength is 5 meV. The reason for the much lower coupling strength than the neutral exciton is that the trion oscillator strength is fundamentally lower, as an electron-hole pair must bind an extra electron to form a trion, slowing down the absorption process.

In this three-level system, the simple mixing between exciton and photon fractions which occurs in the UPB and LPB of a two-level system becomes more complicated, with mixing between three characters to consider within each branch, with the introduction of the trion Hopfield coefficient $\kappa_t^{(i)}(V)$, where

$$(\kappa_x^{(i)}(V))^2 + (\kappa_t^{(i)}(V))^2 + (\kappa_p^{(i)}(V))^2 = 1, \quad i = L, M, U \quad (5.8)$$

represent the excitonic, trionic, and photonic fractions of each branch, respectively. By fitting the cavity data to the exciton-trion-photon coupling Hamiltonian eigenstates, as shown in

Fig. 5.7c, the associated eigenvectors can be calculated, giving the Hopfield coefficients. These are plotted as a function of detuning in Fig. 5.9, where it can be seen that the LPB moves from photonic to trionic, while the MPB goes from trionic, to photonic, to excitonic, while the UPB behaves much as in the two-level case, with inverse exciton and photon fractions crossing at 0.5 at zero detuning.

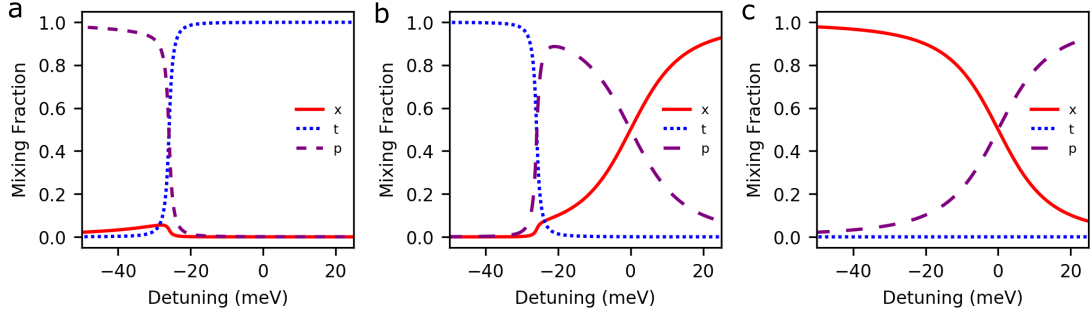


Fig. 5.9 Calculated Hopfield coefficients for the MoSe₂ (a) lower, (b) middle and (c) upper polariton branches. The excitonic, trionic, and photonic fractions of each branch are represented by x, t, and p, respectively. The Hopfield coefficients are calculated from the eigenvectors of the three-level Hamiltonian, based on the fitted cavity spectra shown in Fig. 5.7c.

5.4 Valley addressable exciton-polaritons

Performing polarisation resolved microcavity photoluminescence measurements reveals information about the valley pseudospin of the polaritons, which may be directly compared to the bare flake measurements shown in Section 5.2, to infer details about how the strong coupling regime modifies the valley relaxation and decoherence processes. Of particular interest are the polariton valley polarisation dynamics in MoSe₂, considering that the bare flake retains no valley polarisation in emission (Fig. 5.3a), and the valley coherence of WSe₂, which manifests strongly in the neutral exciton of the bare flake (Fig. 5.4a).

5.4.1 Valley polarised polaritons in MoSe₂ and WSe₂

Fig. 5.10 shows a series of MoSe₂ polariton photoluminescence spectra at various piezo voltages, with the first six panels corresponding to tuning through the trion resonance and the lower six panels tuning through the neutral exciton resonance. The spectra are polarisation resolved in either σ^+ or σ^- circular polarisation, taken under laser excitation in σ^+ polarisation. As can be seen, the σ^+ intensity exceeds σ^- in almost every polariton emission peak, indicating a non-zero degree of circular polarisation and associated retention

Exciton valley dynamics in the strong light-matter coupling regime

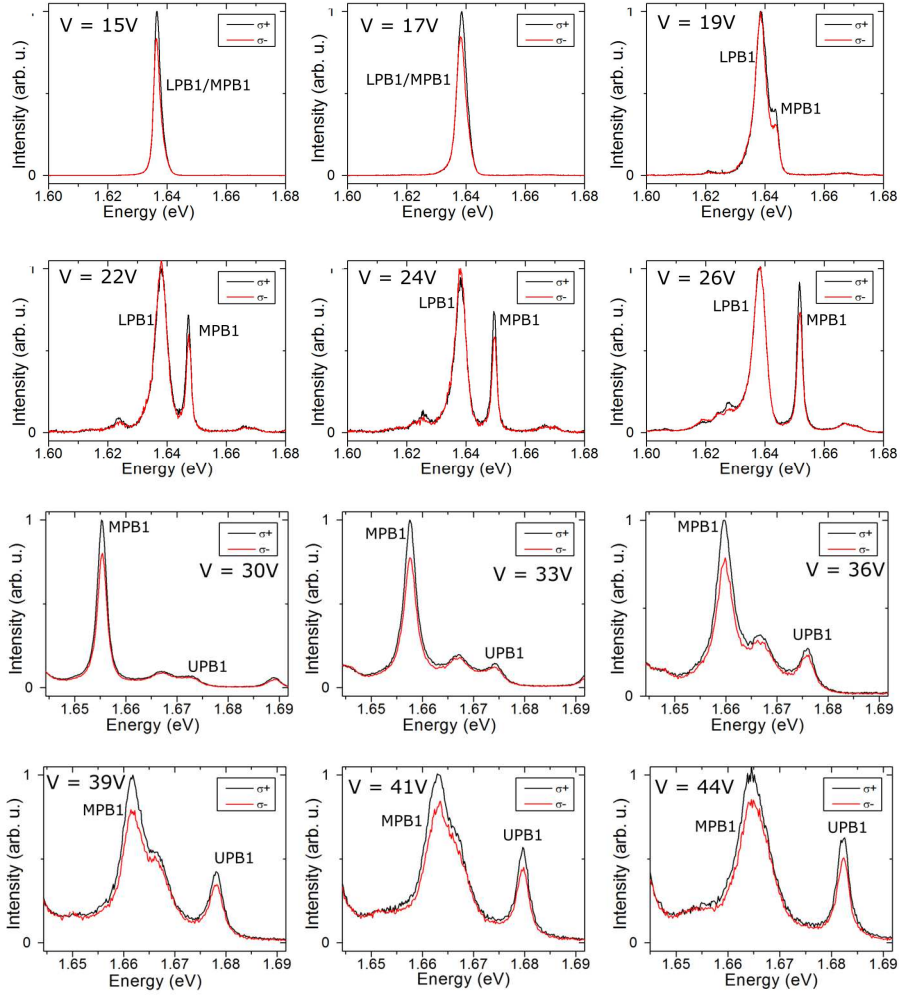


Fig. 5.10 A series of polariton spectra from MoSe₂ embedded in a zero-dimensional optical microcavity. The laser is σ^+ circularly polarised, and the PL detection is in σ^+ and σ^- polarisation, indicating a clear optically injected valley population imbalance surviving beyond the radiative limit. The upper six panels correspond to tuning the cavity mode through resonance with the trion state, while the lower six panels go through the exciton state. Additional non-labelled peaks are higher order modes, visible in the colourmap in Fig. 5.7a.

of optically injected valley polarisation, exceeding the negligible polarisation degree of the bare monolayer (Fig. 5.3a).

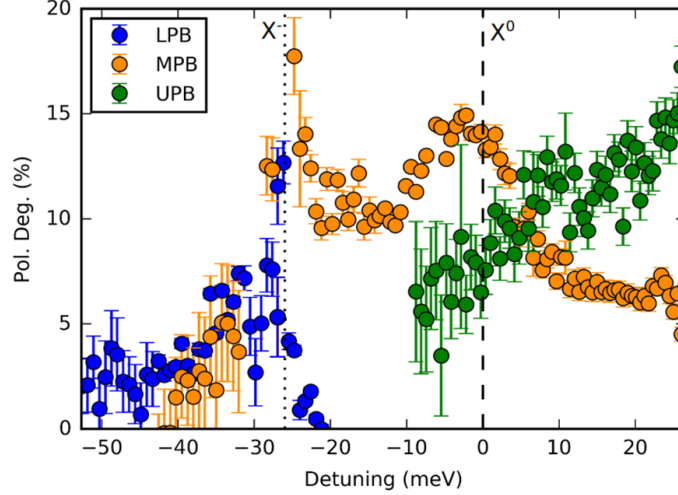


Fig. 5.11 Degree of circular polarisation under σ^+ polarised excitation of MoSe₂ exciton-polariton lower, middle and upper branches, as a function of detuning. The vertical dotted and dashed lines indicate resonance between the cavity mode and the trion and exciton, respectively.

Significantly in Fig. 5.10, the polarisation degree appears to display a complicated dependence on cavity length. To investigate this further, the polarisation degree of each branch is calculated as a function of detuning, by fitting the polarisation resolved polariton spectra at each increment of piezo voltage to Lorentzian functions and applying the equation $\rho = (I_{co} - I_{cross}) / (I_{co} + I_{cross})$. The result is shown in Fig. 5.11, where indeed a complex detuning dependence is revealed. As can be seen, the polarisation degree of the LPB rises from negligible values at very strong negative detuning, reaching a maximum $> 10\%$ when resonant with the trion. The MPB similarly rises to a maximum approaching 20% at the trion energy, before decreasing and then regaining polarisation when approaching resonance with the exciton. At positive detuning the polarisation degree decreases. On the other hand, the UPB displays an almost linear increase in polarisation degree as a function of increasing positive detuning, quite dissimilar to the L/MPB response.

The same experiment can be performed for WSe₂, by measuring the polariton PL in a circular polarisation resolved basis and extracting the polarisation degree as a function of photon-exciton detuning. Unlike MoSe₂, WSe₂ already does retain strong valley polarisation in the bare flake, as shown in Fig. 5.12a, where the polarisation degree of the exciton peak is $\sim 40\%$. In the strong coupling regime, the polariton states also display robust valley coherence, ranging from approximately 25% to 50% depending on the detuning, as shown in

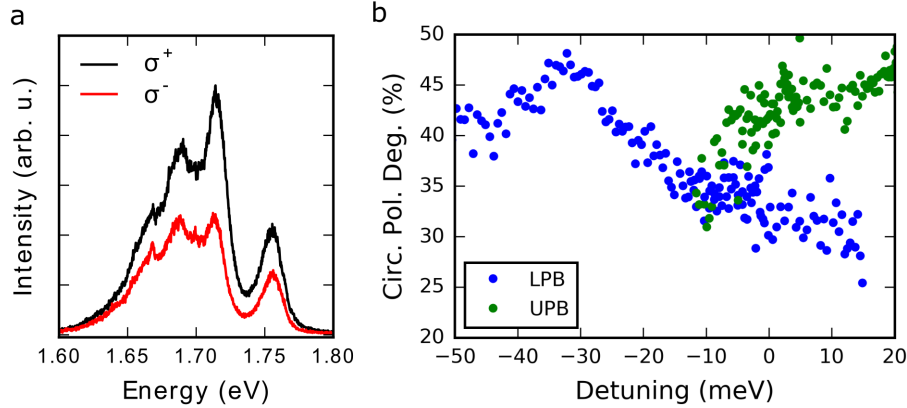


Fig. 5.12 (a) Circular polarisation resolved photoluminescence spectra from a bare WSe_2 monolayer, under σ^+ polarised excitation. (b) Circular polarisation degree of polariton branches from the same monolayer as in (a) embedded in a microcavity, as a function of detuning.

Fig. 5.12b. As no strong coupling with the trion state is observed in WSe_2 , there are only two polariton branches, consistent with the two-level coupled oscillator model.

5.4.2 Valley coherent polaritons in WSe_2

Performing polarisation resolved microcavity spectroscopy in a linear, rather than circular, polarisation basis allows measurement of the degree of valley coherence of exciton polaritons. Section 5.2.2. detailed the retention of optically injected valley coherence in the neutral exciton state of monolayer WSe_2 . Any retention of linear polarisation in WSe_2 exciton-polaritons is therefore indicative of valley coherent polaritons, which are superpositions of exciton valley states, themselves in further superposition between light and matter.

For this experiment, the cavity length is incrementally reduced while WSe_2 polariton photoluminescence spectra are recorded either co-polarised or cross-polarised to the vertically linearly polarised laser (0° on a polar plot such as that shown in Fig. 5.5b). A selection of spectra are presented in Fig. 5.13 for tuning of the cavity mode through resonance with the exciton, where retention of linear polarisation can be seen to varying degrees in the emission. From these spectra, the linear polarisation degree can be measured as a function of detuning, by fitting polariton peaks to Lorentzian functions to extract their intensities. The result is shown in Fig. 5.14, where both branches are observed to increase their polarisation degree as the cavity moves from negative to positive detuning. Strikingly, the degree of linear polarisation reaches 40%, almost double the value of the neutral exciton peak in the bare flake (23%), indicating robust valley coherence within the exciton-polariton population.

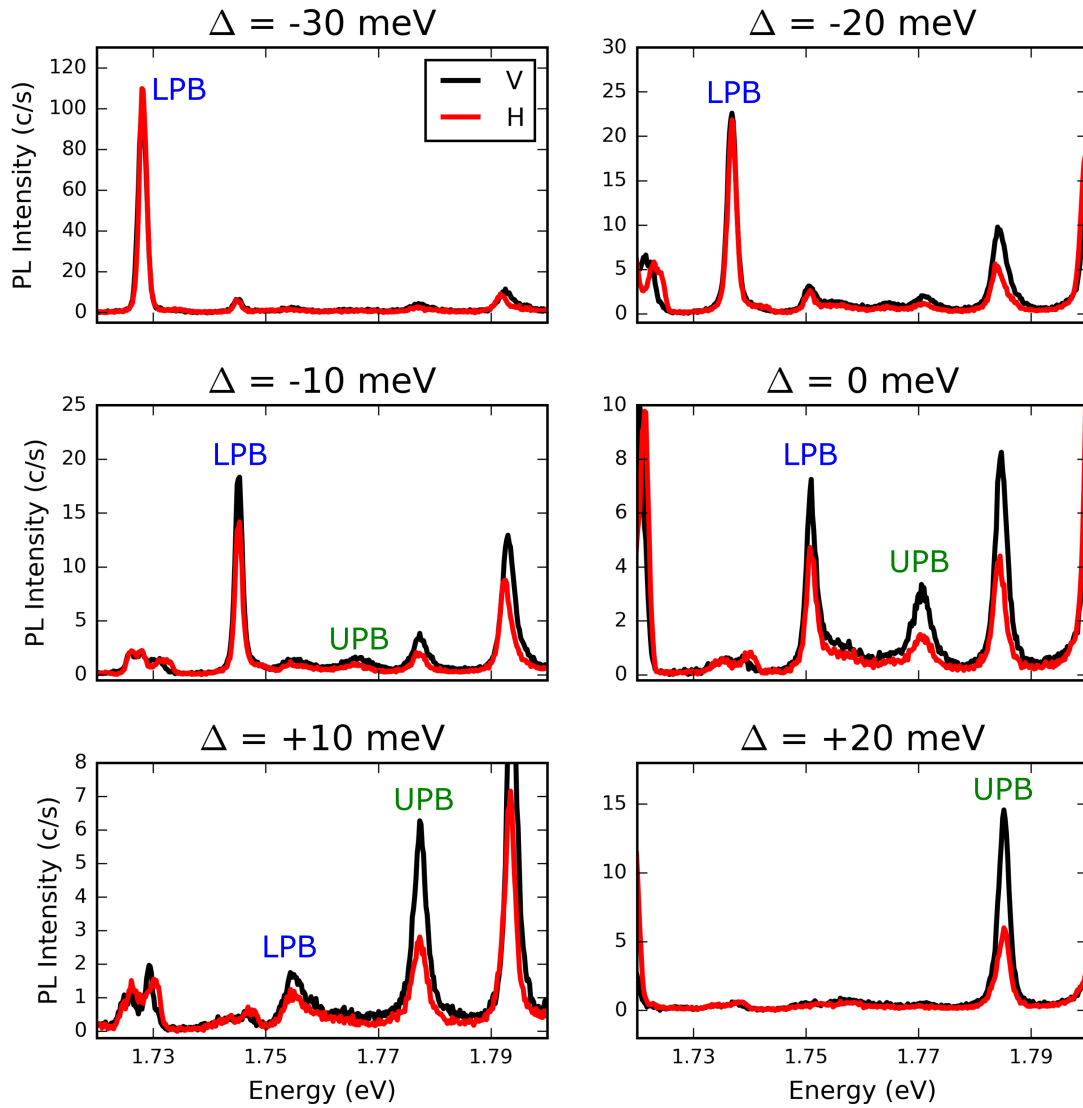


Fig. 5.13 A selection of WSe₂ exciton-polariton photoluminescence spectra taken as the cavity mode is tuned through resonance with the neutral exciton state. The laser is linearly polarised in the vertical (V) plane, and PL is detected in either the vertical or horizontal (H) plane. Brighter vertical emission is indicative of valley coherence in the polariton states.

Exciton valley dynamics in the strong light-matter coupling regime

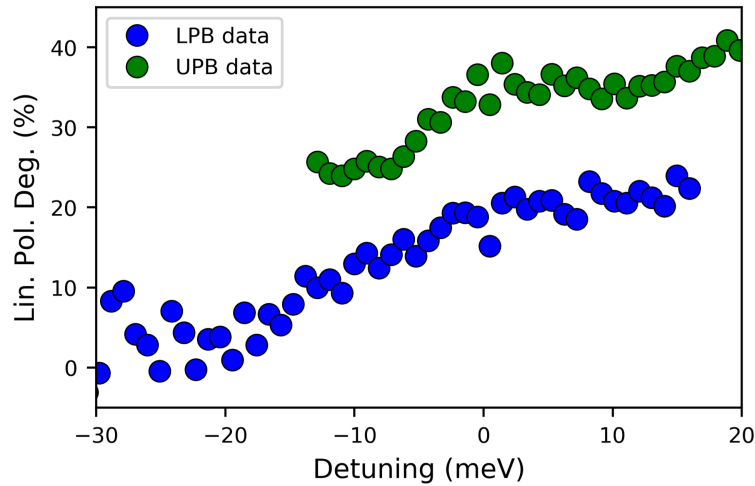


Fig. 5.14 Extracted linear polarisation degree of the LPB and UPB as a function of exciton-cavity detuning. Both branches display an increasing polarisation degree with the cavity moving to positive detuning. The maximum of 40% far exceeds the bare flake value of 23%.

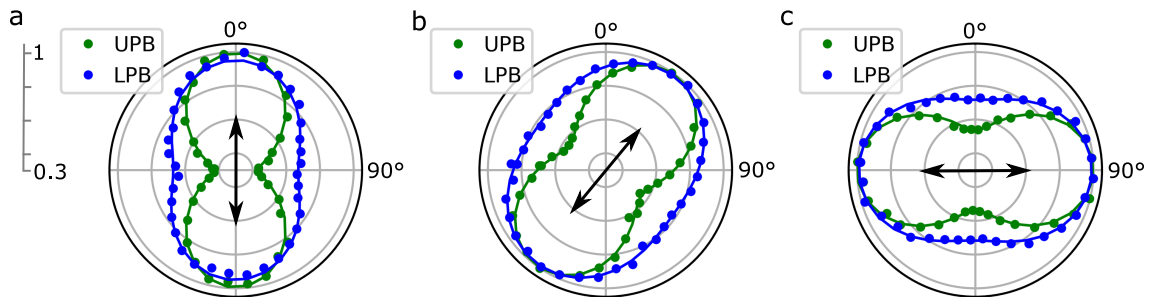


Fig. 5.15 Detection polarisation angle resolved intensity of linearly polarised polariton emission from the LPB and UPB, all taken at zero detuning. The maximum radius of the data indicates the angle of linear polarisation of emission. The black arrows indicate the laser linear polarisation angle. As the laser is rotated, the emission follows suit, pointing to valley coherence as the origin of the polarisation.

To confirm that the origin of the linear polarisation of polariton emission is indeed valley coherence, rather than an artefact such as a structural effect of the microcavity geometry, the angle of linear polarisation of emission is measured for three inequivalent laser polarisation angles. Here, the laser is first vertically linearly polarised, then rotated 45° to diagonal orientation, and finally another 45° to horizontal polarisation. In each case, the linear polarisation plane of the LPB and UPB emission is measured at zero exciton-cavity detuning, by rotating a half wave plate through 180° in front of a linear polariser in the detection path of the optical system. The results are shown in Fig. 5.15, where the polar intensity profiles of both the LPB and UPB correspond exactly to the laser polarisation in each case. This is conclusive evidence of the origin of the polarised emission being optically generated valley coherence.

5.4.3 Coherent manipulation of polariton valley pseudospin

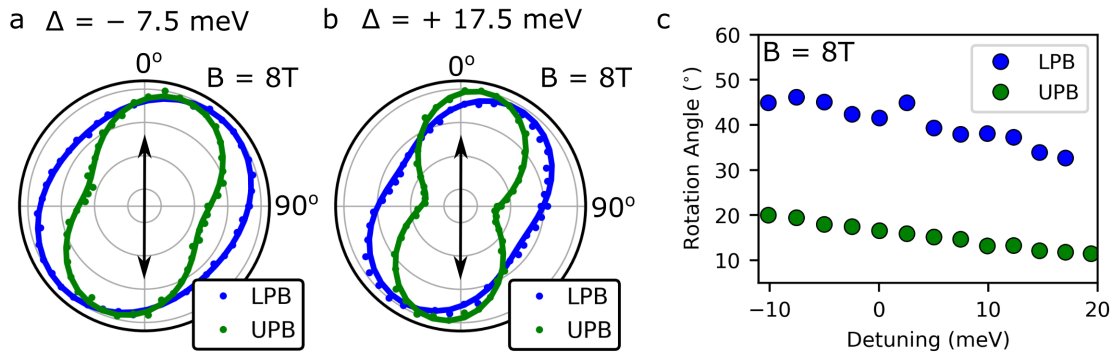


Fig. 5.16 (a,b) Intensity of LPB and UPB PL as a function of detection polariser angle at $B = 8$ T and a detuning of (a) $\Delta = -7.5$ meV and (b) $+17.5$ meV. Black arrows indicate laser linear polarisation. The rotation of the polarisation of emission indicates coherent control of the pseudospin. (b) Extracted linear polarisation rotation angle as a function of detuning for both polariton branches in WSe_2 .

To demonstrate control of the valley coherent polariton population, a magnetic field is applied in the Faraday geometry (perpendicular to the DBRs), to repeat the bare flake experiment from Section 5.2.2 now in the strong coupling regime. Fig. 5.16a and b show the polariton PL as a function of detection angle under vertically linearly polarised laser excitation and at exciton-photon detunings of -7.5 meV and $+17.5$ meV, respectively, for an applied magnetic field of $B = 8$ T. These plots are measured in the same way as those shown in Fig. 5.15, by the rotation of a half waveplate through 180° before a linear polariser

Exciton valley dynamics in the strong light-matter coupling regime

in the detection path. However, the plots in Fig. 5.15 are measured at zero detuning and zero B-field, unlike here, where any rotation of the polarisation plane of emission relative to the laser indicates coherent manipulation of the pseudospin vector [49, 54].

It is clear from the plots that the induced rotation of the LPB is much larger than that of the UPB at both positive and negative detuning. Furthermore, the rotation of each state appears weaker in the +17.5 meV plot than the -7.5 meV plot. To measure the full dependence, a series of polar plots such as these were acquired at several increments of photon-exciton detuning, all at a fixed field of $B = +8$ T applied over the microcavity. Fitting each polar plot to Eq. 5.7 allows the linear polarisation rotation angle to be extracted as a function of detuning for both branches, with the overall detuning dependence shown in Fig. 5.16c. Here, a general trend of decreasing rotation angle with increasing detuning is observed for both polariton branches. Significantly, the LPB rotation approaches 50° at -10 meV, almost double the angle achievable in the bare exciton at an equivalent field strength (Fig. 5.5).

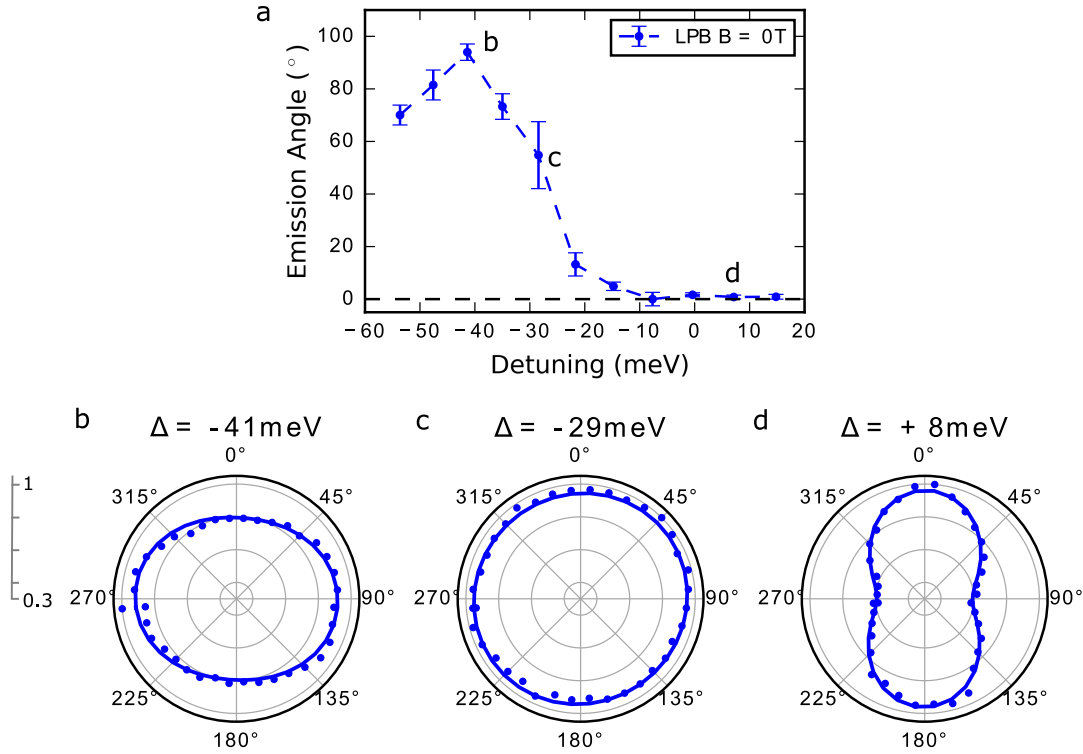


Fig. 5.17 (a) Emission angle of linearly polarised LPB photoluminescence under vertically (0°) linearly polarised excitation as a function of detuning, at $B = 0$ T. (b-d) Detection angle dependent intensity of LPB PL at (b) -41 meV (c) -29 meV and (d) $+8$ meV exciton-photon detuning, under vertically linearly polarised excitation. Data points corresponding to each polar plot are labelled on (a).

5.5 Cavity modified pseudospin relaxation dynamics

At detunings more strongly negative than -10 meV, the influence of lower energy emitters in WSe_2 begin to interfere with the detected angle of LPB linearly polarised emission. The linear polarisation resolved bare flake PL spectrum shown in Fig. 5.4a shows a very small cross-polarisation of emission from all states below the neutral exciton. The origin of this orthogonal polarisation remains unclear, but the effect is very small ($< 3\%$ linear polarisation degree). As such, in the absence of applied fields, at strong negative detuning ~ -40 meV, a measurement of the linear polarisation plane of LPB emission reveals an apparent angle of 90° . This is not attributed to coherent manipulation of the pseudospin vector, but rather the LPB reflecting the intrinsic polarisation orientation of the underlying states with which it is quasi-resonant. As the detuning becomes less negative and the LPB more excitonic, the apparent angle of LPB emission rotates, until it settles at 0° to match the laser polarisation, as expected. As such, the influence of lower energy states in WSe_2 masks the coherent manipulation of the LPB at detunings more negative than -10 meV, and so this is taken as a lower bound in Fig. 5.16c.

5.5 Cavity modified pseudospin relaxation dynamics

This section seeks to develop an understanding of the circular and linear polarisation degrees as functions of detuning shown in Figs. 5.11 and 5.14. The general situation is the same for both valley polarisation and valley coherence, and applies to both MoSe_2 and WSe_2 . Here, 100% valley polarisation or coherence is injected by the laser at 1.946 eV, according to the laser polarisation. When probing valley polarisation, the laser is σ^+ polarised, preparing the valley pseudospin vector at the North pole of the Bloch sphere, while in the case of valley coherence, the linearly polarised laser will direct the pseudospin vector onto the equator, at an azimuthal angle given by the plane of the laser linear polarisation. The exciton ensemble then relaxes down the parabolic dispersion, eventually populating the polariton states which occupy the light cone at low wavevector, $|\mathbf{k}| = \omega_x/c$, before eventually decaying radiatively by escape of a photon from the cavity [30].

As introduced in Section 2.3.1, coupling between $|K\rangle$ and $|K'\rangle$ valley excitons via the long range electron-hole exchange interaction causes the exciton dispersion to split into components with dipole moment parallel (longitudinal) and perpendicular (transverse) to the in-plane wavevector. This LT-splitting is linearly proportional to the \mathbf{k} -vector, and gives rise to an effective valley-orbit coupling which may be treated as an effective magnetic field about which the exciton valley pseudospin precesses, with field strength and orientation determined by the \mathbf{k} -vector [44, 45, 121, 43, 132]. Scattering of the excitons due to disorder creates a randomly varying field which leads to random valley pseudospin precession and associated

Exciton valley dynamics in the strong light-matter coupling regime

decoherence, where the precession is stronger at larger wavevector [49, 53, 54, 127]. This combination of momentum scattering and LT-splitting induced precession is known as the Maialle-Silva-Sham mechanism, and results in loss of definition of the valley pseudospin vector over the ensemble of particles in the momentum-dark high wavevector regions of the dispersion, termed the *exciton reservoir*, as excitons must wait in these states until scattering into the light cone to couple to photons [30].

5.5.1 Valley depolarisation in a three level strongly coupled system

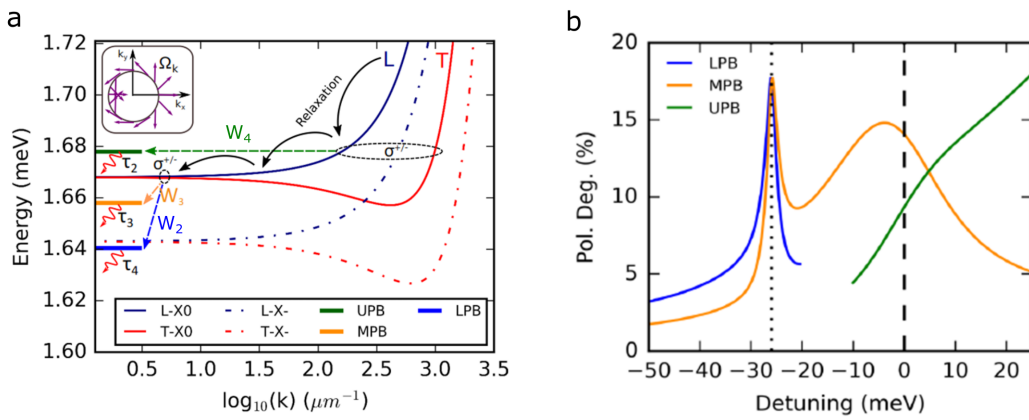


Fig. 5.18 (a) Diagram of the energy relaxation and momentum scattering processes in strongly coupled MoSe₂. Excitons relax down their LT-split dispersion, and populate the polariton branches with characteristic rates derived in the text. Inset shows the orientation of the effective magnetic field arising from the LT-splitting, which acts on the valley pseudospin. The energies of the polariton states correspond to zero exciton-photon detuning. The zero-dimensional cavity restricts the polariton states to small \mathbf{k} -vectors, protecting them from the effective depolarising field. While it may be the case that polariton states are directly populated from the trion dispersion, this is not assumed to be dominant considering the much weaker trion-photon coupling observed in Fig. 5.7. (b) Reproduction of the experimental data shown in Fig. 5.11 using the model of coupled rate equations presented in the text, with parameters listed in Table. 5.1.

To understand the complex detuning dependence of circular polarisation degree shown in Fig. 5.11, a dynamical model incorporating state lifetimes and scattering rates was developed by collaborators at the Institut Pascal, Clermont Auvergne, France, with the end goal to reproduce the data shown in Fig. 5.11. In general, the pseudospin depolarisation in MoSe₂ may be modelled as scattering between opposite valley populations of exciton and exciton-polaritons. To begin, Boltzmann equations describing the $\pm K$ valley populations $n_{i\pm}$ of polaritons in each branch i are given as

5.5 Cavity modified pseudospin relaxation dynamics

$$\frac{dn_{i\pm}}{dt} = W_i n_{x\pm} - \frac{n_{i\pm}}{\tau_i} \mp \frac{n_{i+} - n_{i-}}{\tau_{i\pm}}, \quad i = 2, 3, 4 \quad (5.9)$$

where $n_{x\pm}$ are the exciton reservoir $\pm K$ valley populations, W_i are the scattering rates from the reservoir into each polariton branch i , τ_i is the polariton state lifetime, $\tau_{i\pm}$ is the polariton state valley relaxation time, and $i = 2, 3, 4$ denotes LPB, MPB, UPB. In the above equation, the first term describes valley dependent population of each branch from the reservoir, the second term describes losses due to radiative decay of the polariton states by photons escaping the cavity, or non-radiative decay via the excitonic fraction, and the third term describes intervalley relaxation. The valley exciton reservoir populations evolve as

$$\frac{dn_{x\pm}}{dt} = P_+ - \frac{n_{x\pm}}{\tau_x} - n_{x\pm} \sum_{i=2}^4 W_i \mp \frac{n_{x+} - n_{x-}}{\tau_{x\pm}} \quad (5.10)$$

where P_+ indicates population of the K valley reservoir from the σ^+ polarised pump (as is used to acquire the data in Fig. 5.11), the second term describes non-radiative decay of the excitons, the third term is scattering to each polariton branch, and the final term describes intervalley relaxation. As such, the $-K$ valley reservoir is only populated by scattering of $+K$ valley excitons. By solving these coupled rate equations in the steady state, the circular polarisation degree of each polariton branch may be calculated:

$$\rho_i = \frac{\tau_{i\pm} \tau_{x\pm} \left(1 + \tau_x \sum_{i=2}^4 W_i \right)}{(2\tau_i + \tau_{i\pm}) \left(\tau_{x\pm} + 2\tau_x + \tau_x \tau_{x\pm} \sum_{i=2}^4 W_i \right)} \quad (5.11)$$

Next, the scattering rates W_i must be derived. Here, a crucial distinction must be made between polariton states at higher and lower energy than the bottom of the exciton dispersion. To populate lower states (the LPB and MPB), the rates $W_{2,3}$ describe energy relaxation of excitons from the bottom of the reservoir down into the branches. However, for the UPB, which always lies above the bottom of the reservoir, W_4 describes momentum scattering at constant energy, as shown in Fig. 5.18a.

Considering first the LPB and MPB, the scattering rates may be described in general as the difference between excitons scattering into the branch and excitons backscattering from the branch back into the reservoir:

$$\begin{aligned} W_{x \rightarrow i} &= W_0 x_i \\ W_{i \rightarrow x} &= W_0 x_i e^{-\frac{E_x - E_i}{k_B T}}, \quad i = 2, 3 \end{aligned} \quad (5.12)$$

Exciton valley dynamics in the strong light-matter coupling regime

where k_B is the Boltzmann constant, T the temperature, and x_i the *total* excitonic fraction (i.e. excitonic plus trionic, rather than photonic) of the LPB or MPB ($i = 2, 3$). Here, the scattering mechanism may be the exciton-exciton or exciton-phonon interactions. Both of these rates will increase with excitonic fraction of the branch, because the energy gap between the branch and reservoir decreases, and because only the excitonic fraction can interact with other excitons and phonons to scatter. The basic coefficient W_0 is the same for both rates, however, the upwards scattering rate $W_{i \rightarrow x}$ has a lower probability because energy must be gained rather than lost, i.e. a phonon must be absorbed rather than emitted. Therefore, the difference between these rates becomes

$$W_i = W_0 x_i \left(1 - e^{-\frac{E_x - E_i}{k_B T}} \right), \quad i = 2, 3 \quad (5.13)$$

The form of this equation means that there is a compromise between scattering into the branch and backscattering out of it. As detuning increases from negative towards resonance, the excitonic fraction of the branch increases, leading to more efficient population of the branch. However, as the energy gap between branch and reservoir decreases, the rate of backscattering also increases to balance the population. Eventually, as the branch becomes quasi-resonant with the reservoir, it ceases to be photonic at all, and is essentially simply a part of the reservoir, and the rate W_i approaches zero. Overall, there is a maximum of W_i around $x_i = 0.5$, where the best compromise between scattering rates occurs.

The UPB is a different situation completely, as the polarisation degree of states within the exciton reservoir is assumed to decrease towards the bottom of the reservoir owing to depolarisation during energy relaxation. As shown in Fig. 5.18a, the UPB is directly populated from reservoir states with which it is resonant. The UPB population can therefore be modelled by a pumping rate P with associated polarisation degree ρ_x , where ρ_x decreases from 1 at the top of the reservoir (laser energy) to 0 at the bottom of the reservoir. As the momentum dependent exchange field Ω_k increases linearly with \mathbf{k} , the polarisation degree ρ_x is assumed to decrease linearly with energy. Eq. 5.9 may then be modified and written as

$$\begin{aligned} \frac{dn_{4+}}{dt} &= \frac{P(1 + \rho_x)}{2} - \frac{n_{4+}}{\tau_4} - \frac{n_{4+} - n_{4-}}{2\tau_{4\pm}} \\ \frac{dn_{4-}}{dt} &= \frac{P(1 - \rho_x)}{2} - \frac{n_{4-}}{\tau_4} + \frac{n_{4+} - n_{4-}}{2\tau_{4\pm}} \end{aligned} \quad (5.14)$$

where $n_{4\pm}$ are the UPB valley populations, the first terms describe population as a function of reservoir polarisation degree, the second terms are the UPB lifetime, and the third terms describe depolarisation within the branch. The steady state solutions of these coupled rate equations are:

5.5 Cavity modified pseudospin relaxation dynamics

$$\begin{aligned} n_+ &= \frac{\tau_4(P\tau_4 + P\tau_{4\pm} + P\rho_x\tau_{4\pm})}{2(\tau_4 + \tau_{4\pm})} \\ n_- &= \frac{\tau_4(P\tau_4 + P\tau_{4\pm} - P\rho_x\tau_{4\pm})}{2(\tau_4 + \tau_{4\pm})} \end{aligned} \quad (5.15)$$

from which the polarisation degree of the UPB can be calculated

$$\rho_4 = \frac{\rho_x\tau_{4\pm}}{\tau_4 + \tau_{4\pm}} \quad (5.16)$$

indicating that the polarisation degree of the UPB is proportional to the polarisation degree of the reservoir as a function of energy. This explains the almost linear increase in UPB polarisation degree observed in Fig. 5.11, quite dissimilar from the LPB and MPB behaviour owing to the UPB state always being resonant with some portion of the parabolic exciton dispersion. As the detuning increases and the UPB shifts to higher energy, it becomes populated with exciton reservoir states of increasing polarisation.

The polariton lifetimes may be expressed as

$$\frac{1}{\tau_i} = \frac{x_i}{\tau_x} + \frac{t_i}{\tau_t} + \frac{p_i}{\tau_p} \quad (5.17)$$

where x_i , t_i , p_i are the exciton, trion, and photon fractions of each branch i , τ_x , τ_t are the exciton and trion non-radiative lifetimes, and τ_p is the photon lifetime, corresponding to the time until escape of the photon from the cavity.

The polariton valley relaxation times are

$$\frac{1}{\tau_{i\pm}} = \alpha \frac{x_i}{\tau_{x\pm}} + \beta \frac{t_i}{\tau_{t\pm}} + \frac{p_i}{\tau_{p\pm}} \quad (5.18)$$

where the coefficients α and β are necessary because the depolarisation of the exciton component of the polariton states is always less efficient than the depolarisation of pure exciton states in the reservoir, owing to the restricted polariton wavevector $\mathbf{k} \approx 0$ in the zero-dimensional cavity, with correspondingly weak exchange interaction. Furthermore, the polariton wavefunction spatially extends over the beam waist of the LG₀₀ mode, about 1 μm diameter. This is a much larger area than the typical length scale of lattice associated disorder and defects, making the exciton component of the polaritons less subject to scattering. Taking consideration of these values, the coefficients are estimated to be $\alpha \approx \beta \approx 0.05$, indicating the highly robust nature of polariton states against the Maialle-Silva-Sham mechanism. While there is some depolarisation due to the photonic spin-orbit coupling, arising from cavity mode TE-TM splitting (see Section 3.3.2), it is expected to be a far weaker effect compared to the exciton momentum scattering processes.

Exciton valley dynamics in the strong light-matter coupling regime

Parameter	Description	Value	Source
τ_x	Exciton lifetime	5.3 ps	Ref. [107]
τ_t	Trion lifetime	12 ps	Ref. [107]
τ_p	Photon lifetime	1.3 ps	From cavity Q-factor
$\tau_{x\pm}$	Exciton valley lifetime	0.15 ps	Fitting parameter
$\tau_{t\pm}$	Trion valley lifetime	1 ps	Fitting parameter
$\tau_{p\pm}$	Photon valley lifetime	15 ps	From cavity TE-TM splitting
W_0	Energy relaxation rate	(1/0.15) ps	Fitting parameter
x_i, t_i, p_i	Hopfield coefficients	See Fig. 5.9	Eigenvectors of Hamiltonian
α, β	Depolarisation coefficients	0.05	Estimated, see text

Table 5.1 List of values used to reproduce the experimental data shown in Fig. 5.11 with the rate equation model described in the text. The exciton and trion lifetimes are taken from time resolved measurements in Ref. [107]. A measurement of the LG₀₀ mode Q-factor and TE-TM splitting can be found in methods Section 3.3.2.

Using the rates in Eq. 5.13 for the LPB and MPB with Eq. 5.11, and Eq. 5.16 for the UPB, allows reproduction of the experimental data in Fig. 5.11 with the model, as shown in Fig. 5.18b, where the associated model parameters are given in Table. 5.1. The best reproduction of the data occurs when the exciton and trion valley lifetimes are $\tau_{x\pm} = 0.15$ ps and $\tau_{t\pm} = 1$ ps, respectively, and the energy relaxation rate $W_0 = (1/0.15)$ ps. This relaxation rate is reasonable given the resolution limited rise-time of exciton photoluminescence in time resolved measurements in Ref. [107], inferring a 1 ps upper limit on energy relaxation.

The fitted exciton and trion valley lifetimes are both an order of magnitude faster than the respective state lifetimes. This offers a clue as to the absence of circular polarisation in the PL from the bare flake: no valley polarisation remains by the time the excitons radiatively recombine, owing to very efficient momentum scattering high in the dispersion in the presence of a \mathbf{k} -dependent depolarising field. By coupling the excitons to photonic modes in a microcavity, the excitons occupy polariton states which are highly protected from such depolarisation processes, and emit quickly retaining high polarisation. Indeed, the photons have a much shorter lifetime, and a much longer depolarisation time than the excitons and trions, both leading to weak depolarisation in the polariton states, alongside the cavity geometry which supports only photonic modes of very low wavevector.

5.5.2 Pseudospin decoherence processes

The rate equation model presented above for the case of valley depolarisation in MoSe₂ in the strong light-matter coupling regime is highly instructive when considering the polariton

5.5 Cavity modified pseudospin relaxation dynamics

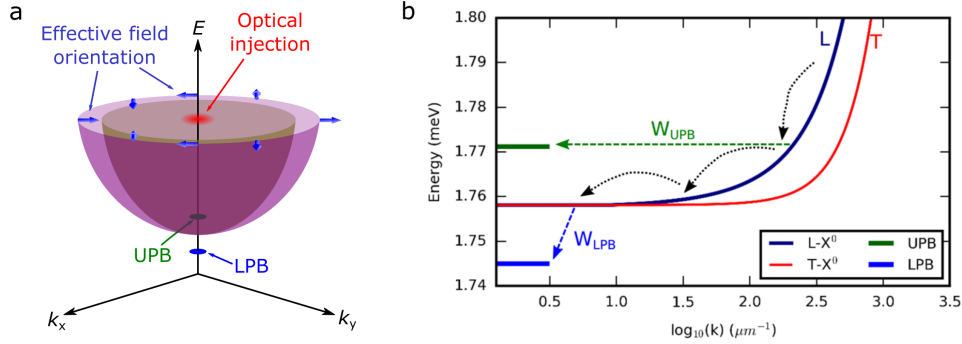


Fig. 5.19 (a) Illustration of the LT-split exciton dispersion in monolayer WSe₂, with the orientation of the effective magnetic field shown by purple arrows. Excitons are injected with strong coherence at the pump energy, and subsequently lose coherence until they populate the UPB and LPB states, which have a very small extent in k -space and so are protected from efficient decoherence. (b) Slice of the exciton dispersion highlighting the energy relaxation which populates the LPB and momentum scattering which populates the UPB.

valley coherence dynamics observed in WSe₂, and shown in Fig. 5.14. The case of WSe₂ is simplified in comparison to MoSe₂ in that no trion strong coupling is observed, and so there are only two polariton branches. As before, the parabolic exciton dispersion is split into two by the long-range electron hole exchange interaction, acting as a \mathbf{k} -dependent effective magnetic field, the orientation of which is indicated in Fig. 5.19a. Precession of the pseudospin about this field causes efficient decoherence when the exciton ensemble experiences random momentum scattering, leading to the effective field orientation to change unpredictably and reduce the overall degree of valley coherence. As such, the linear polarisation degree of the exciton reservoir states decreases towards the bottom of the dispersion, as energy and momentum relaxation take their effect.

As with MoSe₂, the UPB in WSe₂ is degenerate with states within the exciton reservoir, while the LPB occupies a lower energy, as shown in Fig. 5.19a. As such, the LPB is populated by energy relaxation of excitons from low in the reservoir, as shown in Fig. 5.19b, while the UPB is populated by direct momentum scattering of higher energy reservoir states. Correspondingly, when moving from negative to positive detuning, the LPB becomes more excitonic and closer in energy to the exciton reservoir, increasing the population rate, and resulting in a gradual increase in linear polarisation degree from zero (when the LPB is very photonic) to $\sim 23\%$, which is the value of the bare exciton at the bottom of the reservoir, as indicated by the bare flake PL in Fig. 5.4a. The UPB, on the other hand, directly reflects the polarisation degree of the exciton reservoir states with which it is resonant. Therefore, the observed UPB linear polarisation degree at negative detuning, when it is very excitonic

and near the bottom of the reservoir, is also $\sim 23\%$. As detuning becomes more positive, the UPB increases in energy, and probes successively higher energy reservoir states with increasingly strong valley coherence.

This interpretation is fully consistent with the observed polariton pseudospin vector rotation angle as a function of detuning, shown in Fig. 5.16. Here, a larger angle of rotation in the final state photon reflects a slower overall relaxation pathway taken by the initial state exciton. The UPB extracts high- \mathbf{k} excitons from the reservoir before significant pseudospin precession has occurred, while the excitons which accumulate at the bottom of the reservoir eventually populate the LPB at a rate determined by the detuning. The majority of pseudospin vector rotation occurs in the reservoir, due to the reduced exciton fraction of polaritons, which leads to smaller Zeeman splitting and a lower precession frequency than pure excitons.

5.6 Summary

In conclusion, this work presents unambiguous observation of valley polarised exciton-polaritons in monolayer MoSe₂, along with robust valley coherence of polaritons in monolayer WSe₂. In both materials, the degrees of optical polarisation in photoluminescence far exceed the values obtainable in bare, uncoupled monolayers, owing to cavity modified valley pseudospin relaxation dynamics. A theoretical model based on dynamical rate equations which incorporate energy, momentum, and pseudospin relaxation is developed, which accurately reproduces the MoSe₂ polariton circular polarisation degree, confirming that extremely efficient pseudospin relaxation occurring at high exciton wavevectors is responsible for low polarisation degrees in emission.

Furthermore, coherent manipulation of the exciton-polariton valley pseudospin vector is demonstrated, arising from precession of the vector about the Bloch sphere equator under the action of an applied strong magnetic field. While in this work, a magnetic field was used to control the polariton pseudospin, it would be possible to induce ultrafast vector rotation by the application of Stark pulses, with the final state angle easily selectable by adjusting the cavity detuning [127].

The results presented in this chapter unveil the complex valley pseudospin relaxation dynamics of excitons in monolayer TMDs, and demonstrate how the use of optical microcavities allow the efficient depolarisation timescales inherent to these materials to be overcome, by offering highly protected polariton states for the excitons to occupy, in which their pseudospin vector remains well defined over enhanced timescales. The implications of this work include the possibility for study of valley dependent non-linear polariton behaviour,

such as condensation and superfluidity, or the implementation of polaritonic circuit elements for valley pseudospin based information processing at high speeds.

Chapter 6

Exciton valley physics in semiconductor-ferromagnet heterostructures

In this chapter, a fundamental property of 2D materials is exploited to allow unprecedented levels of control over the exciton valley pseudospin, performed entirely at the nano-scale and without the need for strong magnetic fields or bulky macroscopic photonic structures. Successful control at this level is a vital step towards the implementation of 2D materials in future technology, for which miniaturisation is crucial. In this sense, 2D materials already have a great advantage over conventional semiconductors, given their nanometre scale thickness. However, these advantages are significantly diminished when complex external structures and equipment are required in order to interface with the active materials themselves. As discussed in Chapters 2 and 3, 2D films have the unique ability to be stacked on top of each other to form van der Waals heterostructures, which can mimic the layer structure of conventional semiconductor devices without the need for epitaxial or lattice matching considerations. In analogy to the structures studied in the research field of spintronics, and those already employed in information processing and memory technology, it is possible to directly stack a monolayer TMD on top of a ferromagnetic material, to create a ferromagnet-semiconductor heterostructure. In such structures, the TMD experiences the typically very strong interfacial magnetic exchange field from the ferromagnet, and may interact with spin polarised carriers along the interface. This chapter demonstrates the consequences of close proximity to ferromagnets for exciton valley states in monolayer TMDs.

The results presented in this chapter are as yet unpublished.

6.1 Background - ferromagnetism in 2D materials

Few of the materials which have underpinned solid-state physics research over the past century now lack a 2-dimensional crystalline analogue [133]. This is keenly exemplified by recent (as of 2017) discoveries of long range magnetic order persisting into the monolayer limit in layered van der Waals materials, beginning with CrI_3 and $\text{Cr}_2\text{Ge}_2\text{Te}_6$ [134, 135], but ever expanding to encompass a range of 2D magnets with various properties [136–139]. Of particular note is CrI_3 , a van der Waals layered crystal (Fig. 6.1a) which has since 2017 been the focus of extensive research in both its ferromagnetic and antiferromagnetic phases [135, 140–148].

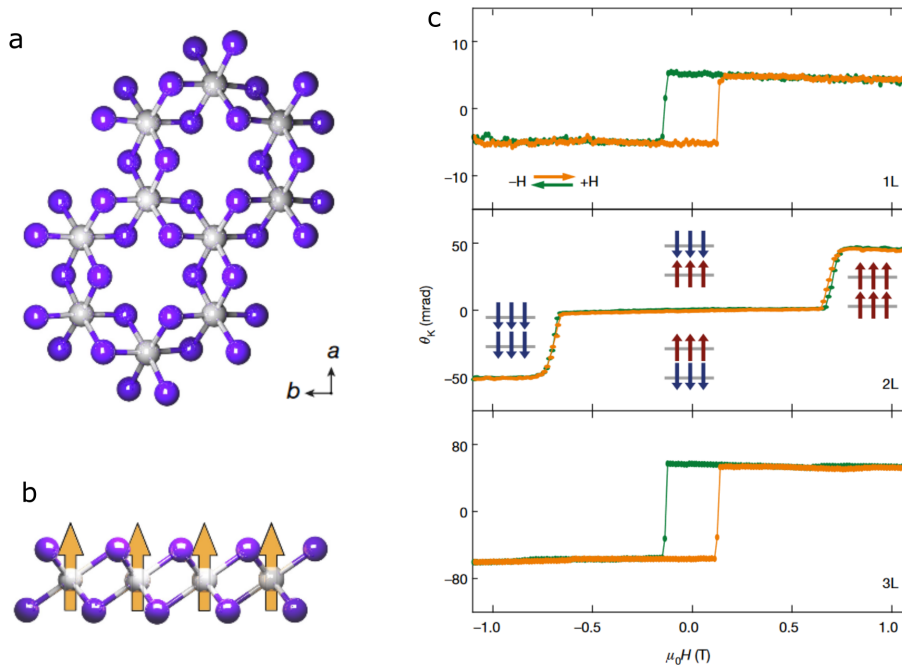


Fig. 6.1 (a) Top view of a monolayer CrX_3 crystal, where X is Cl, Br, or I. (b) Side view of the monolayer, with arrows indicating the out of plane spin orientation of the Cr^{3+} magnetic moments. (c) Polar magneto-optic Kerr effect measurements on monolayer (top panel), bilayer (middle panel) and trilayer (bottom panel) CrI_3 . Results reveal a layer dependent (anti)ferromagnetism. *All subfigures from Ref. [135].*

Truly 2-dimensional ferromagnetism is a prospect which was long thought impossible, owing to the Mermin-Wagner theorem, which posits that thermal fluctuations in a 2D lattice of magnetic moments would lead to breakdown of long range order [149]. However, if magnetic anisotropy is introduced to the 2D structure, Mermin-Wagner theorem can be overcome and long range collective ordering, be it ferromagnetic or otherwise, can exist

6.1 Background - ferromagnetism in 2D materials

at finite temperatures [135, 134]. In 2D van der Waals layered materials with unpaired spins, reduced crystal symmetry can lead to a magnetocrystalline anisotropy out of the plane [135]. As such, in CrI_3 the magnetic moment of each Cr^{3+} ion points along the hexagonal c -axis, either up or down out of the monolayer plane (Fig. 6.1b), leading to long range ferromagnetic order even to the monolayer limit. This is well described by the Ising model of ferromagnetism, in contrast to the Heisenberg model in which the spin at each lattice site may point in any direction [149, 150].

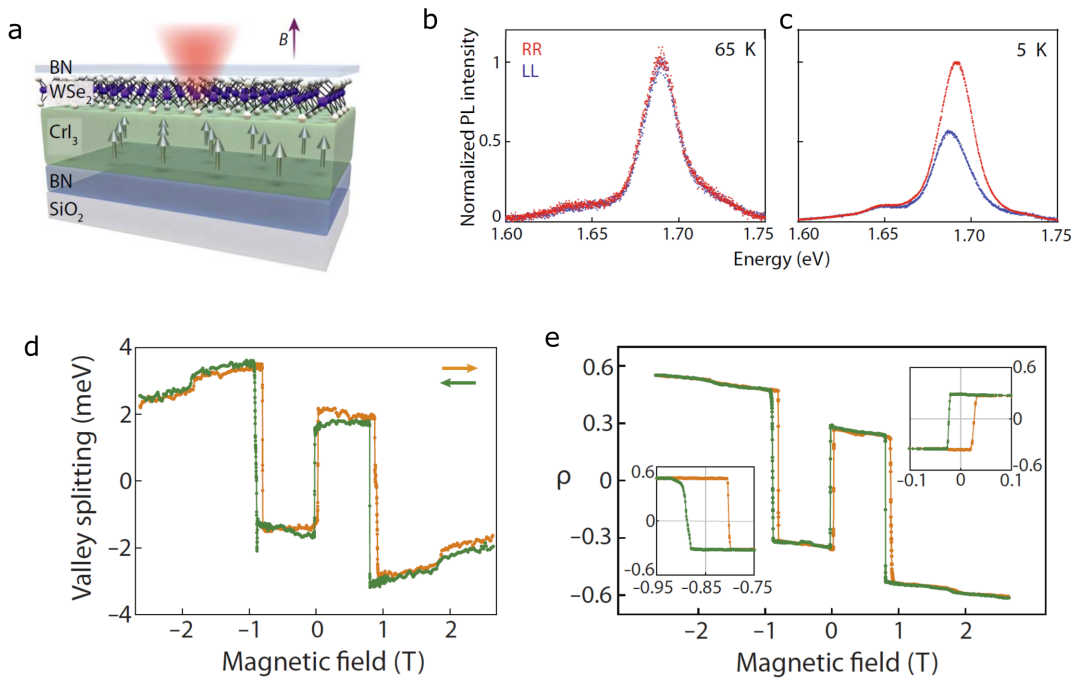


Fig. 6.2 (a) Image of a WSe_2 monolayer on top of multi-layered CrI_3 , with hBN encapsulation. (b,c) Polarisation resolved photoluminescence from the sample above (b) and below (c) the Curie temperature of CrI_3 , ~ 60 K. Red (blue) curves are σ^+ (σ^-) polarisation. (d,e) Measurement of the valley splitting (d) and circular polarisation degree (e) of the sample when sweeping a magnetic field in both directions perpendicular to the sample. *All subfigures from Ref. [141].*

The magnetisation of a planar ferromagnet with perpendicular anisotropy, such as thinned CrI_3 , may be probed via the polar magneto-optic Kerr effect (MOKE). Here, linearly polarised light incident normal to the sample surface will be reflected with a small rotation of the plane of linear polarisation, with the angle of rotation directly dependent on the local magnetisation [135]. MOKE spectroscopy on monolayer CrI_3 reveals a non-zero magnetisation which responds to a weak external magnetic field aligned out of plane, as shown in Fig. 6.1c (top panel). The Kerr angle switches between two values at positive and negative B-field, with

a significant remanent magnetisation leading to hysteresis about zero field, a signature of ferromagnetism [135]. Interestingly, in the bilayer, the magnetisation of the two layers appears to counteract one another, leading to net zero magnetisation, associated with an antiferromagnetic overall state (Fig. 6.1c middle panel). In the trilayer, ferromagnetism is regained, with a stronger magnetisation than the monolayer case (Fig. 6.1c bottom panel) [135]. Overall, these results represent a new paradigm for nanoscale magnetism, and bring to prominence the possibility of devices incorporating van der Waals magnets, semiconductors and more, to create spintronic technology in the 2D limit.

A particularly interesting avenue to explore is the range of interactions between this new class of layered ferromagnets and the well studied monolayer TMDs. In particular, the unique geometry of van der Waals heterostructures may be exploited to allow direct proximity between a layered ferromagnet and monolayer TMD, such that the short range magnetic exchange field may couple to the TMD valley magnetic moment and allow a new regime of control of valley pseudospin. To this end, research has been carried out on a sample of multi-layered CrI_3 with a monolayer of WSe_2 transferred directly on top (Fig. 6.2a) [141]. When cooled below the Curie temperature of CrI_3 , the photoluminescence from the WSe_2 spontaneously displayed a valley splitting and valley polarisation, attributed to proximity effects from the magnet (Fig. 6.2b,c). Upon sweeping a B-field perpendicular to the sample, the valley splitting and polarisation display a response mimicking the magnetisation behaviour of the magnet, with hysteresis and saturation effects (Fig. 6.2d,e) [141].

6.2 $\text{MoSe}_2 / \text{CrBr}_3$ van der Waals heterostructures

Chromium tribromide (CrBr_3) is a ferromagnetic insulator of the same metal trihalide family as CrI_3 [151]. The majority of investigations on the material properties of CrBr_3 were carried out in the 1960s, on bulk crystals typically of several micron thickness. These include spectrally resolved polar MOKE measurements, establishing magnetic resonances at 426 nm and 375 nm [152], a Curie point at 37 K and magnetic moment per Cr ion of $\sim 3\mu_B$ [153], along with studies of the light absorption edge, established to be in the green part of the visible spectrum [154]. The origin of ferromagnetic order was found to be a superexchange interaction between nearest neighbour Cr^{3+} cations via an intermediary bromine anion [153, 155]. Since these initial studies, there has not been much output regarding CrBr_3 , and to this day it remains a relatively little studied material. However, since the renewed interest in van der Waals layered materials, and in particular since the discovery of monolayer ferromagnetism in CrI_3 , there has been a resurgence of interest in CrBr_3 .

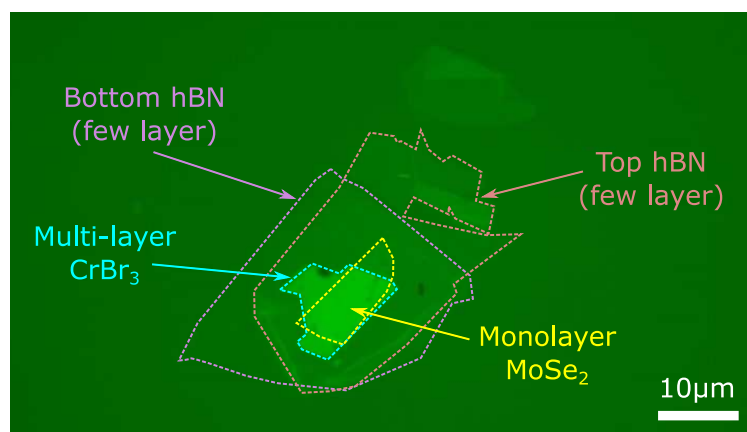


Fig. 6.3 Bright field microscope image of the hBN / CrBr₃ / MoSe₂ / hBN van der Waals heterostructure sample studied in this chapter. This sample was fabricated by Dr. Abhishek Misra at the National Graphene Institute, Manchester, using an argon glove box for the entire process in order to prevent degradation of air-sensitive CrBr₃.

Very recent studies include investigation of CrBr₃ in magnetic tunnel junctions comprised of few-layer CrBr₃ stacked between graphene electrodes [156]. The tunnelling of electrons through the ferromagnetic barrier was found to be accompanied by an electron spin flip with the emission of single magnons, which are quantized spin-waves. This allows CrBr₃ to be used for electrical spin-injection [156]. Beyond electrical measurements, photoluminescence from CrBr₃ flakes has also been observed, in which the intensity of the emission in opposite circular polarizations corresponded with the magnetization of the film [157]. Furthermore, the magneto-photoluminescence changed with decreasing number of CrBr₃ layers, corresponding to a layer dependent response to external magnetic fields, as was also shown in CrI₃ [135, 140].

However, beyond these studies, CrBr₃ remains an ambiguous material. It is therefore of significant scientific interest to study in conjunction with monolayer TMDs in van der Waals heterostructures, as has recently been done very successfully for CrI₃ / WSe₂ [141]. Indeed, the coupling between CrBr₃ and any semiconductor material remains a completely unexplored topic, as so far only graphene has been combined with CrBr₃ in van der Waals heterostructures [156]. To this end, in this project, the magnetic proximity effects between ferromagnetic CrBr₃ and monolayer MoSe₂ are investigated. Coupling these two materials is expected to facilitate interactions between valley polarisation phenomena and spin based magnetic proximity effects [141]. Furthermore, the out of plane anisotropy of CrBr₃ ensures that the magnetic moments are oriented along the same *c*-axis as both the valley and spin magnetic moments in the TMD, helping to ensure a robust interaction. Indeed, the valley magnetic moment of monolayer TMDs is strictly out of plane owing to reduced 2D geometry

and crystal symmetries, resulting in a valley pseudospin insensitivity to in-plane B-fields [13]. In contrast to $\text{WSe}_2 / \text{CrI}_3$, discussed in the previous section, the $\text{MoSe}_2 / \text{CrBr}_3$ structure used here offers advantages of a far less studied material in CrBr_3 , along with a TMD which displays no valley polarisation in photoluminescence in the absence of external magnetic fields. As such, any detected polarisation degree may unambiguously be attributed to the influence of proximity to CrBr_3 . Furthermore, MoSe_2 has an optically bright exciton ground state, which gives much brighter emission than WSe_2 at low temperatures, and generally displays a less ambiguous PL spectrum, consisting normally of only exciton and trion emission, without a strong band of low energy emission of varying intensity. Studying MoSe_2 also avoids the inherent difficulties in measuring trion valley splitting which are present in WSe_2 as a result of the trion fine structure, as exemplified in Chapter 4. Therefore, the PL response of individual exciton and trion states in MoSe_2 are expected to be more amenable for gaining insight into the magnetic proximity effects in the $\text{MoSe}_2 / \text{CrBr}_3$ heterostructure.

The sample used in this investigation was fabricated by collaborators at the National Graphene Institute, Manchester. It consists of a monolayer of MoSe_2 placed directly on top of few tens of nm thickness CrBr_3 , with few-layer hBN encapsulating the structure on both sides, as shown in Fig. 6.3. The hBN encapsulation is necessary here owing to the extreme environmental sensitivity of exfoliated CrBr_3 , which degrades rapidly under exposure to air and moisture, in a reaction catalysed by light [158]. The extreme sensitivity of the material makes it necessary to perform the exfoliation and transfer entirely inside a glovebox with an inert argon atmosphere. The residue-free transfer techniques used during fabrication (see Section 3.1.4) ensure full contact between the MoSe_2 and CrBr_3 , such that interlayer charge transfer and proximity induced magnetic exchange effects are all uninhibited.

6.2.1 Hole doping in optically pumped $\text{MoSe}_2 / \text{CrBr}_3$ interfaces

To aid understanding of the electronic processes in the $\text{MoSe}_2 / \text{CrBr}_3$ van der Waals heterostructure, collaborators at QuantaLab, Iberian International Nanotechnology Laboratory, Portugal, performed density functional theory (DFT) calculations of the electronic band structure of monolayer CrBr_3 . These calculations take as a starting point a unit cell of the crystal, and model the electronic band structure (energy as a function of wavevector) along high symmetry lines of the Brillouin zone, thereby taking a slice or linecut of the overall 3-dimensional band structure. The calculations focus on the electron density associated with the various atomic orbitals which constitute the material, and an overall cumulative electron density distribution is built by addition of all the various electron wavefunctions [159]. The

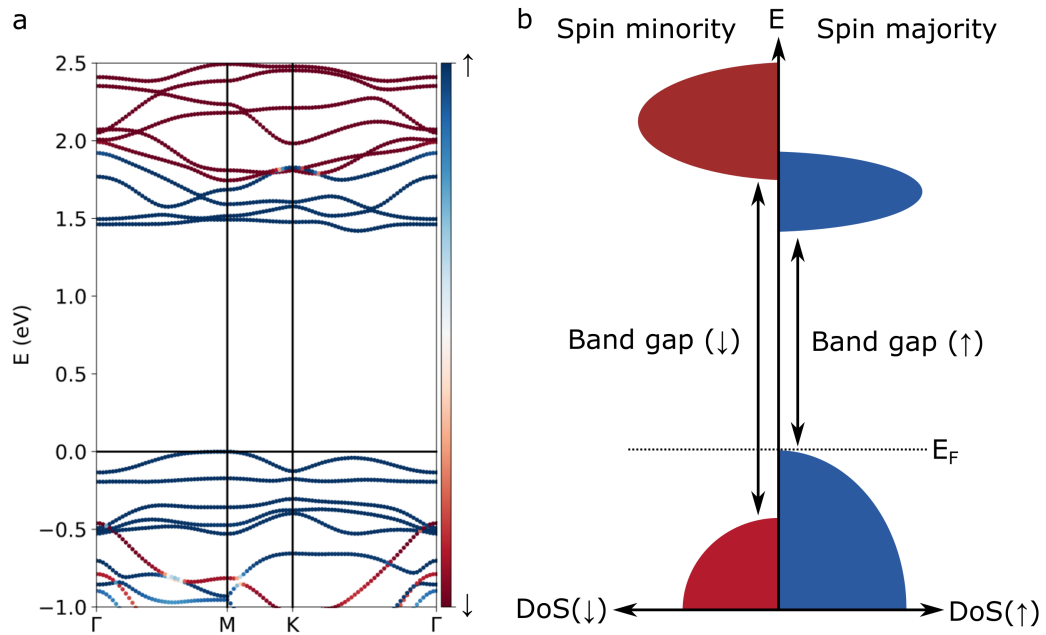


Fig. 6.4 (a) Electronic band structure of monolayer CrBr₃, calculated by density functional theory (DFT), with band projection on spin up or down. There is a band gap ~ 1.5 eV, and bands are spin polarised. (b) Generalised schematic of CrBr₃ spin polarised density of states. Below the Curie temperature, the ferromagnetic exchange interaction splits spin states of each band. Depending on the band energies relative to the Fermi level E_F , there will be an imbalance of electron spins, giving an overall magnetic moment, which manifests as magnetisation. In the figure, the spin majority is spin up, as there are more occupied spin up states (below E_F) than spin down. Application of an external magnetic field can flip the magnetisation, thereby reversing the majority and minority spin orientations between down and up or vice versa. *DFT calculations performed by Dr. Alejandro Molina-Sánchez.*

end result is a plot of the band structure of a material over several high symmetry points in momentum space, as shown in Fig. 6.4a which shows the spin projection of CrBr₃ bands.

In a ferromagnet, the degeneracy between density of states of opposite spin is lifted by the Heisenberg exchange interaction when the sample is cooled below the Curie temperature (Fig. 6.4b). In CrBr₃, the magnetic Cr³⁺ cations are not directly covalently bonded, but are separated by nonmagnetic Br⁻ anions, and so the energy band splitting arises from a superexchange interaction, via wavefunction overlap with an intermediary bromine lattice site [153]. The Cr-Br-Cr path changes angle by 90° (see Fig. 6.1b for a side view of the lattice of CrX₃, X = Cl, Br, I), for which the sign of the superexchange is ferromagnetic [155]. Following the Stoner model, the splitting of bands relative to the Fermi energy will result in an excess of electrons of one spin over the other, allowing definition of the *spin majority* and *spin minority* states [160]. Within a given magnetic domain, the magnetisation is given by the difference in total magnetic moments between spin majority and minority electrons [160]. In the case of CrBr₃, the Fermi energy lies in a gap between spin polarised bands, and so CrBr₃ is a ferromagnetic semiconductor, where the smallest band gap is between parallel electronic spin states, a feature leading to CrBr₃ being also suitable for spin filtering [161, 156].

From the DFT calculations, the electron affinity (energy between the bottom of the conduction band and the vacuum level, analogous to the ionisation energy in atomic physics) can be inferred, indicating a type II band alignment between CrBr₃ and MoSe₂, with the MoSe₂ conduction band (CB) minimum at higher energy than CrBr₃ (Fig. 6.5a). Therefore, it is expected that any excess electron doping inherent to the exfoliated MoSe₂ monolayer is eliminated upon contact with the CrBr₃ flake, as all excess electrons will occupy the empty CrBr₃ CB states at lower energy. Furthermore, any inherent excess hole doping of either layer is not expected to be present in their initial exfoliated conditions. As such, the MoSe₂ layer effectively becomes an intrinsic semiconductor, largely free of excess electrons or holes, before exposure to the pump laser.

Upon continuous wave laser excitation of the sample at 1.946 eV, ~ 300 meV above the MoSe₂ A-exciton resonance, photocarriers are generated in the MoSe₂ layer. Some of these hot electrons will scatter and relax into the lower energy CrBr₃ empty CB states, in a process which will leave resident holes in the MoSe₂ valence band (VB), trapped by the type II band alignment and unable to radiatively recombine due to the diminished MoSe₂ electron population. As such, the MoSe₂ layer becomes hole-doped (Fig. 6.5a). Strong Coulomb interactions in the 2D film cause electrons and holes to bind into neutral excitons, which in turn will interact with the resident holes to form positively charged Coulomb bound complexes known as trions [31, 50].

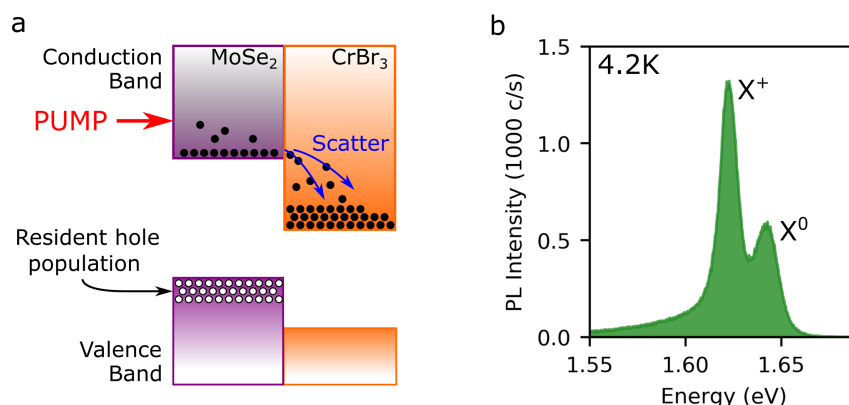


Fig. 6.5 (a) Schematic of the type II band alignment over the MoSe₂ / CrBr₃ heterojunction. Optically injected hot electrons in the MoSe₂ layer may scatter and relax into empty CrBr₃ conduction band states, in a process which generates a static hole doping of the MoSe₂ layer. (b) PL spectrum from the sample under continuous wave laser excitation at 1.946 eV and a sample temperature of 4.2 K. Neutral exciton (X⁰) and positive trion (X⁺) peaks are visible. The low PL intensity, by MoSe₂ standards, is due to reduced quantum yield associated with non-radiative decay of electrons over the heterojunction.

Unpolarised photoluminescence (PL) from the sample at 4.2 K reveals a spectrum characteristic of MoSe₂, in that there are two peaks separated by the trion binding energy ~ 30 meV [31, 32]. This, with consideration of the anticipated hole doping discussed above, leads to assignment of these peaks as intralayer MoSe₂ neutral exciton (X⁰) and positively charged trion (X⁺) (Fig. 6.5b) [31]. One major observation is that the overall PL intensity is very low compared to the usual response of exfoliated MoSe₂, which very reliably and reproducibly tends to emit around 1-2 orders of magnitude brighter PL than this sample under the same conditions and with the same measurement apparatus. Here, a laser power of 300 μ W is used, in the linear pumping regime. This low luminescence intensity is further indicative of interlayer charge transfer between the layers and associated reduced quantum yield, owing to efficient non-radiative loss of photocarriers into the CrBr₃ [162]. No evidence of PL from CrBr₃ itself is seen over the range between the laser energy and the limit of the detector sensitivity, ~ 1.14 eV (given by the band gap of silicon), possibly due to a combination of inefficient photoexcitation owing to low oscillator strength of interband absorption, and the expected loss of holes into MoSe₂. However, it should be noted that any photoexcitation in the CrBr₃ would simply add to the already present MoSe₂ resident hole population, and so would not fundamentally alter the interpretation of the system proposed in Fig. 6.5.

6.3 Polarisation resolved magneto-photoluminescence

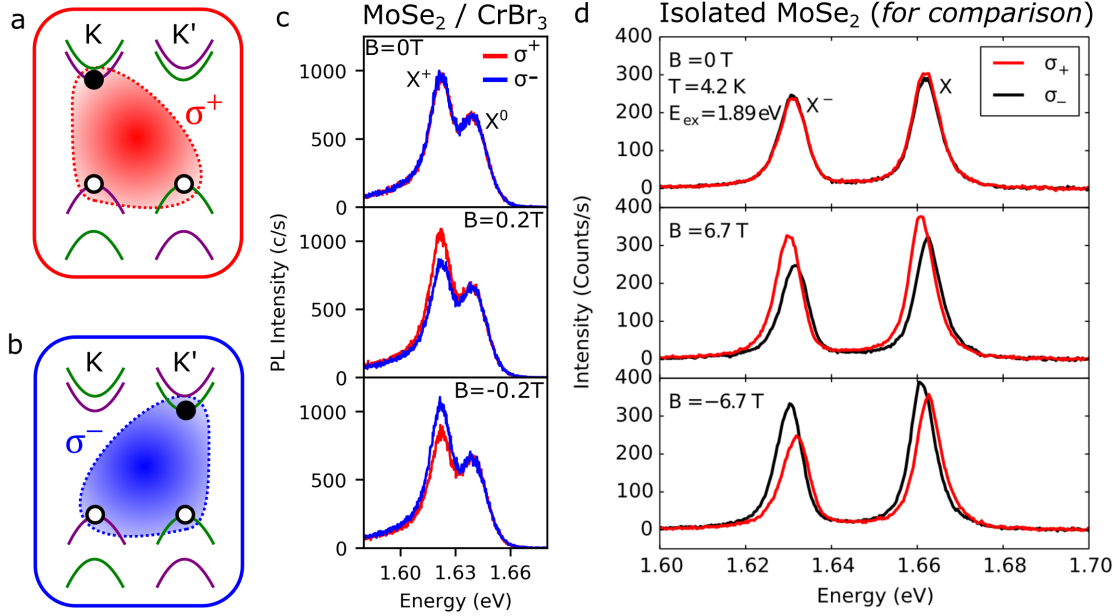


Fig. 6.6 (a,b) Schematic of the electron (solid circle) and hole (hollow circle) spin and valley configurations for the two ground state optically bright positively charged trions in MoSe₂, (a) K and (b) K', showing the helicity of the emitted photon. Purple (green) bands are electron spin up (down). (c) Circular polarisation resolved photoluminescence spectra from the MoSe₂ / CrBr₃ sample at zero, weak positive, and weak negative external B-field strengths, applied out of the sample plane. The peak ascribed to positive trion emission (X⁺) displays valley polarisation, while the neutral exciton (X⁰) does not. (d) Data from literature included for comparison to (c), showing the response of isolated MoSe₂ (i.e. without CrBr₃) to an external B-field. Here, the trion peak is negatively charged, owing to the lack of CrBr₃. Comparison to (c) reveals that the influence of CrBr₃ induces trion valley polarisation comparable to an effective Zeeman field of several Tesla, when only $B = \pm 200$ mT is applied. *Image from Ref. [51].*

As introduced in Chapter 2, the valley degree of freedom of carriers in monolayer MoSe₂ extends to excitons and trions, which may recombine in either the K or K' valley, thereby emitting a σ^+ or σ^- circularly polarised photon, owing to chiral optical selection rules [5, 11, 46]. Positively charged trions consist of an electron-hole pair in one valley, with an additional hole in the opposite valley (Fig 6.6a,b) [46, 31]. There are two intervalley X⁺ ground states, related by time reversal symmetry. This intervalley ground state is highly favoured over the intravalley trion configuration, for which the large ~ 200 meV spin-orbit coupling strength in the VB is prohibitive [46, 31, 10].

6.3 Polarisation resolved magneto-photoluminescence

In order to gain insight into the valley pseudospin dynamics in the sample, PL is detected in σ^+ and σ^- circular polarisations. In the absence of an external magnetic field, the σ^+ and σ^- PL spectra are identical at 4.2 K (Fig 6.6c), which is very consistent with known behaviour of monolayer MoSe₂, arising from ultrafast intervalley relaxation of exciton populations, on a timescale faster than the radiative lifetime, as discussed in Chapter 5.

Upon applying a very weak external magnetic field (B-field) perpendicular to the sample, of $B = 200$ mT, an intensity difference is observed in the trion peak, with σ^+ becoming brighter than σ^- . Any difference in the relative trion PL intensities is indicative of a population imbalance of resident holes between valleys, i.e. a static hole valley polarisation [46, 50]. This change in intensity is much stronger than would be expected purely from the valley Zeeman effect at 200 mT, which would be negligible. This is confirmed by the published MoSe₂ valley Zeeman response, reproduced in Fig 6.6d, which indicates that the valley polarisation induced by a B-field of several Tesla strength is comparable to that observed in this MoSe₂ / CrBr₃ sample at $B = 200$ mT, an order of magnitude difference [50, 51, 57]. Such a drastic response to the external B-field must arise from the influence of CrBr₃ on the MoSe₂ trion valley states. In stark contrast, the neutral exciton peak displays no such intensity differences, indicating some degree of insensitivity to the ferromagnet.

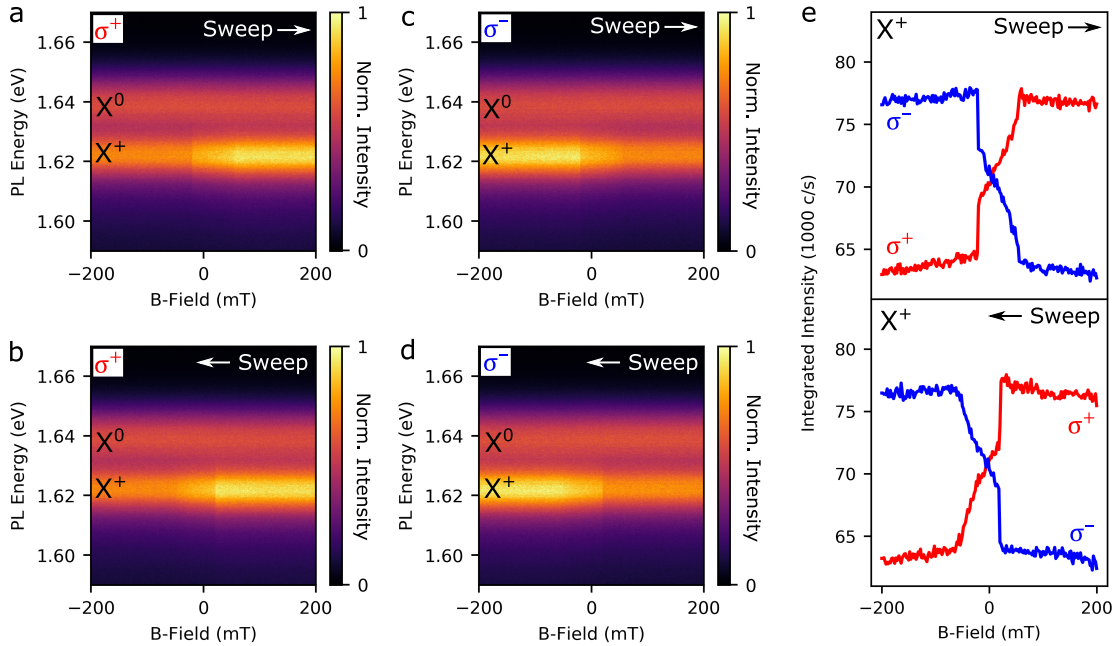


Fig. 6.7 (a-d) Colourmaps of normalised photoluminescence intensity in (a,b) σ^+ and (c,d) σ^- polarisation as a function of B-field while sweeping forwards (a,c) and backwards (b,d). (e) Polarisation resolved integrated PL intensity of the positive trion (X^+) peak in both forwards (upper panel) and backwards (lower panel) B-field sweep directions.

Next, polarisation resolved PL is acquired while sweeping the external field within the range $B = \pm 200$ mT, in both forward (negative to positive) and backward (positive to negative) sweep directions. Fig. 6.7 shows the resulting PL in both circular polarisations and both sweep directions, as a function of emitted photon energy and B-field strength. As can be seen, the trion peak transitions between brighter and dimmer states at opposite B-field strengths, while the exciton peak remains constant, in each polarisation. However, the trion intensity is not linear in B, rather there are sharp discontinuities visible in the data. For instance, sweeping forwards in σ^+ polarisation, the trion is observed to sharply increase in intensity at $B = -20$ mT, followed by a steady further increase, until the intensity reaches a plateau at $B \sim 50$ mT.

To elucidate the trion magneto-optical response, the integrated trion intensity in both circular polarisations is plotted, in both forwards and backwards B-field sweep directions, as shown in Fig. 6.7e. As can be seen, the trion intensities in opposite polarisations behave exactly symmetrically, such that when the intensity of one polarisation decreases the other increases by the same amount. In both sweep directions, the intensities invert as B passes through zero, indicating a clear reversal of trion valley populations when very small B-fields are applied. Looking closer at the very low field response, abrupt discontinuities in the trion intensities are visible at $B = -20$ mT (+20 mT) in the forward (backward) sweep directions. These discontinuities occur only when sweeping towards zero-field from a stronger absolute field strength, either positive or negative. After passing through $B = 0$, in both sweep directions, the intensities change in a more gradual manner until reaching their respective plateaus at $B \sim \pm 50$ mT. A specific response to the sweep direction which is symmetric about zero-field, such as this, is a hallmark of ferromagnetism, confirming the influence of CrBr₃ on the MoSe₂ trion valley states.

6.4 Valley dependent proximity effects

6.4.1 Valley polarisation switching

From the polarisation resolved intensities I_{σ^+} and I_{σ^-} , the degree of circular polarisation can be calculated as $\rho = (I_{\sigma^+} - I_{\sigma^-}) / (I_{\sigma^+} + I_{\sigma^-})$, as plotted in Fig. 6.8 for B-field sweep direction forwards and backwards, respectively. The strong trion intensity dependence on B-field, shown in Fig. 6.7, is manifested clearly in the trion polarisation degree, which switches from negative when $B < 0$ to positive when $B > 0$. There is also a transition zone at very low B-field, between the two polarised conditions. This data realises a valley polarisation switch with three states, negative/off/positive, with the application of mT B-fields allowing

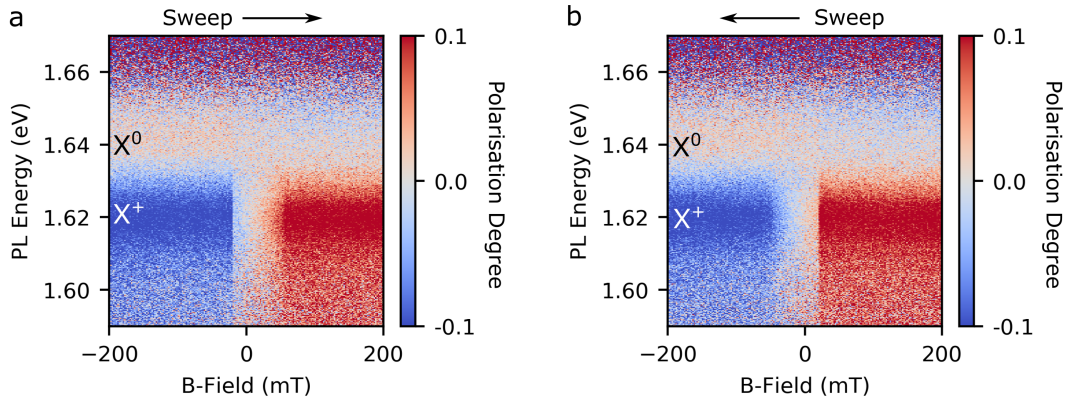


Fig. 6.8 (a,b) Colourmaps of photoluminescence circular polarisation degree, defined in the main text, in both forwards (a) and backwards (b) B-field sweep directions.

rapid and repeatable switching between the three states. Uniquely, the switching only occurs in the trion state, with the exciton (at ~ 1.64 eV) remaining constant at $\rho \sim 0$, effectively serving as a reference off state.

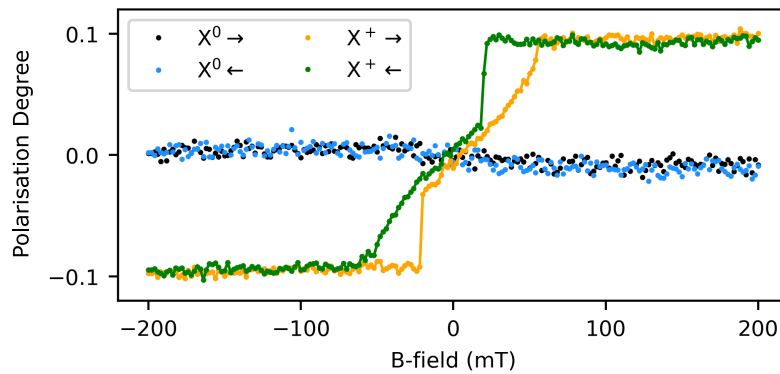


Fig. 6.9 Polarisation degree from integrated intensities of neutral (X^0) and positively charged (X^+) exciton photoluminescence, in both sweep directions. The trion peak displays switching between opposite valley polarisation states as B is reversed, while the neutral exciton polarisation remains constant.

Fig. 6.9 shows the polarisation degree of the X^0 and X^+ peaks calculated from integrated intensities over the range $B = \pm 200$ mT, in both sweep directions. Here, the contrasting response of the two excitonic species becomes abundantly clear, implying a highly trion state specific influence from the ferromagnet on the TMD. Furthermore, two lobes appear in the trion polarisation degree, defined by sharp discontinuities at $B = \pm 20$ mT; artefacts of the abrupt intensity changes seen in Fig. 6.7. The hysteresis-like form of these lobes, despite not

being centred on zero-field, strongly indicates a ferromagnetic response, originating in the CrBr_3 but manifesting through the MoSe_2 excitonic PL.

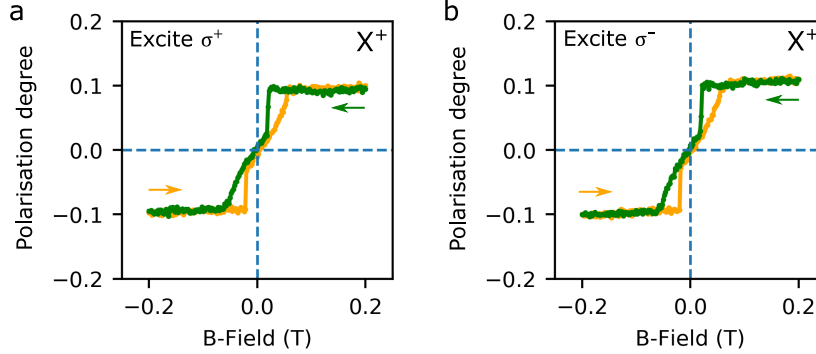


Fig. 6.10 (a,b) Comparison of trion polarisation degree in both sweep directions under (a) σ^+ or (b) σ^- polarised laser excitation. The result is almost identical, indicating an insensitivity to the polarisation state of the laser.

In these experiments, the laser is σ^+ circularly polarised, nominally addressing only the K valley. However, owing to the highly non-resonant pump energy used, alongside the sub-picosecond exciton valley depolarisation time characteristic of MoSe_2 , arising from long range electron-hole Coulomb exchange (see Chapter 5) [163, 43, 121], the laser polarisation has no influence on the final state PL polarisation. To confirm this, the experiment is repeated with σ^- laser polarisation, and an essentially identical result as that shown in Fig. 6.9 is measured, as shown in Fig. 6.10. This confirms that any valley polarisation signatures in the data arise purely from proximity effects with the CrBr_3 in combination with the external B-field, and are not due to selective valley initialisation from the laser.

6.4.2 Extraction of the effective Curie temperature

To further confirm the ferromagnetic origin of the enhanced trion valley polarisation, the B-field is fixed at $B = 200$ mT, thereby saturating the magnetisation, and the polarisation degree is measured as a function of sample temperature. As shown in Fig. 6.11, the polarisation degree tends to zero as the temperature reaches ~ 60 K. The Curie point of CrBr_3 has variously been reported between 33 K and 86 K [153, 164, 165, 156, 166, 167]; the result from this sample, $\sim 50 - 60$ K, lies within the previously reported range. It is possible that multiple factors influence the measured Curie temperature, such as flake thickness, stacking order, or crystal growth technique, possibly explaining the range of values so far reported from different samples.

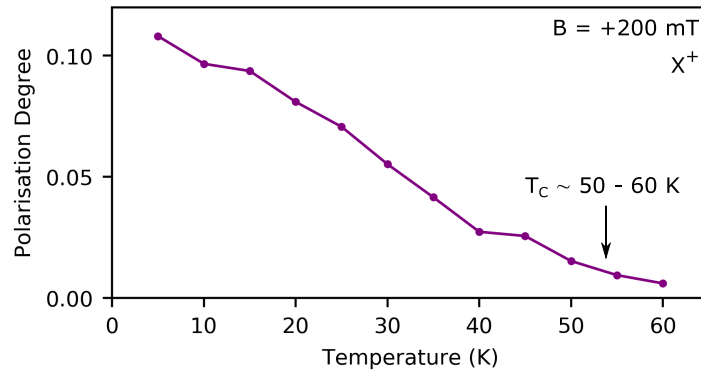


Fig. 6.11 Trion polarisation degree as a function of sample temperature, while heated under a fixed external B-field of strength 200 mT, corresponding to saturation of the CrBr_3 magnetisation parallel to B. The data indicates a Curie temperature of $\text{CrBr}_3 \sim 50 - 60$ K, although this cannot be relied upon to high accuracy considering that MoSe_2 trion photoluminescence itself depends strongly on temperature (as shown in Fig. 2.8c).

6.4.3 Lifting of valley degeneracy

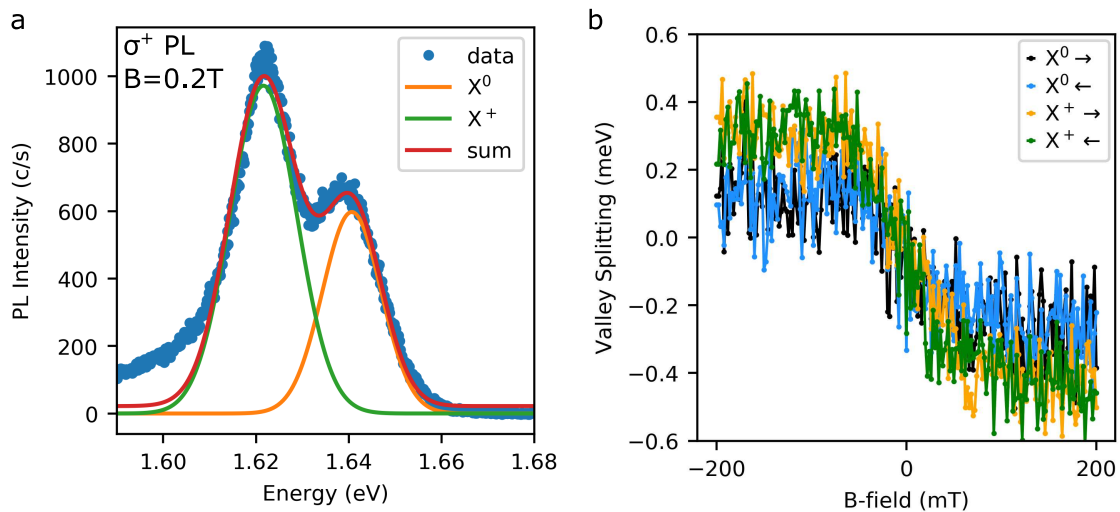


Fig. 6.12 (a) Example of fitting a σ^+ polarised photoluminescence spectrum from the sample to two Gaussian peak functions corresponding to the neutral and positively charged excitons. The red line is the sum of the Gaussian peaks, which closely reproduces the data over the excitonic emission region (the low energy tail of PL arises from defect associated emission and can lead to unpredictable lineshapes). (b) Valley splitting $E(\sigma^+) - E(\sigma^-)$ of exciton and trion as a function of B-field. Both excitonic states display switching of valley splitting upon reversal of the B-field.

By placing MoSe₂ on top of CrBr₃, it is expected that the TMD will experience a strong interfacial magnetic exchange field arising from the spin polarised orbitals of the uppermost CrBr₃ layer in the structure [168, 141, 145]. It is worth noting that this exchange field will be much stronger than the magnetic dipole field associated with the entire volume of the multi-layered CrBr₃ flake, which will be overall quite weak for such a small volume [168]. The exchange field, on the other hand, is very short range and can be several Tesla in strength within a few nm from the surface of a ferromagnet [168, 141]. In direct proximity to this field, the CB and VB valley states in MoSe₂ will shift in energy owing to the spin and valley magnetic moments (see Section 2.3.3), leading to a measurable valley splitting in photoluminescence, from which the exchange field can be estimated assuming a standard valley Zeeman g-factor of -4 [51, 169, 50, 57].

To extract the valley Zeeman splitting, $E(\sigma^+) - E(\sigma^-)$, Gaussian peak fitting of the polarisation resolved PL spectra was performed and the peak energies extracted. A valley Zeeman splitting is indeed observed, which is attributed to the short range magnetic exchange field from the topmost CrBr₃ layer. The strength of the valley splitting, ~ 0.3 meV, indicates the magnetic exchange field is ~ 1.3 T. Although the valley splitting appears to differ slightly between the exciton and trion, this is most likely an artefact of the fitting procedure, considering that the valley splitting is much smaller than the linewidths. A further consideration is that the strength of the exchange field experienced by the MoSe₂ will depend on the exact distance between layers over the van der Waals gap, along with the particular form of the adjacent atomic orbitals in the two layers [170].

6.4.4 High magnetic field regime

When applying a much stronger B-field, up to $B = \pm 8$ T, no other sharp discontinuities in ρ are observed, simply a gradual linear increase, nominally consistent with the intrinsic MoSe₂ response to an external B-field arising from the valley Zeeman effect (Fig. 6.13a) [50, 57]. This firmly suggests that the influence of the ferromagnet ceases at $B \sim \pm 50$ mT, which is taken to correspond to saturation of the CrBr₃ magnetisation parallel to the B-field. However, the gradients of the exciton and trion polarisation degrees are not equivalent, as should be the case for the valley Zeeman effect in MoSe₂ [50, 57]. Furthermore, the gradients of the exciton and trion valley splittings are also inequivalent (Fig. 6.13b), with the trion appearing to reach a maximum valley splitting upon CrBr₃ saturation, while the exciton shifts linearly with the field. This is also not consistent purely with the MoSe₂ valley Zeeman effect, in which a linear shift is generally observed in both exciton and trion emission [50, 57, 51, 169]. The origin of these inequivalent gradients at raised B-field strengths is as yet unknown and

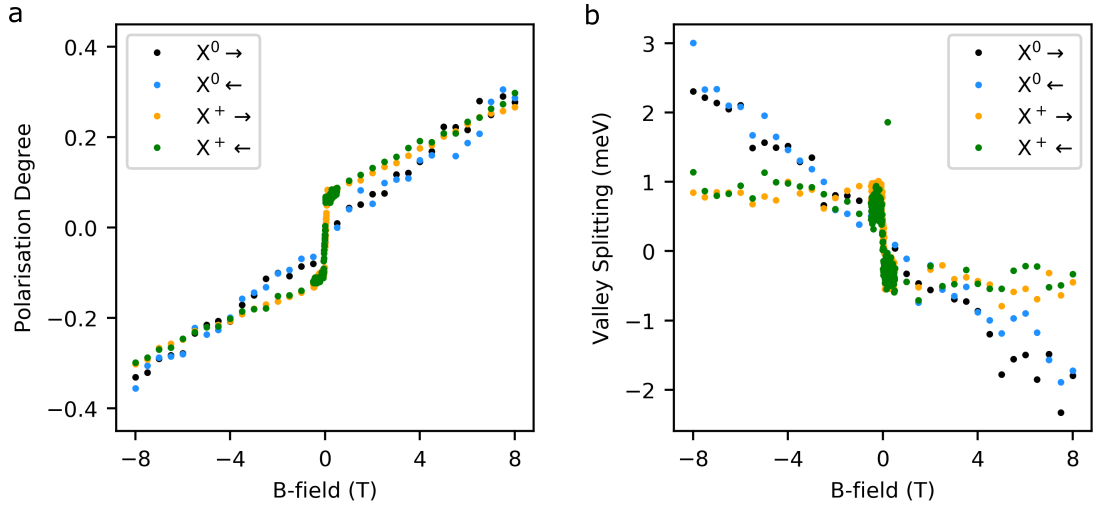


Fig. 6.13 (a) Polarisation degree and (b) valley splitting of exciton and trion photoluminescence peaks as a function of B-field in the strong magnetic field range up to $B = \pm 8$ T. For the trion, both low and high B-field ranges are shown.

should be investigated further, most obviously by repeating the measurements in additional samples to see if the effect is reproduced.

The absence of additional switching (i.e. sign reversal) or discontinuities and jumps in ρ or valley splitting at raised field strengths is in contrast to reported behaviour of CrI_3 , whereby such additional switching is attributed to layer dependent antiferromagnetic ordering, i.e. a vertically resolved domain structure in multi-layered samples [135, 141, 171]. In this situation, the top layer may reverse magnetisation at arbitrary non-zero field strengths to compensate domain alignment with the external B-field occurring in deeper layers within the flake. A measurement of the local magnetisation of the top CrI_3 layer, as is the case for a TMD monolayer in direct proximity owing to the short range of spin polarised wavefunction interactions, will therefore only reveal the magnetisation state of the top layer, and remain largely insensitive to the cumulative magnetisation of the multi-layered flake as a whole. The fact that no such arbitrary switching at raised field strengths is observed in this sample points to robust ferromagnetism in CrBr_3 , as opposed to the layer dependent antiferromagnetism of CrI_3 [135, 141, 171]. However, it is also the case that such layer dependent effects may have an overall thickness dependence, and so a systematic study of the magnetic properties of CrBr_3 flakes of varying thickness would be required before such a conclusion can be drawn with full confidence.

6.5 Spin dependent interlayer scattering

6.5.1 Heterobilayer electronic band structure

To interpret the data presented in Fig. 6.9, it may be separated into three distinct regimes. Firstly, there is negative saturation, when $B < -50$ mT, then positive saturation, when $B > 50$ mT, and thirdly the intermediate regime when $|B| < 50$ mT. Making the assumption that $|B| > 50$ mT corresponds to saturation of the CrBr_3 magnetisation, it follows that the complex form of the trion ρ vs B dependence in the intermediate regime is due to the CrBr_3 magnetisation dynamics responding to the external B -field. As such, if the trion polarisation degree can be understood in the saturation regimes, then it becomes possible to consider how these two regimes mix to produce the unusual behaviour seen in the intermediate regime (for instance, the hysteretic lobes in ρ).

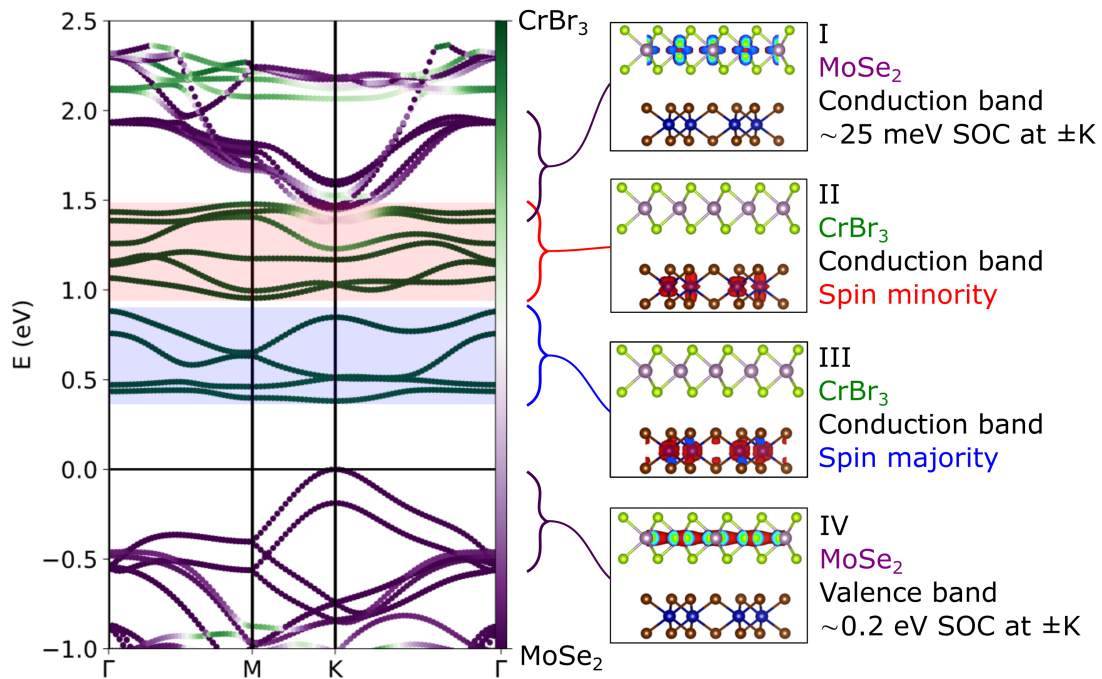


Fig. 6.14 DFT calculated electronic band structure of $\text{CrBr}_3 / \text{MoSe}_2$ heterobilayer, with bands colour-coded green or purple to indicate the CrBr_3 or MoSe_2 layer in which they are localised. The CrBr_3 spin majority (minority) bands are highlighted with blue (red). On the right, the corresponding atomic orbitals which constitute each series of bands are illustrated and labelled I-IV. They are all d -orbitals of the metal ions. There is indication of band hybridisation (white coloured bands) at the K point where the electron states are mixed between the layers, allowing highly efficient electron scattering over the van der Waals gap.

The plateaus in trion polarisation degree may be understood as saturation of the CrBr₃ magnetisation, uniformly aligned with the external B-field along the *c*-axis, essentially in a single magnetic domain state. Consequently, the CrBr₃ spin majority electrons will be aligned with B, while the spin minority electrons anti-aligned. From this starting point, the spin-resolved electronic band structure of a MoSe₂ / CrBr₃ heterobilayer is modelled, as shown in Fig. 6.14, using density functional theory (these calculations were performed by collaborators at INL, Portugal). The MoSe₂ CB and VB extrema can be seen at the K point (bands I and IV in Fig. 6.14), and part of the CrBr₃ CB is visible from 0.4 – 1.5 eV above the MoSe₂ VB maximum (bands II and III in Fig. 6.14). The ferromagnetic exchange interaction in CrBr₃ splits the CB into spin polarised bands, with the spin majority (minority) states at lower (higher) energy.

The DFT model confirms that the band alignment is type II, with the MoSe₂ CB and VB extrema both at higher energy than those of CrBr₃. Crucially, however, the calculation reveals a degeneracy between the MoSe₂ CB minimum at the K point (band I in Fig. 6.14), and the CrBr₃ spin minority CB (band II in Fig. 6.14). In this region of overlap, the electronic bands in the two materials hybridise, and can no longer be associated purely with the TMD or ferromagnet. Electrons in the hybridised CB therefore are not localised in either layer, and may scatter between CB states of either material completely elastically using the hybridised bands as an efficient bridge. Furthermore, around the hybridisation energy the CrBr₃ CB is characterised by very flat bands, associated with a high density of states, and so it is expected that electrons will preferentially leave the MoSe₂ CB and occupy the CrBr₃ CB. Crucially, the band hybridisation is only present for one spin character, owing to the ferromagnetic spin polarisation of CrBr₃ bands. Therefore, only MoSe₂ electrons with spin parallel to the spin minority band are in a hybridised state.

6.5.2 Valley selective non-radiative decay channel

The spin-valley locking effect inherent to MoSe₂ ensures that the spin-selective band hybridisation extends to also include valley pseudospin. As such, the band hybridisation constitutes an additional non-radiative decay channel for electrons in one MoSe₂ CB valley only, absent for electrons with opposite spin and valley index. It is important to note that this consideration involves only the lowest energy MoSe₂ CB spin subbands, which are involved in radiative recombination for the A exciton and A trion [128]. Indeed, there should be some hybridisation in both valleys, albeit at different energies, owing to the spin-orbit coupling of the MoSe₂ CB. However, the interlayer scattering of electrons is expected to be more dominant in the lowest energy CB subbands, as scattering in the higher energy bands will only be from hot electrons which are in the process of relaxing, whereas electrons will

accumulate in the bottom subbands and therefore have a longer window of time in which to scatter into the CrBr₃.

Given that the spin orientation of the conduction and valence states in CrBr₃ may be reversed by changing the sign of the weak perpendicular external B-field, the band hybridisation may be considered as spin-selective, as the band II reverses spin. Consequently, the efficient relaxation pathways for spin-valley polarised electrons may also be controlled via the B-field orientation. However, electrons are likely to scatter from the MoSe₂ CB to the CrBr₃ CB regardless of spin, as evidenced by the overall much weaker PL intensity from this sample than typical exfoliated MoSe₂, in both circular polarisations. This is supported by the DFT calculations, which show CrBr₃ bands of both spin orientations (bands II and III) lying at lower energy than the MoSe₂ K-point (band I), suggesting relaxation is possible from both MoSe₂ valleys without any spin flip required. However, the band hybridisation will ensure that the relaxation is significantly more efficient and rapid from one valley over the other. Additionally, electron scattering from MoSe₂ band I into the CrBr₃ band III will inevitably be slower than into band II, regardless of any hybridisation, owing to the large energy gap (~ 500 meV) between the MoSe₂ K-point and the uppermost spin majority states.

The scheme of valley dependent interlayer electron transfer is presented in Fig. 6.15a and c for the two situations of opposite magnetisation of CrBr₃. Here, any scattering of optically excited electrons from MoSe₂ to CrBr₃ generates a resident hole population in the MoSe₂ VB. The spin-selective band hybridisation ensures that a valley polarisation of holes is generated, as a result of faster electron loss from one CB valley, combined with the long valley lifetime characteristic of holes in monolayer TMDs (approaching 1 ns) [14, 172]. A larger population of resident holes in one valley will lead to brighter trion PL from the opposite valley, owing to the intervalley X^+ ground state, and considering that the intensity of trion PL is a reflection of excess charge density [31]. In this way, the magnetisation of CrBr₃ is directly linked to the polarisation resolved PL intensity of positive trions in MoSe₂, as shown in Fig. 6.7. In essence, the specific form of the interlayer band alignment in this heterostructure directly leads to generation of a static hole valley polarisation in optically pumped MoSe₂, which is reflected in the trion ρ plotted in Fig. 6.9 when $|B| > 50$ mT. If the pumping is ceased, the hole valley polarisation is expected to decay in line with the reported hole valley lifetime in MoSe₂ $\sim 500 - 700$ ps [172].

The attribution of spin selective band hybridisation as giving rise to the robust trion polarisation degree is confirmed when the exciton and trion polarisation resolved PL linewidths are considered, as plotted in Fig. 6.15b. The trion linewidth closely follows the polarisation resolved intensity switching behaviour seen in Fig. 6.7, while the exciton linewidth remains constant. The PL linewidth of an excitonic transition is comprised of homogeneous and

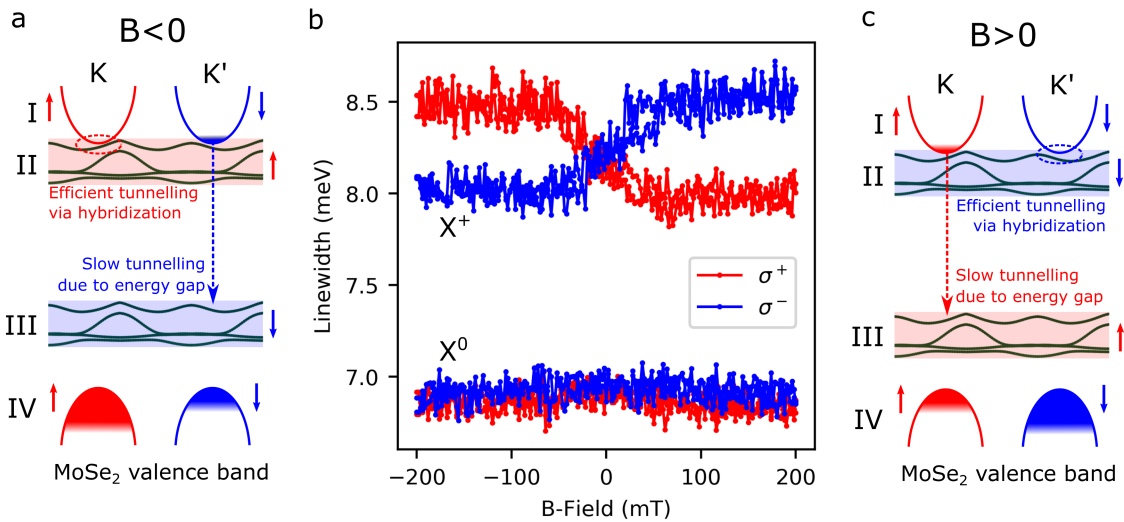


Fig. 6.15 (a) Schematic of excess hole doping in the valence band K valley (band IV in Fig. 6.14) owing to spin-selective band hybridisation allowing electrons to efficiently scatter from the K valley of MoSe₂ (band I in Fig. 6.14) into the CrBr₃ spin minority band (band II in Fig. 6.14). Interlayer tunnelling of electrons from the K' valley into the CrBr₃ spin majority band (band III in Fig. 6.14) is much slower owing to the ~ 500 meV energy gap. In this situation, the B-field is positive (antiparallel to the spin minority), and the resulting PL is brighter from positive trions emitting in σ^- polarisation, as they bind to holes in the K valley. (b) Photoluminescence linewidths of exciton and trion, extracted from Gaussian peak fitting. The trion displays switching of linewidth between broader and narrower regimes, while the exciton linewidth remains constant, indicating a trion specific interaction with the CrBr₃. (c) As (a), but for the case of band hybridisation in the K' valley, which leads to excess hole doping in the K' valley, in turn leading to a greater population of positive trions emitting in σ^+ polarisation. The situations shown in (a) and (c) may be selected by reversing the external B-field, allowing control of the spin-selective band hybridisation and engineering of the valley relaxation dynamics.

inhomogeneous contributions. The homogeneous part is directly related to the lifetime of the emitter, comprising both radiative and non-radiative processes [173, 52, 174]. Therefore, a broader linewidth is suggestive of an additional decay channel shortening the lifetime of the trion state, which is attributed here to efficient electron scattering into CrBr_3 via the hybridised bands. As such, a reversal of magnetisation leads to switching of the hybridisation between opposite valleys, and so the trion linewidth switches between broader and narrower values to reflect the altered carrier relaxation dynamics [175, 141]. Although the measured linewidths of the exciton and trion from this sample are inhomogeneously broadened (the homogeneous linewidth of an exciton PL peak in monolayer TMDs is around 1-2 meV [42]), the clear reversal of σ^+ and σ^- trion linewidths indicates a change in the lifetime, arising from proximity with CrBr_3 . This argument assumes that the inhomogeneous linewidth, arising from scattering with lattice defects and phonons, does not depend on B . An estimate of the upper bound for the timescale of the additional decay channel can be inferred from the difference in σ^+ and σ^- trion linewidths when $|B| > 50$ mT as $\hbar/\Delta_{LW} \sim 1.3$ ps, although it may be much faster.

Consideration of the PL linewidths helps to shed light on the apparent insensitivity of the neutral exciton peak to the magnetisation dynamics, a very clear indication of the PL measurements. The radiative lifetime of the exciton and trion in MoSe_2 have been reported to be only a few ps and > 10 ps, respectively [107, 47, 176]. Although these measurements were considering the negative rather than positive trion, it is safe to assume a significantly longer radiative lifetime of the positive trion than the neutral exciton, owing to the reduced oscillator strength. Considering that the approximate timescale of the valley selective additional decay channel is up to ~ 1 ps, of the same order as the exciton radiative lifetime, it is likely that the insensitivity of the exciton emission to the B -field is due to ultrafast recombination, before feeling the influence of carrier population imbalances. The trion, on the other hand, is both highly sensitive to any resident carrier populations, and has a lifetime an order of magnitude longer than the interlayer scattering time. This firmly suggests that the origin of the PL polarisation lies in the valley selective interlayer charge transfer and associated resident hole valley polarisation.

6.6 Insight into ferromagnetic domain dynamics in CrBr_3

The above sections and associated DFT models offer explanations as to why the trion polarisation degree acts as a switch between positive and negative plateaus depending on the magnetic saturation state of the CrBr_3 . However, they offer few clues about the trion ρ vs B dependence in the regime of $|B| < 50$ mT. Here, the trion polarisation degree moves between

positive and negative values along a path which depends upon the sweep direction, leading to the formation of hysteretic loops. As such, it must have its origins in ferromagnetism. Therefore, to complete the picture, the magnetisation dynamics of CrBr₃ in response to the external B-field must be considered.

6.6.1 Perpendicular magnetocrystalline anisotropy

CrBr₃ is an Ising-type ferromagnet with perpendicular magnetocrystalline anisotropy [153]. As such, the ferromagnetic domains will have magnetisation (M) pointing either up or down along the c -axis, and in the absence of an external B-field, will tend to form a lateral in-plane domain pattern with adjacent domains having opposite M , arranged in such a way as to minimise the overall stray field associated energy [177]. Upon the application of a B-field parallel to the c -axis, domains with M parallel to B will grow, at the expense of domains with M antiparallel to B , which will shrink. This growing and shrinking occurs via lateral domain wall motion, where a domain wall may be thought of as a border region of finite width over which the electron spin states gradually transition from pointing up to pointing down, or vice versa. At the saturation field, B_{sat} , the system is uniformly magnetised parallel to B , and may be considered as a single domain state. In this sample, saturation occurs when B reaches ± 50 mT (as can be seen in Fig. 6.9).

In these experiments, PL measurements are taken from a laser spot of FWHM diameter $2.4 \mu\text{m}$. Consequently, the measurement takes an average of proximity effects within this area, giving an averaged PL spectrum. Considering that the influence of CrBr₃ appears to cease when $|B| > 50$ mT, this is expected to correspond to single domain behaviour within the laser spot area. When $|B| < 50$ mT, there is a mixture of upwards and downwards oriented domains within the laser spot, with their relative areas determining the average magnetisation, and consequently, the measured ρ of X^+ .

6.6.2 Spontaneous magnetic nucleation

The unusual shape of the ρ vs B traces in Fig. 6.9, when treated as a measure of M vs B , as shown schematically in Fig. 6.16, is highly characteristic of a spontaneous magnetic nucleation process. This is a known feature of thin ferromagnetic films with perpendicular anisotropy [177], whereby the saturation state persists even as the strength of B is reduced below B_{sat} , due to existing in a metastable state. Here, there is an energy penalty associated with domain wall formation, and so the magnet remains saturated, trapped in a local potential minimum. Eventually, at a certain nucleation field strength, a domain with magnetisation antiparallel to B will appear, and will rapidly expand, leading to a sudden drop in overall M ,

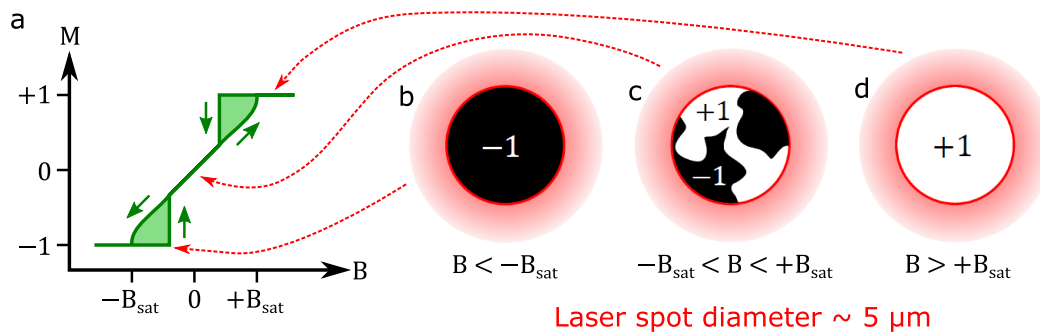


Fig. 6.16 (a) Schematic of magnetisation (M) vs B curve of the CrBr_3 flake in this sample, as indicated by the trion polarisation degree in Fig. 6.9. B_{sat} is the saturation B -field. (b-d) Illustrations of the domain alignment of CrBr_3 within the laser spot area, where ± 1 indicates a domain with magnetisation pointing directly up or down out of the plane, respectively. The strong perpendicular anisotropy of CrBr_3 ensures that every domain must have magnetisation parallel to the c -axis. The three regimes are (b) negative saturation, (c) mixed domain state within the laser spot, and (d) positive saturation. Red arrows indicate position on the schematic of magnetisation curve measured by the laser.

as is observed. This occurs at the point when the energy associated with the demagnetising field (stray field arising around the ferromagnet due to the magnetisation) becomes larger than the energy required to form a domain wall, and so domain wall formation becomes energetically favourable. In Fig. 6.9, this energy balance is tipped at $B = \pm 20$ mT. After the nucleation event, the magnetisation should become equal to its value at the same B -field strength in the opposite sweep direction, as is indeed the case in Fig. 6.9. This is indicative of freely moving domain walls, whereby adjacent domains grow and shrink unimpeded, in response to the external field. As B passes through zero, the mixed domain state evolves easily via domain wall motion. If there is substantial disorder in the lattice, domain walls can become pinned, which leads to the introduction of zero-field hysteresis [177]. The fact that negligible coercivity is observed in this sample points to a relatively defect-free crystal structure in CrBr_3 .

For the case of a much smaller laser spot size, it is possible that the magnetic length scale may exceed the spot diameter and the measurement will only observe a single domain responding to the B -field. In this case, the magnetisation will flip between ± 1 without observing any gradual change in M . The flip may occur either side of $B = 0$, depending on the laser spot position on the sample, considering that it may or may not happen to probe a nucleating domain. This zero-field hysteresis and associated coercivity is reminiscent of measurements performed on CrI_3 (Fig. 6.2) [141], and highlights an unusual source of uncertainty when measuring the magnetic properties of 2D magnetic materials using a relatively local optical technique.

6.7 Summary

In conclusion, the significant potential of van der Waals heterostructures to engineer the band structures of emergent spin-valleytronic devices is demonstrated, which may have applications ranging from new data memories to nanoscale sensing. Clear proximity induced switching of hole valley polarisation in a MoSe₂ monolayer is observed, attributed to a complex interplay between carrier relaxation dynamics, radiative recombination timescales and spin-selective band hybridisation. Furthermore, starkly contrasting proximity effects between neutral and charged exciton states are seen, and high B-field measurements imply that CrBr₃ does not display layer dependent antiferromagnetism inherent to CrI₃ [135, 141, 171], or indeed the easy-plane anisotropy of CrCl₃ [178, 179]. This completes the set of easily stackable metal trihalides with complementary magnetic properties (Fig. 6.17), constituting an ideal basis for development of van der Waals spintronic devices.

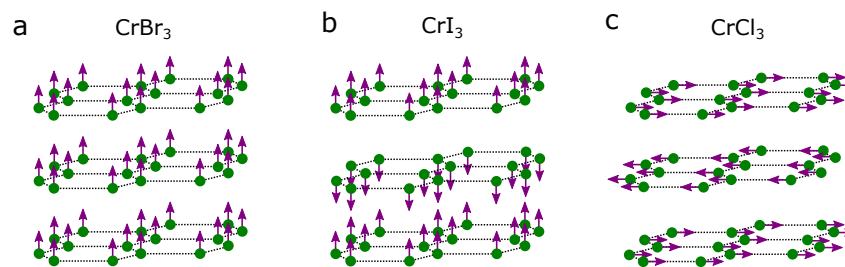


Fig. 6.17 Characteristic magnetic anisotropy and ordering in multi-layered (a) CrBr₃, which is an Ising-type ferromagnet with out of plane anisotropy and appears to have ferromagnetic layer coupling, (b) CrI₃, with Ising-type ferromagnetism within each monolayer, but a tendency for antiferromagnetic ordering between layers, and (c) CrCl₃, which also has intralayer ferromagnetic order and interlayer antiferromagnetism, but unlike CrI₃ it has in-plane shape anisotropy, giving an easy-plane. This most likely arises from the expected out of plane magnetocrystalline anisotropy being weak. These figures represent the magnetic order upon zero-field cooling below T_C .

The measurements of polarisation resolved trion photoluminescence indicate thin CrBr₃ to have perpendicular magnetic anisotropy and a micron-scale typical lateral domain size, possibly even a maze or labyrinthine domain arrangement. Easily switchable ferromagnets with perpendicular anisotropy have direct applications in magnetic memory technology utilising spin-transfer torque, which is highly amenable to scaling down for ultra-high density memories [180–182]. Recent gains in the electrical field control of magnetisation in CrI₃ may now be incorporated with the results of this work, to fully realise and understand the combined electrical, optical and magnetic interactions within ferromagnet-semiconductor nanostructures, with a view to the creation of functional optically or electrically switchable valleytronic devices.

Chapter 7

Conclusion

7.1 Summary of findings

The trion valley Zeeman effect in WSe₂

In Chapter 4, the response of the trion fine structure in monolayer WSe₂ to strong external magnetic fields was studied. The four ground state trion valley configurations, characterised by a zero-field fine structure splitting owing to short range electron-hole Coulomb exchange, were observed to have a strong temperature dependence, whereby heating the sample thermally populates the higher energy triplet trions.

This study uncovers the complexities of the trion valley Zeeman effect in monolayer WSe₂, demonstrating that the trion energy splitting in PL does not reflect the underlying valley Zeeman splitting of the initial state. Instead, the process of trion radiative recombination itself modifies the emitted photon energy, via electron recoil to valley polarised conduction band states, having the effect of enhancing the singlet-singlet splitting, and diminishing the triplet-triplet splitting. On top of this asymmetry, the action of a third process is observed, also associated with the electron recoil, attributed to Landau level quantization of both initial and final states.

Each of the four trion fine structure valley configurations are seen to display inequivalent rates of field-dependent spectral shift, which is incompatible with the valley Zeeman framework reported for neutral excitons. A true valley Zeeman splitting of $(-7.9 \pm 0.1)\mu_B B$ is extracted for all trion states, which may be measured only by consideration of both singlet and triplet trions. The deviation of this value from the known atomic orbital contribution of $\sim -4\mu_B B$ is attributed to a strong Berry curvature associated magnetic moment unique to WSe₂ trions. However, this true trion valley Zeeman splitting is observed to be masked by energetic recoil processes of the additional electron, which modify the measured trion energy

Conclusion

shifts in low temperature magneto-PL studies and are likely to depend heavily on external factors such as doping level, which vary from sample to sample.

Exciton valley dynamics in the strong light-matter coupling regime

Chapter 5 presented experiments involving the incorporation of monolayer MoSe₂ and WSe₂ into energy-tunable zero dimensional optical microcavities, which allowed the formation of exciton-polaritons. These composite quasiparticles are part-light part-matter, resulting in modifications to the state lifetimes and valley depolarisation times.

This work presented both unambiguous observation of valley polarised exciton-polaritons in monolayer MoSe₂, along with robust valley coherence of polaritons in monolayer WSe₂. In both materials, the degrees of optical polarisation in photoluminescence far exceed the values obtainable in bare, uncoupled monolayers, owing to cavity modified valley pseudospin relaxation dynamics. A theoretical model based on dynamical rate equations which incorporate energy, momentum, and pseudospin relaxation is presented, which accurately reproduces the MoSe₂ polariton circular polarisation degree, confirming that extremely efficient pseudospin relaxation occurring at high exciton wavevectors is responsible for low polarisation degrees in emission. Furthermore, coherent manipulation of the exciton-polariton valley pseudospin vector is demonstrated, arising from precession of the vector about the Bloch sphere equator under the action of an applied strong magnetic field.

The results presented in this chapter unveil the complex valley pseudospin relaxation dynamics of excitons in monolayer TMDs, and demonstrate how the use of optical microcavities allow the efficient depolarisation timescales inherent to these materials to be overcome, by offering highly protected polariton states for the excitons to occupy, in which their pseudospin vector remains well defined over enhanced timescales. The implications of this work include the possibility for study of valley dependent non-linear polariton behaviour, such as condensation and superfluidity, or the implementation of polaritonic circuit elements for valley pseudospin based information processing at high speeds.

Valley physics in semiconductor-ferromagnet van der Waals heterostructures

Chapter 6 discussed the valley effects which arise when a monolayer of MoSe₂ is placed in direct proximity to a layered van der Waals ferromagnetic material, CrBr₃. The resulting heterostructure was found to display a hybridised and spin-polarised band structure, which resulted in efficient valley dependent carrier hopping between the layers, leading to non-zero valley polarisation in MoSe₂ photoluminescence despite only very weak, milliTesla range magnetic fields being applied.

The results indicate the significant potential of van der Waals heterostructures to engineer the band structures of emergent spin-valleytronic devices, which may have applications ranging from new data memories to nanoscale sensing. Clear proximity induced switching of hole valley polarisation in a MoSe₂ monolayer is observed, attributed to a complex interplay between carrier relaxation dynamics, radiative recombination timescales and spin-selective band hybridisation. Furthermore, starkly contrasting proximity effects between neutral and charged exciton states are seen, explained by the discrepancy in radiative lifetimes.

The measurements of polarisation resolved trion photoluminescence indicate thin CrBr₃ to have perpendicular magnetic anisotropy and a micron-scale typical lateral domain size, possibly even a maze or labyrinthine domain arrangement. Easily switchable ferromagnets with perpendicular anisotropy have direct applications in magnetic memory technology utilising spin-transfer torque, which is highly amenable to scaling down for ultra-high density memories [180–182]. Recent gains in the electrical field control of magnetisation in CrI₃ may now be incorporated with the results of this work, to fully realise and understand the combined electrical, optical and magnetic interactions within ferromagnet-semiconductor nanostructures, with a view to the creation of functional optically or electrically switchable valleytronic devices.

7.2 Outlook

7.2.1 Optical routing of exciton-polariton valley pseudospin

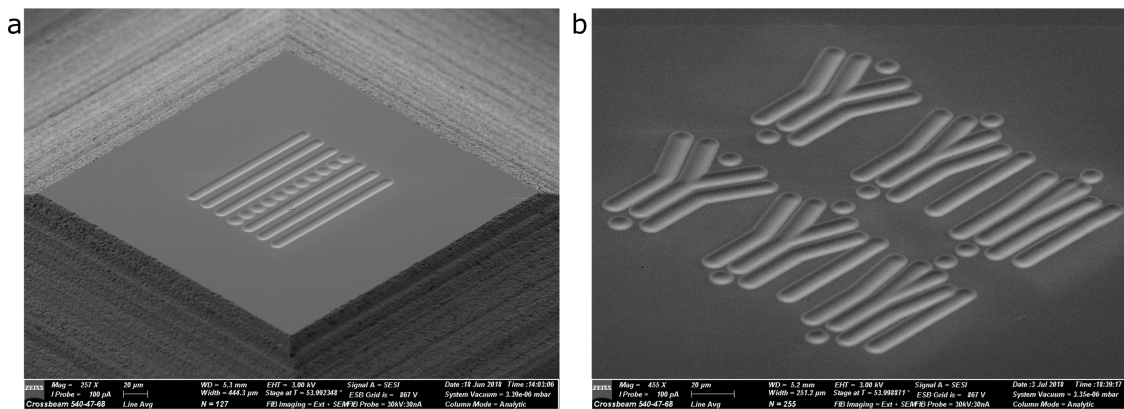


Fig. 7.1 Scanning electron microscope images of (a) Focused ion beam milled waveguides in open cavity top-plinth structures (see Chapter 3). (b) Y-shaped waveguide routers for creating valley polarised polariton currents *Image credit: Aurelien Trichet.*

Conclusion

Beyond control of the exciton valley pseudospin as demonstrated in this thesis, another key milestone towards implementation of opto-valleytronics would be long range valley transport between distant systems. Excitons are charge neutral and are free to move through the lattice, and so are nominally suitable for valley transport. Indeed, exciton integrated circuits have been demonstrated in other material systems [183]. However, in TMDs, their propagation length is severely limited by their short lifetime, as uncovered in chapter 5. A potential way around this would be to use exciton-polaritons to transport the valley pseudospin, considering they retain robust polarisation as demonstrated earlier. They also have a very low effective mass and high propagation speed, owing to their photonic component.

To this end, a variety of novel cavity DBR plinth designs have been fabricated (by collaborators at the University of Oxford), as shown in Fig. 7.1, in contrast to the circular concave plinth designs used in this thesis in Chapter 5. These include linear waveguides, which are essentially 1-dimensional cavities, restricting the polariton motion along the axis of the cavity. Such an experiment would therefore involve testing the diffusion of polaritons from a pump source, or investigating how the polaritons could be accelerated along the waveguide, for instance by pumping at an angle (to inject in-plane momentum) or by tilting the cavity mirrors to create a wedge shaped cavity with an energy gradient along the waveguide.

In Fig. 7.1b, a series of Y-shaped cavity waveguides are shown. These may act as polariton valley routers, whereby polaritons created at the bottom of the Y travel to the junction, and then preferentially move down one arm or the other owing to the the finite Berry curvature of the exciton component, which induces a transverse velocity with sign depending on the polariton valley index. Essentially this represents a polariton valley Hall effect, coupled to a router, constituting the proof of principle for polariton valley circuits.

7.2.2 Ferromagnetic proximity coupling to TMD exciton-polaritons

An interesting avenue to explore would be the incorporation of ferromagnetic layered materials inside optical microcavities. This effectively combines the results of Chapters 5 and 6, where microcavities and ferromagnets were both demonstrated to enhance the valley polarisation of monolayer MoSe₂. Quite possibly, in combination their effects could multiply to produce near unity valley polarised polariton populations, arising due to lifting of degeneracy between the opposite valley exciton resonances. This may allow easy switching of the entire polariton population pseudospin via milliTesla magnetic fields.

Another related prospect is the incorporation of electrically pumped TMD-ferromagnet heterostructures into microcavities, whereby current injection through the ferromagnet may act as a spin pump, leading to electroluminescence in only one MoSe₂ valley. The microcavity

could operate in the weak coupling regime, vastly enhancing the radiative rate of emission, and resulting in electrically pumped rapidly switchable σ^+ or σ^- polarised emission.

7.2.3 Enhanced valley splitting in MoSe₂ on EuS substrates via interfacial magnetic exchange field

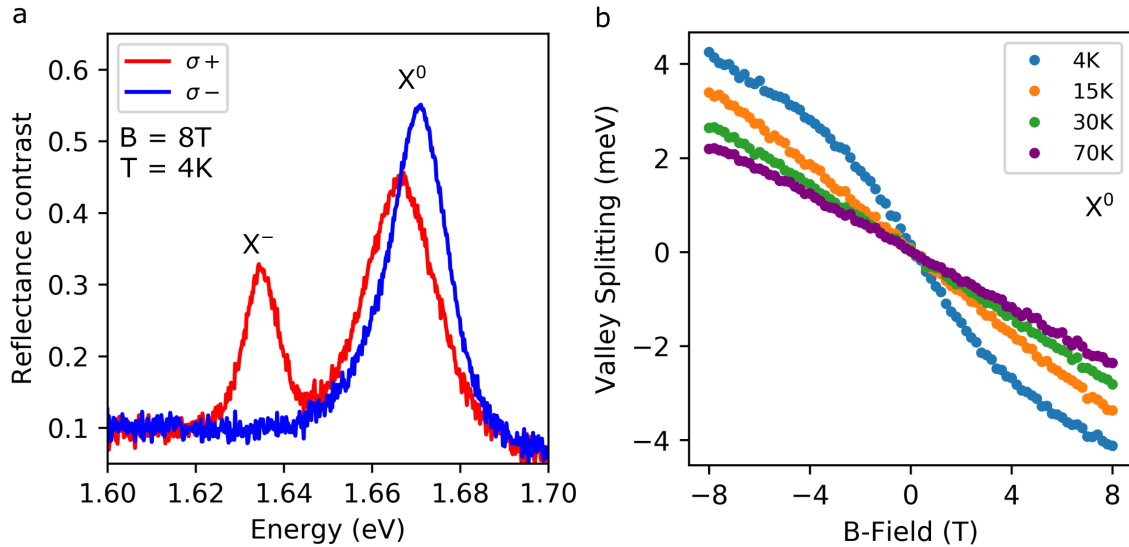


Fig. 7.2 (a) Reflectance contrast spectrum of MoSe₂ on a europium sulphide 10nm film substrate under an external magnetic field of $B = 8$ T. The neutral exciton absorption displays a strong valley splitting between σ^+ and σ^- , while the trion absorption is 100% valley polarised. (b) Valley Zeeman splitting of the neutral exciton absorption from MoSe₂ on EuS as a function of external B-field strength. Below the Curie temperature of EuS, ~ 17 K, the MoSe₂ valley splitting is strongly enhanced by the exchange field, as indicated by the non-linear response, mimicking the EuS magnetisation.

In contrast to fabrication of elaborate van der Waals heterostructures combining monolayer TMDs with layered ferromagnets, as was demonstrated in Chapter 6, an easy alternative is to simply polymer stamp a TMD monolayer onto a non-van der Waals ferromagnetic substrate. To this end, preliminary experiments have been performed on a sample consisting of monolayer MoSe₂ stamped onto a 10nm thin film of europium sulphide (EuS), a ferromagnetic insulator with a rock-salt crystal structure, grown by electron beam deposition by collaborators at the University of Tokyo. The reflectance contrast spectrum from the sample ($(R_0 - R)/R_0$, where R_0 and R are the reflectance of the substrate and monolayer, respectively) displays two absorption resonances ascribed to neutral and negatively charged exciton absorption (Fig. 7.2a). The EuS layer strongly modifies the magneto-optical response

Conclusion

of the MoSe₂ excitons, leading to a 100% degree of circular polarisation of the trion absorption under an external magnetic field of $B = 8$ T, indicating complete spin polarisation of conduction band electrons [184]. Furthermore, the valley splitting of the neutral exciton is strongly enhanced by the EuS short range interfacial magnetic exchange field, and follows a non-linear curve mimicking the magnetisation response of EuS to the applied field (Fig. 7.2b) [168]. The valley splitting is several times stronger than the valley Zeeman effect for applied B-fields $\sim 1 - 2$ T, indicating that EuS serves to strongly amplify the external field. The ferromagnetic origin of the enhanced valley splitting is confirmed by heating the sample above the Curie temperature of EuS, ~ 17 K, at which point the conventional valley Zeeman splitting of MoSe₂ is regained [168]. Coupling monolayer TMDs with non-layered materials in this way plays to the strengths of 2D materials, in that their van der Waals forces allow them to be arbitrarily transferred onto a variety of substrates, creating hybrid structures potentially associated with a wealth of unexplored interactions.

References

- [1] S. Manzeli, D. Ovchinnikov, D. Pasquier, O. V. Yazyev, and A. Kis, “2D transition metal dichalcogenides,” *Nature Reviews Materials*, vol. 2, no. 8, p. 17033, 2017.
- [2] J. R. Schaibley, H. Yu, G. Clark, P. Rivera, J. S. Ross, K. L. Seyler, W. Yao, and X. Xu, “Valleytronics in 2D materials,” *Nature Reviews Materials*, vol. 1, p. 16055, 2016.
- [3] H. Zeng and X. Cui, “An optical spectroscopic study on two-dimensional group-VI transition metal dichalcogenides,” *Chemical Society Reviews*, vol. 44, no. 9, pp. 2629–2642, 2015.
- [4] X. Xu, W. Yao, D. Xiao, and T. F. Heinz, “Spin and pseudospins in layered transition metal dichalcogenides,” *Nature Physics*, vol. 10, no. 5, pp. 343–350, 2014.
- [5] D. Xiao, G.-B. Liu, W. Feng, X. Xu, and W. Yao, “Coupled spin and valley physics in monolayers of MoS₂ and other group-VI dichalcogenides,” *Physical Review Letters*, vol. 108, no. 19, p. 196802, 2012.
- [6] T. Brumme, M. Calandra, and F. Mauri, “First-principles theory of field-effect doping in transition-metal dichalcogenides: structural properties, electronic structure, hall coefficient, and electrical conductivity,” *Physical Review B*, vol. 91, no. 15, p. 155436, 2015.
- [7] K. F. Mak, C. Lee, J. Hone, J. Shan, and T. F. Heinz, “Atomically thin MoS₂: a new direct-gap semiconductor,” *Physical Review Letters*, vol. 105, no. 13, p. 136805, 2010.
- [8] B. Averill and P. Eldredge, *General chemistry: principles, patterns, and applications*. The Saylor Foundation, 2011.
- [9] Z. Zhu, Y. Cheng, and U. Schwingenschlögl, “Giant spin-orbit-induced spin splitting in two-dimensional transition-metal dichalcogenide semiconductors,” *Physical Review B*, vol. 84, no. 15, p. 153402, 2011.
- [10] A. Kormányos, G. Burkard, M. Gmitra, J. Fabian, V. Zólyomi, N. D. Drummond, and V. Fal’ko, “k·p theory for two-dimensional transition metal dichalcogenide semiconductors,” *2D Materials*, vol. 2, no. 2, p. 022001, 2015.
- [11] K. F. Mak, K. He, J. Shan, and T. F. Heinz, “Control of valley polarization in monolayer MoS₂ by optical helicity,” *Nature Nanotechnology*, vol. 7, no. 8, pp. 494–498, 2012.
- [12] Z. Song, R. Quhe, S. Liu, Y. Li, J. Feng, Y. Yang, J. Lu, and J. Yang, “Tunable valley polarization and valley orbital magnetic moment hall effect in honeycomb systems with broken inversion symmetry,” *Scientific Reports*, vol. 5, p. 13906, 2015.

References

- [13] G. Sallen, L. Bouet, X. Marie, G. Wang, C. Zhu, W. Han, Y. Lu, P. Tan, T. Amand, B. Liu, *et al.*, “Robust optical emission polarization in MoS₂ monolayers through selective valley excitation,” *Physical Review B*, vol. 86, no. 8, p. 081301, 2012.
- [14] W.-T. Hsu, Y.-L. Chen, C.-H. Chen, P.-S. Liu, T.-H. Hou, L.-J. Li, and W.-H. Chang, “Optically initialized robust valley-polarized holes in monolayer WSe₂,” *Nature Communications*, vol. 6, p. 8963, 2015.
- [15] P. Leek, J. Fink, A. Blais, R. Bianchetti, M. Göppl, J. Gambetta, D. Schuster, L. Frunzio, R. Schoelkopf, and A. Wallraff, “Observation of Berry’s phase in a solid-state qubit,” *Science*, vol. 318, no. 5858, pp. 1889–1892, 2007.
- [16] T. Cao, G. Wang, W. Han, H. Ye, C. Zhu, J. Shi, Q. Niu, P. Tan, E. Wang, B. Liu, *et al.*, “Valley-selective circular dichroism of monolayer molybdenum disulphide,” *Nature Communications*, vol. 3, p. 887, 2012.
- [17] D. Xiao, M.-C. Chang, and Q. Niu, “Berry phase effects on electronic properties,” *Reviews of Modern Physics*, vol. 82, no. 3, p. 1959, 2010.
- [18] K. F. Mak, K. L. McGill, J. Park, and P. L. McEuen, “The valley Hall effect in MoS₂ transistors,” *Science*, vol. 344, no. 6191, pp. 1489–1492, 2014.
- [19] W. Yao, D. Xiao, and Q. Niu, “Valley-dependent optoelectronics from inversion symmetry breaking,” *Physical Review B*, vol. 77, no. 23, p. 235406, 2008.
- [20] M. Glazov, E. Ivchenko, G. Wang, T. Amand, X. Marie, B. Urbaszek, and B. Liu, “Spin and valley dynamics of excitons in transition metal dichalcogenide monolayers,” *Physica Status Solidi (B)*, vol. 252, no. 11, pp. 2349–2362, 2015.
- [21] A. Srivastava, M. Sidler, A. V. Allain, D. S. Lembke, A. Kis, and A. Imamoglu, “Valley Zeeman effect in elementary optical excitations of monolayer WSe₂,” *Nature Physics*, vol. 11, no. 2, p. 141, 2015.
- [22] T. Thonhauser, D. Ceresoli, D. Vanderbilt, and R. Resta, “Orbital magnetization in periodic insulators,” *Physical Review Letters*, vol. 95, no. 13, p. 137205, 2005.
- [23] H. Zeng, J. Dai, W. Yao, D. Xiao, and X. Cui, “Valley polarization in MoS₂ monolayers by optical pumping,” *Nature Nanotechnology*, vol. 7, no. 8, p. 490, 2012.
- [24] G. Wang, A. Chernikov, M. M. Glazov, T. F. Heinz, X. Marie, T. Amand, and B. Urbaszek, “Colloquium: excitons in atomically thin transition metal dichalcogenides,” *Reviews of Modern Physics*, vol. 90, no. 2, p. 021001, 2018.
- [25] M. Fox, *Optical properties of solids*, vol. 3. Oxford University Press, 2010.
- [26] A. Chernikov, T. C. Berkelbach, H. M. Hill, A. Rigosi, Y. Li, O. B. Aslan, D. R. Reichman, M. S. Hybertsen, and T. F. Heinz, “Exciton binding energy and nonhydrogenic Rydberg series in monolayer WS₂,” *Physical Review Letters*, vol. 113, no. 7, p. 076802, 2014.
- [27] D. Y. Qiu, H. Felipe, and S. G. Louie, “Optical spectrum of MoS₂: many-body effects and diversity of exciton states,” *Physical Review Letters*, vol. 111, no. 21, p. 216805, 2013.

- [28] M. M. Ugeda, A. J. Bradley, S.-F. Shi, H. Felipe, Y. Zhang, D. Y. Qiu, W. Ruan, S.-K. Mo, Z. Hussain, Z.-X. Shen, *et al.*, “Giant bandgap renormalization and excitonic effects in a monolayer transition metal dichalcogenide semiconductor,” *Nature Materials*, vol. 13, no. 12, pp. 1091–1095, 2014.
- [29] K. He, N. Kumar, L. Zhao, Z. Wang, K. F. Mak, H. Zhao, and J. Shan, “Tightly bound excitons in monolayer WSe₂,” *Physical Review Letters*, vol. 113, no. 2, p. 026803, 2014.
- [30] C. Schneider, M. M. Glazov, T. Korn, S. Höfling, and B. Urbaszek, “Two-dimensional semiconductors in the regime of strong light-matter coupling,” *Nature Communications*, vol. 9, no. 1, p. 2695, 2018.
- [31] J. S. Ross, S. Wu, H. Yu, N. J. Ghimire, A. M. Jones, G. Aivazian, J. Yan, D. G. Mandrus, D. Xiao, W. Yao, *et al.*, “Electrical control of neutral and charged excitons in a monolayer semiconductor,” *Nature Communications*, vol. 4, p. 1474, 2013.
- [32] K. F. Mak, K. He, C. Lee, G. H. Lee, J. Hone, T. F. Heinz, and J. Shan, “Tightly bound trions in monolayer MoS₂,” *Nature Materials*, vol. 12, no. 3, p. 207, 2013.
- [33] Z. Li, T. Wang, Z. Lu, C. Jin, Y. Chen, Y. Meng, Z. Lian, T. Taniguchi, K. Watanabe, S. Zhang, *et al.*, “Revealing the biexciton and trion-exciton complexes in BN encapsulated WSe₂,” *Nature Communications*, vol. 9, 2018.
- [34] Z. Ye, L. Waldecker, E. Y. Ma, D. Rhodes, A. Antony, B. Kim, X.-X. Zhang, M. Deng, Y. Jiang, Z. Lu, *et al.*, “Efficient generation of neutral and charged biexcitons in encapsulated WSe₂ monolayers,” *Nature Communications*, vol. 9, no. 1, p. 3718, 2018.
- [35] S.-Y. Chen, T. Goldstein, T. Taniguchi, K. Watanabe, and J. Yan, “Coulomb-bound four- and five-particle intervalley states in an atomically-thin semiconductor,” *Nature Communications*, vol. 9, no. 1, p. 3717, 2018.
- [36] M. Barbone, A. R.-P. Montblanch, D. M. Kara, C. Palacios-Berraquero, A. R. Cadore, D. De Fazio, B. Pingault, E. Mostaani, H. Li, B. Chen, *et al.*, “Charge-tuneable biexciton complexes in monolayer WSe₂,” *Nature Communications*, vol. 9, no. 1, p. 3721, 2018.
- [37] M. Sidler, P. Back, O. Cotlet, A. Srivastava, T. Fink, M. Kroner, E. Demler, and A. Imamoglu, “Fermi polaron-polaritons in charge-tunable atomically thin semiconductors,” *Nature Physics*, vol. 13, no. 3, p. 255, 2017.
- [38] Z. Li, T. Wang, C. Jin, Z. Lu, Z. Lian, Y. Meng, M. Blei, S. Gao, T. Taniguchi, K. Watanabe, *et al.*, “Emerging photoluminescence from the dark-exciton phonon replica in monolayer WSe₂,” *Nature Communications*, vol. 10, no. 1, p. 2469, 2019.
- [39] A. Branny, S. Kumar, R. Proux, and B. D. Gerardot, “Deterministic strain-induced arrays of quantum emitters in a two-dimensional semiconductor,” *Nature Communications*, vol. 8, p. 15053, 2017.

References

- [40] C. Palacios-Berraquero, D. M. Kara, A. R.-P. Montblanch, M. Barbone, P. Latawiec, D. Yoon, A. K. Ott, M. Loncar, A. C. Ferrari, and M. Atatüre, “Large-scale quantum-emitter arrays in atomically thin semiconductors,” *Nature Communications*, vol. 8, p. 15093, 2017.
- [41] S. Kumar, M. Brotóns-Gisbert, R. Al-Khuzheyri, A. Branny, G. Ballesteros-Garcia, J. F. Sánchez-Royo, and B. D. Gerardot, “Resonant laser spectroscopy of localized excitons in monolayer WSe₂,” *Optica*, vol. 3, no. 8, pp. 882–886, 2016.
- [42] F. Cadiz, E. Courtade, C. Robert, G. Wang, Y. Shen, H. Cai, T. Taniguchi, K. Watanabe, H. Carrere, D. Lagarde, *et al.*, “Excitonic linewidth approaching the homogeneous limit in MoS₂ based van der Waals heterostructures,” *Physical Review X*, vol. 7, no. 2, p. 021026, 2017.
- [43] M. Glazov, T. Amand, X. Marie, D. Lagarde, L. Bouet, and B. Urbaszek, “Exciton fine structure and spin decoherence in monolayers of transition metal dichalcogenides,” *Physical Review B*, vol. 89, no. 20, p. 201302, 2014.
- [44] H. Yu, G.-B. Liu, P. Gong, X. Xu, and W. Yao, “Dirac cones and Dirac saddle points of bright excitons in monolayer transition metal dichalcogenides,” *Nature Communications*, vol. 5, p. 3876, 2014.
- [45] T. Yu and M. Wu, “Valley depolarization due to intervalley and intravalley electron-hole exchange interactions in monolayer MoS₂,” *Physical Review B*, vol. 89, no. 20, p. 205303, 2014.
- [46] H. Yu, X. Cui, X. Xu, and W. Yao, “Valley excitons in two-dimensional semiconductors,” *National Science Review*, vol. 2, no. 1, pp. 57–70, 2015.
- [47] C. Robert, D. Lagarde, F. Cadiz, G. Wang, B. Lassagne, T. Amand, A. Balocchi, P. Renucci, S. Tongay, B. Urbaszek, *et al.*, “Exciton radiative lifetime in transition metal dichalcogenide monolayers,” *Physical Review B*, vol. 93, no. 20, p. 205423, 2016.
- [48] A. M. Jones, H. Yu, N. J. Ghimire, S. Wu, G. Aivazian, J. S. Ross, B. Zhao, J. Yan, D. G. Mandrus, D. Xiao, *et al.*, “Optical generation of excitonic valley coherence in monolayer WSe₂,” *Nature Nanotechnology*, vol. 8, no. 9, pp. 634–638, 2013.
- [49] G. Wang, X. Marie, B. Liu, T. Amand, C. Robert, F. Cadiz, P. Renucci, and B. Urbaszek, “Control of exciton valley coherence in transition metal dichalcogenide monolayers,” *Physical Review Letters*, vol. 117, no. 18, p. 187401, 2016.
- [50] Y. Li, J. Ludwig, T. Low, A. Chernikov, X. Cui, G. Arefe, Y. D. Kim, A. M. Van Der Zande, A. Rigosi, H. M. Hill, *et al.*, “Valley splitting and polarization by the Zeeman effect in monolayer MoSe₂,” *Physical Review Letters*, vol. 113, no. 26, p. 266804, 2014.
- [51] D. MacNeill, C. Heikes, K. F. Mak, Z. Anderson, A. Kormányos, V. Zólyomi, J. Park, and D. C. Ralph, “Breaking of valley degeneracy by magnetic field in monolayer MoSe₂,” *Physical Review Letters*, vol. 114, no. 3, p. 037401, 2015.

- [52] K. F. Mak and J. Shan, "Photonics and optoelectronics of 2D semiconductor transition metal dichalcogenides," *Nature Photonics*, vol. 10, no. 4, pp. 216–226, 2016.
- [53] K. Hao, G. Moody, F. Wu, C. K. Dass, L. Xu, C.-H. Chen, L. Sun, M.-Y. Li, L.-J. Li, A. H. MacDonald, *et al.*, "Direct measurement of exciton valley coherence in monolayer WSe₂," *Nature Physics*, vol. 12, no. 7, p. 677, 2016.
- [54] R. Schmidt, A. Arora, G. Plechinger, P. Nagler, A. G. del Águila, M. V. Ballottin, P. C. Christianen, S. M. de Vasconcellos, C. Schüller, T. Korn, *et al.*, "Magnetic-field-induced rotation of polarized light emission from monolayer WS₂," *Physical Review Letters*, vol. 117, no. 7, p. 077402, 2016.
- [55] A. Zhang, J. Fan, Y. Li, J. Ji, G. Zhao, T. Xia, T. Yan, X. Zhang, W. Zhang, X. Wang, *et al.*, "Anomalous valley polarization in monolayer MoSe₂," *arXiv preprint arXiv:1503.08631*, 2015.
- [56] G. Aivazian, Z. Gong, A. M. Jones, R.-L. Chu, J. Yan, D. G. Mandrus, C. Zhang, D. Cobden, W. Yao, and X. Xu, "Magnetic control of valley pseudospin in monolayer WSe₂," *Nature Physics*, vol. 11, no. 2, p. 148, 2015.
- [57] G. Wang, L. Bouet, M. M. Glazov, T. Amand, E. L. Ivchenko, E. Palleau, X. Marie, and B. Urbaszek, "Magneto-optics in transition metal diselenide monolayers," *2D Materials*, vol. 2, no. 3, p. 034002, 2015.
- [58] M. Koperski, M. R. Molas, A. Arora, K. Nogajewski, A. O. Slobodeniuk, C. Faugeras, and M. Potemski, "Optical properties of atomically thin transition metal dichalcogenides: observations and puzzles," *Nanophotonics*, vol. 6, no. 6, pp. 1289–1308, 2017.
- [59] M. Koperski, K. Nogajewski, A. Arora, V. Cherkez, P. Mallet, J.-Y. Veuillen, J. Marcus, P. Kossacki, and M. Potemski, "Single photon emitters in exfoliated WSe₂ structures," *Nature Nanotechnology*, vol. 10, no. 6, p. 503, 2015.
- [60] E. M. Alexeev, A. Catanzaro, O. V. Skrypka, P. K. Nayak, S. Ahn, S. Pak, J. Lee, J. I. Sohn, K. S. Novoselov, H. S. Shin, *et al.*, "Imaging of interlayer coupling in van der waals heterostructures using a bright-field optical microscope," *Nano letters*, vol. 17, no. 9, pp. 5342–5349, 2017.
- [61] K. S. Novoselov, A. K. Geim, S. Morozov, D. Jiang, Y. Zhang, S. Dubonos, , I. Grigorieva, and A. Firsov, "Electric field effect in atomically thin carbon films," *Science*, vol. 306, no. 5696, pp. 666–669, 2004.
- [62] K. Novoselov, D. Jiang, F. Schedin, T. Booth, V. Khotkevich, S. Morozov, and A. Geim, "Two-dimensional atomic crystals," *Proceedings of the National Academy of Sciences of the United States of America*, vol. 102, no. 30, pp. 10451–10453, 2005.
- [63] Y. Huang, E. Sutter, N. N. Shi, J. Zheng, T. Yang, D. Englund, H.-J. Gao, and P. Sutter, "Reliable exfoliation of large-area high-quality flakes of graphene and other two-dimensional materials," *ACS Nano*, vol. 9, no. 11, pp. 10612–10620, 2015.

References

- [64] A. Splendiani, L. Sun, Y. Zhang, T. Li, J. Kim, C.-Y. Chim, G. Galli, and F. Wang, “Emerging photoluminescence in monolayer MoS₂,” *Nano Letters*, vol. 10, no. 4, pp. 1271–1275, 2010.
- [65] Y. Zhan, Z. Liu, S. Najmaei, P. M. Ajayan, and J. Lou, “Large-area vapor-phase growth and characterization of MoS₂ atomic layers on a SiO₂ substrate,” *Small*, vol. 8, no. 7, pp. 966–971, 2012.
- [66] S. Najmaei, Z. Liu, W. Zhou, X. Zou, G. Shi, S. Lei, B. I. Yakobson, J.-C. Idrobo, P. M. Ajayan, and J. Lou, “Vapour phase growth and grain boundary structure of molybdenum disulphide atomic layers,” *Nature Materials*, vol. 12, no. 8, p. 754, 2013.
- [67] A. M. Van Der Zande, P. Y. Huang, D. A. Chenet, T. C. Berkelbach, Y. You, G.-H. Lee, T. F. Heinz, D. R. Reichman, D. A. Muller, and J. C. Hone, “Grains and grain boundaries in highly crystalline monolayer molybdenum disulphide,” *Nature Materials*, vol. 12, no. 6, p. 554, 2013.
- [68] Y.-H. Lee, X.-Q. Zhang, W. Zhang, M.-T. Chang, C.-T. Lin, K.-D. Chang, Y.-C. Yu, J. T.-W. Wang, C.-S. Chang, L.-J. Li, *et al.*, “Synthesis of large-area MoS₂ atomic layers with chemical vapor deposition,” *Advanced Materials*, vol. 24, no. 17, pp. 2320–2325, 2012.
- [69] Y. Kim, H. Bark, G. H. Ryu, Z. Lee, and C. Lee, “Wafer-scale monolayer MoS₂ grown by chemical vapor deposition using a reaction of MoO₃ and H₂S,” *Journal of Physics: Condensed Matter*, vol. 28, no. 18, p. 184002, 2016.
- [70] A. Castellanos-Gomez, M. Buscema, R. Molenaar, V. Singh, L. Janssen, H. S. van der Zant, and G. A. Steele, “Deterministic transfer of two-dimensional materials by all-dry viscoelastic stamping,” *2D Materials*, vol. 1, no. 1, p. 011002, 2014.
- [71] H. Liu, L. Jiao, L. Xie, F. Yang, J. Chen, W. Ho, C. Gao, J. Jia, X. Cui, and M. Xie, “Molecular-beam epitaxy of monolayer and bilayer WSe₂: a scanning tunneling microscopy/spectroscopy study and deduction of exciton binding energy,” *2D Materials*, vol. 2, no. 3, p. 034004, 2015.
- [72] M. Marx, S. Nordmann, J. Knoch, C. Franzen, C. Stampfer, D. Andrzejewski, T. Kümmell, G. Bacher, M. Heuken, H. Kalisch, *et al.*, “Large-area MoS₂ deposition via MOVPE,” *Journal of Crystal Growth*, vol. 464, pp. 100–104, 2017.
- [73] E. M. Alexeev, D. A. Ruiz-Tijerina, M. Danovich, M. J. Hamer, D. J. Terry, P. K. Nayak, S. Ahn, S. Pak, J. Lee, J. I. Sohn, *et al.*, “Resonantly hybridized excitons in Moiré superlattices in van der Waals heterostructures,” *Nature*, vol. 567, no. 7746, p. 81, 2019.
- [74] A. K. Geim and I. V. Grigorieva, “Van der Waals heterostructures,” *Nature*, vol. 499, no. 7459, pp. 419–425, 2013.
- [75] C. R. Dean, A. F. Young, I. Meric, C. Lee, L. Wang, S. Sorgenfrei, K. Watanabe, T. Taniguchi, P. Kim, K. L. Shepard, *et al.*, “Boron nitride substrates for high-quality graphene electronics,” *Nature Nanotechnology*, vol. 5, no. 10, p. 722, 2010.

- [76] S. Haigh, A. Gholinia, R. Jalil, S. Romani, L. Britnell, D. Elias, K. Novoselov, L. Ponomarenko, A. Geim, and R. Gorbachev, "Cross-sectional imaging of individual layers and buried interfaces of graphene-based heterostructures and superlattices," *Nature Materials*, vol. 11, no. 9, pp. 764–767, 2012.
- [77] L. Wang, I. Meric, P. Huang, Q. Gao, Y. Gao, H. Tran, T. Taniguchi, K. Watanabe, L. Campos, D. Muller, *et al.*, "One-dimensional electrical contact to a two-dimensional material," *Science*, vol. 342, no. 6158, pp. 614–617, 2013.
- [78] S. Schwarz, A. Kozikov, F. Withers, J. Maguire, A. Foster, S. Dufferwiel, L. Hague, M. Makhonin, L. Wilson, A. Geim, *et al.*, "Electrically pumped single-defect light emitters in WSe₂," *2D Materials*, vol. 3, no. 2, p. 025038, 2016.
- [79] B. Radisavljevic, A. Radenovic, J. Brivio, i. V. Giacometti, and A. Kis, "Single-layer MoS₂ transistors," *Nature Nanotechnology*, vol. 6, no. 3, pp. 147–150, 2011.
- [80] F. Koppens, T. Mueller, P. Avouris, A. Ferrari, M. Vitiello, and M. Polini, "Photodetectors based on graphene, other two-dimensional materials and hybrid systems," *Nature Nanotechnology*, vol. 9, no. 10, p. 780, 2014.
- [81] F. Withers, O. Del Pozo-Zamudio, A. Mishchenko, A. Rooney, A. Gholinia, K. Watanabe, T. Taniguchi, S. Haigh, A. Geim, A. Tartakovskii, *et al.*, "Light-emitting diodes by band-structure engineering in van der Waals heterostructures," *Nature Materials*, vol. 14, no. 3, pp. 301–306, 2015.
- [82] R. Frisenda, E. Navarro-Moratalla, P. Gant, D. P. De Lara, P. Jarillo-Herrero, R. V. Gorbachev, and A. Castellanos-Gomez, "Recent progress in the assembly of nanodevices and van der Waals heterostructures by deterministic placement of 2D materials," *Chemical Society Reviews*, vol. 47, no. 1, pp. 53–68, 2018.
- [83] M. H. Gass, U. Bangert, A. L. Bleloch, P. Wang, R. R. Nair, and A. Geim, "Free-standing graphene at atomic resolution," *Nature Nanotechnology*, vol. 3, no. 11, pp. 676–681, 2008.
- [84] S. Dufferwiel, F. Fras, A. Trichet, P. Walker, F. Li, L. Giriunas, M. Makhonin, L. Wilson, J. Smith, E. Clarke, *et al.*, "Strong exciton-photon coupling in open semiconductor microcavities," *Applied Physics Letters*, vol. 104, no. 19, p. 192107, 2014.
- [85] L. Allen, M. W. Beijersbergen, R. Spreeuw, and J. Woerdman, "Orbital angular momentum of light and the transformation of Laguerre-Gaussian laser modes," *Physical Review A*, vol. 45, no. 11, p. 8185, 1992.
- [86] A. Singh, G. Moody, K. Tran, M. E. Scott, V. Overbeck, G. Berghäuser, J. Schaibley, E. J. Seifert, D. Pleskot, N. M. Gabor, *et al.*, "Trion formation dynamics in monolayer transition metal dichalcogenides," *Physical Review B*, vol. 93, no. 4, p. 041401, 2016.
- [87] A. Singh, K. Tran, M. Kolarczik, J. Seifert, Y. Wang, K. Hao, D. Pleskot, N. M. Gabor, S. Helmrich, N. Owschimikow, *et al.*, "Long-lived valley polarization of intravalley trions in monolayer WSe₂," *Physical Review Letters*, vol. 117, no. 25, p. 257402, 2016.

References

- [88] G. Plechinger, P. Nagler, A. Arora, R. Schmidt, A. Chernikov, A. Grenados del Águila, P. C. M. Christianen, R. Bratschitsch, C. Schüller, and T. Korn, “Trion fine structure and coupled spin–valley dynamics in monolayer tungsten disulfide,” *Nature Communications*, vol. 7, 2016.
- [89] D. Vaclavkova, J. Wyzula, K. Nogajewski, M. Bartos, A. O. Slobodeniuk, C. Faugeras, M. Potemski, and M. R. Molas, “Singlet and triplet trions in WS₂ monolayer encapsulated in hexagonal boron nitride,” *Nanotechnology*, vol. 29, no. 32, p. 325705, 2018.
- [90] G. Plechinger, P. Nagler, A. Arora, A. Grenados del Águila, M. V. Ballottin, T. Frank, P. Steinleitner, M. Gmitra, J. Fabian, P. C. M. Christianen, *et al.*, “Excitonic valley effects in monolayer WS₂ under high magnetic fields,” *Nano Letters*, vol. 16, no. 12, pp. 7899–7904, 2016.
- [91] A. M. Jones, H. Yu, J. R. Schaibley, J. Yan, D. G. Mandrus, T. Taniguchi, K. Watanabe, H. Dery, W. Yao, and X. Xu, “Excitonic luminescence upconversion in a two-dimensional semiconductor,” *Nature Physics*, vol. 12, no. 4, pp. 323–327, 2016.
- [92] T. Taniguchi and K. Watanabe, “Synthesis of high-purity boron nitride single crystals under high pressure by using Ba–BN solvent,” *Journal of Crystal Growth*, vol. 303, no. 2, pp. 525–529, 2007.
- [93] S. Lippert, L. M. Schneider, D. Renaud, K. N. Kang, O. Ajayi, J. Kuhnert, M.-U. Halbich, O. M. Abdulmunem, X. Lin, K. Hassoon, *et al.*, “Influence of the substrate material on the optical properties of tungsten diselenide monolayers,” *2D Materials*, vol. 4, no. 2, p. 025045, 2017.
- [94] A. Singh, A. Knorr, C. K. Dass, C.-H. Chen, E. Malic, G. Moody, G. Clark, G. Berghäuser, K. Hao, K. Tran, *et al.*, “Intrinsic homogeneous linewidth and broadening mechanisms of excitons in monolayer transition metal dichalcogenides,” *Nature Communications*, vol. 6, p. 8315, 2015.
- [95] D. Andronikov, M. Fehr, V. Kochereshko, S. Crooker, and G. Karczewski, “Behavior of excitons and trions in CdTe / CdMgTe quantum-well structures with variations in temperature,” *Physics of the Solid State*, vol. 49, no. 8, pp. 1567–1571, 2007.
- [96] I. Kylänpää and H.-P. Komsa, “Binding energies of exciton complexes in transition metal dichalcogenide monolayers and effect of dielectric environment,” *Physical Review B*, vol. 92, no. 20, p. 205418, 2015.
- [97] E. Courtade, M. Semina, M. Manca, M. Glazov, C. Robert, F. Cadiz, G. Wang, T. Taniguchi, K. Watanabe, M. Pierre, *et al.*, “Charged excitons in monolayer WSe₂: experiment and theory,” *Physical Review B*, vol. 96, no. 8, p. 085302, 2017.
- [98] M. Van der Donck, M. Zarenia, and F. Peeters, “Excitons and trions in monolayer transition metal dichalcogenides: a comparative study between the multiband model and the quadratic single-band model,” *Physical Review B*, vol. 96, no. 3, p. 035131, 2017.

- [99] A. V. Stier, K. M. McCreary, B. T. Jonker, J. Kono, and S. A. Crooker, “Exciton diamagnetic shifts and valley Zeeman effects in monolayer WS₂ and MoS₂ to 65 Tesla,” *Nature Communications*, vol. 7, p. 10643, 2016.
- [100] M. V. Gustafsson, M. Yankowitz, C. Forsythe, D. Rhodes, K. Watanabe, T. Taniguchi, J. Hone, X. Zhu, and C. R. Dean, “Ambipolar Landau levels and strong band-selective carrier interactions in monolayer WSe₂,” *Nature Materials*, vol. 17, no. 5, p. 411, 2018.
- [101] D. Xiao, W. Yao, and Q. Niu, “Valley-contrasting physics in graphene: magnetic moment and topological transport,” *Physical Review Letters*, vol. 99, no. 23, p. 236809, 2007.
- [102] Z. Wang, J. Shan, and K. F. Mak, “Valley-and spin-polarized Landau levels in monolayer WSe₂,” *Nature Nanotechnology*, vol. 12, no. 2, p. 144, 2017.
- [103] Q. Zhang, C. H. Naylor, Z. Gao, R. Wu, I. H. Abidi, M.-Q. Zhao, Y. Ding, A. A. Cagang, M. Zhuang, X. Ou, *et al.*, “Recoil effect and photoemission splitting of trions in monolayer MoS₂,” *ACS Nano*, vol. 11, no. 11, pp. 10808–10815, 2017.
- [104] C. Yang, F. Peeters, and W. Xu, “Landau-level broadening due to electron-impurity interaction in graphene in strong magnetic fields,” *Physical Review B*, vol. 82, no. 7, p. 075401, 2010.
- [105] J. W. Christopher, B. B. Goldberg, and A. K. Swan, “Long tailed trions in monolayer MoS₂: temperature dependent asymmetry and resulting red-shift of trion photoluminescence spectra,” *Scientific Reports*, vol. 7, no. 1, p. 14062, 2017.
- [106] M. Van der Donck, M. Zarenia, and F. Peeters, “Excitons, trions, and biexcitons in transition-metal dichalcogenides: magnetic-field dependence,” *Physical Review B*, vol. 97, no. 19, p. 195408, 2018.
- [107] S. Dufferwiel, S. Schwarz, F. Withers, A. Trichet, F. Li, M. Sich, O. Del Pozo-Zamudio, C. Clark, A. Nalitov, D. Solnyshkov, *et al.*, “Exciton-polaritons in van der Waals heterostructures embedded in tunable microcavities,” *Nature Communications*, vol. 6, 2015.
- [108] N. Lundt, S. Klemmt, E. Cherotchenko, S. Betzold, O. Iff, A. V. Nalitov, M. Klaas, C. P. Dietrich, A. V. Kavokin, S. Höfling, *et al.*, “Room-temperature Tamm-plasmon exciton-polaritons with a WSe₂ monolayer,” *Nature Communications*, vol. 7, p. 13328, 2016.
- [109] L. Zhang, R. Gogna, W. Burg, E. Tutuc, and H. Deng, “Photonic-crystal exciton-polaritons in monolayer semiconductors,” *Nature Communications*, vol. 9, no. 1, p. 713, 2018.
- [110] X. Liu, T. Galfsky, Z. Sun, F. Xia, E.-c. Lin, Y.-H. Lee, S. Kéna-Cohen, and V. M. Menon, “Strong light–matter coupling in two-dimensional atomic crystals,” *Nature Photonics*, vol. 9, no. 1, pp. 30–34, 2015.
- [111] D. Sanvitto and S. Kéna-Cohen, “The road towards polaritonic devices,” *Nature Materials*, vol. 15, no. 10, pp. 1061–1073, 2016.

References

- [112] H. Deng, D. Press, S. Götzinger, G. S. Solomon, R. Hey, K. H. Ploog, and Y. Yamamoto, “Quantum degenerate exciton-polaritons in thermal equilibrium,” *Physical Review Letters*, vol. 97, no. 14, p. 146402, 2006.
- [113] A. Amo, J. Lefrère, S. Pigeon, C. Adrados, C. Ciuti, I. Carusotto, R. Houdré, E. Giacobino, and A. Bramati, “Superfluidity of polaritons in semiconductor microcavities,” *Nature Physics*, vol. 5, no. 11, p. 805, 2009.
- [114] M. Sich, D. Krizhanovskii, M. Skolnick, A. V. Gorbach, R. Hartley, D. V. Skryabin, E. Cerda-Méndez, K. Biermann, R. Hey, and P. Santos, “Observation of bright polariton solitons in a semiconductor microcavity,” *Nature Photonics*, vol. 6, no. 1, p. 50, 2012.
- [115] C. Whittaker, E. Cancellieri, P. Walker, D. Gulevich, H. Schomerus, D. Vaitiekus, B. Royall, D. Whittaker, E. Clarke, I. Iorsh, *et al.*, “Exciton polaritons in a two-dimensional Lieb lattice with spin-orbit coupling,” *Physical Review Letters*, vol. 120, no. 9, p. 097401, 2018.
- [116] H. Ohadi, Y. d. V.-I. Redondo, A. Dreismann, Y. Rubo, F. Pinsker, S. Tsintzos, Z. Hatzopoulos, P. Savvidis, and J. Baumberg, “Tunable magnetic alignment between trapped exciton-polariton condensates,” *Physical Review Letters*, vol. 116, no. 10, p. 106403, 2016.
- [117] R. Suzuki, M. Sakano, Y. Zhang, R. Akashi, D. Morikawa, A. Harasawa, K. Yaji, K. Kuroda, K. Miyamoto, T. Okuda, *et al.*, “Valley-dependent spin polarization in bulk MoS₂ with broken inversion symmetry,” *Nature Nanotechnology*, vol. 9, no. 8, p. 611, 2014.
- [118] B. Zhu, H. Zeng, J. Dai, Z. Gong, and X. Cui, “Anomalously robust valley polarization and valley coherence in bilayer WS₂,” *Proceedings of the National Academy of Sciences*, vol. 111, no. 32, pp. 11606–11611, 2014.
- [119] A. Surrente, D. Dumcenco, Z. Yang, A. Kuc, Y. Jing, T. Heine, Y.-C. Kung, D. K. Maude, A. Kis, and P. Plochocka, “Defect healing and charge transfer-mediated valley polarization in MoS₂ / MoSe₂ / MoS₂ trilayer van der Waals heterostructures,” *Nano Letters*, vol. 17, no. 7, pp. 4130–4136, 2017.
- [120] C. Zhu, K. Zhang, M. Glazov, B. Urbaszek, T. Amand, Z. Ji, B. Liu, and X. Marie, “Exciton valley dynamics probed by Kerr rotation in WSe₂ monolayers,” *Physical Review B*, vol. 90, no. 16, p. 161302, 2014.
- [121] M. Maialle, E. d. A. e Silva, and L. Sham, “Exciton spin dynamics in quantum wells,” *Physical Review B*, vol. 47, no. 23, p. 15776, 1993.
- [122] G. Kioseoglou, A. Hanbicki, M. Currie, A. Friedman, D. Gunlycke, and B. Jonker, “Valley polarization and intervalley scattering in monolayer MoS₂,” *Applied Physics Letters*, vol. 101, no. 22, p. 221907, 2012.
- [123] A. T. Hanbicki, G. Kioseoglou, M. Currie, C. S. Hellberg, K. M. McCreary, A. L. Friedman, and B. T. Jonker, “Anomalous temperature-dependent spin-valley polarization in monolayer WS₂,” *Scientific Reports*, vol. 6, p. 18885, 2016.

- [124] T. Smoleński, M. Goryca, M. Koperski, C. Faugeras, T. Kazimierczuk, A. Bogucki, K. Nogajewski, P. Kossacki, and M. Potemski, “Tuning valley polarization in a WSe₂ monolayer with a tiny magnetic field,” *Physical Review X*, vol. 6, no. 2, p. 021024, 2016.
- [125] G. Wang, E. Palleau, T. Amand, S. Tongay, X. Marie, and B. Urbaszek, “Polarization and time-resolved photoluminescence spectroscopy of excitons in MoSe₂ monolayers,” *Applied Physics Letters*, vol. 106, no. 11, p. 112101, 2015.
- [126] G. Wang, M. Glazov, C. Robert, T. Amand, X. Marie, and B. Urbaszek, “Double resonant raman scattering and valley coherence generation in monolayer WSe₂,” *Physical Review Letters*, vol. 115, no. 11, p. 117401, 2015.
- [127] Z. Ye, D. Sun, and T. F. Heinz, “Optical manipulation of valley pseudospin,” *Nature Physics*, vol. 13, no. 1, p. 26, 2017.
- [128] H. Yu, X. Cui, X. Xu, and W. Yao, “Valley excitons in two-dimensional semiconductors,” *National Science Review*, vol. 2, no. 1, pp. 57–70, 2015.
- [129] L. Yang, N. A. Sinitsyn, W. Chen, J. Yuan, J. Zhang, J. Lou, and S. A. Crooker, “Long-lived nanosecond spin relaxation and spin coherence of electrons in monolayer MoS₂ and WS₂,” *Nature Physics*, vol. 11, no. 10, p. 830, 2015.
- [130] J. Kim, C. Jin, B. Chen, H. Cai, T. Zhao, P. Lee, S. Kahn, K. Watanabe, T. Taniguchi, S. Tongay, *et al.*, “Observation of ultralong valley lifetime in WSe₂ / MoS₂ heterostructures,” *Science Advances*, vol. 3, no. 7, p. e1700518, 2017.
- [131] M. Palummo, M. Bernardi, and J. C. Grossman, “Exciton radiative lifetimes in two-dimensional transition metal dichalcogenides,” *Nano Letters*, vol. 15, no. 5, pp. 2794–2800, 2015.
- [132] A. Kavokin, G. Malpuech, and M. Glazov, “Optical spin hall effect,” *Physical Review Letters*, vol. 95, no. 13, p. 136601, 2005.
- [133] G. R. Bhimanapati, Z. Lin, V. Meunier, Y. Jung, J. Cha, S. Das, D. Xiao, Y. Son, M. S. Strano, V. R. Cooper, *et al.*, “Recent advances in two-dimensional materials beyond graphene,” *ACS Nano*, vol. 9, no. 12, pp. 11509–11539, 2015.
- [134] C. Gong, L. Li, Z. Li, H. Ji, A. Stern, Y. Xia, T. Cao, W. Bao, C. Wang, Y. Wang, *et al.*, “Discovery of intrinsic ferromagnetism in two-dimensional van der Waals crystals,” *Nature*, vol. 546, no. 7657, p. 265, 2017.
- [135] B. Huang, G. Clark, E. Navarro-Moratalla, D. R. Klein, R. Cheng, K. L. Seyler, D. Zhong, E. Schmidgall, M. A. McGuire, D. H. Cobden, *et al.*, “Layer-dependent ferromagnetism in a van der Waals crystal down to the monolayer limit,” *Nature*, vol. 546, no. 7657, p. 270, 2017.
- [136] M. Bonilla, S. Kolekar, Y. Ma, H. C. Diaz, V. Kalappattil, R. Das, T. Eggers, H. R. Gutierrez, M.-H. Phan, and M. Batzill, “Strong room-temperature ferromagnetism in VSe₂ monolayers on van der Waals substrates,” *Nature Nanotechnology*, vol. 13, no. 4, p. 289, 2018.

References

- [137] J.-U. Lee, S. Lee, J. H. Ryoo, S. Kang, T. Y. Kim, P. Kim, C.-H. Park, J.-G. Park, and H. Cheong, “Ising-type magnetic ordering in atomically thin FePS₃,” *Nano Letters*, vol. 16, no. 12, pp. 7433–7438, 2016.
- [138] Y. Deng, Y. Yu, Y. Song, J. Zhang, N. Z. Wang, Z. Sun, Y. Yi, Y. Z. Wu, S. Wu, J. Zhu, *et al.*, “Gate-tunable room-temperature ferromagnetism in two-dimensional Fe₃GeTe₂,” *Nature*, vol. 563, no. 7729, p. 94, 2018.
- [139] Z. Fei, B. Huang, P. Malinowski, W. Wang, T. Song, J. Sanchez, W. Yao, D. Xiao, X. Zhu, A. F. May, *et al.*, “Two-dimensional itinerant ferromagnetism in atomically thin Fe₃GeTe₂,” *Nature Materials*, vol. 17, no. 9, p. 778, 2018.
- [140] K. L. Seyler, D. Zhong, D. R. Klein, S. Gao, X. Zhang, B. Huang, E. Navarro-Moratalla, L. Yang, D. H. Cobden, M. A. McGuire, *et al.*, “Ligand-field helical luminescence in a 2D ferromagnetic insulator,” *Nature Physics*, vol. 14, no. 3, p. 277, 2018.
- [141] D. Zhong, K. L. Seyler, X. Linpeng, R. Cheng, N. Sivadas, B. Huang, E. Schmidgall, T. Taniguchi, K. Watanabe, M. A. McGuire, *et al.*, “Van der Waals engineering of ferromagnetic semiconductor heterostructures for spin and valleytronics,” *Science Advances*, vol. 3, no. 5, p. e1603113, 2017.
- [142] S. Jiang, J. Shan, and K. F. Mak, “Electric-field switching of two-dimensional van der Waals magnets,” *Nature Materials*, vol. 17, no. 5, p. 406, 2018.
- [143] M. A. McGuire, H. Dixit, V. R. Cooper, and B. C. Sales, “Coupling of crystal structure and magnetism in the layered, ferromagnetic insulator CrI₃,” *Chemistry of Materials*, vol. 27, no. 2, pp. 612–620, 2015.
- [144] S. Jiang, L. Li, Z. Wang, K. F. Mak, and J. Shan, “Controlling magnetism in 2D CrI₃ by electrostatic doping,” *Nature Nanotechnology*, vol. 13, no. 7, p. 549, 2018.
- [145] K. Zollner, P. E. F. Junior, and J. Fabian, “Proximity exchange effects in MoSe₂ and WSe₂ heterostructures with CrI₃: twist angle, layer, and gate dependence,” *Physical Review B*, vol. 100, no. 8, p. 085128, 2019.
- [146] Z. Sun, Y. Yi, T. Song, G. Clark, B. Huang, Y. Shan, S. Wu, D. Huang, C. Gao, Z. Chen, *et al.*, “Giant nonreciprocal second-harmonic generation from antiferromagnetic bilayer CrI₃,” *Nature*, p. 1, 2019.
- [147] N. Sivadas, S. Okamoto, X. Xu, C. J. Fennie, and D. Xiao, “Stacking-dependent magnetism in bilayer CrI₃,” *Nano Letters*, vol. 18, no. 12, pp. 7658–7664, 2018.
- [148] B. Huang, G. Clark, D. R. Klein, D. MacNeill, E. Navarro-Moratalla, K. L. Seyler, N. Wilson, M. A. McGuire, D. H. Cobden, D. Xiao, *et al.*, “Electrical control of 2D magnetism in bilayer CrI₃,” *Nature Nanotechnology*, vol. 13, no. 7, p. 544, 2018.
- [149] N. D. Mermin and H. Wagner, “Absence of ferromagnetism or antiferromagnetism in one- or two-dimensional isotropic Heisenberg models,” *Physical Review Letters*, vol. 17, no. 22, p. 1133, 1966.

- [150] R. B. Griffiths, “Peierls proof of spontaneous magnetization in a two-dimensional Ising ferromagnet,” *Physical Review*, vol. 136, no. 2A, p. A437, 1964.
- [151] W.-B. Zhang, Q. Qu, P. Zhu, and C.-H. Lam, “Robust intrinsic ferromagnetism and half semiconductivity in stable two-dimensional single-layer chromium trihalides,” *Journal of Materials Chemistry C*, vol. 3, no. 48, pp. 12457–12468, 2015.
- [152] W. Jung, “Dielectric constant and magneto-optical Kerr rotation of ferromagnetic chromium tribromide above the absorption band edge,” *Journal of Applied Physics*, vol. 36, no. 8, pp. 2422–2426, 1965.
- [153] I. Tsubokawa, “On the magnetic properties of a CrBr₃ single crystal,” *Journal of the Physical Society of Japan*, vol. 15, no. 9, pp. 1664–1668, 1960.
- [154] J. Dillon Jr, H. Kamimura, and J. Remeika, “Magneto-optical properties of ferromagnetic chromium trihalides,” *Journal of Physics and Chemistry of Solids*, vol. 27, no. 9, pp. 1531–1549, 1966.
- [155] J. Kanamori, “Superexchange interaction and symmetry properties of electron orbitals,” *Journal of Physics and Chemistry of Solids*, vol. 10, no. 2-3, pp. 87–98, 1959.
- [156] D. Ghazaryan, M. T. Greenaway, Z. Wang, V. H. Guarochico-Moreira, I. J. Vera-Marun, J. Yin, Y. Liao, S. V. Morozov, O. Kristanovski, A. I. Lichtenstein, *et al.*, “Magnon-assisted tunnelling in van der Waals heterostructures based on CrBr₃,” *Nature Electronics*, vol. 1, no. 6, p. 344, 2018.
- [157] Z. Zhang, J. Shang, C. Jiang, A. Rasmita, W. Gao, and T. Yu, “Direct photoluminescence probing of ferromagnetism in monolayer two-dimensional CrBr₃,” *Nano Letters*, vol. 19, no. 5, pp. 3138–3142, 2019.
- [158] D. Shcherbakov, P. Stepanov, D. Weber, Y. Wang, J. Hu, Y. Zhu, K. Watanabe, T. Taniguchi, Z. Mao, W. Windl, *et al.*, “Raman spectroscopy, photocatalytic degradation, and stabilization of atomically thin chromium tri-iodide,” *Nano Letters*, vol. 18, no. 7, pp. 4214–4219, 2018.
- [159] R. O. Jones, “Density functional theory: its origins, rise to prominence, and future,” *Reviews of Modern Physics*, vol. 87, no. 3, p. 897, 2015.
- [160] S. Blundell, *Magnetism in condensed matter*. Oxford University Press, 2003.
- [161] J. S. Moodera, T. S. Santos, and T. Nagahama, “The phenomena of spin-filter tunnelling,” *Journal of Physics: Condensed Matter*, vol. 19, no. 16, p. 165202, 2007.
- [162] M.-H. Chiu, C. Zhang, H.-W. Shiu, C.-P. Chuu, C.-H. Chen, C.-Y. S. Chang, C.-H. Chen, M.-Y. Chou, C.-K. Shih, and L.-J. Li, “Determination of band alignment in the single-layer MoS₂ / WSe₂ heterojunction,” *Nature Communications*, vol. 6, p. 7666, 2015.
- [163] S. Dufferwiel, T. P. Lyons, D. D. Solnyshkov, A. A. P. Trichet, F. Withers, S. Schwarz, G. Malpuech, J. M. Smith, K. S. Novoselov, M. S. Skolnick, *et al.*, “Valley-addressable polaritons in atomically thin semiconductors,” *Nature Photonics*, vol. 11, no. 8, p. 497, 2017.

References

- [164] J. Liu, Q. Sun, Y. Kawazoe, and P. Jena, “Exfoliating biocompatible ferromagnetic Cr-trihalide monolayers,” *Physical Chemistry Chemical Physics*, vol. 18, no. 13, pp. 8777–8784, 2016.
- [165] V. Alyoshin, V. Berezin, and V. Tulin, “RF susceptibility of single-crystal CrBr₃ near the Curie temperature,” *Physical Review B*, vol. 56, no. 2, p. 719, 1997.
- [166] E. Samuelsen, R. Silberglitt, G. Shirane, and J. Remeika, “Spin waves in ferromagnetic CrBr₃ studied by inelastic neutron scattering,” *Physical Review B*, vol. 3, no. 1, p. 157, 1971.
- [167] J. T. Ho and J. Litster, “Magnetic equation of state of CrBr₃ near the critical point,” *Physical Review Letters*, vol. 22, no. 12, p. 603, 1969.
- [168] C. Zhao, T. Norden, P. Zhang, P. Zhao, Y. Cheng, F. Sun, J. P. Parry, P. Taheri, J. Wang, Y. Yang, *et al.*, “Enhanced valley splitting in monolayer WSe₂ due to magnetic exchange field,” *Nature Nanotechnology*, vol. 12, no. 8, p. 757, 2017.
- [169] M. Koperski, M. R. Molas, A. Arora, K. Nogajewski, M. Bartos, J. Wyzula, D. Vavclavkova, P. Kossacki, and M. Potemski, “Orbital, spin and valley contributions to Zeeman splitting of excitonic resonances in MoSe₂, WSe₂ and WS₂ monolayers,” *2D Materials*, vol. 6, no. 1, p. 015001, 2018.
- [170] T. Norden, C. Zhao, P. Zhang, R. Sabirianov, A. Petrou, and H. Zeng, “Giant valley splitting in monolayer WS₂ by magnetic proximity effect,” *Nature Communications*, vol. 10, p. 4163, 2019.
- [171] K. L. Seyler, D. Zhong, B. Huang, X. Linpeng, N. P. Wilson, T. Taniguchi, K. Watanabe, W. Yao, D. Xiao, M. A. McGuire, *et al.*, “Valley manipulation by optically tuning the magnetic proximity effect in WSe₂ / CrI₃ heterostructures,” *Nano Letters*, vol. 18, no. 6, pp. 3823–3828, 2018.
- [172] S. Anghel, F. Passmann, C. Ruppert, A. Bristow, and M. Betz, “Coupled exciton-trion spin dynamics in a MoSe₂ monolayer,” *2D Materials*, vol. 5, no. 4, p. 045024, 2018.
- [173] J. Feldmann, G. Peter, E. Göbel, P. Dawson, K. Moore, C. Foxon, and R. Elliott, “Linewidth dependence of radiative exciton lifetimes in quantum wells,” *Physical Review Letters*, vol. 59, no. 20, p. 2337, 1987.
- [174] G. Moody, C. K. Dass, K. Hao, C.-H. Chen, L.-J. Li, A. Singh, K. Tran, G. Clark, X. Xu, G. Berghäuser, *et al.*, “Intrinsic homogeneous linewidth and broadening mechanisms of excitons in monolayer transition metal dichalcogenides,” *Nature Communications*, vol. 6, p. 8315, 2015.
- [175] M. Selig, G. Berghäuser, A. Raja, P. Nagler, C. Schüller, T. F. Heinz, T. Korn, A. Chernikov, E. Malic, and A. Knorr, “Excitonic linewidth and coherence lifetime in monolayer transition metal dichalcogenides,” *Nature Communications*, vol. 7, p. 13279, 2016.

-
- [176] T. Godde, D. Schmidt, J. Schmutzler, M. Aßmann, J. Debus, F. Withers, E. Alexeev, O. Del Pozo-Zamudio, O. Skrypka, K. Novoselov, *et al.*, “Exciton and trion dynamics in atomically thin MoSe₂ and WSe₂: effect of localization,” *Physical Review B*, vol. 94, no. 16, p. 165301, 2016.
- [177] E. A. Jagla, “Hysteresis loops of magnetic thin films with perpendicular anisotropy,” *Physical Review B*, vol. 72, no. 9, p. 094406, 2005.
- [178] D. MacNeill, J. T. Hou, D. R. Klein, P. Zhang, P. Jarillo-Herrero, and L. Liu, “Gigahertz frequency antiferromagnetic resonance and strong magnon-magnon coupling in the layered crystal CrCl₃,” *Physical Review Letters*, vol. 123, no. 4, p. 047204, 2019.
- [179] D. R. Klein, D. MacNeill, Q. Song, D. T. Larson, S. Fang, M. Xu, R. Ribeiro, P. C. Canfield, E. Kaxiras, R. Comin, *et al.*, “Enhancement of interlayer exchange in an ultrathin 2-dimensional magnet,” *Nature Physics*, 2019.
- [180] S. Ikeda, K. Miura, H. Yamamoto, K. Mizunuma, H. Gan, M. Endo, S. Kanai, J. Hayakawa, F. Matsukura, and H. Ohno, “A perpendicular-anisotropy CoFeB–MgO magnetic tunnel junction,” *Nature Materials*, vol. 9, no. 9, p. 721, 2010.
- [181] A. D. Kent, “Spintronics: perpendicular all the way,” *Nature Materials*, vol. 9, no. 9, p. 699, 2010.
- [182] S. Bhatti, R. Sbiaa, A. Hirohata, H. Ohno, S. Fukami, and S. Piramanayagam, “Spintronics based random access memory: a review,” *Materials Today*, vol. 20, no. 9, pp. 530–548, 2017.
- [183] A. A. High, E. E. Novitskaya, L. V. Butov, M. Hanson, and A. C. Gossard, “Control of exciton fluxes in an excitonic integrated circuit,” *Science*, vol. 321, no. 5886, pp. 229–231, 2008.
- [184] J. G. Roch, G. Froehlicher, N. Leisgang, P. Makk, K. Watanabe, T. Taniguchi, and R. J. Warburton, “Spin-polarized electrons in monolayer MoS₂,” *Nature Nanotechnology*, vol. 14, no. 5, p. 432, 2019.

